

IntechOpen

High Entropy Materials

Microstructures and Properties

Edited by Yong Zhang



High Entropy Materials - Microstructures and Properties

Edited by Yong Zhang

Published in London, United Kingdom

High Entropy Materials – Microstructures and Properties
<http://dx.doi.org/10.5772/intechopen.100682>
Edited by Yong Zhang

Contributors

Yoshimitsu Okazaki, Kiyoyuki Chinzei, Yu Yin, Andrej Atrens, Han Huang, Ming-Xing Zhang, Yong A Zhang, Xuehui Yan, Jian Wang, Kaisheng Ming, Shijian Zheng, Yuanying Yue, Agripa Hamweendo, Chiluba I. Nsofu, Terence Malama, Adrina Silva, Thiago Costa, Emmanuelle Feitosa, Paulo Monteiro Jr, Camila Konno, Cassio Silva, José Braga, Mohamed El Garah, Frederic Schuster, Frederic Sanchette, Wei Wang, Zhou Li, Shunmuga Priyan, Ibrahim Ondicho, Benard Alunda, Kahinga Kamau, Gedefaw Mebratie Bogale, Dagne Atnafu Shiferaw

© The Editor(s) and the Author(s) 2023

The rights of the editor(s) and the author(s) have been asserted in accordance with the Copyright, Designs and Patents Act 1988. All rights to the book as a whole are reserved by INTECHOPEN LIMITED. The book as a whole (compilation) cannot be reproduced, distributed or used for commercial or non-commercial purposes without INTECHOPEN LIMITED's written permission. Enquiries concerning the use of the book should be directed to INTECHOPEN LIMITED rights and permissions department (permissions@intechopen.com).

Violations are liable to prosecution under the governing Copyright Law.



Individual chapters of this publication are distributed under the terms of the Creative Commons Attribution 3.0 Unported License which permits commercial use, distribution and reproduction of the individual chapters, provided the original author(s) and source publication are appropriately acknowledged. If so indicated, certain images may not be included under the Creative Commons license. In such cases users will need to obtain permission from the license holder to reproduce the material. More details and guidelines concerning content reuse and adaptation can be found at <http://www.intechopen.com/copyright-policy.html>.

Notice

Statements and opinions expressed in the chapters are these of the individual contributors and not necessarily those of the editors or publisher. No responsibility is accepted for the accuracy of information contained in the published chapters. The publisher assumes no responsibility for any damage or injury to persons or property arising out of the use of any materials, instructions, methods or ideas contained in the book.

First published in London, United Kingdom, 2023 by IntechOpen
IntechOpen is the global imprint of INTECHOPEN LIMITED, registered in England and Wales,
registration number: 11086078, 5 Princes Gate Court, London, SW7 2QJ, United Kingdom

British Library Cataloguing-in-Publication Data

A catalogue record for this book is available from the British Library

Additional hard and PDF copies can be obtained from orders@intechopen.com

High Entropy Materials – Microstructures and Properties
Edited by Yong Zhang

p. cm.

Print ISBN 978-1-80356-110-3

Online ISBN 978-1-80356-111-0

eBook (PDF) ISBN 978-1-80356-112-7

We are IntechOpen, the world's leading publisher of Open Access books Built by scientists, for scientists

6,200+

Open access books available

168,000+

International authors and editors

185M+

Downloads

156

Countries delivered to

Our authors are among the
Top 1%

most cited scientists

12.2%

Contributors from top 500 universities



WEB OF SCIENCE™

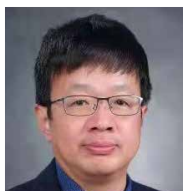
Selection of our books indexed in the Book Citation Index
in Web of Science™ Core Collection (BKCI)

Interested in publishing with us?
Contact book.department@intechopen.com

Numbers displayed above are based on latest data collected.
For more information visit www.intechopen.com



Meet the editor



Professor Zhang Yong prepared the first high-entropy single-crystal alloys. He proposed a balance criterion of high-entropy alloys to predict the phase formation for amorphous and solid solutions and found that trace rare earth elements can improve the glass-forming ability of metallic alloys. He has studied high-entropy alloy fibers and high-entropy alloy spectral selective absorption films and authored and edited several books. His book, *Advanced High-entropy Alloy Technology*, won first prize from the China Petroleum and Chemical Industry Federation, first prize in Natural Science from the Ministry of Education, and second prize from the National Natural Science Foundation of China. Professor Yong is a fellow member of the Chinese Materials Research Society and a committee member of the Chinese Nuclear Society. He has organized and served as chairman of numerous conferences on high-entropy alloys and serration behavior. He is a doctoral supervisor, a flexibly appointed professor for the North Minzu University, China, a scientific special commissioner of Guangdong Province, and a guest professor at the North University of China. Professor Yong studies serration behavior, high-throughput technology, and collective effect in materials science.

Contents

Preface	XI
Section 1 Fundamentals	1
Chapter 1 Microstructures and Deformation Mechanisms of FCC-Phase High-Entropy Alloys <i>by Kaisheng Ming, Shijian Zheng and Jian Wang</i>	3
Chapter 2 Cost-Effective Fe-Rich High-Entropy Alloys: A Brief Review <i>by Yu Yin, Andrej Atrens, Han Huang and Ming-Xing Zhang</i>	29
Chapter 3 Breaking the Property Trade-Offs by Using Entropic Conceptions <i>by Yong Zhang and Xuehui Yan</i>	51
Chapter 4 Solid Solution Strengthening in High-Entropy Alloys <i>by Ibrahim Ondicho, Benard Alunda and Kahinga Kamau</i>	67
Section 2 Processing	85
Chapter 5 Proposition of a Growth Law as a Function of Solidification Parameters for Monotectic Alloy Systems <i>by Adrina Silva, José Braga, Paulo Monteiro Jr, Cassio Silva, Camila Konno, Thiago Costa and Emmanuelle Feitosa</i>	87
Chapter 6 High Entropy Thin Films by Magnetron Sputtering: Deposition, Properties and Applications <i>by Mohamed El Garah, Frederic Schuster and Frederic Sanchette</i>	107

Chapter 7	127
Optimization of Retained Austenite and Corrosion Properties on EN-31 Bearing Steel by Cryogenic Treatment Process <i>by Shunmuga Priyan Murugan</i>	
Section 3	141
Modelling and Calculations	
Chapter 8	143
Simulation and Calculation for Predicting Structures and Properties of High-Entropy Alloys <i>by Yong Zhang and Yuanying Yue</i>	
Chapter 9	163
CALPHAD as a Toolbox to Facilitate the Development of HEAs <i>by Wei Wang and Zhou Li</i>	
Section 4	187
Applications	
Chapter 10	189
Development of Orthopedic Implants with Highly Biocompatible Ti Alloys <i>by Yoshimitsu Okazaki and Kiyoyuki Chinzei</i>	
Chapter 11	227
High-Entropy Alloys for Bone Tissue Engineering: Recent Developments in New Methods of Manufacture <i>by Agripa Hamweendo, Chiluba I. Nsofu and Terence Malama</i>	
Chapter 12	237
Iron-Based Superconductors <i>by Gedefaw Mebratie Bogale and Dagne Atnafu Shiferaw</i>	

Preface

Entropy is an important physical parameter to reflect the disordered state of a certain system, which is mainly expressed in three different forms: Clausius entropy, Boltzmann entropy, and Shannon entropy. Clausius entropy originated from the second law of thermodynamics, which describes the heat flow from a high-temperature region to a low-temperature region. The equation is:

$$dS = -dQ/T$$

where Q is heat and T is the absolute temperature.

Boltzmann entropy is based on the thermodynamic statistics principle, which is in the form of:

$$S_{\text{Boltzmann}} = k \ln W$$

where k is the Boltzmann's constant ($k = 1.38 \times 10^{-23} \text{ J/K}$) and W is the thermodynamic probability, which is the total number of micro-states corresponding to a certain macro-state.

The expression of Shannon entropy is:

$$S_{\text{Shannon}} = -k \sum P_i \ln P_i$$

where P_i is the probability of occurrence of the i -th information of the information source. Shannon entropy mainly measures the information; the greater the entropy, the more the randomness and the less the information.

For entropic materials, the content of each component X_i is used to replace the P_i in the Shannon entropy equation as:

$$S = -R \sum X_i \ln X_i$$

where R is the gas constant ($R = 8.314 \text{ J/mol}\cdot\text{K}$) and X_i is the content of the i -th component (at. %).

For a random solid solution, the possibility of the i -th component to occupy the fixed lattice site is proportional to its content. High-entropy materials are closely related to information entropy.

This book summarizes recent developments in high-entropy materials, including their properties, processing, modeling, and applications.

Yong Zhang
North Minzu University and State Key Laboratory
for Advanced Metals and Materials,
University of Science and Technology Beijing,
Beijing, China

Section 1

Fundamentals

Chapter 1

Microstructures and Deformation Mechanisms of FCC-Phase High-Entropy Alloys

Kaisheng Ming, Shijian Zheng and Jian Wang

Abstract

Strength and ductility are the most fundamental mechanical properties of structural materials. Most metallurgical mechanisms for enhancing strength often sacrifice ductility, referred to as the strength–ductility trade-off. Over the past few decades, a new family of alloys—high-entropy alloys (HEAs) with multi-principal elements, has appeared great potential to overcome the strength–ductility trade-off. Among various HEAs systems, CrFeCoNi-based HEAs with a face-centered cubic (fcc) structure exhibit a great combination of strength, ductility, and toughness via tailoring microstructures. This chapter summarizes recent works on realizing strength–ductility combinations of fcc CrFeCoNi-based HEAs by incorporating multiple strengthening mechanisms, including solid solution strengthening, dislocation strengthening, grain boundary strengthening, and precipitation strengthening, through compositional and microstructural engineering. The abundant plastic deformation mechanisms of fcc HEAs, including slips associated with Shockley partial dislocation and full dislocations, nanotwinning, martensitic phase transformation, deformation-induced amorphization, and dynamically reversible shear transformation, are reviewed. The design strategies of advanced HEAs are also discussed in this chapter, which provides a helpful guideline to explore the enormous number of HEA compositions and their microstructures to realize exceptional strength–ductility combinations.

Keywords: high-entropy alloys, strength, ductility, twinning, phase transformation, amorphization, reversible shear transformation

1. Introduction

Developing structural materials with both high-strength and ductility could mitigate the ecological and economical concerns for decreasing weight and improving energy efficiency. Unfortunately, these properties are generally mutually exclusive, i.e., increasing strength will inevitably lead to ductility loss, an effect referred to as the strength–ductility trade-off [1–4]. Various strengthening mechanisms, including solid solution strengthening, dislocation strengthening, grain boundary strengthening, precipitation strengthening, twinning, and phase transformation-induced hardening, have been widely utilized to produce high-strength and high-ductility alloys that are based on one principal element [5]. Recently, a new idea—high-entropy alloys (HEAs),

has appeared that shows great potential to overcome the strength–ductility trade-off, and thus break through the mechanical property limits [6–13]. HEAs were founded independently by two different research groups in 2004 [6, 7], which emphasize the unexplored regions in the center of multi-element phase diagrams, in which all elements are concentrated and there is no base element. HEAs are generally defined as an alloy that is composed of four or more elements in an equiatomic or near-equiatomic composition [7]. Each HEA can be considered as a new alloy base because its properties can be further optimized by minor elemental additions, similar to alloying in conventional alloys. HEAs provide near-infinite new alloy bases for designing structural materials with excellent performance. Depending on the composition and microstructure, HEAs display attractive mechanical properties, and possible combinations of some properties, including high strength/hardness, outstanding wear resistance, excellent fatigue resistance, exceptional high-temperature strength, good structural stability, good corrosion and oxidation resistance, and high radiation tolerance [8, 10, 12, 14]. Particularly, single-phase face-centered cubic (fcc) HEAs and medium-entropy alloys (MEAs) based on the transition metal elements Cr, Mn, Fe, Co, or Ni generally display some of the best mechanical properties reported to date [9–12, 15–25]. For example, equiatomic CrMnFeCoNi HEA and CoCrNi MEA possess exceptional combinations of tensile strength and ductility (tensile strength of ~ 1 GPa as well as ductility exceeding 60%) at 77 K, and ultra-high fracture toughness at both room temperature and 77 K ($K_{IC} > 200$ MPa \sqrt{m}), making them one class of the toughest metallic materials reported so far [17, 23, 26]. Such exceptional mechanical properties are attributed to continuous steady strain-hardening, resulting from extensive dislocation activities and deformation-induced nanotwinning [18, 21, 22, 27]. These fcc-structured HEAs can be used as ideal alloy bases to design high-strength and high-ductility structural materials through further compositional and microstructural engineering.

Intensive studies have been invested in overcoming the strength–ductility trade-off of the single-phase fcc CrFeCoNi-based HEAs through tailoring the chemical composition and microstructure [9–12, 15–24]. It has been reported that metastable high-entropy dual-phase alloys can overcome the strength–ductility trade-off by interface hardening and transformation-induced hardening, realized by reducing the stacking fault energy (SFE) via tailoring chemical composition [15, 19, 24, 28–33]. The tensile strength and ductility are simultaneously enhanced due to heterogeneous microstructures, such as gradient nanotwins, gradient nano-grains, or recrystallized and non-recrystallized grains arranged in hierarchical structures with characteristic dimensions spanning from submicron scale to micro-scale, that are obtained by cold-rolling and annealing [9, 16, 27, 34, 35]. Note that single-phase fcc CrFeCoNi-based HEAs often have a very low SFE, which promotes deformation-induced nanotwinning and martensitic phase transformation [36–42]. The simultaneous increase in tensile strength and ductility is related to the enhanced strain-hardening capability enabled by nanotwinning and/or phase transformation. However, they generally possess very low yield strength since the nanotwinning and phase transformation cannot be activated at the early stages of plastic deformation [12].

Multiple strengthening mechanisms (such as solid solution strengthening, dislocation strengthening, grain boundary strengthening, and precipitation strengthening, et al.) show great potential to enhance the yield strength and tensile strength of fcc CrFeCoNi-based HEAs while maintaining their excellent ductility and strain-hardening capability [43–62]. In addition, some new strengthening mechanisms are also proposed to improve the mechanical properties, such as magnetic hardening [60]. This chapter summarizes recent works on realizing strength–ductility combinations of fcc

CrFeCoNi-based HEAs by incorporating multiple strengthening mechanisms, achieved through compositional and microstructural engineering. The abundant plastic deformation modes of fcc HEAs, including slips associated with Shockley partial dislocation and full dislocations, twinning, martensitic phase transformation, deformation-induced amorphization, and dynamically reversible shear transformation, are also summarized. We also demonstrate some HEA design strategies to provide guidelines for exploring the enormous number of HEA compositions and their microstructures to realize exceptional strength–ductility combinations.

2. Strengthening via tailoring composition and microstructure

2.1 Ductile nanoprecipitates

Single-phase fcc HEAs generally exhibit excellent ductility and strain-hardening capability but low yield strength at room temperature. Extensive studies demonstrate that nanoprecipitation strengthening is one of the most effective approaches to strengthen HEAs without apparent ductility loss. For example, Ming et al. [61] introduced highly dispersed nano-sized, coherent precipitates in the grain interior of coarse-grained fcc CrFeCoNi-based HEAs (grain size ~ 1 mm) via alloying a small addition of Al and Ti elements, which realizes exceptional combinations of strength and ductility (**Figure 1**). Yang et al. [47] produce a CrFeCoNi-based HEA with a superb yield strength of above 1.0 GPa while maintaining 50% ductility in tension at room temperature via introducing high-density ductile multicomponent intermetallic nanoparticles with coherent phase boundaries, enabled by alloying a small addition of Ti and Al elements. The size and distribution of nanoprecipitates can be tailored by the content of alloying elements (Ti and Al), aging temperature, and aging time [61]. As shown in **Figure 1a–g**, the strength and ductility can be optimized corresponding to the aging time-dependent size and spacing of nanoprecipitates in an $\text{Al}_{0.2}\text{Co}_{1.5}\text{CrFeNi}_{1.5}\text{Ti}_{0.3}$ HEA. When aged at 800°C for 1–5 h, numerous uniformly dispersed, nano-sized, spherical L_{12} precipitates are formed in coarse grains (grain size ~ 1 mm), which results in a significant increase in both yield strength and ultimate tensile strength without apparent sacrificing of ductility (**Figure 1a, b, f**). With increasing aging time, the average diameter of precipitates increases from 6 nm at 1 h of aging to 51 nm at 100 h of aging (**Figure 1e**). **Figure 1f** presents that aging time does not show a significant effect on the yield strength and ultimate tensile strength, but increasing aging time results in an apparent decrease in ductility. As shown in **Figure 1g**, the strain-hardening rate obviously increases with increasing aging time, in particular, for the aging time equal and longer than 5 h. The samples aged for 1–5 h exhibit superior combinations of strength and ductility (yield strength of ~ 760 MPa, ultimate tensile strength of ~ 1160 MPa, elongation of $\sim 40\%$).

The nature of dislocation interaction with the nanoprecipitates in $\text{Al}_{0.2}\text{Co}_{1.5}\text{CrFeNi}_{1.5}\text{Ti}_{0.3}$ HEA samples is revealed by using transmission electron microscopy (TEM) analysis, as shown in **Figure 2**. The TEM bright-field image of the sample aging at 800°C for 1 h (**Figure 2a**) shows high-density dislocations tangled with stacking faults after tensile deformation to fracture. As shown in **Figure 2b**, original spherical precipitates have changed to an irregular shape after tensile deformation, which indicates the dislocations cutting through precipitates. In contrast to dislocation cutting through nano-sized precipitates, dislocations bypass relatively large precipitates by looping them in the sample aging at 800°C for 50 h, as demonstrated in **Figure 2c**. **Figure 2d**

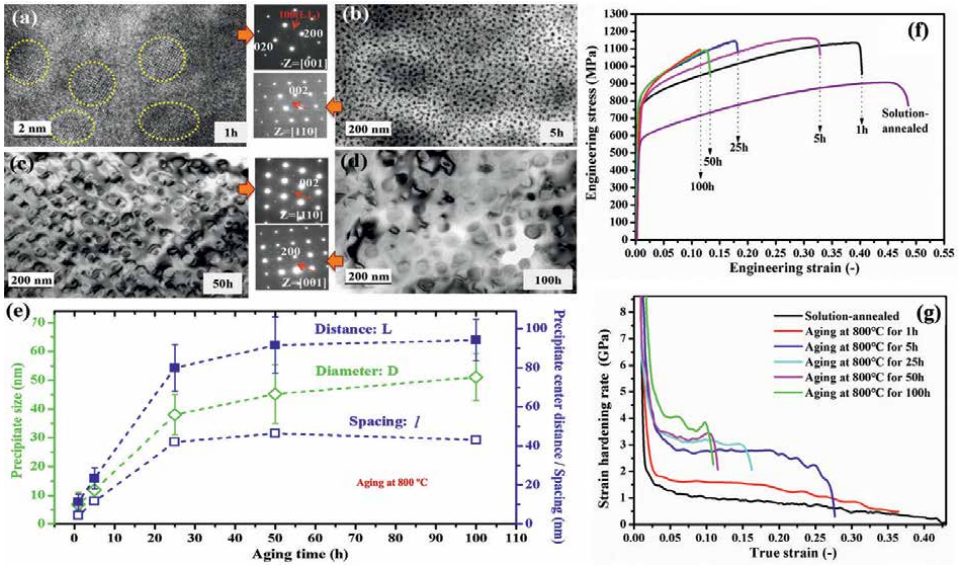


Figure 1. TEM images of the $Al_{0.2}Co_{1.5}CrFeNi_{1.5}Ti_{0.3}$ HEA after aging at $800^{\circ}C$ for: (a) 1 h (b) 5 h, (c) 50 h, and (d) 100 h, with the corresponding selected area electron diffraction patterns inset. (e) Influence of aging time on the diameter of the precipitate (D), separation distance (L) between the centers of neighboring precipitates, and edge-to-edge inter-precipitate distance (l). (f) Engineering stress–strain curves of the solution-annealed and aged samples. (g) Variation of strain-hardening rates with plastic strain [61].

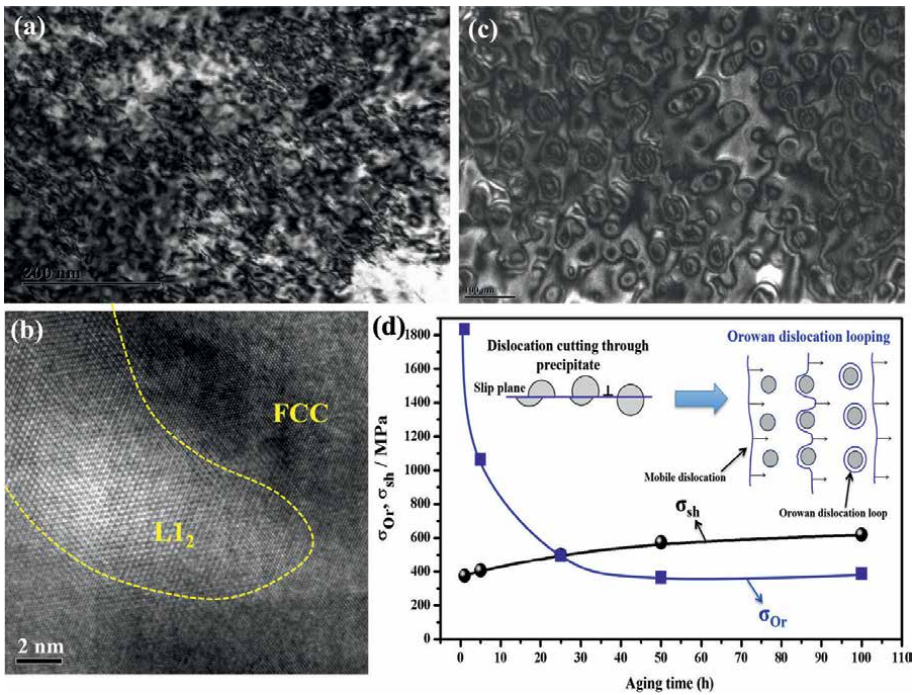


Figure 2. (a) TEM image of the 1 h aged $Al_{0.2}Co_{1.5}CrFeNi_{1.5}Ti_{0.3}$ HEA at a tensile strain of 36%, (b) HRTEM image of a precipitate with an irregular shape. (c) TEM image of the 50 h aged sample at a tensile strain of 3%. (d) Variation of precipitate shearing stress (σ_{sh}) and Orowan dislocation looping stress (σ_{Or}) with aging time [61].

schematically illustrates that dislocation cutting through precipitates is the primary strengthening mechanism for the 1 h and 5 h aged HEA with small precipitates (diameter < 10 nm), while the dominant strengthening mechanism is dislocation bypassing precipitates by looping them in HEAs aged for >25 h with large precipitates (diameter > 30 nm). Based on the tensile testing and TEM characterizations, it can be concluded that nanoscale coherent precipitation strengthening is a very effective approach for strengthening coarse-grained fcc-structured HEAs without loss of ductility. The exceptional combinations of strength and ductility can be achieved via introducing uniformly distributed, nano-sized, coherent precipitates in the coarse-grained HEAs, where gliding dislocations cut through nano-sized coherent precipitates. In contrast, with increasing the size of precipitates, the ductility is reduced due to the strong barrier of large precipitates to dislocation motion where gliding dislocations bypass a precipitate by looping it, resulting in dislocations pileups at precipitate-matrix interfaces which generate high stress/strain concentration and micro-crack initiation.

It should be noted that the sluggish diffusion effect in HEAs enables easily tailoring the size of precipitates by adjusting aging processing and optimizing compositions. Recently, the coarsening kinetics and thermal stability of nanoscale precipitates in HEAs at elevated temperatures have also been widely studied to explore their applications at high temperatures [63–66]. In a word, precipitation strengthening is one of the most promising approaches for enhancing the mechanical properties of fcc HEAs to meet the requirements for engineering applications both at room temperatures and high temperatures.

2.2 Brittle intermetallic compounds

The original concept employed in the HEAs design is to suppress the formation of brittle intermetallic compounds which can lead to poor ductility [6, 7]. Unfortunately, most HEAs reported to date contain various brittle intermetallic compounds [63–66]. Therefore, it is required to manipulate the intermetallic compounds to reconcile the strength and ductility of HEAs. It has been shown that the brittle but hard intermetallic compound μ phase can be effectively used as a strengthening unit in CrFeCoNiMo HEAs while relieving its harmful effect on ductility by manipulating its dimension and distribution via tailoring Mo contents [62, 67–69]. Moreover, by further coupling solid solution hardening and nanotwinning induced hardening, a superb yield strength–tensile strength–ductility combination is realized [62]. As shown in **Figure 3**, the dimension and distribution of the μ phase can be tuned through thermal-mechanical processing and annealing. The μ phases grow mainly at boundaries (grain boundaries, triple junctions, and annealing twin boundaries), and secondarily in the interior of grains. The corresponding engineering stress–strain curves in **Figure 4a, b** demonstrate that dual-phase (fcc matrix + nanoscale μ phase) $\text{Cr}_{15}\text{Fe}_{20}\text{Co}_{35}\text{Ni}_{20}\text{Mo}_{10}$ (Mo_{10}) HEA displays high strength (yield strength of 0.8–1.3 GPa and ultimate tensile strength of 1.1–1.4 GPa) but moderate ductility (elongation to fracture is approximately 13–28%). The single-phase fcc $\text{Cr}_{12.5}\text{Fe}_{20}\text{Co}_{42.5}\text{Ni}_{20}\text{Mo}_5$ (Mo_5) HEAs have superb ductility (elongation to fracture of 45–75%) but moderate strength (yield strength of 0.3–0.8 GPa and ultimate tensile strength of 0.7–1.0 GPa). **Figure 4c** demonstrates that dual-phase Mo_{10} HEAs annealed at 850–1000°C exhibit a higher strain-hardening rate than single-phase Mo_5 HEAs, and Mo_{10} HEA annealed at 1150°C as the true strain is less than half the maximum elongation. The high strain-hardening rate in Mo_{10} HEAs annealed at 850–1000°C is ascribed to the formation of distributed μ phase precipitates while the low strain-hardening

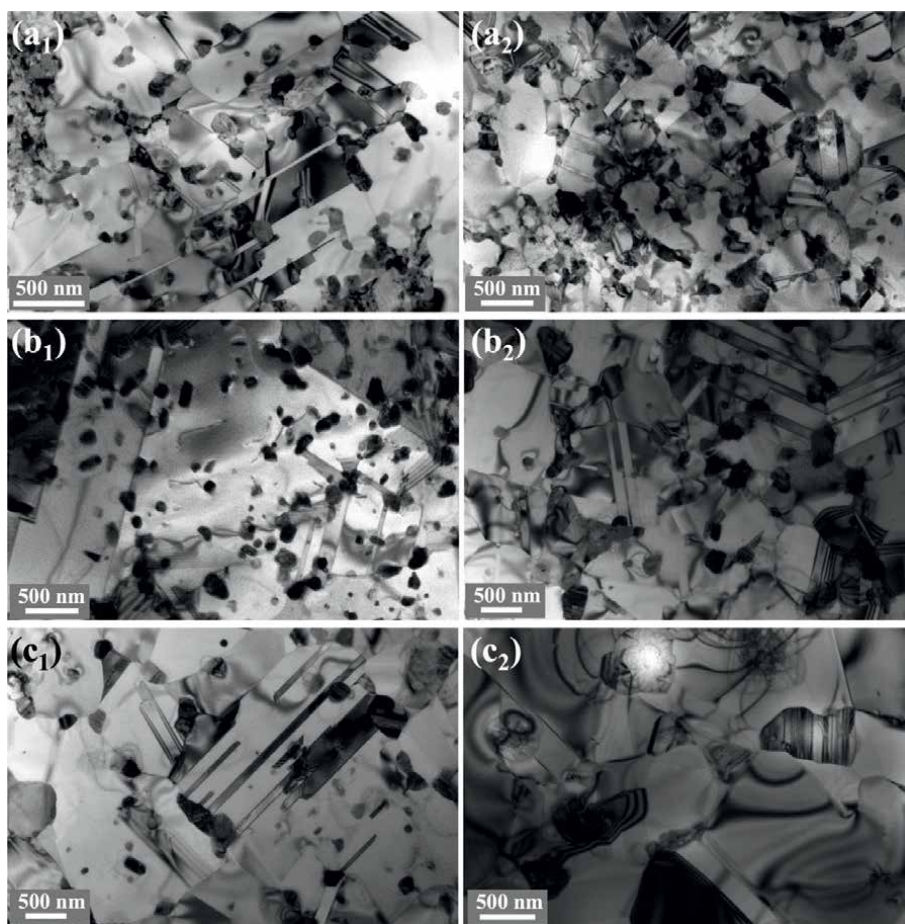


Figure 3. TEM images of cold-rolled Mo_{10} HEAs after annealing at 800°C for (a₁) 5 min, (a₂) 1 h; 900°C for (b₁) 5 min, (b₂) 1 h; 1000°C for (c₁) 5 min, (c₂) 1 h [62].

rate in Mo_{10} HEAs annealed at 1150°C is due to the decomposition and disappearance of clustered μ phase precipitates. **Figure 4d** compares the mechanical properties of the dual-phase Mo_{10} HEA and single-phase Mo_5 HEA with various other fcc HEAs [70–75]. An exceptional combination of strength and ductility of Mo_{10} and Mo_5 HEAs is attributed to the synergetic effect of solid solution strengthening, precipitation hardening, and twinning-induced hardening. The solution strengthening effect of the Mo addition in single-phase Mo_{10} alloys is evidenced by the higher strain-hardening rate of single-phase Mo_{10} alloy after true strain exceeds 13%

(**Figure 4c**). **Figure 5a, b** demonstrates dislocations are bowing out or piled up at the μ phase interfaces. It is noted that μ precipitates are plastically non-shearable by gliding dislocations, which accounts for the high strength of Mo_{10} alloy according to the precipitation strengthening mechanism and the high strain-hardening rate at the early stage of plastic deformation. As demonstrated in **Figure 5c**, numerous deformation nano-twins are observed in single-phase Mo_{10} alloy at a strain of 25%, which provides a steady source of strain-hardening by blocking the motion of dislocations.

Other brittle intermetallic compounds, such as the sigma phase, Laves phases, have been also frequently observed in HEAs, which generally deteriorate the ductility

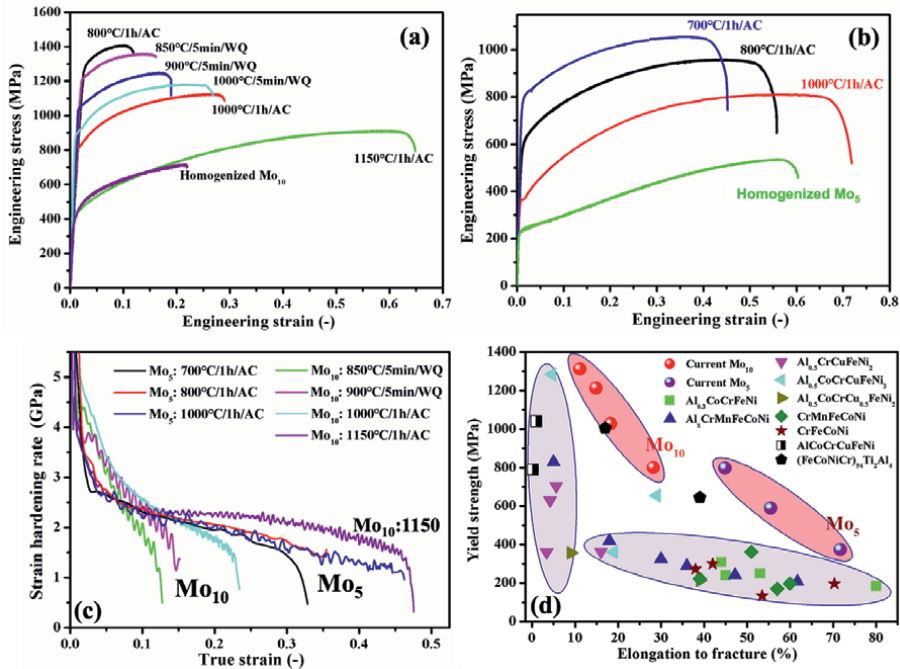


Figure 4. Engineering stress–strain curves for the (a) homogenized and recrystallized Mo₁₀ alloys and (b) Mo₅ alloys. (c) the strain-hardening rates of Mo₁₀ and Mo₅ alloys as a function of plastic strain. (d) Comparing the yield strength and elongation of the Mo₁₀ and Mo₅ alloys with various HEAs [62].

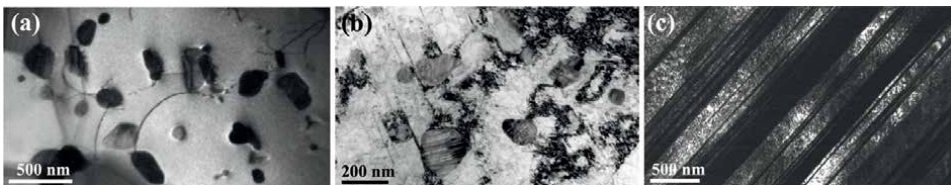


Figure 5. TEM bright-field images of annealed Mo₁₀ alloy at tension strains of 15–25%, (a) bow-out of gliding dislocations, (b) pile-up of dislocations at interfaces, and (c) high-density deformation nano-twins [62].

[76–80]. Similarly, if the size, distribution, and morphology of intermetallic compounds can be tailored via controlling the chemical composition and thermomechanical treatment, an excellent combination of strength and ductility can be achieved in multi-component HEAs.

2.3 Hierarchically heterogeneous microstructures

Hierarchically heterogeneous microstructures at scales from a few nanometers to hundreds of micrometers can be easily produced in fcc HEAs by conventional cold work and annealing treatment, which could generate superior mechanical properties to those with simple microstructures due to the hetero-deformation induced strengthening [81]. As shown in **Figure 6**, single-phase fcc Cr₂₀Fe₆Co₃₄Ni₃₄Mo₆ HEAs with hierarchical microstructures that comprise high-density annealing

nanotwins in recrystallized fine grains (grain size $\sim 1 \mu\text{m}$), and dislocation walls and stacking faults in non-fully recrystallized fine grains are produced by cold-rolling and annealing [82]. The formation of numerous annealing nanotwins and stacking faults is obviously attributed to the very low SFE of the $\text{Cr}_{20}\text{Fe}_6\text{Co}_{34}\text{Ni}_{34}\text{Mo}_6$ alloy. The addition of Mo in the Cr-Fe-Co-Ni system is found to be very effective in retarding the recrystallization and grain growth, promoting the formation of recrystallized fine grains. Such hierarchical microstructures can be generated in various single-phase fcc HEAs with low SFE by cold-rolling and annealing.

Comparing the mechanical properties of the samples with hierarchical microstructures and fully recrystallized coarse-grained microstructures, the former exhibit exceptional combinations of yield strength-ultimate tensile strength-ductility. As shown in **Figure 7a**, the single-phase HEAs with hierarchical microstructure (annealed

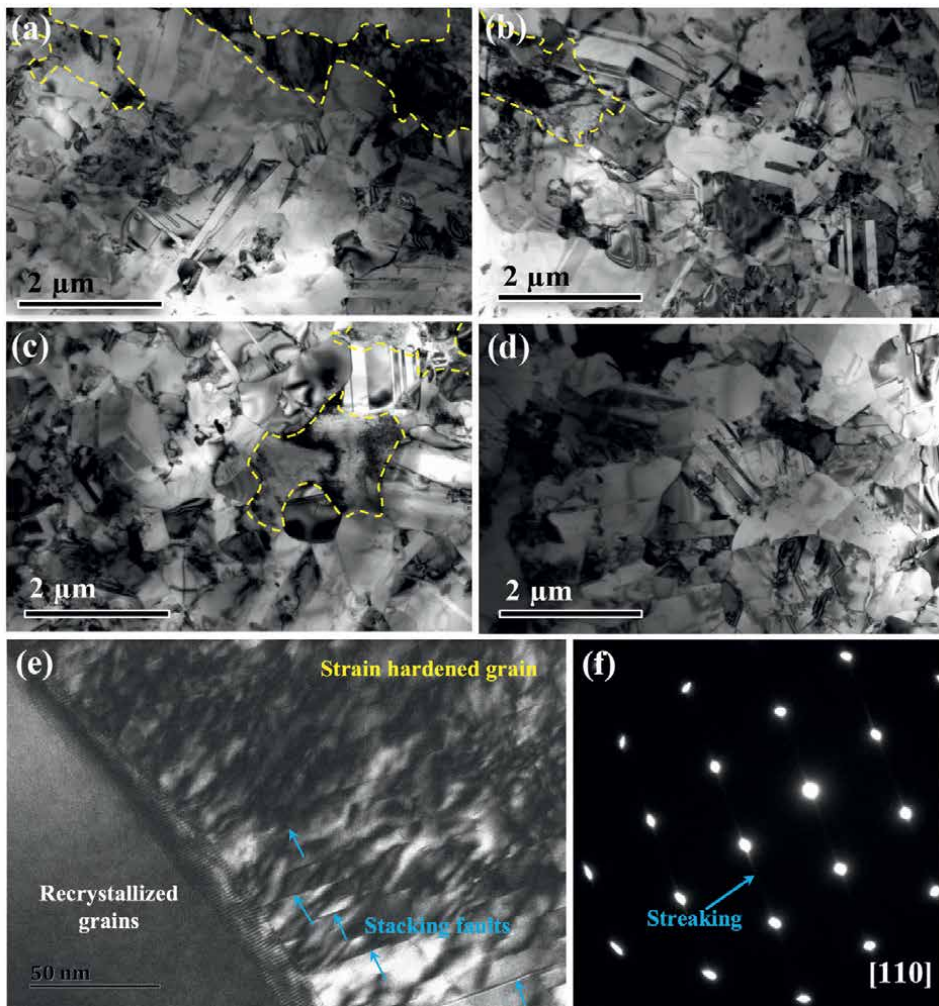


Figure 6. TEM images of the cold-rolled $\text{Cr}_{20}\text{Fe}_6\text{Co}_{34}\text{Ni}_{34}\text{Mo}_6$ HEAs after annealing at (a) 675°C for 1 h; (b) 700°C for 0.5 h; (c) 700°C for 1 h; (d) 800°C for 1 h. (e) Higher magnification micrograph of the interface between fully recrystallized grain and non-fully recrystallized grain, showing high density of dislocations, (f) selected area electron diffraction pattern patterns corresponding to non-fully recrystallized grain in (e) [82].

at 675–800°C for 3 min, 0.5 h, 1 h, 5 h, or 10 h) exhibit a very high strength ($Y_S = 0.95\text{--}1.1$ GPa and $UTS = 1.2\text{--}1.3$ GPa, **Figure 7a₁**) as well as a high ductility (EL is around 30–40%), which is much superior to that of the HEAs (annealed at 800–1150°C for 1 h) with simple fully recrystallized microstructures (**Figure 7a₂**). Such high yield strengths exceeding 1.0 GPa at enhanced ductility (30%) in single-phase HEAs are comparable to the nanoprecipitation strengthened HEAs (**Figure 7b₁, b₂**) [17, 23, 70, 71, 83–89]. This indicates that enhancing yield strength while retaining good ductility of single-phase fcc HEAs can be achieved by developing hierarchical microstructures. The grain boundaries, annealing nanotwins, and dislocation walls play important roles in enhancing the strength, ductility, and strain-hardening capability of the annealed sample with hierarchical microstructure. **Figure 7c** plots the yield strength (σ_y) as a function of the grain size (d), which follows the well-known Hall–Petch relationship, $\sigma_y = \sigma_0 + k \cdot d^{-1/2}$. The σ_0 is 246 MPa. The Hall–Petch coefficient $k = 743 \text{ MPa} \cdot \mu\text{m}^{1/2}$ is higher than that of most fcc metals ($600 \text{ MPa} \cdot \mu\text{m}^{1/2}$) [90], which indicates that the grain-boundary strengthening mechanism is very effective for improving yield strength. Microstructure characterizations reveal that both twin boundaries and dislocation walls act as strong barriers for dislocation motion, strengthening the alloy, as shown in **Figure 8**. **Figure 8a** shows a large number of stacking faults (marked by red arrows) around twin boundaries. The enlarged HRTEM image in **Figure 8b** shows high-density stacking faults in the twin and matrix, indicating slip transmission associated with dislocations crossing through the coherent twin boundaries (CTBs). Consequently, atomically flat CTBs develop stepped or serrated CTBs that contain interface defects. These interfacial defects along stepped or serrated CTBs then provide sources for nucleating and blocking dislocations. **Figure 8c, d** shows that dislocation

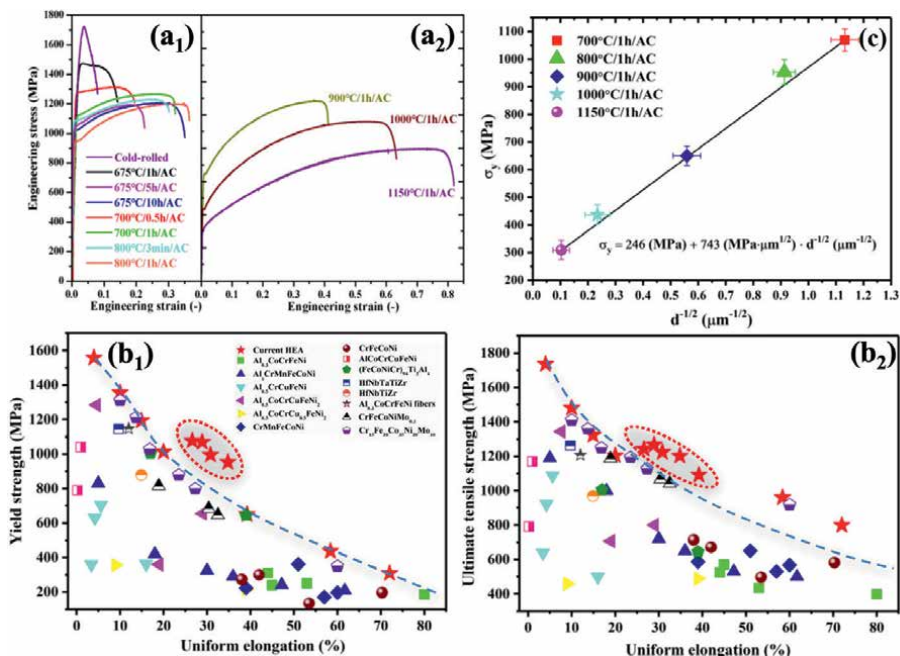


Figure 7. (a₁, a₂) engineering stress–strain curves of the cold-rolled and annealed $\text{Cr}_{20}\text{Fe}_6\text{Co}_{34}\text{Ni}_{34}\text{Mo}_6$ HEAs at various temperatures of 675–1150°C. (b₁, b₂) yield strength and ultimate tensile strength versus uniform elongation of annealed alloys compared with various HEAs. (c) the variation of yield strength with average grain size [82].

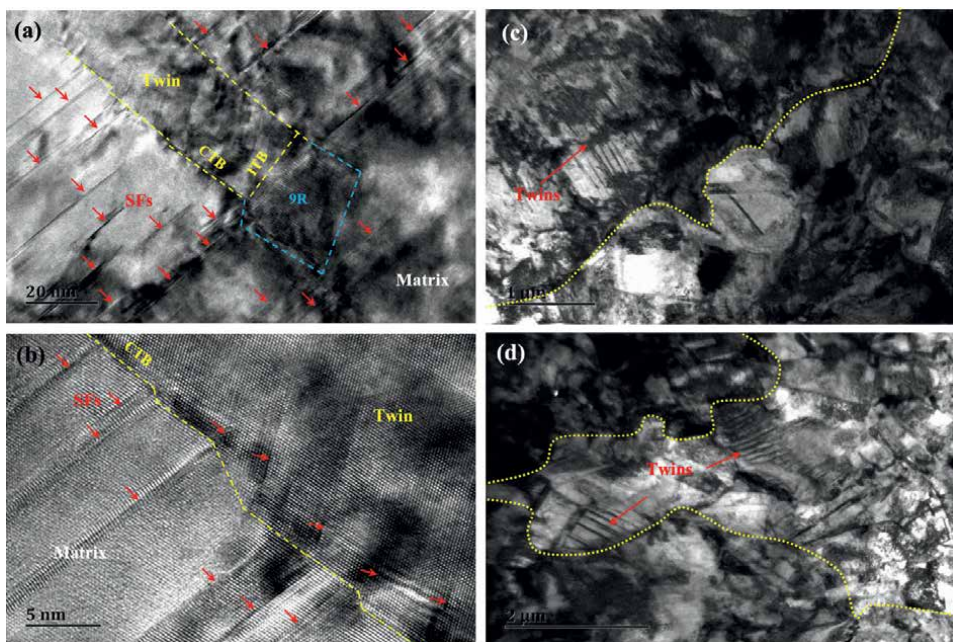


Figure 8. (a, b) TEM micrographs of the recrystallized grains in annealed $\text{Cr}_{20}\text{Fe}_6\text{Co}_{34}\text{Ni}_{34}\text{Mo}_6$ HEAs (700°C for 1 h) at a strain of ~30%. (c, d) TEM micrographs of non-fully recrystallized grains at strains of 15–30% [82].

walls act as sources for dislocations and deformation twins at large deformation stages, contributing to strain-hardening by continually introducing new interfaces and blocking the motion of dislocations. The enhanced strength enables the production of dislocations at serrated/stepped CTBs, preventing the early onset of necking instability. Therefore, the strength is enhanced without apparent ductility loss.

Other hierarchically heterogeneous microstructures, such as gradient grain structure, gradients in twin and dislocation densities, hierarchical nano-twins, could be introduced into fcc HEAs via surface mechanical grinding treatment, which contributes to the strain hardening capability and thus exceptional strength–ductility combinations, owing to the hetero-deformation induced strengthening. These results demonstrate that engineering the hierarchical microstructure should be an efficient strategy for enhancing the strength and ductility of single-phase fcc HEAs with low and medium SFE.

2.4 Shear transformation bands

Depending on chemical composition and deformation temperature, fcc HEAs with relatively low SFE generate various types of nanoscale shear transformation bands during plastic deformation, including stacking fault bands, nanotwin bands, phase transformation bands, deformation bands with ultrahigh density dislocation, and amorphous bands [10]. The shear transformation banding plays an important role in enhancing strain-hardening capability and thus contributes to enhanced strength and ductility simultaneously. The typical examples are twinning-induced plasticity (TWIP) and transformation-induced plasticity (TRIP) effects in metastable HEAs, which could overcome the long-standing strength–ductility dilemma

[18, 21, 22, 27]. For example, the strength, ductility, and toughness of single-phase fcc CrMnFeCoNi HEAs can be improved simultaneously with decreasing temperature from room temperature to 77 K, owing to the transition of deformation mechanisms from dislocation slip to nanotwinning [17, 20, 21, 23]. As shown in **Figure 9**, the formation of stacking faults, nanotwinning, and martensitic phase transformation could be generated sequentially in a non-equiatomeric CrMnFeCoNi HEA with increasing tensile strains at low temperatures, leading to the formation of various nanoscale bands [91]. Such shear transformation banding, by continually introducing new interfaces and decreasing the mean free path of dislocations during tensile testing (“dynamic Hall–Petch”), produces a high degree of work-hardening and a significant increase in the ultimate tensile strength [92–94].

Recently, amorphous bands (one type of shear transformation bands) have been observed in a non-equiatomeric CrMnFeCoNi HEA under tensile deformation at 93 K [91]. These amorphous bands are generated by deformation-induced solid-state amorphization, as summarized in **Figure 10**. The nanoscale amorphous bands, stacking fault bands, nanotwin bands, phase transformation bands can be generated simultaneously in HEAs, which contributes to enhanced strength, ductility, and strain-hardening rate synergistically. In particular, the nanoscale amorphous bands exhibit much higher thermal stability than nanotwins and phase transformation bands. Amorphous bands ensure the enhanced strength and good ductility of high-temperature tempered samples. Amorphous bands can plastically co-deform with the matrix. The interfaces between the amorphous band and fcc matrix provide not only strong barriers for dislocation motion, strengthening materials, but also natural sinks of dislocations, disrupting stress concentrations and delaying decohesion and fracture initiation. These results demonstrate that engineering amorphous bands could be an efficient strategy in remaining enhanced mechanical properties of fcc HEAs at high temperatures.

In addition, Ming et al. design nano-laminated dual-phase structures in a non-equiatomeric CrMnFeCoNi HEA via dynamically reversible shear transformations associated with reversible martensitic phase transformation and nanotwinning. The detailed mechanism for dynamically reversible shear transformations can be seen in the following sections. The nano-laminated dual-phase structures could evade the

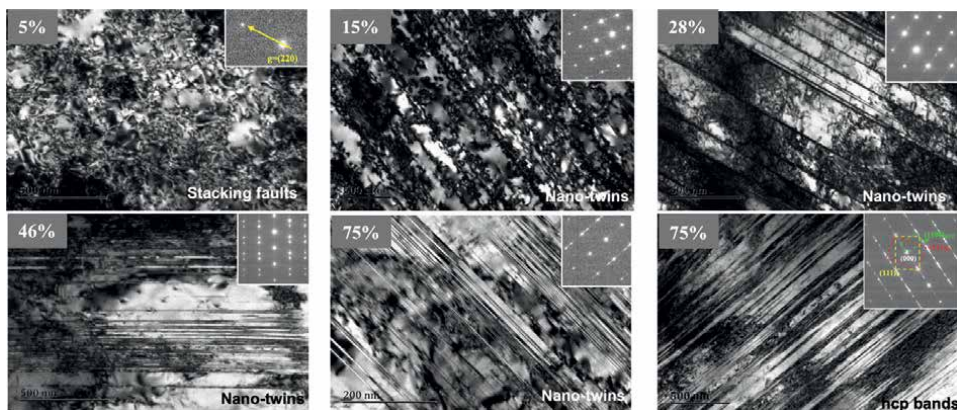


Figure 9. TEM images of the single-phase fcc CrMnFeCoNi HEA after tension to different strains at 93 K, show the sequential formation of stacking faults, nanotwinning, and martensitic phase transformation [91].

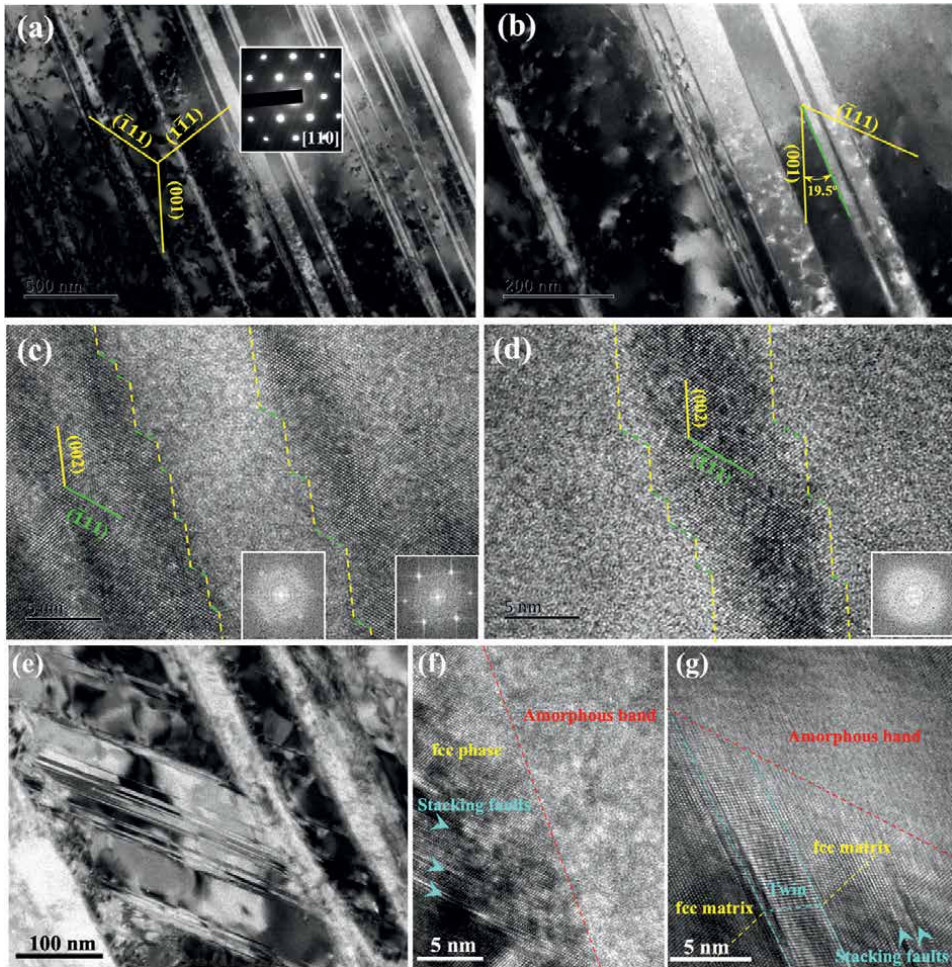


Figure 10. (a, b) TEM images of the non-equiatomic CrMnFeCoNi HEA after tension to a strain of 36% at 93 K, (c, d) the corresponding high-resolution TEM images showing the amorphous bands. (e–g) TEM images show the interactions of stacking faults, nano-twins, and amorphous bands [91].

strength–ductility dilemma due to the synergistic operations of the TRIP effect, TWIP effect, and associated with “dynamic Hall–Petch” effect. In a word, the abundant deformation mechanisms of fcc HEAs, as described below, enable us to design various types of microstructures to achieve an exceptional combination of strength and ductility.

3. Deformation mechanisms

Similar to conventional fcc metals and alloys, fcc HEAs plastically deform through three deformation mechanisms: dislocation slip, twinning, and phase transformation. Recently, some unique deformation pathways of deformation-induced amorphization and dynamically reversible shear transformations which rarely occur in conventional materials are found in fcc HEAs.

3.1 Deformation-induced amorphization

Various mechanical processes can partially or fully amorphized crystalline materials, including high-pressure treatments, severe plastic deformation, or mechanical alloying [95–103]. From the thermodynamic driving force perspective, amorphization starts from the massive displacement of atoms into metastable positions and occurs when the free energy of the crystalline phase is higher than that of the amorphous phase [104–106]. From the kinetic hindrance perspective, the formation of a metastable amorphous phase requires the kinetic hindrances which block the formation of a more stable equilibrium crystalline phase [104]. It should be noted that deformation-induced solid-state amorphization under stresses can take place in the elastic regime at an extremely high strain rate, or in the plastic stage at severe strain [95]. At an extremely high strain rate, there is not enough time to activate plastic deformation modes such as dislocation slips or even the faster twinning mode. Thus, the large elastic strains promote the crystalline phase mechanically unstable due to the loss of shear rigidity, which leads to amorphization [107–109].

Interestingly, Ming et al. [91] for the first time observed deformation-induced amorphization in a non-equiatomic $\text{Cr}_{26}\text{Mn}_{20}\text{Fe}_{20}\text{Co}_{20}\text{Ni}_{14}$ HEA at cryogenic temperature. Such deformation-induced amorphization was later observed by several groups [110–113]. The deformation-induced amorphization generates extensive nanoscale amorphous bands, as shown in **Figure 10a–d**. The formation of extensive nanoscale amorphous bands is attributed to the significant dislocation accumulation in a constrained region inside shear bands, which raises the free energy of the original fcc phase to a point higher than that of the amorphous phase, then the energy difference drives amorphization. Subsequently, the deformation-induced amorphization was also observed in equiatomic CrMnFeCoNi HEA under severe plastic deformation through swaging followed by either quasi-static compression or dynamic deformation in shear [110]. In addition, the deformation-induced localized amorphization can also occur at the tip of cracks, which enhances the toughness significantly by blunting cracks and impeding the expansion of cracks [111]. Subsequently, the nanoscale origin of the mechanism of amorphization is revealed by using molecular dynamics simulation [112, 113]. The amorphization originates from the formation of multi-dislocation junctions due to the low SFE, which results in high lattice resistance to dislocation glide and facilitates nucleation of amorphous nuclei. The deformation mechanisms in the amorphous/crystalline dual-phase regions include high-density Shockley partial dislocations, multi-dislocation junctions, and nanotwinning in the crystalline region (TEM observations in **Figure 10e–g**), as well as radiation-shaped shear bands and amorphous bridges in the amorphous region.

Based on the mechanism of deformation-induced solid-state amorphization in HEAs, nanoscale amorphization bands can be introduced into HEAs to optimize mechanical properties. It is demonstrated that the yield strength of the HEAs could be enhanced without apparent loss of ductility by introducing high-density nanoscale amorphous bands. TEM characterizations (**Figure 10e–g**) reveal that introducing nanoscale amorphous bands can achieve three key benefits: (i) amorphous-crystalline interface (ACI) hardening, i.e., ACIs not only act as high-capacity sources for dislocations nucleation but also barriers for dislocation motion; (ii) large stress concentrations at the ACIs can be disrupted and relieved by the amorphous bands since ACIs act as natural sinks of dislocations, averting dislocation pileups at ACIs, which delay decohesion and fracture initiation at the ACIs; (iii) high thermal stability of amorphous bands enables to increase strain-hardening capability through the tempering at relatively higher temperatures without sacrificing the high yield strength. Wang

et al. [111] observed the formation of the amorphous area ahead of the crack tip after amorphization in equiatomic CrMnFeCoNi HEA by using in situ straining TEM experiments and found that the amorphous bridges in the crack wake provided effective toughening of the HEA. Ji et al. [112] provided atomistic insights, via molecular dynamics simulations, into the origin of the solid-state amorphization ahead of a crack tip and report the deformation mechanisms contributing to cryogenic damage-tolerance. It is believed that a much better combination of yield strength, ductility, and toughness can be achieved through optimizing the amorphization. These results demonstrate that engineering amorphous bands could be an efficient strategy in remaining enhanced mechanical properties of fcc-structured HEAs.

3.2 Dynamically reversible shear transformations

Traditional shear transformation banding, such as deformation-induced {111} twinning and martensitic phase transformation ($\text{fcc-}\gamma \rightarrow \text{hcp-}\varepsilon$), has been widely observed in fcc HEAs with low SFE. Recently, Ming et al. [114] found two dynamically reversible shear transformation mechanisms in a CrMnFeCoNi HEA under uniaxial tension at 4.2 K, featured by $\gamma \rightarrow \varepsilon \rightarrow \{10\bar{1}1\}$ twin $\rightarrow \gamma/\gamma_{\text{tw}}$ and $\gamma \rightarrow \varepsilon \rightarrow \gamma/\gamma_{\text{tw}}$. When deformed at cryogenic temperature, the lower SFE promotes $\gamma \rightarrow \varepsilon$ shear transformation, forming hcp grains which gradually deplete the original fcc grains. Meanwhile, high-density {0001} stacking faults and {10 $\bar{1}$ 1} nanotwinning are activated to accommodate plastic deformation, as shown in **Figure 11a, b**. More intriguingly, reverse hcp \rightarrow fcc shear transformations are stimulated within {10 $\bar{1}$ 1} twin and surrounding hcp matrix by deformation-induced local dissipative heating (**Figure 11c**). When the {10 $\bar{1}$ 1} twins transform into fcc structure, Shockley partial dislocations are activated on {111} planes, leading to formation of {111} SFs and {111} nanotwins in the newly formed fcc domain. **Figure 11c** shows two fcc domains with {111} twin orientation inside an {10 $\bar{1}$ 1} twin. This shear transformation mechanism is described by $\gamma \rightarrow \varepsilon \rightarrow \{10\bar{1}1\}$ twin $\rightarrow \gamma/\gamma_{\text{tw}}$.

In addition, for high-density basal stacking faults in the hcp- ε phase, the faulted regions can transform back into fcc structure through correcting SFs via nucleation and glide of Shockley partial dislocations, which is energetically favorable since the process will reduce the density of stacking faults. It is noted that fcc laminates frequently have two orientations, forming a {111} twin orientation relationship (**Figure 11d, e**). This shear transformation mechanism is described by $\gamma \rightarrow \varepsilon \rightarrow \gamma/\gamma_{\text{tw}}$. The reversible fcc \leftrightarrow hcp shear transformations and both {10 $\bar{1}$ 1} and {111} nanotwinning lead to dynamic nano-laminated dual-phase structures, which advance the monotonic “dynamic Hall–Petch” effect in enhancing strength, strain-hardening ability, and ductility by dynamically tailoring the type and width of shear transformation bands.

3.3 Nano-segregation of multi-principal elements

The unique multiple principal elements endow HEAs with adjustable microstructures and corresponding excellent mechanical properties. Extensive efforts invest in tailoring the chemical compositions of fcc-structured HEAs to optimize the strength and ductility simultaneously. When designing the compositions of HEAs, one should realize two important facts. The first one is that the stronger HEAs are not necessarily the ones with the most elements. The nature of the constituent elements is also important, with the Cr-containing alloys, in general, being the strongest in a family of

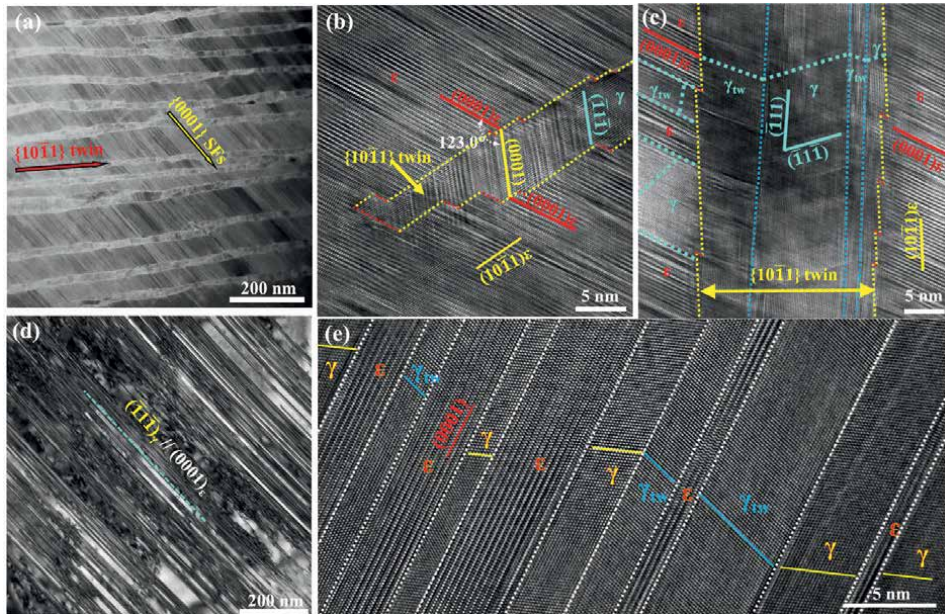


Figure 11. (a–c) TEM images of CrMnFeCoNi HEA after uniaxial tension to fracture at 4.2 K, showing the reversible shear transformation mechanism featured by $\gamma \rightarrow \epsilon \rightarrow \{1\ 0\ \bar{1}\ 1\}$ twin $\rightarrow \gamma/\gamma_{tw}$, (d, e) the reversible shear transformation mechanism of $\gamma \rightarrow \epsilon \rightarrow \gamma/\gamma_{tw}$ [114].

equiatomic binary, ternary and quaternary alloys based on the elements Fe, Ni, Co, Cr, and Mn [71]. Secondly, when designing the compositions of HEAs, nano-segregation of principal elements at grain boundaries (GBs) should be cause for concern since it could deteriorate the ductility significantly. As shown in **Figure 12**, nanoclustering Cr, Ni, and Mn separately at GBs, as detected by atom probe tomography, reduce GB cohesion, and promotes crack initiation along GBs, leading to ductility loss in the CrMnFeCoNi HEA [115]. The GB segregation engineering strategy is then proposed to avoid ductility loss by shifting the fast segregation of principal elements from GBs into preexisting Cr-rich secondary phases. Such GB decohesion by nanoclustering multi-principal elements is a common phenomenon in HEAs. Linlin Li et al. also found that Ni and Mn co-segregate to some regions of the GBs along with the depletion of Fe, Co, and Cr, while Cr is enriched in other regions of the GBs where Ni and Mn are depleted [116–118].

Generally, only nano-segregation of several elements occurs in fully annealed HEAs with coarse and clean grains after short-time annealing treatment, which can lead to GB decohesion and thus ductility loss. However, with very long-time annealing, such as annealing at intermediate temperatures for tens to hundreds of days, intermetallic phases are precipitated at GBs in coarse-grained HEAs [119, 120]. When the grain size of HEAs is decreased to the nanoscale, annealing at intermediate temperatures for mere minutes can lead to precipitation of nanoscale intermetallic phases at GBs, such as Cr-rich phase, NiMn phase, and FeCo phase in equiatomic CrMnFeCoNi HEA [121]. The formation of intermetallic phases at GBs will reduce the ductility significantly. Therefore, the nature of the constituent elements and their nano-segregation behavior should be considered when we design high-strength and high-ductility HEAs.

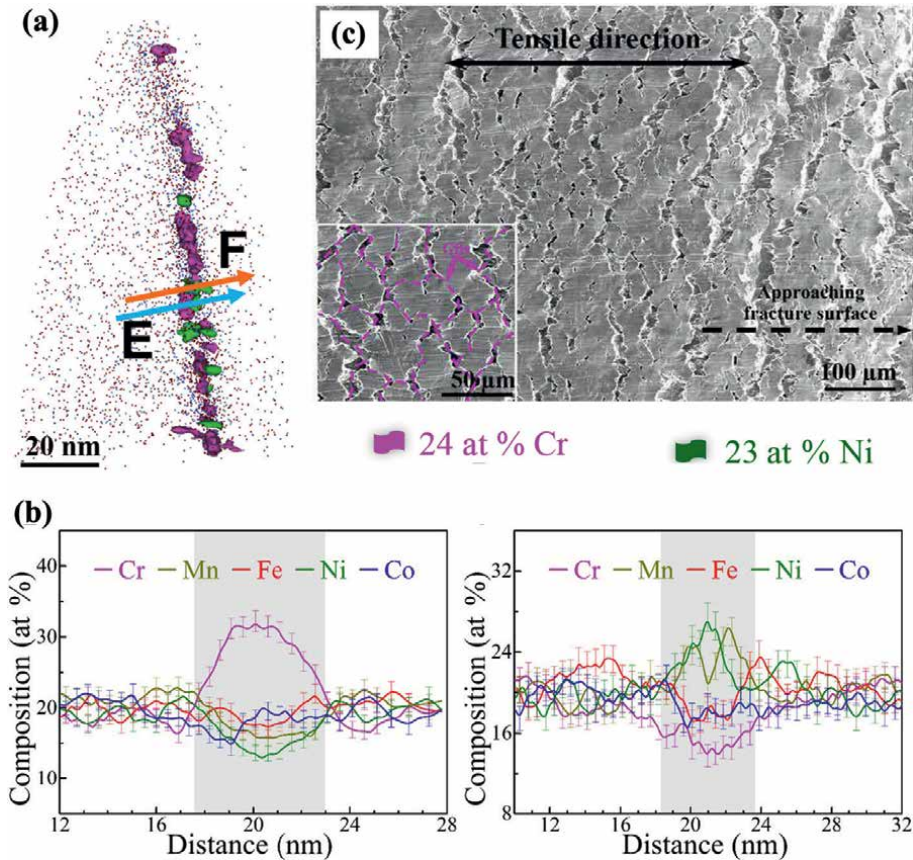


Figure 12. Atom probe tomography of the GB in a CrMnFeCoNi HEA after uniaxial tension to fracture at 700°C: (a) atom map of the tip showing Cr (24 at %) and Ni (23 at %) isocomposition surfaces viewed with the GB edge-on. (b) 1D compositional profiles along the cyan arrow E and the orange arrow F are indicated in (a). (c) Fracture lateral surface of the tensile sample after tensile tests at 700 °C, showing many cracks along the GBs [115].

4. Conclusion

This chapter summarizes recent works on realizing strength–ductility combinations in fcc CrFeCoNi-based HEAs via composition and microstructure engineering: (I) Nanoprecipitation strengthening associated with tailoring the size, distribution, and morphology of second phases via alloying a small addition of Ti and Al elements; and (II) The synergistic operations of multiple strengthening mechanisms, such as solid solution strengthening, dislocation strengthening, grain boundary strengthening, precipitation strengthening, TWIP/TRIP effect, and amorphization-induced strengthening. The abundant deformation mechanisms, including slips associated with Shockley partial dislocation and full dislocations, nanotwinning, martensitic phase transformation, deformation-induced amorphization, and dynamically reversible shear transformation, are also summarized. Among them, the recently reported deformation-induced amorphization and dynamically reversible shear transformation are highlighted in terms of their nanoscale origins and strengthening effects for overcoming the strength–ductility trade-off. Finally, this chapter points out that the nature of the constituent

elements and their nano-segregation behavior should be considered when we design high-strength and high-ductility HEAs via engineering the compositions.

Acknowledgements

The authors acknowledge the financial support from the National Natural Science Foundation of China (No. 52002109), the Natural Science Foundation of the Hebei province (No. E2020202088), and the Overseas Scientists Sponsorship Program by Hebei Province (C20210331).

Conflict of interest

The authors declare no competing financial interests.

Author details


Kaisheng Ming¹, Shijian Zheng¹ and Jian Wang^{2*}

1 State Key Laboratory of Reliability and Intelligence of Electrical Equipment, School of Materials Science and Engineering, Hebei University of Technology, Tianjin, China

2 Mechanical and Materials Engineering, University of Nebraska-Lincoln, Lincoln, NE, USA

*Address all correspondence to: jianwang@unl.edu

IntechOpen

© 2022 The Author(s). Licensee IntechOpen. This chapter is distributed under the terms of the Creative Commons Attribution License (<http://creativecommons.org/licenses/by/3.0>), which permits unrestricted use, distribution, and reproduction in any medium, provided the original work is properly cited. 

References

- [1] Ritchie RO. The conflicts between strength and toughness. *Nature Materials*. 2011;**10**:817-822. DOI: 10.1038/nmat3115
- [2] Launey ME, Ritchie RO. On the fracture toughness of advanced materials. *Advanced Materials*. 2009;**21**:2103-2110. DOI: 10.1002/adma.200803322
- [3] Han SZ, Choi E-A, Lim SH, Kim S, Lee J. Alloy design strategies to increase strength and its trade-offs together. *Progress in Materials Science*. 2020;**117**:100720. DOI: 10.1016/j.pmatsci.2020.100720
- [4] Wu H, Fan G. An overview of tailoring strain delocalization for strength-ductility synergy. *Progress in Materials Science*. 2020;**113**:100675. DOI: 10.1016/j.pmatsci.2020.100675
- [5] Argon A. *Strengthening Mechanisms in Crystal Plasticity*. 1st ed. Vol. 4. Oxford: OUP; 2007. DOI: 10.1093/acprof:oso/9780198516002.001.0001
- [6] Zhang Y, Zuo TT, Tang Z, Gao MC, Dahmen KA, Liaw PK, et al. Microstructures and properties of high-entropy alloys. *Progress in Materials Science*. 2014;**61**:1-93. DOI: 10.1016/j.pmatsci.2013.10.001
- [7] Yeh JW, Chen SK, Lin SJ, Gan JY, Chin TS, Shun TT, et al. Nanostructured high-entropy alloys with multiple principal elements: Novel alloy design concepts and outcomes. *Advanced Engineering Materials*. 2004;**6**:299-303. DOI: 10.1002/adem.200300567
- [8] Li W, Xie D, Li D, Zhang Y, Gao Y, Liaw PK. Mechanical behavior of high-entropy alloys. *Progress in Materials Science*. 2021;**118**:100777. DOI: 10.1016/j.pmatsci.2021.100777
- [9] Sathiyamoorthi P, Kim HS. High-entropy alloys with heterogeneous microstructure: Processing and mechanical properties. *Progress in Materials Science*. 2020;**123**:100709. DOI: 10.1016/j.pmatsci.2020.100709
- [10] George EP, Curtin WA, Tasan CC. High entropy alloys: A focused review of mechanical properties and deformation mechanisms. *Acta Materialia*. 2020;**188**:435-474. DOI: 10.1016/j.actamat.2019.12.015
- [11] Cantor B. Multicomponent high-entropy Cantor alloys. *Progress in Materials Science*. 2020;**120**:100754. DOI: 10.1016/j.pmatsci.2020.100754
- [12] Li Z, Zhao S, Ritchie RO, Meyers MA. Mechanical properties of high-entropy alloys with emphasis on face-centered cubic alloys. *Progress in Materials Science*. 2019;**102**:296-345. DOI: 10.1016/j.pmatsci.2018.12.003
- [13] Miracle DB, Senkov ON. A critical review of high entropy alloys and related concepts. *Acta Materialia*. 2017;**122**:448-511. DOI: 10.1016/j.actamat.2016.08.081
- [14] Zhang Z, Armstrong DEJ, Grant PS. The effects of irradiation on CrMnFeCoNi high-entropy alloy and its derivatives. *Progress in Materials Science*. 2021;**123**:100807. DOI: 10.1016/j.pmatsci.2021.100807
- [15] Li Z, Pradeep KG, Deng Y, Raabe D, Tasan CC. Metastable high-entropy dual-phase alloys overcome the strength-ductility trade-off. *Nature*. 2016;**534**:227-230. DOI: 10.1038/nature17981
- [16] Ma E, Wu X. Tailoring heterogeneities in high-entropy alloys to promote strength-ductility synergy.

- Nature Communications. 2019;**10**:1-10.
DOI: 10.1038/s41467-019-13311-1
- [17] Gludovatz B, Hohenwarter A, Catoor D, Chang EH, George EP, Ritchie RO. A fracture-resistant high-entropy alloy for cryogenic applications. *Science*. 2014;**345**:1153-1158.
DOI: 10.1126/science.1254581
- [18] Chen S, Oh HS, Gludovatz B, Kim SJ, Park ES, Zhang Z, et al. Real-time observations of TRIP-induced ultrahigh strain hardening in a dual-phase CrMnFeCoNi high-entropy alloy. *Nature Communications*. 2020;**11**:1-8.
DOI: 10.1038/s41467-020-14641-1
- [19] Lu W, Liebscher CH, Dehm G, Raabe D, Li Z. Bidirectional transformation enables hierarchical Nanolaminate dual-phase high-entropy alloys. *Advanced Materials*. 2018;**30**:e1804727. DOI: 10.1002/adma.201804727
- [20] Naeem M, He H, Zhang F, Huang H, Harjo S, Kawasaki T, et al. Cooperative deformation in high-entropy alloys at ultralow temperatures. *Science Advances*. 2020;**6**:eaax4002.
DOI: 10.1126/sciadv.aax4002
- [21] Zhang Z, Mao MM, Wang J, Gludovatz B, Zhang Z, Mao SX, et al. Nanoscale origins of the damage tolerance of the high-entropy alloy CrMnFeCoNi. *Nature Communications*. 2015;**6**:10143.
DOI: 10.1038/ncomms10143
- [22] Zhang Z, Sheng H, Wang Z, Gludovatz B, Zhang Z, George EP, et al. Dislocation mechanisms and 3D twin architectures generate exceptional strength-ductility-toughness combination in CrCoNi medium-entropy alloy. *Nature Communications*. 2017;**8**:14390.
DOI: 10.1038/ncomms14390
- [23] Otto F, Dlouhý A, Somsen C, Bei H, Eggeler G, George EP. The influences of temperature and microstructure on the tensile properties of a CoCrFeMnNi high-entropy alloy. *Acta Materialia*. 2013;**61**:5743-5755. DOI: 10.1016/j.actamat.2013.06.018
- [24] Su J, Wu X, Raabe D, Li Z. Deformation-driven bidirectional transformation promotes bulk nanostructure formation in a metastable interstitial high entropy alloy. *Acta Materialia*. 2019;**167**:23-39. DOI: 10.1016/j.actamat.2019.01.030
- [25] Moon J, Tabachnikova E, Shumilin S, Hryhorova T, Estrin Y, Brechtel J, et al. Deformation behavior of a Co-Cr-Fe-Ni-Mo medium-entropy alloy at extremely low temperatures. *Materials Today*. 2021;**50**:55-68. DOI: 10.1016/j.mattod.2021.08.001
- [26] Gludovatz B, Hohenwarter A, Thurston KV, Bei H, Wu Z, George EP, et al. Exceptional damage-tolerance of a medium-entropy alloy CrCoNi at cryogenic temperatures. *Nature Communications*. 2016;**7**:10602.
DOI: 10.1038/ncomms10602
- [27] He H, Naeem M, Zhang F, Zhao Y, Harjo S, Kawasaki T, et al. Stacking fault driven phase transformation in CrCoNi medium entropy alloy. *Nano Letters*. 2021;**21**:1419-1426. DOI: 10.1021/acs.nanolett.0c04244
- [28] Li Z, Tasan CC, Pradeep KG, Raabe D. A TRIP-assisted dual-phase high-entropy alloy: Grain size and phase fraction effects on deformation behavior. *Acta Materialia*. 2017;**131**:323-335.
DOI: 10.1016/j.actamat.2017.03.069
- [29] Li Z, Tasan CC, Springer H, Gault B, Raabe D. Interstitial atoms enable joint twinning and transformation induced plasticity in strong and ductile high-entropy alloys. *Scientific Reports*. 2017;**7**:40704. DOI: 10.1038/srep40704

- [30] Su J, Raabe D, Li Z. Hierarchical microstructure design to tune the mechanical behavior of an interstitial TRIP-TWIP high-entropy alloy. *Acta Materialia*. 2019;**163**:40-54. DOI: 10.1016/j.actamat.2018.10.017
- [31] Wang M, Li Z, Raabe D. In-situ SEM observation of phase transformation and twinning mechanisms in an interstitial high-entropy alloy. *Acta Materialia*. 2018;**147**:236-246. DOI: 10.1016/j.actamat.2018.01.036
- [32] Li Z, CemTasan C, Pradeep KG, Raabe D. A TRIP-assisted dual-phase high-entropy alloy: Grain size and phase fraction effects on deformation behavior. *Acta Materialia*. 2017;**131**:323-335. DOI: 10.1016/j.actamat.2017.03.069
- [33] Li Z, Körmann F, Grabowski B, Neugebauer J, Raabe D. Ab initio assisted design of quinary dual-phase high-entropy alloys with transformation-induced plasticity. *Acta Materialia*. 2017;**136**:262-270. DOI: 10.1016/j.actamat.2017.07.023
- [34] Jo YH, Jung S, Choi WM, Sohn SS, Kim HS, Lee BJ, et al. Cryogenic strength improvement by utilizing room-temperature deformation twinning in a partially recrystallized VCrMnFeCoNi high-entropy alloy. *Nature Communications*. 2017;**8**:15719. DOI: 10.1038/ncomms15719
- [35] Pan Q, Zhang L, Feng R, Lu Q, An K, Chuang AC, et al. Gradient-cell-structured high-entropy alloy with exceptional strength and ductility. *Science*. 2021;**374**:eabj8114. DOI: 10.1126/science.abj8114
- [36] Ding J, Yu Q, Asta M, Ritchie RO. Tunable stacking fault energies by tailoring local chemical order in CrCoNi medium-entropy alloys. *Proceedings of the National Academy of Sciences*. 2018;**115**:8919-8924. DOI: 10.1073/pnas.1808660115
- [37] Huang S, Huang H, Li W, Kim D, Lu S, Li X, et al. Twinning in metastable high-entropy alloys. *Nature Communications*. 2018;**9**:1-7. DOI: 10.1038/s41467-018-04780-x
- [38] Shih M, Miao J, Mills M, Ghazisaeidi M. Stacking fault energy in concentrated alloys. *Nature Communications*. 2021;**12**:3590. DOI: 10.1038/s41467-021-23860-z
- [39] Khan TZ, Kirk T, Vazquez G, Singh P, Smirnov AV, Johnson DD, et al. Towards stacking fault energy engineering in FCC high entropy alloys. *Acta Materialia*. 2022;**224**:117472. DOI: 10.1016/j.actamat.2021.117472
- [40] Wagner C, Ferrari A, Schreuer J, Couzinié J-P, Ikeda Y, Körmann F, et al. Effects of Cr/Ni ratio on physical properties of Cr-Mn-Fe-Co-Ni high-entropy alloys. *Acta Materialia*. 2022;**227**:117693. DOI: 10.1016/j.actamat.2022.117693
- [41] Zhao S, Stocks GM, Zhang Y. Stacking fault energies of face-centered cubic concentrated solid solution alloys. *Acta Materialia*. 2017;**134**:334-345. DOI: 10.1016/j.actamat.2017.05.001
- [42] Huang S, Li W, Lu S, Tian F, Shen J, Holmström E, et al. Temperature dependent stacking fault energy of FeCrCoNiMn high entropy alloy. *Scripta Materialia*. 2015;**108**:44-47. DOI: 10.1016/j.scriptamat.2015.05.041
- [43] Yang Y, Chen T, Tan L, Poplawsky JD, An K, Wang Y, et al. Bifunctional nanoprecipitates strengthen and ductilize a medium-entropy alloy. *Nature*. 2021;**595**:245-249. DOI: 10.1038/s41586-021-03607-y

- [44] Jang TJ, Choi WS, Kim DW, Choi G, Jun H, Ferrari A, et al. Shear band-driven precipitate dispersion for ultrastrong ductile medium-entropy alloys. *Nature Communications*. 2021;**12**:4703. DOI: 10.1038/s41467-021-25031-6
- [45] Han L, Rao Z, Souza Filho IR, Maccari F, Wei Y, Wu G, et al. Ultrastrong and ductile soft magnetic high-entropy alloys via coherent ordered Nanoprecipitates. *Advanced Materials*. 2021;**33**:e2102139. DOI: 10.1002/adma.202102139
- [46] Feng R, Rao Y, Liu C, Xie X, Yu D, Chen Y, et al. Enhancing fatigue life by ductile-transformable multicomponent B₂ precipitates in a high-entropy alloy. *Nature Communications*. 2021;**12**:3588. DOI: 10.1038/s41467-021-23689-6
- [47] Yang T, Zhao Y, Tong Y, Jiao Z, Wei J, Cai J, et al. Multicomponent intermetallic nanoparticles and superb mechanical behaviors of complex alloys. *Science*. 2018;**362**:933-937. DOI: 10.1126/science.aas8815
- [48] Liang YJ, Wang L, Wen Y, Cheng B, Wu Q, Cao T, et al. High-content ductile coherent nanoprecipitates achieve ultrastrong high-entropy alloys. *Nature Communications*. 2018;**9**:4063. DOI: 10.1038/s41467-018-06600-8
- [49] Oh HS, Kim SJ, Odbadrakh K, Ryu WH, Yoon KN, Mu S, et al. Engineering atomic-level complexity in high-entropy and complex concentrated alloys. *Nature Communications*. 2019;**10**:2090. DOI: 10.1038/s41467-019-10012-7
- [50] Sohn SS, Kwiatkowski da Silva A, Ikeda Y, Kormann F, Lu W, Choi WS, et al. Ultrastrong medium-entropy single-phase alloys designed via severe lattice distortion. *Advanced Materials*. 2019;**31**:e1807142. DOI: 10.1002/adma.201807142
- [51] Lei Z, Liu X, Wu Y, Wang H, Jiang S, Wang S, et al. Enhanced strength and ductility in a high-entropy alloy via ordered oxygen complexes. *Nature*. 2018;**563**:546-550. DOI: 10.1038/s41586-018-0685-y
- [52] Ding Q, Zhang Y, Chen X, Fu X, Chen D, Chen S, et al. Tuning element distribution, structure and properties by composition in high-entropy alloys. *Nature*. 2019;**574**:223-227. DOI: 10.1038/s41586-019-1617-1
- [53] Li QJ, Sheng H, Ma E. Strengthening in multi-principal element alloys with local-chemical-order roughened dislocation pathways. *Nature Communications*. 2019;**10**:3563. DOI: 10.1038/s41467-019-11464-7
- [54] Zhang R, Zhao S, Ding J, Chong Y, Jia T, Ophus C, et al. Short-range order and its impact on the CrCoNi medium-entropy alloy. *Nature*. 2020;**581**:283-287. DOI: 10.1038/s41586-020-2275-z
- [55] Chen S, Aitken ZH, Pattamatta S, Wu Z, Yu ZG, Srolovitz DJ, et al. Simultaneously enhancing the ultimate strength and ductility of high-entropy alloys via short-range ordering. *Nature Communications*. 2021;**12**:4953. DOI: 10.1038/s41467-021-25264-5
- [56] Wu X, Wang B, Rehm C, He H, Naeem M, Lan S, et al. Ultra-small-angle neutron scattering study on temperature-dependent precipitate evolution in CoCrFeNiMo_{0.3} high entropy alloy. *Acta Materialia*. 2022;**222**:117446. DOI: 10.1016/j.actamat.2021.117446
- [57] Wang L, Wang L, Zhou S, Xiao Q, Xiao Y, Wang X, et al. Precipitation and micromechanical behavior of the coherent ordered nanoprecipitation strengthened Al-Cr-Fe-Ni-V high entropy alloy. *Acta Materialia*. 2021;**216**:117121. DOI: 10.1016/j.actamat.2021.117121

- [58] Huang X, Huang L, Peng H, Liu Y, Liu B, Li S. Enhancing strength-ductility synergy in a casting non-equiatomc NiCoCr-based high-entropy alloy by Al and Ti combination addition. *Scripta Materialia*. 2021;**200**:113898. DOI: 10.1016/j.scriptamat.2021.113898
- [59] He F, Yang Z, Liu S, Chen D, Lin W, Yang T, et al. Strain partitioning enables excellent tensile ductility in precipitated heterogenous high-entropy alloys with gigapascal yield strength. *International Journal of Plasticity*. 2021;**144**:103022. DOI: 10.1016/j.ijplas.2021.103022
- [60] Niu C, LaRosa CR, Miao J, Mills J, Mills M, Ghazisaeidi M. Magnetically-driven phase transformation strengthening in high entropy alloys. *Nature Communications*. 2018;**9**:1363. DOI: 10.1038/s41467-018-03846-0
- [61] Ming K, Bi X, Wang J. Realizing strength-ductility combination of coarse-grained Al_{0.2}Co_{1.5}CrFeNi_{1.5}Ti_{0.3} alloy via nano-sized, coherent precipitates. *International Journal of Plasticity*. 2018;**100**:177-191. DOI: 10.1016/j.ijplas.2017.10.005
- [62] Ming K, Bi X, Wang J. Precipitation strengthening of ductile Cr₁₅Fe₂₀Co₃₅Ni₂₀Mo₁₀ alloys. *Scripta Materialia*. 2017;**137**:88-93. DOI: 10.1016/j.scriptamat.2017.05.019
- [63] Cao B, Kong H, Ding Z, Wu S, Luan J, Jiao Z, et al. A novel L12-strengthened multicomponent Co-rich high-entropy alloy with both high γ' -solvus temperature and superior high-temperature strength. *Scripta Materialia*. 2021;**199**:113826. DOI: 10.1016/j.scriptamat.2021.113826
- [64] Zhao Y, Yang T, Li Y, Fan L, Han B, Jiao Z, et al. Superior high-temperature properties and deformation-induced planar faults in a novel L12-strengthened high-entropy alloy. *Acta Materialia*. 2020;**188**:517-527. DOI: 10.1016/j.actamat.2020.02.028
- [65] Cao B, Yang T, W-h L, Liu C. Precipitation-hardened high-entropy alloys for high-temperature applications: A critical review. *MRS Bulletin*. 2019;**44**:854-859. DOI: 10.1557/mrs.2019.255
- [66] Zhao Y, Yang T, Han B, Luan J, Chen D, Kai W, et al. Exceptional nanostructure stability and its origins in the CoCrNi-based precipitation-strengthened medium-entropy alloy. *Materials Research Letters*. 2019;**7**:152-158. DOI: 10.1080/21663831.2019.1568315
- [67] Liu WH, Lu ZP, He JY, Luan JH, Wang ZJ, Liu B, et al. Ductile CoCrFeNiMo_x high entropy alloys strengthened by hard intermetallic phases. *Acta Materialia*. 2016;**116**:332-342. DOI: 10.1016/j.actamat.2016.06.063
- [68] Bae JW, Park JM, Moon J, Choi WM, Lee B-J, Kim HS. Effect of μ -precipitates on the microstructure and mechanical properties of non-equiatomc CoCrFeNiMo medium-entropy alloys. *Journal of Alloys and Compounds*. 2019;**781**:75-83. DOI: 10.1016/j.jallcom.2018.12.040
- [69] Kwon H, Asghari-Rad P, Park JM, Sathiyamoorthi P, Bae JW, Moon J, et al. Synergetic strengthening from grain refinement and nano-scale precipitates in non-equiatomc CoCrFeNiMo medium-entropy alloy. *Intermetallics*. 2021;**135**:107212. DOI: 10.1016/j.intermet.2021.107212
- [70] He JY, Liu WH, Wang H, Wu Y, Liu XJ, Nieh TG, et al. Effects of Al addition on structural evolution and tensile properties of the FeCoNiCrMn high-entropy alloy system. *Acta Materialia*. 2014;**62**:105-113. DOI: 10.1016/j.actamat.2013.09.037

- [71] Wu Z, Bei H, Pharr GM, George EP. Temperature dependence of the mechanical properties of equiatomic solid solution alloys with face-centered cubic crystal structures. *Acta Materialia*. 2014;**81**:428-441. DOI: 10.1016/j.actamat.2014.08.026
- [72] Ma S, Zhang S, Qiao J, Wang Z, Gao M, Jiao Z, et al. Superior high tensile elongation of a single-crystal CoCrFeNiAl₀. 3 high-entropy alloy by Bridgman solidification. *Intermetallics*. 2014;**54**:104-109. DOI: 10.1016/j.intermet.2014.05.018
- [73] Shun T-T, Du Y-C. Microstructure and tensile behaviors of FCC Al₀. 3CoCrFeNi high entropy alloy. *Journal of Alloys and Compounds*. 2009;**479**:157-160. DOI: 10.1016/j.jallcom.2008.12.088
- [74] Hemphill MA, Yuan T, Wang G, Yeh J, Tsai C, Chuang A, et al. Fatigue behavior of Al₀. 5CoCrCuFeNi high entropy alloys. *Acta Materialia*. 2012;**60**:5723-5734. DOI: 10.1016/j.actamat.2012.06.046
- [75] Kuznetsov AV, Shaysultanov DG, Stepanov ND, Salishchev GA, Senkov ON. Tensile properties of an AlCrCuNiFeCo high-entropy alloy in as-cast and wrought conditions. *Materials Science and Engineering A*. 2012;**533**:107-118. DOI: 10.1016/j.msea.2011.11.045
- [76] Ming K, Bi X, Wang J. Microstructures and deformation mechanisms of Cr 26 Mn 20 Fe 20 Co 20 Ni 14 alloys. *Materials Characterization*. 2017;**134**:194-201. DOI: 10.1016/j.matchar.2017.10.022
- [77] Tsai M-H, Yuan H, Cheng G, Xu W, Jian WW, Chuang M-H, et al. Significant hardening due to the formation of a sigma phase matrix in a high entropy alloy. *Intermetallics*. 2013;**33**:81-86. DOI: 10.1016/j.intermet.2012.09.022
- [78] Tsai MH, Tsai KY, Tsai CW, Chi L, Juan CC, Yeh JW. Criterion for sigma phase formation in Cr- and V-containing high-entropy alloys. *Materials Research Letters*. 2013;**1**:207-212. DOI: 10.1080/21663831.2013.831382
- [79] Zhang L, Huo X, Wang A, Du X, Zhang L, Li W, et al. A ductile high entropy alloy strengthened by nano sigma phase. *Intermetallics*. 2020;**122**:106813. DOI: 10.1016/j.intermet.2020.106813
- [80] Jo YH, Choi W-M, Sohn SS, Kim HS, Lee B-J, Lee S. Role of brittle sigma phase in cryogenic-temperature-strength improvement of non-equi-atomic Fe-rich VCrMnFeCoNi high entropy alloys. *Materials Science and Engineering A*. 2018;**724**:403-410. DOI: 10.1016/j.msea.2018.03.115
- [81] Zhu Y, Ameyama K, Anderson PM, Beyerlein IJ, Gao H, Kim HS, et al. Heterostructured materials: Superior properties from hetero-zone interaction. *Materials Research Letters*. 2020;**9**:1-31. DOI: 10.1080/21663831.2020.1796836
- [82] Ming K, Bi X, Wang J. Strength and ductility of CrFeCoNiMo alloy with hierarchical microstructures. *International Journal of Plasticity*. 2019;**113**:255-268. DOI: 10.1016/j.ijplas.2018.10.005
- [83] Gali A, George EP. Tensile properties of high- and medium-entropy alloys. *Intermetallics*. 2013;**39**:74-78. DOI: 10.1016/j.intermet.2013.03.018
- [84] Daoud H, Manzoni A, Völkl R, Wanderka N, Glatzel U. Microstructure and tensile behavior of Al₈Co₁₇Cr₁₇Cu₈Fe₁₇Ni₃₃ (at.%) high-entropy alloy. *JOM journal of the minerals metals and materials. Society*. 2013;**65**:1805-1814. DOI: 10.1007/s11837-013-0756-3
- [85] He JY, Wang H, Huang HL, Xu XD, Chen MW, Wu Y, et al.

- A precipitation-hardened high-entropy alloy with outstanding tensile properties. *Acta Materialia*. 2016;**102**:187-196. DOI: 10.1016/j.actamat.2015.08.076
- [86] Liu L, Zhang Y, Han J, Wang X, Jiang W, Liu CT, et al. Nanoprecipitate-strengthened high-entropy alloys. *Advanced Science*. 2021;**8**:2100870. DOI: 10.1002/advs.202100870
- [87] Li D, Li C, Feng T, Zhang Y, Sha G, Lewandowski JJ, et al. High-entropy Al 0.3 CoCrFeNi alloy fibers with high tensile strength and ductility at ambient and cryogenic temperatures. *Acta Materialia*. 2017;**123**:285-294. DOI: 10.1016/j.actamat.2016.10.038
- [88] Ma SG, Zhang SF, Qiao JW, Wang ZH, Gao MC, Jiao ZM, et al. Superior high tensile elongation of a single-crystal CoCrFeNiAl 0.3 high-entropy alloy by Bridgman solidification. *Intermetallics*. 2014;**54**:104-109. DOI: 10.1016/j.intermet.2014.05.018
- [89] Fu Z, Chen W, Wen H, Zhang D, Chen Z, Zheng B, et al. Microstructure and strengthening mechanisms in an FCC structured single-phase nanocrystalline Co 25 Ni 25 Fe 25 Al 7.5 Cu 17.5 high-entropy alloy. *Acta Materialia*. 2016;**107**:59-71. DOI: 10.1016/j.actamat.2016.01.050
- [90] Wu D, Zhang J, Huang J, Bei H, Nieh T-G. Grain-boundary strengthening in nanocrystalline chromium and the Hall-Petch coefficient of body-centered cubic metals. *Scripta Materialia*. 2013;**68**:118-121. DOI: 10.1016/j.scriptamat.2012.09.025
- [91] Ming K, Lu W, Li Z, Bi X, Wang J. Amorphous bands induced by low temperature tension in a non-equiatomic CrMnFeCoNi alloy. *Acta Materialia*. 2020;**188**:354-365. DOI: 10.1016/j.actamat.2020.02.024
- [92] Beladi H, Timokhina I, Estrin Y, Kim J, De Cooman B, Kim S. Orientation dependence of twinning and strain hardening behaviour of a high manganese twinning induced plasticity steel with polycrystalline structure. *Acta Materialia*. 2011;**59**:7787-7799. DOI: 10.1016/j.actamat.2011.08.031
- [93] Gutierrez-Urrutia I, Raabe D. Dislocation and twin substructure evolution during strain hardening of an Fe-22 wt.% Mn-0.6 wt.% C TWIP steel observed by electron channeling contrast imaging. *Acta Materialia*. 2011;**59**:6449-6462. DOI: 10.1016/j.actamat.2011.07.009
- [94] Karaman I, Sehitoglu H, Beaudoin A, Chumlyakov YI, Maier H, Tome C. Modeling the deformation behavior of Hadfield steel single and polycrystals due to twinning and slip. *Acta Materialia*. 2000;**48**:2031-2047. DOI: 10.1016/S1359-6454(00)00051-3
- [95] Ma E. Amorphization in mechanically driven material systems. *Scripta Materialia*. 2003;**49**:941-946. DOI: 10.1016/s1359-6462(03)00477-9
- [96] Suryanarayana C. Mechanical alloying and milling. *Progress in Materials Science*. 2001;**46**:1-184. DOI: 10.1016/S0079-6425(99)00010-9
- [97] Sharma SM, Sikka S. Pressure induced amorphization of materials. *Progress in Materials Science*. 1996;**40**:1-77. DOI: 10.1016/0079-6425(95)00006-2
- [98] Sundeep R, Glezer A, Shalimova A. Phase transformations «Amorphization↔ crystallization» In metallic materials induced by severe plastic deformation. *Reviews on Advanced Materials Science*. 2018;**54**:93-105. DOI: 10.1515/rams-2018-0021
- [99] Lin ZJ, Zhuo MJ, Sun ZQ, Veyssièrè P, Zhou YC. Amorphization by dislocation

- accumulation in shear bands. *Acta Materialia*. 2009;**57**:2851-2857. DOI: 10.1016/j.actamat.2009.02.040
- [100] Li N, Wang YD, Lin Peng R, Sun X, Liaw PK, Wu GL, et al. Localized amorphism after high-strain-rate deformation in TWIP steel. *Acta Materialia*. 2011;**59**:6369-6377. DOI: 10.1016/j.actamat.2011.06.048
- [101] Zhao S, Hahn EN, Kad B, Remington BA, Wehrenberg CE, Bringa EM, et al. Amorphization and nanocrystallization of silicon under shock compression. *Acta Materialia*. 2016;**103**:519-533. DOI: 10.1016/j.actamat.2015.09.022
- [102] Zhao S, Kad B, Remington BA, LaSalvia JC, Wehrenberg CE, Behler KD, et al. Directional amorphization of boron carbide subjected to laser shock compression. *Proceedings of the National Academy of Sciences*. 2016;**113**:12088-12093. DOI: 10.1073/pnas.1604613113
- [103] Zhao S, Flanagan R, Hahn EN, Kad B, Remington BA, Wehrenberg CE, et al. Shock-induced amorphization in silicon carbide. *Acta Materialia*. 2018;**158**:206-213. DOI: 10.1016/j.actamat.2018.07.047
- [104] Johnson WL. Thermodynamic and kinetic aspects of the crystal to glass transformation in metallic materials. *Progress in Materials Science*. 1986;**30**:81-134. DOI: 10.1016/0079-6425(86)90005-8
- [105] Fecht HJ, Desré PJ, Johnson WL. Thermodynamic aspects of solid-state amorphization: Polymorphous melting Clapeyron diagram. *Philosophical Magazine B*. 2006;**59**:577-585. DOI: 10.1080/13642818908211178
- [106] Wolf D, Okamoto PR, Yip S, Lutsko JF, Kluge M. Thermodynamic parallels between solid-state amorphization and melting. *Journal of Materials Research*. 2011;**5**:286-301. DOI: 10.1557/jmr.1990.0286
- [107] Koike J. Elastic instability of crystals caused by static atom displacement: A mechanism for solid-state amorphization. *Physical Review B*. 1993;**47**:7700. DOI: 10.1103/PhysRevB.47.7700
- [108] Li M, Johnson WL. Instability of metastable solid solutions and the crystal to glass transition. *Physical Review Letters*. 1993;**70**:1120-1123. DOI: 10.1103/PhysRevLett.70.1120
- [109] Delogu F. Connection between shear instability and amorphisation. *Materials Science and Engineering A*. 2004;**367**:162-165. DOI: 10.1016/j.msea.2003.10.248
- [110] Zhao S, Li Z, Zhu C, Yang W, Zhang Z, Armstrong D, et al. Amorphization in extreme deformation of the CrMnFeCoNi high-entropy alloy. *Science Advances*. 2021;**7**:eabb3108. DOI: 10.1126/sciadv.abb3108
- [111] Wang H, Chen D, An X, Zhang Y, Sun S, Tian Y, et al. Deformation-induced crystalline-to-amorphous phase transformation in a CrMnFeCoNi high-entropy alloy. *Science Advances*. 2021;**7**:eabe3105. DOI: 10.1126/sciadv.abe3105
- [112] Ji W, Wu MS. Nanoscale origin of the crystalline-to-amorphous phase transformation and damage tolerance of Cantor alloys at cryogenic temperatures. *Acta Materialia*. 2022;**226**:117639. DOI: 10.1016/j.actamat.2022.117639
- [113] Li J, Chen H, He Q, Fang Q, Liu B, Jiang C, et al. Unveiling the atomic-scale origins of high damage tolerance of single-crystal high entropy alloys. *Physical Review Materials*.

2020;4:103612. DOI: 10.1103/PhysRevMaterials.4.103612

[114] Ming K, Li B, Bai L, Jiang P, Wu X, Zheng S, et al. Dynamically reversible shear transformations in a CrMnFeCoNi high-entropy alloy at cryogenic temperature. *Acta Materialia*. 2022;232:117937. DOI: 10.1016/j.actamat.2022.117937

[115] Ming K, Li L, Li Z, Bi X, Wang J. Grain boundary decohesion by nanoclustering Ni and Cr separately in CrMnFeCoNi high-entropy alloys. *Science Advances*. 2019;5:eaay0639. DOI: 10.1126/sciadv.aay0639

[116] Li L, Kamachali RD, Li Z, Zhang Z. Grain boundary energy effect on grain boundary segregation in an equiatomic high-entropy alloy. *Physical Review Materials*. 2020;4:053603. DOI: 10.1103/PhysRevMaterials.4.053603

[117] Li L, Li Z. Aging induced segregation and nanoprecipitation in a severely deformed equiatomic high-entropy alloy. *Materials Characterization*. 2020;165:110369. DOI: 10.1016/j.matchar.2020.110369

[118] Li L, Li Z, Kwiatkowski da Silva A, Peng Z, Zhao H, Gault B, et al. Segregation-driven grain boundary spinodal decomposition as a pathway for phase nucleation in a high-entropy alloy. *Acta Materialia*. 2019;178:1-9. DOI: 10.1016/j.actamat.2019.07.052

[119] Otto F, Dlouhý A, Pradeep KG, Kuběnová M, Raabe D, Eggeler G, et al. Decomposition of the single-phase high-entropy alloy CrMnFeCoNi after prolonged anneals at intermediate temperatures. *Acta Materialia*. 2016;112:40-52. DOI: 10.1016/j.actamat.2016.04.005

[120] Pickering EJ, Muñoz-Moreno R, Stone HJ, Jones NG. Precipitation in the equiatomic high-entropy alloy CrMnFeCoNi. *Scripta Materialia*. 2016;113:106-109. DOI: 10.1016/j.scriptamat.2015.10.025

[121] Schuh B, Mendez-Martin F, Völker B, George EP, Clemens H, Pippan R, et al. Mechanical properties, microstructure and thermal stability of a nanocrystalline CoCrFeMnNi high-entropy alloy after severe plastic deformation. *Acta Materialia*. 2015;96:258-268. DOI: 10.1016/j.actamat.2015.06.025

Chapter 2

Cost-Effective Fe-Rich High-Entropy Alloys: A Brief Review

Yu Yin, Andrej Atrens, Han Huang and Ming-Xing Zhang

Abstract

High-entropy alloys (HEAs) have attracted increased attention due to their extraordinary properties. However, the multicomponent characteristic of equiatomic HEAs inevitably leads to high material costs, which thus limits their widespread industrial applications. Although HEAs are claimed to be suitable for applications in extreme environment due to their comprehensive properties, the actual properties of HEAs dramatically vary with compositions and processes. Therefore, the development of cost-effective HEAs with comprehensive properties is indispensable for industrial uses. Till now, although comprehensive review papers on HEAs are available, few works focused on the cost-effectiveness of HEAs, particularly Fe-rich HEAs recently developed. This review thus aims to fill this gap by reviewing the current research progress in Fe-rich HEAs with a focus on the composition design, microstructure, and properties, including mechanical properties, and resistances for oxidation, wear, and corrosion. The challenges for applying cost-effective Fe-rich HEAs into industries are also arising as future research topics.

Keywords: cost-effective, high-entropy alloys, multicomponent alloys, composition complex alloys, alloy design, microstructure, properties, application

1. Introduction

Since the concept of high-entropy alloys (HEAs) was first proposed by Yeh and Cantor in 2004 [1–3], this type of new metallic material has drawn increasingly more attention due to their unique characteristics (e.g. high configuration entropy, sluggish atomic diffusion, and large lattice distortion) and resultant extraordinary properties (e.g. high strength, high low-temperature fracture toughness, good corrosion resistance and high-temperature properties) [4–6]. Yeh and co-workers firstly defined HEAs as alloys composed of five or more principal elements in equiatomic ratios [1], with single-phase solid-solution (SS) microstructure in either face-centered cubic (FCC) or body-centered cubic (BCC) or hexagonal close-packed (HCP) lattice [4–9], due to the “high-entropy effect” [10, 11]. At the early stage of research on HEAs, the majority of the works focused on the exploration of single-phase HEAs and their corresponding microstructure and mechanical properties. In recent years, the coverage

of HEAs has been extended to include the multiple phase structure with less than five non-equiatomic principal elements [5, 11]. As a result, numerous non-equiatomic alloys were designed and studied based on the equiatomic single-phase HEA system in pursuit of superior mechanical properties [12, 13]. Different terms have been used for these non-equiatomic variants, including multicomponent alloys, multi-principal element alloys and composition complex alloys (CCAs).

It is noteworthy that the current composition design strategy for HEAs usually results in alloys with a high content of expensive metals (e.g. Co, Ta, Hf, V, Nb, W, and Mo). For instance, the above-mentioned HEAs usually contain a Co element, which is common in most of the HEAs [5]. Obviously, using expensive elements increases the overall cost of HEAs. On the other hand, high-entropy alloys usually exhibit comprehensive properties due to their combined effects of multi-principal elements, which makes them suitable for applications in extreme environments. However, majority of the current researches focuses on the mechanical properties only while other properties are ignored. Thus, the development of cost-effective HEAs with comprehensive properties is critical to promote industrial applications of HEAs.

In the past decade, some cost-effective Fe-rich HEAs have been designed and developed, such as the FeNiCrMo alloy that has comprehensive properties [14] and the metastable FeMnCoCr that exhibits superior mechanical properties [12]. Fe-rich HEAs are also named as Fe-rich CCAs [15], Fe-rich medium-entropy alloy (MEA) [16], high-entropy steel [17] and compositionally complex steels [18]. As the entropy value of this type of alloys is not at the high-entropy level, they are generally classified as medium-entropy alloys according to the classification proposed by Yeh [7]. Nevertheless, the entropy of the Fe-rich alloys is indeed higher than traditional steels due to their multicomponent characteristic. To avoid the ambiguity, Fe-rich HEAs are used in this review.

Several reviews on HEAs [4–6, 19, 20] focused on the microstructure and mechanical properties of different types of HEAs, but there is a lack of reviews with a focus on cost-effective HEAs, particularly on Fe-rich HEAs, that is badly needed to guide industrial applications. The present work would fill the gap through overviewing the composition design, manufacturing, processing, microstructure, and properties of the cost-effective Fe-rich HEAs. Based on the review, key challenges for promoting the industry applications of the cost-effective HEAs are proposed.

2. Alloy design strategy

In the past decades, various methods have been developed for composition design of traditional alloys, including physical model methods, computational methods and machine learning methods [21, 22]. These design strategies have also been proved effective to assist the development of HEAs, which has been reviewed several times. More details can be found in Refs. [14, 22, 23]. Using these design strategies, many cost-effective HEAs have been developed. For instance, the Co-free HEAs with relatively lower cost include the equiatomic FeMnCrNi, AlCrFeNi [24], FeCrNiMnCu [25], NiMnFeCu [26], AlFeMnSi [27] and FeCrNiTiAl [28] alloys. But these alloy systems are equiatomic or near-equiatomic, there is less potency for further exploitation of the new alloys with better performance. In recent years, several non-equiatomic HEAs with one enriched element have been developed, which includes the Fe-rich HEAs [14], Ni-rich HEAs [29, 30], Cr-rich HEAs [31, 32], Co-rich HEAs [33–35], Ti-rich HEAs [36] and Al-rich HEAs [37, 38]. Among these non-equiatomic HEAs,

Alloy system	Composition (at. %)	Phase constituent	Status	Ref.
FeNiCrMo	$Fe_{50-x}Ni_{25}Cr_{25}Mo_x$	FCC + IMs	As-cast	[14]
	$Fe_{50-2x}NiCr_xMo_x$	FCC + IMs	As-cast	[14]
	$Fe_{35}Ni_{15}Cr_{25}Mo_5$	FCC	Solid solution treatment	[39]
FeMnCoCr	$Fe_{80-x}Mn_xCo_{10}Cr_{10}$	FCC + HCP	Hot rolling + homogenization	[12]
	$Fe_{49.5}Mn_{30}Co_{10}Cr_{10}C_{0.5}$	FCC + HCP	Hot rolling + homogenization	[40]
	$Fe_{49.5}Mn_{30}Co_{10}Cr_{10}C_{0.5}$	FCC	Hot rolling + homogenization	[41]
FeMnNiCr	$Fe_{50}Mn_{27}Ni_{10}Cr_{13}$	FCC	As-cast/cold rolling/rolling + annealing	[42]
FeMnNiCoCr	$Fe_{40}Mn_{27}Ni_{26}Co_5Cr_2$	FCC	As-cast/homogenization	[43]
FeMnNiAlCr	$Fe_{34}Mn_{20}Co_{20}Cr_{20}Ni_6$	FCC + HCP	Hot rolling+homogenization	[13]
	$(Fe_{40.4}Mn_{34.8}Ni_{11.3}Al_{75}Cr_{16})_{100-x}C_x$	FCC	As-cast	[44]
	$(Fe_{40.4}Mn_{34.8}Ni_{11.3}Al_{75}Cr_{16})_{100-x}B_x$	FCC	As-cast	[44]
FeMnNiAlCr	$Fe_{60}Mn_{21}Cr_{18}Ni_{15}Al_{10}$	BCC + B2	As-cast	[45]
FeNiCrMoTiC	$Fe_{40.5}Ni_{22.5}Cr_{22.5}Mo_{4.5}Ti_{1.5}C_5$	FCC + IMs + Carbides	As-cast/As-aged	[46]

Table 1.
 The currently reported Fe-rich HEAs.

Fe-rich HEAs show high potential for industrial applications due to their superior properties and relatively low cost. To the best of the authors' knowledge, there is no definition for Fe-rich HEAs. Generally, Fe content of these Fe-rich HEAs is in the range of 35–50%, while the content of expensive elements (e.g. Co, Mo, V) is less than 10 at.%. As aforementioned, Fe-rich HEAs are also named Fe-rich CCAs [15], Fe-rich medium-entropy alloy (MEA) [16], high-entropy steel [17] and compositionally complex steels [18]. Up to now, a few Fe-rich HEAs have been developed based on the equiatomic 3d transition metal HEAs, including the FeNiCrMo, FeMnCoCr, FeMnNiCr, FeCoNiCr, FeNiMnAlCr, FeMnNiAlCr and FeMnCrSiNi, through increasing the Fe content in the equiatomic HEAs system. The compositions of these Fe-rich HEAs are listed in **Table 1**.

Previous research work has confirmed that the increasing Fe content may result in different effects on the microstructure and properties in different HEA systems. For instance, Yu and co-workers proposed a new strategy to develop Fe-rich HEAs with eutectic structures [47]. Based on the current pseudo-binary design strategy of eutectic HEAs, the eutectic composition can be experimentally identified by adjusting the atomic content ratio of the intermetallic forming elements to the face-centered cubic (FCC) forming elements in an equiatomic HEA system [47]. As shown in **Figure 1**, a series of cost-effective Fe-rich HEAs with various compositions ($\text{Fe}_{50-x}\text{Ni}_{25}\text{Cr}_{25}\text{Mo}_x$) and corresponding structures (i.e. the hyper-eutectic, eutectic, hypo-eutectic and near single FCC structure) were produced through decreasing the ratio of the intermetallic forming elements (Mo) to the FCC forming elements (Fe) from 1 to 3/7 [47].

The strategies proposed by Yu and co-workers [47] is suitable for HEAs with intermetallic-dominated phase. For HEAs with a single solid solution phase, the increase in the ratio of Fe to other elements may not result in the formation of a eutectic structure. Instead, it may change the phase constituents of the solid solution phase matrix. For instance, by increasing the Fe content in the $\text{Fe}_{80-x}\text{Mn}_x\text{Co}_{10}\text{Cr}_{10}$ [12] and $\text{Fe}_{40-x}\text{Mn}_{20}\text{Co}_{20}\text{Cr}_{20}\text{Ni}_x$ [13] HEAs, the structure of the alloys shifted from single FCC phase to dual-phase (FCC and HCP). By increasing the content of Fe or decreasing the content of other elements in an equiatomic HEA, the thermal stability and mechanical stability can be decreased due to the reduced “high-entropy effect”, which may result in precipitation during heat treatment [48] or TRIP effect during deformation [13], which will be further discussed in Sections 3 and 4.

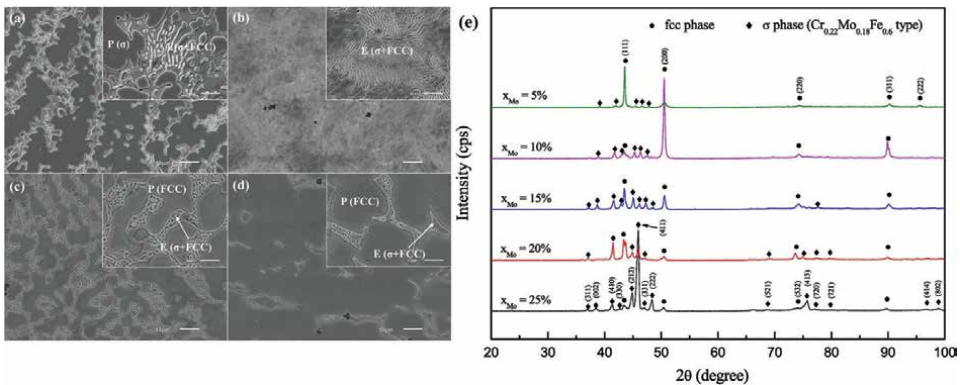


Figure 1. (a–d) Microstructure of as-cast $\text{Fe}_{50-x}\text{Ni}_{25}\text{Cr}_{25}\text{Mo}_x$ alloys: (a) $x = 20$, hyper-eutectic; (b) $x = 15$, fully-eutectic; (c) $x = 10$, hypo-eutectic; (d) $x = 5$, divorced-eutectic; (e) XRD analyses of $\text{Fe}_{50-x}\text{Ni}_{25}\text{Cr}_{25}\text{Mo}_x$ HEAs [47].

3. Microstructure

3.1 Microstructure of the as-cast and homogenization treated alloys

The currently reported Fe-rich HEAs can be classified into different groups in terms of their phase constituent, namely single or near single FCC phase alloys, FCC/HCP dual-phase alloys and BCC/B2 dual-phase alloys. The FCC single phase and FCC/HCP dual-phase Fe-rich HEAs have been comprehensively studied while very few researches focus on the BCC/B2 dual-phase Fe-rich HEAs.

As shown in **Table 1**, the Fe-rich HEAs with single FCC phase include the $\text{Fe}_{50}\text{Mn}_{27}\text{Ni}_{10}\text{Cr}_{13}$, $\text{Fe}_{40}\text{Mn}_{27}\text{Ni}_{26}\text{Co}_5\text{Cr}_2$ and $\text{Fe}_{40.4}\text{Mn}_{34.8}\text{Ni}_{11.3}\text{Al}_{7.5}\text{Cr}_6$. The $\text{Fe}_{50-x}\text{Ni}_{25}\text{Cr}_{25}\text{Mo}_x$ HEAs have a near single FCC structure matrix with an intermetallic phase. Yao and co-workers developed a non-equiatomic $\text{Fe}_{40}\text{Mn}_{27}\text{Ni}_{26}\text{Co}_5\text{Cr}_2$ alloy based on the equiatomic FeMnNiCoCr Cantor alloy and their microstructure is shown in **Figure 2a-f** [42]. The EBSD and EDS results of the recrystallized alloy in **Figure 2** reveals that the non-equiatomic variant of Cantor alloy has a homogenized solid solution matrix despite its comparably low configurational entropy [42], indicating that equimolarity may not be a compulsory requirement to achieve single-phase solid solution in multicomponent systems [42]. A similar conclusion can be drawn from Yu and co-workers' work. As shown in **Figure 1**, with the increasing of the ratio of Fe to Mo in the FeNiCrMo HEA, the equiatomic FeNiCrMo was transformed into a non-equiatomic alloy, resulting in a lower configuration entropy value of the alloy system. However, the equiatomic FeNiCrMo is composed of an intermetallic phase while the non-equiatomic $\text{Fe}_{45}\text{Ni}_{25}\text{Cr}_{25}\text{Mo}_5$ alloy with the lowest entropy value shows the near FCC phase with low fraction of intermetallic (**Figure 2g-i**). Obviously, this cannot be explained using the "high-entropy effect" proposed by Yeh and co-workers. This can be related to the decreased atom size difference due to the increasing of Fe content, which is usually ignored by the current "high-entropy effect". As a consequence, much more compositions of non-equiatomic HEAs can be designed to gain single solid solution phase by decreasing the atom size difference even the maximum entropy value may not be achieved.

The current dual-phase Fe-rich HEAs were developed based on the equiatomic FeMnCoCr and FeMnCoCrNi. Increasing the ratio of Fe to Mn in the FeMnCoCr HEA and the ratio of Fe to Ni in the FeMnCoCrNi HEA decreased the phase stability of single solid solution phase. Hence, both the non-equiatomic $\text{Fe}_{80-x}\text{Mn}_x\text{Co}_{10}\text{Cr}_{10}$ ($x < 30$ at.%) and $\text{Fe}_{40-x}\text{Mn}_{20}\text{Co}_{20}\text{Cr}_{20}\text{Ni}_x$ ($x < 6$ at.%) systems involved partial martensitic transformation from FCC to the HCP phase during quenching (**Figures 2j-m** and **3**). As shown in **Figure 2j-m**, the homogenized $\text{Co}_{20}\text{Cr}_{20}\text{Fe}_{34}\text{Mn}_{20}\text{Ni}_6$ alloy after water quenching shows an FCC and HCP dual-phase structure with homogeneous composition. The SEM-BSE image reveals a high density of stacking faults in the FCC phase, indicating a very low stacking fault energy of the new alloy. The effect of the metastable phase on the mechanical properties will be further discussed in Section 4.1.

In addition, in contrast to the FeMnCrNiAl variant ($\text{Fe}_{40.4}\text{Mn}_{34.8}\text{Ni}_{11.3}\text{Al}_{7.5}\text{Cr}_6$) with a single FCC phase, a Fe-rich HEA ($\text{Fe}_{36}\text{Mn}_{21}\text{Cr}_{18}\text{Ni}_{15}\text{Al}_{10}$) with BCC/B2 dual-phase structure has been developed. As shown in **Figure 2n-o**, the as-cast alloy has a dual-phase structure consisting of a BCC matrix and homogeneously distributed cuboidal B2 ordered particles. The BCC/B2 dual-phase structure has been widely reported in the refractory HEAs [49, 50], which usually exhibit superior high-temperature properties. However, nearly all the current refractory HEAs (e.g. MoNbTaW, MoNbTaVW and HfNbTaTiZr) contain expensive elements, such as the Ta, Hf, V, Nb, Mo, W.

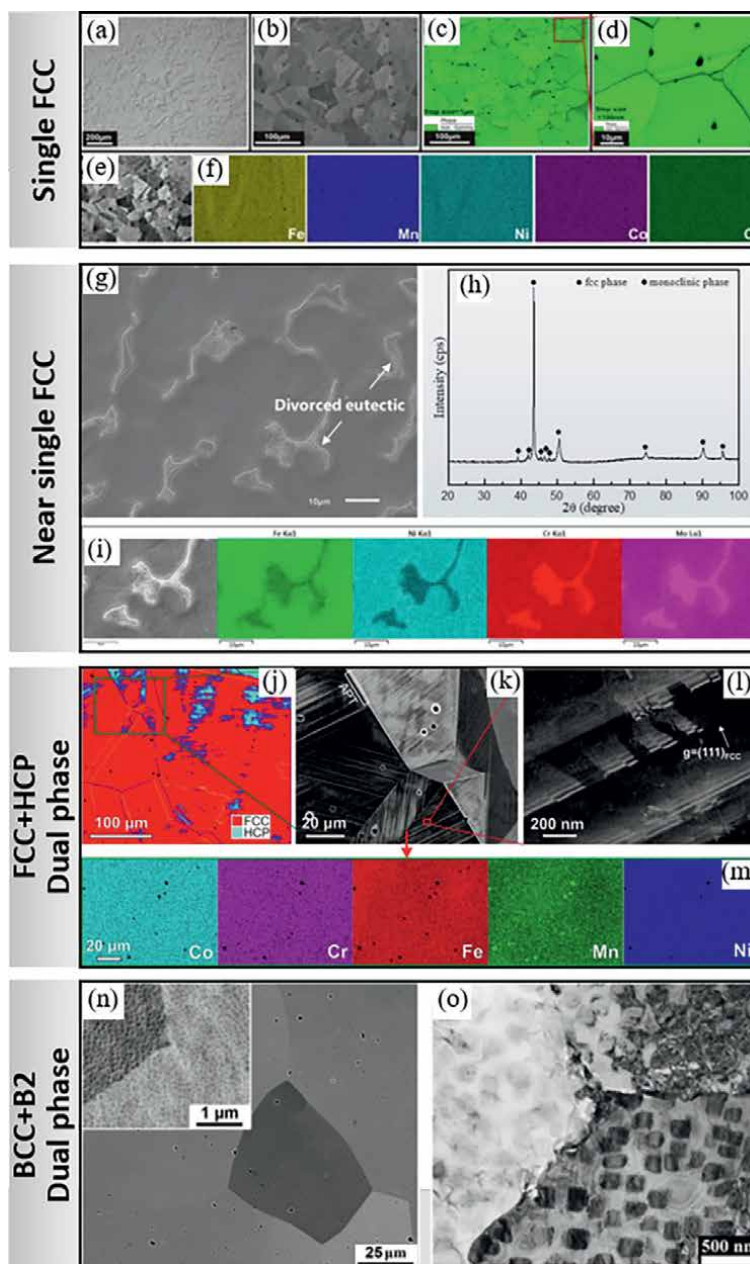


Figure 2. (a–f) Microstructure of the recrystallized $\text{Fe}_{40}\text{Mn}_{27}\text{Ni}_{26}\text{Co}_5\text{Cr}_2$: a. OM image, b. SE image, c and d. EBSD phase maps and e and f. EDS maps [42]; (g–i) Microstructure of the as-cast $\text{Fe}_{15}\text{Ni}_{25}\text{Cr}_{25}\text{Mo}_5$; g. SEM image, h. EDS mapping and i. XRD spectrum [15]; (j–m) Microstructure of the homogenized and water-quenched $\text{Co}_{20}\text{Cr}_{20}\text{Fe}_{34}\text{Mn}_{20}\text{Ni}_6$ HEA: j. EBSD phase map; k and l. ECCI image; m. EDS maps [13]; (n and o) Microstructure of the $\text{Fe}_{36}\text{Mn}_{21}\text{Cr}_{18}\text{Ni}_{15}\text{Al}_{10}$ alloy in the as-cast condition: a. BSE image, c. bright-field TEM image [45].

In contrast, the newly developed BCC/B2 dual-phase HEA ($\text{Fe}_{36}\text{Mn}_{21}\text{Cr}_{18}\text{Ni}_{15}\text{Al}_{10}$) is Fe-enriched and only contains inexpensive elements, which sheds light on the development of cost-effective refractory HEAs.

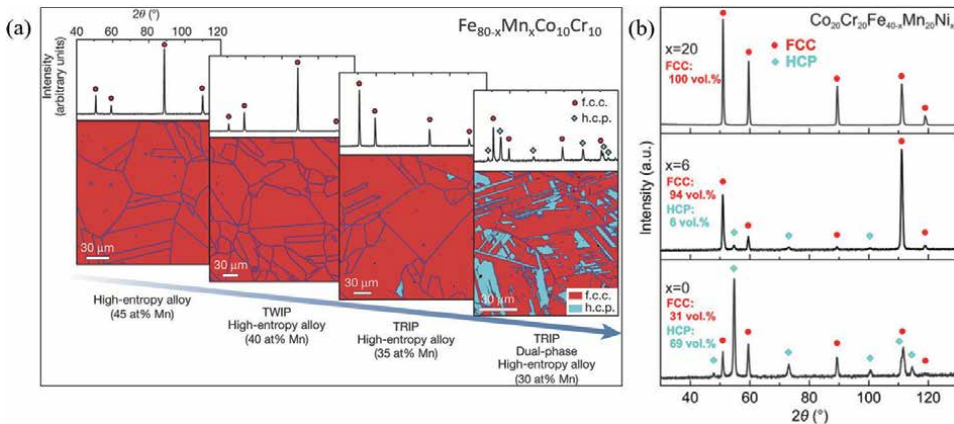


Figure 3. XRD patterns and EBSD phase maps of $Fe_{80-x}Mn_xCo_{10}Cr_{10}$ ($x = 45$ at.%, 40 at.%, 35 at.% and 30 at.%) HEAs [12]; XRD patterns of homogenized $Co_{20}Cr_{20}Fe_{10-x}Mn_{20}Ni_4$ ($x = 20$ at.%, 6 at.% and 0) HEAs reveal the variations of phase configurations with changing the x value [13].

3.2 Microstructure after annealing

Although HEAs with single-phase were initially considered more stable due to the high-entropy effect, such as the CoCrFeMnNi HEA, they are recognized as a supersaturated solid solution at intermediate temperature in recent years because precipitation of the second phase or decomposition in the single solid solution phase occurs in the alloys. Decomposition was observed in both the FCC and BCC HEAs, such as the CoCrFeMnNi [51] with FCC structure and HfNbTaTiZr HEA [52, 53] with BCC structure, after long-period annealing at intermediate temperatures. It is believed that the annealing at intermediate temperatures for a long-time results in a weakened “high-entropy effect” due to the temperature-dependent contribution of mixing entropy to total Gibbs free energy and thus decreases the phase stability of the solid solution phase.

For Fe-rich HEAs, the phase stability of their solid solution can be further weakened due to the non-equiatomic and reduced entropy value, including thermal stability and mechanical stability. As aforementioned, the decreased thermal stability of the solid solution phase results in phase transformation during cooling, such as the partial martensitic transformation from FCC to the HCP phase when quenching as shown in **Figures 2j** and **3**. The decreased mechanical stability will introduce phase transformation during deformation. Both the reduced thermal stability and mechanical stability contribute to the improvement of mechanical properties, which will be further discussed in Section 4.1. In addition, the decreased thermal stability may result in the precipitation of the second phase in the metastable solid solution phase, which can be used to manipulate the microstructure and thus their mechanical properties. For instance, Yu and co-workers investigated the precipitation behavior of the cost-effective $Fe_{45}Ni_{25}Cr_{25}Mo_5$ HEA with a face-centered cubic (FCC) matrix [48]. As shown in **Figure 4**, with the increasing aging time at 900°C , the volume fraction of needle-shaped precipitates increased significantly in the FCC matrix of $Fe_{45}Ni_{25}Cr_{25}Mo_5$ HEA. This resulted in a high age-hardening effect, which raised the hardness from 192 HV_5 to nearly 300 HV_5 . However, the peak-aged sample exhibited room-temperature brittleness due to the precipitation of a large needle-shaped

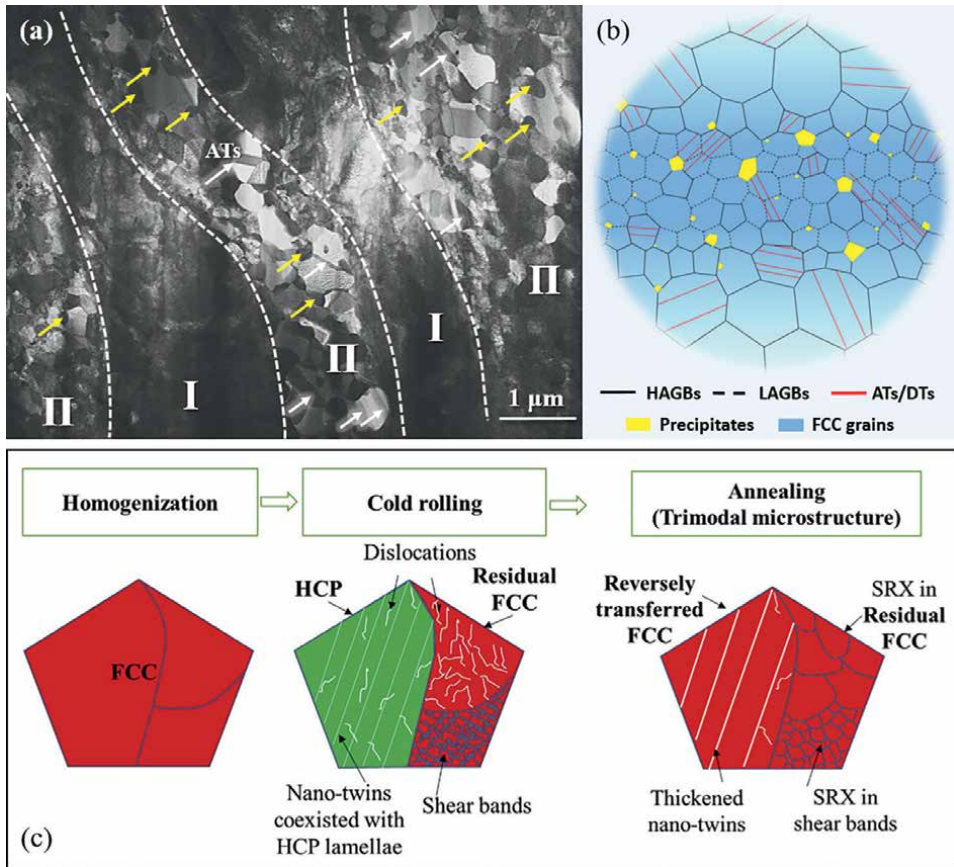


Figure 4. (a and b) Novel heterogeneous lamella (HL) structure in the $Fe_{35}Ni_{35}C_{25}Mo_5$ HEA: STEM bright-field image of the thin-foil sample. The yellow arrows indicate the σ precipitates (a) [39]; Schematic illustration of the HL microstructure with nanoprecipitates and twins (b). (c) Schematic plot of producing hierarchical grain structure in the $Fe_{49.5}Mn_{30}Co_{10}Cr_{10}C_{0.5}$ alloy [41].

intermetallic phase. To decrease the brittleness, thermomechanical processing can be applied to decrease the size of precipitates, which will be discussed in Section 3.3.

Precipitation or phase decomposition is also reported in the dual-phase Fe-rich HEAs, for instance, the $Fe_{36}Mn_{21}Cr_{18}Ni_{15}Al_{10}$ HEA with BCC and B2 phases. Interestingly, annealing at a high temperature of 1200°C for 24 h barely changed the structure (Figures 2n–o and 5h), but annealing at a relatively lower temperature of 1000°C resulted in precipitation of the FCC phase along the grain boundaries and within the matrix (Figure 5i–j). Due to the presence of the soft and ductile FCC phase at temperatures lower than 1000°C, the alloy is softened and thus may not be suitable for applications under 1000°C. However, the nanometer scaled cuboid B2 phase remains unchanged at 1200°C for 24 h, which is abnormal. Generally, high-temperature treatment will result in the coarsening of the second phase. This suggests a high stability of the nanometer scaled dual-phase structure, and therefore maintaining superior mechanical properties at temperatures close to 1200°C. Future work is needed to verify the high stability and evaluate the high-temperature (>1000°C) properties.

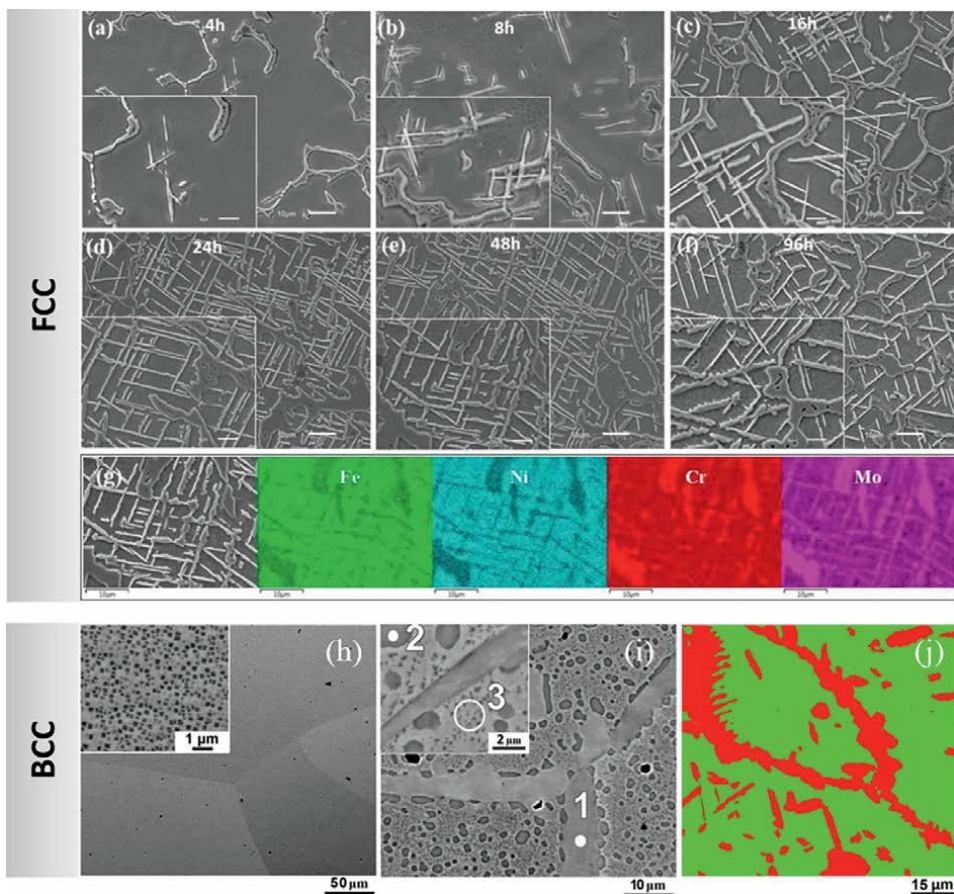


Figure 5. (a–f) SEM images of the $\text{Fe}_{45}\text{Ni}_{25}\text{Cr}_{25}\text{Mo}_5$ samples aged at 900°C for different hours; (g) EDS map of the peaked aged $\text{Fe}_{45}\text{Ni}_{25}\text{Cr}_{25}\text{Mo}_5$ HEA [48]; (h–j) Microstructure of the $\text{Fe}_{36}\text{Mn}_{21}\text{Cr}_{18}\text{Ni}_{35}\text{Al}_{10}$ alloy after annealing at 1200°C (h) and 1000°C (i, j) for 24 h: h and i. BSE images, j. EBSD phase map (FCC phase in red and BCC/B2 phase in green) [45].

3.3 Microstructure after the thermomechanical process

In contrast to the simplicity of microstructure in the as-cast and as-aged Fe-rich HEAs, microstructure after thermomechanical processing can be more diverse, which provides much more opportunities for microstructure and mechanical properties manipulation. Similar to traditional alloys or equiatomic HEAs, thermomechanical processing is performed to control the grain size, phase constituents or phase fraction in Fe-rich HEAs ($\text{Fe}_{80-x}\text{Mn}_x\text{Co}_{10}\text{Cr}_{10}$ and $\text{Fe}_{49.5}\text{Mn}_{30}\text{Co}_{10}\text{Cr}_{10}\text{C}_{0.5}$) [12, 13, 40, 54], which corresponds to the grain-refinement strengthening, TWIP or TRIP effect. Except for the above traditional microstructure control methods, heterogeneous or hierarchical microstructure design (e.g. heterogeneous lamella structures, gradient structures, laminate structures, and harmonic structures) [19, 55, 56] has been proved effective in the property improvement of HEAs. This has been an active research topic.

Unique heterogeneous lamella (HL) structure was introduced in a cost-effective FCC HEA ($\text{Fe}_{35}\text{Ni}_{35}\text{Cr}_{25}\text{Mo}_5$) through a single-step heat treatment (800°C for 1 h) after

cold rolling. As shown in **Figure 4a** and **b**, the HL structure consists of alternative layers of coarse-grained FCC matrix, and ultra-fine grains or subgrains layer with nanoprecipitates and annealing twins (ATs). According to Yu and co-workers, the preferential precipitation of σ phase at the shear bands with a high density of lattice defects (e.g. high-density dislocation walls and nano deformation twins) restrict the growth of recrystallized grains, resulting in the partial recrystallization and thus the formation of HL structure [39]. In addition, Su and co-workers [41] demonstrated a hierarchical microstructure design strategy to improve the mechanical properties of an Fe-rich HEA ($\text{Fe}_{49.5}\text{Mn}_{30}\text{Co}_{10}\text{Cr}_{10}\text{C}_{0.5}$) by a thermomechanical processing. As shown in **Figure 4c**, three distinguished regions with different levels of dislocation density formed in the as-homogenized FCC matrix after cold rolling, including the deformation-induced HCP phase with the lowest dislocation density, residual FCC region with medium dislocation density, and severe shear bands region with the highest dislocation density. After annealing at a temperature above 400°C , the HCP phase is reversed to FCC phase while twins which co-existed with martensite lamellae got thickened in the parent grains. Due to the different dislocation densities and thus different recrystallization kinetics, trimodal grain structures were finally produced and characterized by small recrystallized grains associated with shear bands, medium-sized grains recrystallized from parent grains and unrecrystallized large grains. Such a grain size hierarchy promotes the variation in phase stability and results in a joint activation of transformation-induced plasticity (TRIP) and twinning-induced plasticity (TWIP) effects upon loading and thus a good strength-ductility synergy [41].

The above findings indicate that the non-equiatomical alloys (e.g. Fe-rich HEAs) not only enable more alloys with different compositions to be designed, but also broaden the window for microstructure and properties tuning due to the reduced thermal and mechanical stability of the solid solution phase.

3.4 Microstructure during deformation

As aforementioned, the decreased thermal stability and mechanical stability of Fe-rich HEAs can be applied to manipulate the microstructure via different deformation mechanisms (e.g. dislocation slip, twinning and the formation of stacking faults) and strengthening effects (e.g. TRIP effect, precipitation strengthening or integrated strengthening effect), and thus to achieve better mechanical properties. For instance, Zhiming and co-workers [12] reported that the improvement in the mechanical property of the metastable DP HEA ($\text{Fe}_{50}\text{Mn}_{30}\text{Co}_{10}\text{Cr}_{10}$) is related to the thermally induced DP structure and mechanically induced HCP phase [12]. As shown in **Figure 6a** and **b**, a large number of stacking faults is observed in the metastable FCC phase in the $\text{Fe}_{50}\text{Mn}_{30}\text{Co}_{10}\text{Cr}_{10}$ HEA, which acted as phase-formation nuclei (FCC \rightarrow HCP) during deformation. When strain is lower than 30%, the stress-induced transformation from the FCC to HCP phase is the dominant deformation mechanism. With increasing strain to over 30%, the density of stacking faults and nano-twins increased in both the initial and mechanically induced HCP phase, which contributes significantly to strain hardening. Further increase of the strain to over 45% resulted in the formation of a high density of dislocations. Therefore, the thermally and mechanically induced HCP phase plays an important role in plastic accommodation and hardening at later stages of deformation via multiple deformation mechanisms, including dislocation slip, twinning, and the formation of stacking faults [12]. In addition, Yu and co-workers [39] introduced a unique heterogeneous lamella (HL) grain structure with a high density of nanoprecipitates, annealing twins and low angle boundaries in the

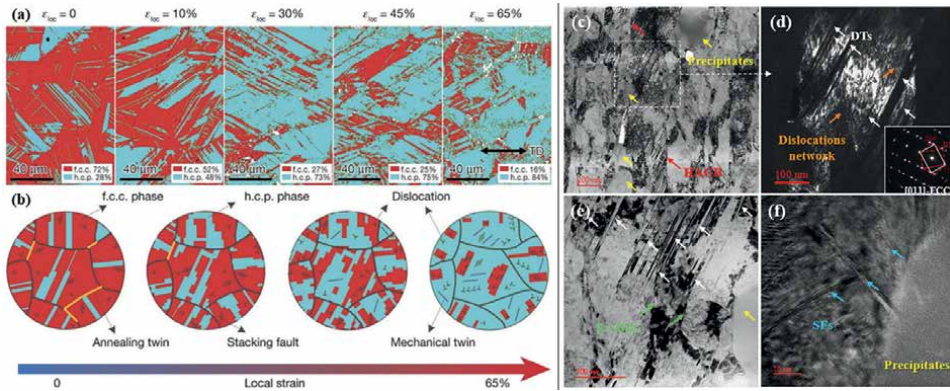


Figure 6. Deformation micro-mechanisms in the TRIP-DP-HEA with increasing tensile deformation at room temperature [12]; (c–f) Microstructural evolution upon tensile deformation in the HL $\text{Fe}_{35}\text{Ni}_{35}\text{Cr}_{25}\text{Mo}_5$ HEA [39].

$\text{Fe}_{35}\text{Ni}_{35}\text{Cr}_{25}\text{Mo}_5$ HEA (Figure 4a and b), resulting in a superior tensile property, with yield strength over 1.0 GPa and total elongation of ~13%. It is reported that the superior tensile properties were resulted from the hetero-deformation induced (HDI) strengthening, precipitation strengthening and the coexistence of multiple deformation mechanisms [39]. As shown in Figure 6c–f, the as-deformed $\text{Fe}_{35}\text{Ni}_{35}\text{Cr}_{25}\text{Mo}_5$ HEA shows a complex hierarchical microstructure including stacking faults (SFs), dislocation, annealing/deformation twins (DTs), low-angle grain boundaries (LAGBs), nanoprecipitates and HL interfaces. During deformation, the hierarchical microstructure (a high density of LAGBs, HL interfaces and precipitates) in the HL $\text{Fe}_{35}\text{Ni}_{35}\text{Cr}_{25}\text{Mo}_5$ alloy interact with the subsequently activated dislocations, SFs and DTs and thus significantly promote the strain hardening ability and prevent early necking.

4. Properties

4.1 Mechanical properties

The room-temperature tensile properties (yield strength and fracture strain) of the current cost-effective Fe-rich HEAs/CCAs and a few commercial steels (for comparison purpose) are summarized in Figure 7. Obviously, the tensile properties of the current Fe-rich HEAs significantly vary, depending on their composition and microstructure. The widely reported strength-ductility trade-off can be identified in both the Fe-rich HEAs and commercial steels. Most Fe-rich HEAs or steels with high yield strength correspond to low elongation and vice versa. For instance, the ductile $\text{Fe}_{50}\text{Mn}_{30}\text{Co}_{10}\text{Cr}_{10}$ alloy with high elongation of over 70% has a yield strength of less than 500 MPa [12], while the $\text{Fe}_{35}\text{Ni}_{35}\text{Cr}_{25}\text{Mo}_5$ HEAs [39] and $\text{Fe}_{49.5}\text{Mn}_{30}\text{Co}_{10}\text{Cr}_{10}\text{C}_{0.5}$ [41] after thermomechanical process exhibit a very high strength over 1 GPa but with ductility around 10%. Some HEAs exhibit balanced strength and ductility, such as the $\text{Fe}_{49.5}\text{Mn}_{30}\text{Co}_{10}\text{Cr}_{10}\text{C}_{0.5}$ HEA [41]. After cold rolling and annealing at 650°C for 3 min, a good combination of yield strength (824 MPa), UTS (1.05 GPa) and ductility (33%) are attained due to the hierarchical grain structure (Figure 4c) and the sequential activation of transformation-induced plasticity (TRIP) and twinning-induced

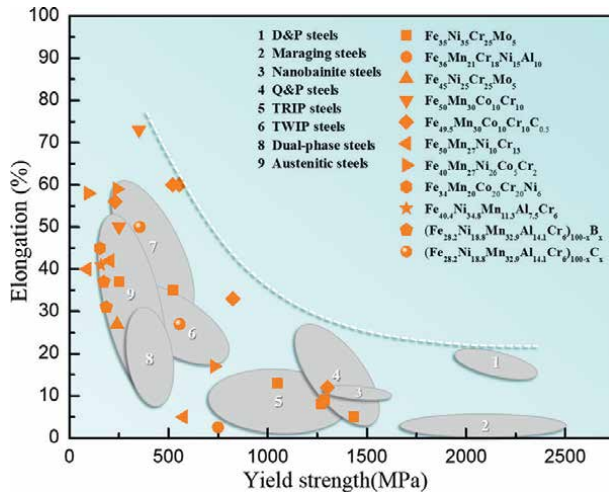


Figure 7. Tensile properties of most currently reported Fe-rich HEAs [12–14, 39–46] compared with different types of steels (Data of steels is from Ref. [57, 58]).

plasticity (TWIP) effects during deformation [41]. Some HEAs also exhibit quite low tensile performance, for instance, the BCC/B2 dual-phase $\text{Fe}_{36}\text{Mn}_{21}\text{Cr}_{18}\text{Ni}_{15}\text{Al}_{10}$ HEA with severe brittleness, the elongation of which is less than 3%. Furthermore, most FCC Fe-rich HEAs exhibit very low strength (<250 MPa) at as-cast condition, which is close to that of the 316 L stainless steel.

Compared with commercial steels, the mechanical properties of the currently reported Fe-rich HEAs overlap most of the commercial steels, but are still lower than some high strength steels, particularly the maraging steels (number 2 in **Figure 6**) and D&P steels (number 1 in **Figure 6**) with ultra-high strength [57, 59, 60]. For instance, the low-cost D&P steel ($\text{FeMn}_{9.95}\text{Co}_{0.44}\text{Al}_{1.87}\text{V}_{0.67}$) possesses a superior tensile property, with the yield strength and elongation of nearly 2 GPa and 22.0%, respectively [60]. Thus, it is essential to improve the mechanical properties of Fe-rich HEAs to further enhance their application potential.

4.2 Wear resistance

Except for the tensile or compressive properties, data of other mechanical properties, such as wear resistance, impact toughness, fatigue properties, or creep resistance, of Fe-rich HEAs is very limited. Based on the cost-effective age-hardenable $\text{Fe}_{45}\text{Ni}_{25}\text{Cr}_{25}\text{Mo}_5$ HEA, Yu and co-workers developed an intermetallics and carbides reinforced $\text{Fe}_{40.5}\text{Ni}_{22.5}\text{Cr}_{22.5}\text{Mo}_{4.5}\text{Ti}_5\text{C}_5$ HEA with superior wear resistance [46]. As shown in **Figure 8a-d**, the as-cast FeNiCrMoTiC alloy consists of an FCC solid solution matrix with randomly-distributed carbides and FCC/intermetallics eutectic structures. Aging at 800°C for 96 h effectively increases the hardness (**Figure 8e**) and wear resistance (**Figure 8f**) of the alloy due to the precipitation strengthening of intermetallics. It is noteworthy that, although the hardness of high-chromium cast iron (HCCI) is much higher than that of the peak-aged FeNiCrMoTiC alloy, the wear resistance of the latter is superior (**Figure 8f**). This is attributed to their different wear behavior during dry friction (**Figure 8g**). In contrast to the severe delamination in the HCCI, the peak-aged FeNiCrMoTiC alloy shows moderate abrasive wear and

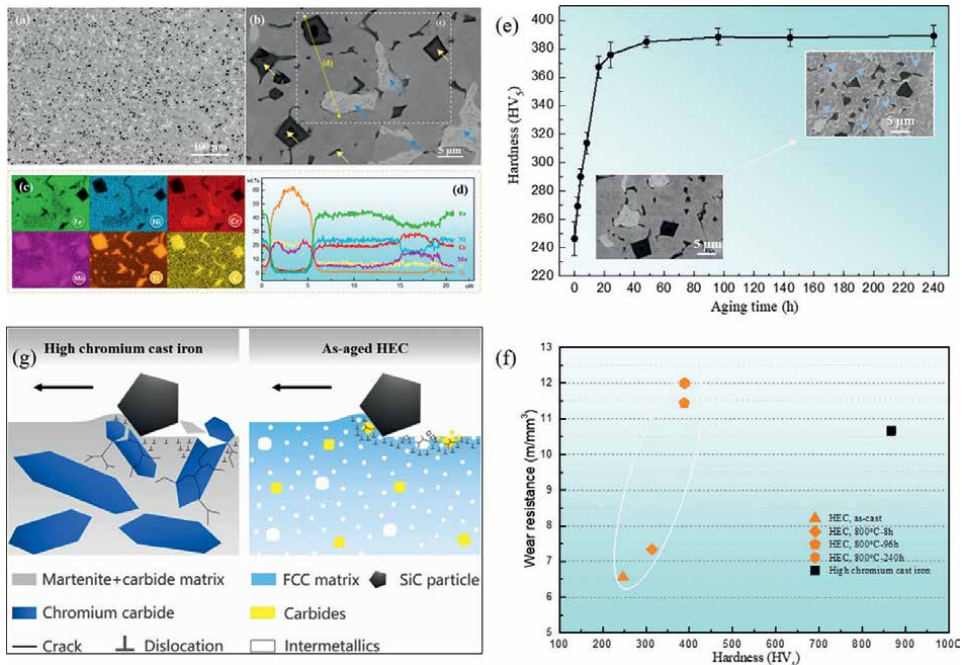


Figure 8. SEM-BSE images (a–b) and the corresponding EDS map (c) and line-scan results (d) of the as-cast $Fe_{40.5}Ni_{22.5}Cr_{22.5}Mo_{4.5}Ti_{5}C_5$ HEC; (e) Hardness aging curves of the HEC at 800°C for up to 240 h, with inserted BSE images of the as-cast sample and peak-aged (800°C, 96 h) HEC; (f) Wear resistance of the HECs and destabilized HCCI are plotted against their hardness values; (g) Comparison of wear mechanism of the HCCI and as-aged HEC [46].

minor delamination under sliding friction due to its combined effect of ductile FCC matrix and fine reinforced particles, including the in-situ formed carbides/eutectic structures and precipitates formed during aging treatment [46]. On one hand, the fine reinforced particles with lower cracking susceptibility effectively strengthen the soft FCC matrix and thus reduce both the material loss by abrasive wear and severe brittle delamination. Moreover, the spalled fine particles (e.g. carbides or intermetallics) were found welded back into the FCC phase during friction and thus further strengthening the matrix and decreasing the abrasive wear. On the other hand, the propagation of micro-cracks from the brittle particles is inhibited by the ductile FCC matrix, which also suppresses the severe brittle delamination [46].

4.3 Oxidation and corrosion resistance

As shown in **Table 1**, all the currently reported Fe-rich HEAs contain Cr, most of which is over 10 at.%. Generally, alloys with high content of Cr show high oxidation and corrosion resistance. It is reasonable to assume that most currently reported Fe-rich HEAs possess superior oxidation and corrosion resistance. However, corrosion behavior of Fe-rich HEAs is rarely reported. Yu and co-workers evaluated the high-temperature oxidation resistance of the Fe-rich $Fe_{45}Ni_{25}Cr_{25}Mo_5$ HEA in comparison to two commercial alloys (i.e. 316 L stainless steel and Inconel 625 superalloy) [15]. In contrast to the catastrophic oxidation behavior of 316 L stainless steel and severe oxide spallation on Inconel 625 superalloy, the Fe-rich HEA showed outstanding

oxidation resistance at 1200°C, including low oxidation rate and high spallation resistance. As shown in **Figure 9a-l**, catastrophic oxidation and spallation occurred on the 316 L stainless steel at 1200°C mainly due to the high oxidation rate and the intergranular cracking in the coarse-grained FeO scale. For Inconel 625 superalloy, the high densities of pores, cracks and Nb oxides in the Cr₂O₃ scale promoted the oxidation process. Meanwhile, the selective formation of Nb₂O₅ along the Cr₂O₃ scale/substrate interface resulted in severe oxide spallation and thus reduction of the oxidation resistance [15]. In contrast, an exclusive and compact chromia scale with better mechanical properties (e.g. high hardness and elastic modulus) formed on the Fe-rich HEA, protecting the matrix from further oxidation and high resistance against interface cracking during the oxidation process. As a result, the Fe-rich HEA showed the lowest oxidation rate at 1200°C compared with that of 316 L stainless steel and Inconel superalloy (**Figure 9m**) [15].

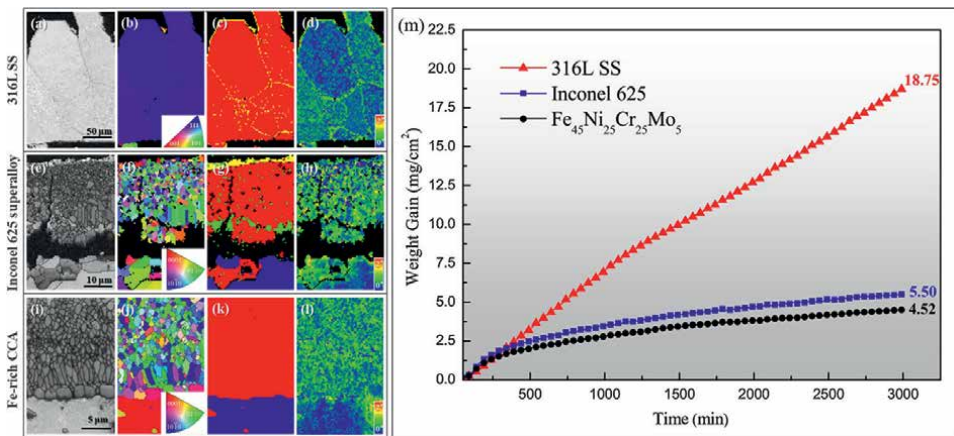


Figure 9. EBSD analysis of the FeO oxide scale formed on the 316 L SS (a–d), on the Inconel 625 superalloy (e–h) and the Fe₄₅Ni₂₅Cr₂₅Mo₅ CCA (i–l) after oxidation at 1200°C in the air for 48 h: (a, e, and i) band contrast map; (b, f, and j) IPF map; (c, g, and k) phase map; (d, h, and l) KAM map; The isothermal oxidation kinetics of the Fe-rich CCA as compared with the 316 L SS and the Inconel 625 alloy at 1200°C in the air for 48 h [15].

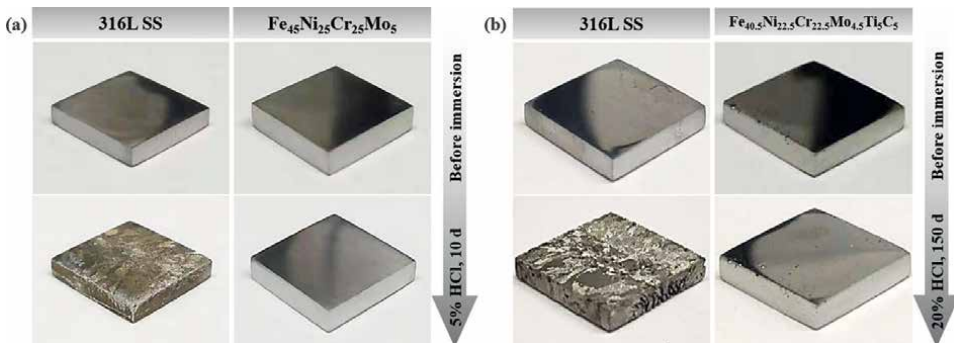


Figure 10. (a) Surface morphologies of the Fe₄₅Ni₂₅Cr₂₅Mo₅ HEA and the 316 L SS after immersion in the 5% HCl solution at room temperature for 10 days. (b) Surface morphologies of the aged Fe_{40.5}Ni_{22.5}Cr_{22.5}Mo_{4.5}Ti₅C₅ HEA and 316 L SS before and after immersion in the 20% HCl solution at room temperature for 150 days [46, 48].

Yu and co-workers also qualitatively evaluated the corrosion resistance of the $\text{Fe}_{45}\text{Ni}_{25}\text{Cr}_{25}\text{Mo}_5$ and $\text{Fe}_{40.5}\text{Ni}_{22.5}\text{Cr}_{22.5}\text{Mo}_{4.5}\text{Ti}_5\text{C}_5$ alloys using the immersion experiment [46, 48], both of which have superior corrosion resistance in an acid environment. As shown in **Figure 10a**, after immersion in the 5% HCl solution at room temperature for 10 days, obvious surface corrosion occurred on the 316 L stainless steel, but no visible corrosion was found on the $\text{Fe}_{45}\text{Ni}_{25}\text{Cr}_{25}\text{Mo}_5$ HEA [48]. Similarly, catastrophic corrosion was identified in the stainless steel while only minor corrosion pits are visible on the $\text{Fe}_{40.5}\text{Ni}_{22.5}\text{Cr}_{22.5}\text{Mo}_{4.5}\text{Ti}_5\text{C}_5$ HEA after immersion in 20% HCl solution for 150 days (**Figure 10b**) [46]. In-depth future work about the corrosion mechanisms of the Fe-rich HEAs is necessary.

5. Conclusions and outlook

Fe-rich HEAs exhibit a high potential for industrial applications owing to their superior properties and relatively low cost. Upon reviewing the currently reported Fe-rich HEAs the following conclusions are achieved.

1. The Fe-rich HEAs reported most recently were developed based on the 3d transition-metal HEAs, including single or near single FCC, FCC/HCP dual-phase and BCC/B2 dual-phase alloys. The FCC and FCC/HCP dual-phase Fe-rich HEAs have been widely studied, but few researches focused on the BCC/B2 dual-phase Fe-rich HEAs.
2. The compositions of various Fe-rich HEAs can be designed by simply increasing the Fe content in the equiatomic HEAs system, which may result in different effects on the microstructure and properties of different HEA systems. By increasing the content of Fe or decreasing the content of other elements in equiatomic HEAs, the thermal stability and mechanical stability are reduced because of lowering the “high-entropy effect”. The decreased thermal stability of the solid solution phase facilitates precipitation during heat treatment or phase transformation (e.g., FCC to HCP transformation) during cooling. The decreased mechanical stability enables stress-induced phase transformation during deformation. Like conventional alloys, these phenomena can be used to tailor the microstructure, introduce different deformation mechanisms (e.g., dislocation slip, twinning and the formation of stacking faults) and strengthening effects (e.g. TRIP effect, precipitation strengthening or integrated strengthening effect), and thus achieve improved mechanical properties.
3. Like the processing of traditional alloys or equiatomic HEAs, a thermomechanical process can be used to tailor the grain size, phase constituents or fraction of the Fe-rich HEAs (e.g., $\text{Fe}_{80-x}\text{Mn}_x\text{Co}_{10}\text{Cr}_{10}$ and $\text{Fe}_{49.5}\text{Mn}_{30}\text{Co}_{10}\text{Cr}_{10}\text{C}_{0.5}$), in order to improve the mechanical properties of the alloys.
4. The tensile properties of the currently reported Fe-rich HEAs vary within a wide range, depending on their composition and microstructure. The widely reported strength-ductility trade-off can be identified in both the Fe-rich HEAs and commercial steels. The mechanical properties of the currently reported Fe-rich HEAs are better than most of the commercial steels, but are still lower than some high strength steels, such as the maraging steels and D&P steels with ultra-high strength.

5. Except for the tensile or compressive properties, data of other mechanical properties of Fe-rich HEAs is limited, such as wear resistance, impact toughness, fatigue properties or creep resistance. In addition, although most Fe-rich HEAs are supposed to possess superior oxidation and corrosion resistance, very few research results are reported.

Some Fe-rich HEAs exhibit superior properties including mechanical properties, and oxidation and corrosion resistance. However, the greatest challenge is how to commercialize such alloys for industrial application. Systematic and comprehensive research is needed, which should focus more on the aspects of composition design, microstructure control, and properties evaluation and improvement. Here, combining the opinions proposed by other experts in the field of HEAs [23, 61] the authors propose a few topics that are of particular significance for the application of Fe-rich HEAs.

1. Except for the current 3d transition metal Fe-rich HEAs with FCC or FCC/HCP dual-phase structure, the Fe-rich HEAs with BCC structure should also be developed. Such studies are expected to shed some light on the development of low-cost refractory alloys. This can be achieved by introducing refractory elements (i.e., Ti, V, Zr, Nb, Hf, and W) or other elements (e.g., Al, Si) with a low valence electron concentration (VEC) value. Due to the high strength of the BCC phase at elevated temperatures, the cost-effective Fe-rich HEAs with BCC structure can be a new type of promising refractory HEAs. For instance, the Fe-rich HEAs ($\text{Fe}_{36}\text{Mn}_{21}\text{Cr}_{18}\text{Ni}_{15}\text{Al}_{10}$) exhibit a very stable fine BCC/B2 DP structure at 1200°C, which can be a cost-effective alloy for high-temperature application [45].
2. The mechanical properties of the Fe-rich HEAs developed need further improvement. Different strategies should be explored to optimize their composition, microstructure, and process. For instance, other than C, the addition of other interstitial elements e.g., N, B, O, in Fe-rich HEAs may be used for property improvement. In addition, thermomechanical processing can be an effective method for microstructure control and properties manipulation.
3. The properties of Fe-rich HEAs need to be evaluated comprehensively to explore their potential applications in extreme environments. Except for the most widely reported room-temperature tensile properties, other mechanical properties like low/high-temperature tensile properties, impact toughness, fatigue resistance, creep resistance and wear resistance should be characterized. Further exploration of other properties like oxidation and corrosion resistance should also be conducted.

Acknowledgements

This work was financially supported by the ARC Discovery Project (No. DP200101408).

Conflict of interest


The authors declare no conflict of interest.

Author details

Yu Yin, Andrej Atrens, Han Huang* and Ming-Xing Zhang*
School of Mechanical and Mining Engineering, University of Queensland, Brisbane,
Australia

*Address all correspondence to: han.huang@uq.edu.au
and mingxing.zhang@uq.edu.au

IntechOpen

© 2022 The Author(s). Licensee IntechOpen. This chapter is distributed under the terms of the Creative Commons Attribution License (<http://creativecommons.org/licenses/by/3.0>), which permits unrestricted use, distribution, and reproduction in any medium, provided the original work is properly cited. 

References

- [1] Yeh JW, Chen SK, Lin SJ, Gan JY, Chin TS, Shun TT, et al. Nanostructured high-entropy alloys with multiple principal elements: Novel alloy design concepts and outcomes. *Advanced Engineering Materials*. 2004;**6**(5):299-303
- [2] Cantor B, Chang ITH, Knight P, Vincent AJB. Microstructural development in equiatomic multicomponent alloys. *Materials Science and Engineering A*. 2004;**375**:213-218
- [3] Huang PK, Yeh JW, Shun TT, Chen SK. Multi-principal-element alloys with improved oxidation and wear resistance for thermal spray coating. *Advanced Engineering Materials*. 2004;**6**(12):74-78
- [4] George EP, Raabe D, Ritchie RO. High-entropy alloys. *Nature Reviews Materials*. 2019;**4**(8):515-534
- [5] Miracle DB, Senkov ON. A critical review of high entropy alloys and related concepts. *Acta Materialia*. 2017;**122**:448-511
- [6] Zhang Y, Zuo TT, Tang Z, Gao MC, Dahmen KA, Liaw PK, et al. Microstructures and properties of high-entropy alloys. *Progress in Materials Science*. 2014;**61**:1-93
- [7] Ye YF, Wang Q, Lu J, Liu CT, Yang Y. High-entropy alloy: Challenges and prospects. *Materials Today*. 2016;**19**(6):349-362
- [8] Chen J, Zhou X, Wang W, Liu B, Lv Y, Yang W, et al. A review on fundamental of high entropy alloys with promising high-temperature properties. *Journal of Alloys and Compounds*. 2018;**760**:15-30
- [9] George EP, Curtin WA, Tasan CC. High entropy alloys: A focused review of mechanical properties and deformation mechanisms. *Acta Materialia*. 2020;**188**:435-474
- [10] Tsai MH, Yeh JW. High-entropy alloys: A critical review. *Materials Research Letters*. 2014;**2**(3):107-123
- [11] Yeh J-W. Recent progress in high-entropy alloys. *Annales de Chimie Science des Matériaux*. 2006;**31**(6):633-648
- [12] Li Z, Pradeep KG, Deng Y, Raabe D, Tasan CC. Metastable high-entropy dual-phase alloys overcome the strength-ductility trade-off. *Nature*. 2016;**534**(7606):227-230
- [13] Li ZM, Kormann F, Grabowski B, Neugebauer J, Raabe D. Ab initio assisted design of quinary dual-phase high-entropy alloys with transformation-induced plasticity. *Acta Materialia*. 2017;**136**:262-270
- [14] Yin Y. Development of cost-effective high-entropy alloys with superior mechanical properties. University of Queensland. 2021:1-224
- [15] Yin Y, Tan Q, Zhao Y, Sun Q, Shi Z, Bermingham M, et al. A cost-effective Fe-rich compositionally complicated alloy with superior high-temperature oxidation resistance. *Corrosion Science*. 2021;**180**:109190
- [16] Bae JW, Seol JB, Moon J, Sohn SS, Jang MJ, Um HY, et al. Exceptional phase-transformation strengthening of ferrous medium-entropy alloys at cryogenic temperatures. *Acta Materialia*. 2018;**161**:388-399

- [17] Raabe D, Tasan CC, Springer H, Bausch M. From high-entropy alloys to high-entropy steels. *Steel Research International*. 2015;**86**(10):1127-1138
- [18] Wang Z, Lu W, Zhao H, Liebscher CH, He J, Ponge D, et al. Ultrastrong lightweight compositionally complex steels via dual-nanoprecipitation. *Science Advances*. 2020;**6**(46):eaba9543
- [19] Sathiyamoorthi P, Kim HS. High-entropy alloys with heterogeneous microstructure: Processing and mechanical properties. *Progress in Materials Science*. 2020;**123**:100709
- [20] Li Z, Zhao S, Ritchie RO, Meyers MA. Mechanical properties of high-entropy alloys with emphasis on face-centered cubic alloys. *Progress in Materials Science*. 2019;**102**:296-345
- [21] Li J-H, Tsai M-H. Theories for predicting simple solid solution high-entropy alloys: Classification, accuracy, and important factors impacting accuracy. *Scripta Materialia*. 2020;**188**:80-87
- [22] Murty BS, Yeh J-W, Ranganathan S, Bhattacharjee P. *High-entropy Alloys*. Amsterdam: Elsevier; 2019
- [23] Körmann F, Li Z, Raabe D, Sluiter MHF. Iron-rich high entropy alloys. In: Rana R, editor. *High-Performance Ferrous Alloys*. Cham: Springer International Publishing; 2021. pp. 389-421
- [24] Wu H, Xie J, Yang H-Y, Shu D-L, Hou G-C, Li J-G, et al. Comparative study of mechanical and corrosion behaviors of cost-effective AlCrFeNi high entropy alloys. *Journal of Materials Engineering and Performance*. 2022;**396**:1-11
- [25] Rao ZY, Wang X, Zhu J, Chen XH, Wang L, Si JJ, et al. Affordable FeCrNiMnCu high entropy alloys with excellent comprehensive tensile properties. *Intermetallics*. 2016;**77**:23-33
- [26] Kumar A, Mucalo M, Bolzoni L, Li Y, Kong F, Yang F. Fabrication, microstructure, mechanical, and electrochemical properties of NiMnFeCu high entropy alloy from elemental powders. *Metals*. 2022;**12**(1):167
- [27] O'Brien SP, Christudasjustus J, Esteves L, Vijayan S, Jinschek JR, Birbilis N, et al. A low-cost, low-density, and corrosion resistant AlFeMnSi compositionally complex alloy. *npj Materials Degradation*. 2021;**5**(1):12
- [28] Liu Y, Qu N, Zhao X, Chen J, Zhu J, Lai Z. Stability of FeCrNiTiAl high-entropy alloy at high temperature. *Heat Treatment and Surface Engineering*. 2021;**3**(1):29-36
- [29] Jin X, Bi J, Zhang L, Zhou Y, Du X, Liang Y, et al. A new CrFeNi₂Al eutectic high entropy alloy system with excellent mechanical properties. *Journal of Alloys and Compounds*. 2019;**770**:655-661
- [30] Jin X, Zhou Y, Zhang L, Du X, Li B. A novel Fe₂₀Co₂₀Ni₄₁Al₁₉ eutectic high entropy alloy with excellent tensile properties. *Materials Letters*. 2018;**216**:144-146
- [31] Fang W, Yu H, Chang R, Zhang X, Ji P, Liu B, et al. Microstructure and mechanical properties of Cr-rich Co-Cr-Fe-Ni high entropy alloys designed by valence electron concentration. *Materials Chemistry and Physics*. 2019;**238**:121897
- [32] Cho K, Fujioka Y, Nagase T, Yasuda HY. Grain refinement of non-equiatomic Cr-rich CoCrFeMnNi high-entropy alloys through combination of cold rolling and precipitation of sigma phase.

Materials Science and Engineering A. 2018;**735**:191-200

[33] Wei D, Li X, Heng W, Koizumi Y, He F, Choi W-M, et al. Novel Co-rich high entropy alloys with superior tensile properties. *Materials Research Letters*. 2019;**7**(2):82-88

[34] Coury FG, Santana D, Guo Y, Copley J, Otani L, Fonseca S, et al. Design and in-situ characterization of a strong and ductile co-rich multicomponent alloy with transformation induced plasticity. *Scripta Materialia*. 2019;**173**:70-74

[35] Hsu C-Y, Wang W-R, Tang W-Y, Chen S-K, Yeh J-W. Microstructure and mechanical properties of new AlCo_xCrFeMo_{0.5}Ni high-entropy alloys. *Advanced Engineering Materials*. 2010;**12**(1-2):44-49

[36] Hori T, Nagase T, Todai M, Matsugaki A, Nakano T. Development of non-equiatom Ti-Nb-Ta-Zr-Mo high-entropy alloys for metallic biomaterials. *Scripta Materialia*. 2019;**172**:83-87

[37] Li C, Zhao M, Li JC, Jiang Q. B2 structure of high-entropy alloys with addition of Al. *Journal of Applied Physics*. 2008;**104**(11):113504

[38] Yang T, Xia S, Liu S, Wang C, Liu S, Zhang Y, et al. Effects of AL addition on microstructure and mechanical properties of Al_xCoCrFeNi High-entropy alloy. *Materials Science and Engineering: A*. 2015;**648**:15-22

[39] Yin Y, Tan Q, Sun Q, Ren W, Zhang J, Liu S, et al. Heterogeneous lamella design to tune the mechanical behaviour of a new cost-effective compositionally complicated alloy. *Journal of Materials Science & Technology*. 2022;**96**:113-125

[40] Li Z, Tasan CC, Springer H, Gault B, Raabe D. Interstitial atoms enable joint twinning and transformation induced plasticity in strong and ductile high-entropy alloys. *Scientific Reports*. 2017;**7**:40704

[41] Su J, Raabe D, Li Z. Hierarchical microstructure design to tune the mechanical behavior of an interstitial TRIP-TWIP high-entropy alloy. *Acta Materialia*. 2019;**163**:40-54

[42] Nutor RK, Azeemullah M, Cao QP, Wang XD, Zhang DX, Jiang JZ. Microstructure and properties of a Co-free Fe₅₀Mn₂₇Ni₁₀Cr₁₃ high entropy alloy. *Journal of Alloys and Compounds*. 2021;**851**:156842

[43] Yao MJ, Pradeep KG, Tasan CC, Raabe D. A novel, single phase, non-equiatom FeMnNiCoCr high-entropy alloy with exceptional phase stability and tensile ductility. *Scripta Materialia*. 2014;**72-73**:5-8

[44] Wang Z, Baker I. Interstitial strengthening of a f.c.c. FeNiMnAlCr high entropy alloy. *Materials Letters*. 2016;**180**:153-156

[45] Shaysultanov DG, Salishchev GA, Ivanisenko YV, Zherebtsov SV, Tikhonovsky MA, Stepanov ND. Novel Fe₃₆Mn₂₁Cr₁₈Ni₁₅Al₁₀ high entropy alloy with bcc/B2 dual-phase structure. *Journal of Alloys and Compounds*. 2017;**705**:756-763

[46] Yin Y, Zhao Y, En Koey K, Tan Q, Zhang M-X, Huang H. In-situ synthesized age-hardenable high-entropy composites with superior wear resistance. *Composites Part B: Engineering*. 2022;**235**:109795

[47] Yin Y, Zhang JQ, Tan QY, Zhuang W, Mo N, Birmingham M, et al. Novel cost-effective Fe-based high

- entropy alloys with balanced strength and ductility. *Materials & Design*. 2019;**162**:24-33
- [48] Yin Y, Chen Z, Mo N, Kent D, Candella AR, Koey KE, et al. High-temperature age-hardening of a novel cost-effective Fe₄₅Ni₂₅Cr₂₅Mo₅ high entropy alloy. *Materials Science and Engineering: A*. 2020;**788**:139580
- [49] Senkov ON, Miracle DB, Chaput KJ, Couzinie J-P. Development and exploration of refractory high entropy alloys—A review. *Journal of Materials Research*. 2018;**33**(19):3092-3128
- [50] Soni V, Gwalani B, Alam T, Dasari S, Zheng Y, Senkov ON, et al. Phase inversion in a two-phase, BCC+B₂, refractory high entropy alloy. *Acta Materialia*. 2019;**185**:89-97
- [51] Otto F, Dlouhý A, Pradeep KG, Kuběnová M, Raabe D, Eggeler G, et al. Decomposition of the single-phase high-entropy alloy CrMnFeCoNi after prolonged anneals at intermediate temperatures. *Acta Materialia*. 2016;**112**:40-52
- [52] Chen SY, Tong Y, Tseng KK, Yeh JW, Poplawsky JD, Wen JG, et al. Phase transformations of HfNbTaTiZr high-entropy alloy at intermediate temperatures. *Scripta Materialia*. 2019;**158**:50-56
- [53] Stepanov ND, Yurchenko NY, Zherebtsov SV, Tikhonovsky MA, Salishchev GA. Aging behavior of the HfNbTaTiZr high entropy alloy. *Materials Letters*. 2018;**211**:87-90
- [54] Li ZM, Tasan CC, Pradeep KG, Raabe D. A TRIP-assisted dual-phase high-entropy alloy: Grain size and phase fraction effects on deformation behavior. *Acta Materialia*. 2017;**131**:323-335
- [55] Zhu Y, Ameyama K, Anderson PM, Beyerlein IJ, Gao H, Kim HS, et al. Heterostructured materials: Superior properties from hetero-zone interaction. *Materials Research Letters*. 2021;**9**(1):1-31
- [56] Hasan MN, Liu YF, An XH, Gu J, Song M, Cao Y, et al. Simultaneously enhancing strength and ductility of a high-entropy alloy via gradient hierarchical microstructures. *International Journal of Plasticity*. 2019;**123**:178-195
- [57] He BB, Hu B, Yen HW, Cheng GJ, Wang ZK, Luo HW, et al. High dislocation density-induced large ductility in deformed and partitioned steels. *Science*. 2017;**357**(6355):1029-1032
- [58] Huang H, Wu Y, He J, Wang H, Liu X, An K, et al. Phase-transformation ductilization of brittle high-entropy alloys via metastability engineering. *Advanced Materials*. 2017;**29**(30):1701678
- [59] Xu SS, Li JP, Cui Y, Zhang Y, Sun LX, Li J, et al. Mechanical properties and deformation mechanisms of a novel austenite-martensite dual phase steel. *International Journal of Plasticity*. 2020;**128**:102677
- [60] Liu L, Yu Q, Wang Z, Ell J, Huang MX, Ritchie RO. Making ultrastrong steel tough by grain-boundary delamination. *Science*. 2020;**368**(6497):1347-1352
- [61] Li Z, Raabe D. Strong and ductile non-equiatom high-entropy alloys: Design, processing, microstructure, and mechanical properties. *JOM*. 2017;**69**(11):2099-2106

Chapter 3

Breaking the Property Trade-Offs by Using Entropic Conceptions

Yong Zhang and Xuehui Yan

Abstract

Entropic conception has been used as an effective strategy for developing materials to break the property recordings of current materials, for example, breaking the trade-off between the high-strength and low-ductility structural alloys. The performance of materials usually under a complex circumstance, a balance of multiple properties, for example, combined the high-strength, high ductility, high conductivity, high corrosion resistance, high irradiation resistance, etc., the strategy of high-entropy-alloy (HEA) will provide a materials design and development technology to realize the goal. Magnetic materials usually exhibit excellent magnetic properties but weak mechanical properties and corrosion resistance. The reported unique behaviors of HEAs, for example, self-healing effects may be the mechanism for the high irradiation resistance of the HEAs, and self-sharpening behaviors of the tungsten-based HEAs main closely be related to the serration behaviors.

Keywords: high-entropy-alloy, strength, conductivity, toughness, corrosion resistance, self-healing, self-sharpening, serration behaviors, irradiation resistance, performance, trade-off, properties limits

1. Introduction

1.1 Definition and development of HEAs

Entropy is an important physical parameter to reflect the disordered state of a certain system, which is mainly expressed by three different forms including Clausius entropy, Boltzmann entropy, and Shannon entropy. Among them, entropy measured by Boltzmann's thermodynamic statistics principle is in the form of:

$$\Delta S_{\text{cnof}} = k \ln w \quad (1)$$

where k is the Boltzmann's constant ($k = 1.38 \times 10^{-23} \text{J/K}$), and w is the thermodynamic probability, which is the total number of micro-states corresponding to a certain state. Entropy measured by Clausius entropy is in the form of:

$$dS = dQ/T \quad (2)$$

where Q is heat and T is temperature. The physical meaning of this expression is that the entropy of a system is equal to the amount of heat absorbed (or dissipated) by

the system in a certain process divided by its absolute temperature. Different from Boltzmann entropy, Clausius entropy reflects the macroscopic quantity of thermodynamics. Probability is involved in the definition of Boltzmann entropy. The probability is not only used in physics but also in mathematics, information science, etc, which enables the application of entropy in other fields. Shannon entropy is one of the representatives, the expression is as follows:

$$H(X) = - \sum P(a_i) \log_2 P(a_i) \quad (3)$$

Based on this, information entropy has been measured in the form of:

$$S = -K \sum P_i \ln P_i \quad (4)$$

where P_i is the probability of occurrence of the i -th information of the information source. Briefly, the higher the entropy value of the system, the more disordered the system. For a material system, order can be defined in terms of a fully crystalline space group symmetry or another correlation. Ordered materials generally referred to materials with standard crystal structures, such as silicon single crystals, graphite, diamond, and intermetallic. In contrast, the common disordered materials mainly include amorphous materials and continuous solid solution materials (namely high-entropy materials) [1].

The concept of high entropy introduces a new path of developing advanced materials with unique properties, which cannot be achieved by the conventional micro-alloying approach based on only one dominant element. In contrast with traditional alloys composed of one principal element, HEAs generally have equimolar or near-equimolar atomic fractions of multiple constituents (generally more than 4 components), as shown in **Figure 1a**. As displayed in **Figure 1b**, the ternary or pseudo-ternary phase diagram can be roughly divided into the ordered alloys region (blue) near the corners and relatively disordered alloys region (dotted circle) near the center. The center of the phase diagram, relatively high-disordered region, often has few alloy systems available, especially for traditional alloy systems. In recent years, many new alloys with promising properties are likely to be discovered near the centers (as opposed to the corners) of phase diagrams, which no longer contain a single major component, but multiple major elements and form a concentrated solid-solution structure, namely high-entropy alloy systems. The development of HEAs has provided a novel design philosophy for alloy design and draw significant interest

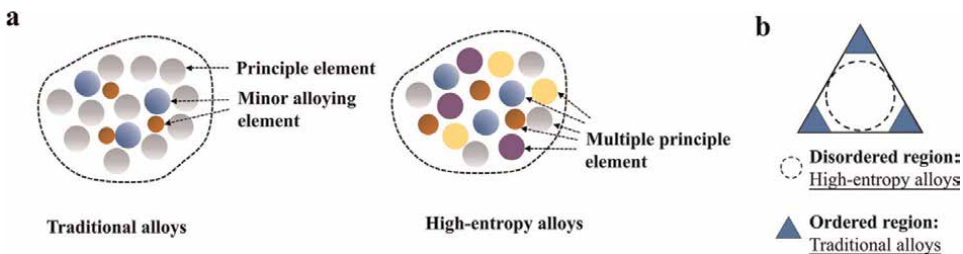


Figure 1. Schematic diagram of traditional and high-entropy alloy systems. (a) atomic proportions of traditional alloys and high-entropy alloys; and (b) Ordered and disordered regions in a ternary phase diagram.

in designing its chemical disorder to bring different structural and physical characteristics.

Here, we would like to discuss the definition of HEAs from the perspective of entropy. For a certain material system, the entropy mainly includes configuration entropy, vibration entropy, magnetic entropy, and thermal entropy. For HEAs with concentrated solid solution structures, the configuration entropy caused by the mixing of different atoms is the primary consideration. In order to simplify the calculation, the regular solution model is usually used to derive the mixed entropy of the HEAs in the state of random mutual dissolution [2]. The calculation formula is as follows:

$$\Delta S_{mix} = -R \sum_{i=1}^n (c_i \ln c_i) \quad (5)$$

where R is the gas constant ($R = 8.314 \text{ J/mol}\cdot\text{K}$); n is the number of alloy components; c_i is the content of the i -th component (at. %). The mixing entropy of HEAs is much greater than that of traditional alloys, and even exceeds the melting entropy of most metals (generally no more than $1R$). According to this feature of HEAs, the commonly used definitions of multi-component HEAs are as follows [3]: (1) Alloy contains more than four main elements is equal to or near equal atomic ratio (at. %); (2) The content of each principal element is greater than 5 at. %, and less than 35 at. %. With the development of HEAs, the HEAs can be loosely divided into two generations [4]: the first-generation alloys generally show a single solid-solution structure and contain more than five principal elements in equal atomic ratio, and the second-generation alloys show non-equi-molar components and multiple phases, as shown in **Figure 2**.

1.2 Classification of HEAs

With the development of HEAs, various HEAs with different forms have been reported. Here, the HEAs have been classified from different dimensions, as shown in **Figure 3**, mainly including three-dimensional (3-D) bulk materials, two-dimensional (2-D) film and sheet materials, one-dimensional (1-D) fiber materials, and zero-dimensional (0-D) powder materials [5].


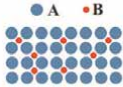
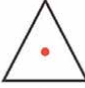


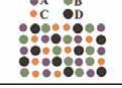
Classification	Component	Feature	Composition	Atoms arrangement	Typical alloys
The traditional alloys	1~2 principal elements	Tougher than the elementary substance			Fe-Ni, Fe-C, Cu-Al, Al-Mg
The 1 st generation HEAs	At least 5 principal elements	Single phase, equimolar			CoCrFeNiMn, AlCoCrFeNi
The 2 nd generation HEAs	At least 4 principal elements	Dual or complex phases, non-equi-molar			NbMoTaW, Al ₁₃ CoCrFeNi, Fe ₅₀ Mn ₃₀ Cr ₁₀ Co ₁₀

Figure 2. Characteristics for the traditional alloys and two generations of HEAs [4].

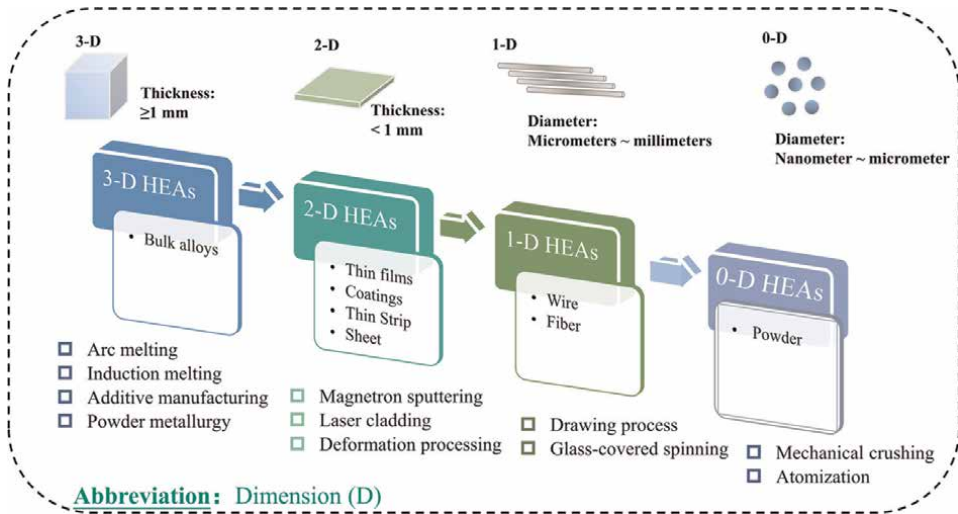


Figure 3. Classification and general preparation methods of high-entropy alloys with different dimensions [5].

The 3-D HEAs, also referred to as bulk HEAs, are generally fabricated by alloy melting, additive manufacturing, and sintering methods, with a weight from several grams to tens of kilograms. Different cross-sectional shapes can also be obtained by casting, such as round rods and square rods. The 2-D HEAs are thinner than bulk alloys, and have several main types including thin films, coating, sheets, and thin strips. The high-entropy wire and fiber are the 1-D HEAs, which are generally obtained by drawing method and glass-covered spinning method. At present, micron-scale high-entropy wire can be obtained, and possess attractive mechanical properties. For the 0-D HEAs, mainly refers to high-entropy powders, which can be obtained through mechanical crushing and atomization. Currently, the high-entropy powder is used as raw materials for powder metallurgy and additive manufacturing, as well as a novel catalyst for functional applications.

2. Performance properties

2.1 Representative performance advantages

As a novel complex emerging material, many unique characteristics of HEAs in dynamics, thermodynamics, and structure have aroused great interest. The ability of HEAs to be designed with unique properties in an unlimited space of alloy compositions is encouraging. At present, many outstanding works have been carried out and proved many attractive properties that break the trade-offs and limits of properties. Here, several representative performance advantages including overcoming the strength-ductility trade-off, outcoming low-temperature ductility, excellent thermal stability, good corrosion resistance, and irradiation resistance have been illustrated [6].

- I. Overcoming the strength-ductility trade-off: In general, strength and plasticity are two opposing properties. In other words, the increase of strength is often

accompanied by the loss of plasticity, and the increase of plasticity requires the sacrifice of strength. It is exciting to find that the HEAs show the potential to break through the strength-plastic trade-off. The high strength of HEAs can be mainly attributed to two strengthening mechanisms. One of the most key issues for breaking strength-ductility trade-off is tailoring the stability of the constituent phases in HEAs, such as designing phase transformation, twinning, and regulating the chemical short-order and nanoprecipitates.

- II. Low-temperature ductility: Traditional materials tend to exhibit brittleness at low temperatures, which limits their application in extreme low-temperature conditions. Recent results prove that HEAs with fcc structure show excellent mechanical properties under low temperatures, such as CoCrFeMnNi alloy [7] (Cantor alloy), CoCrFeNi alloy [8], and Al_{0.3}CoCrFeNi fiber [9]. This unique property is facilitated by the ability to form twin crystals, enabling defect storage and microstructural refinement at low temperatures.
- III. Thermal stability: The diffusion rate is significantly slower than that in conventional materials. Severe lattice distortion directly is the key issue. Multiple components and complex interactions between the different atoms seriously affect the cooperative diffusion, and thereby slowing down the phase transition rate, hindering grain growth, and improving creep resistance.
- IV. Corrosion resistance: The synergistic effect of slow diffusion, easy to obtain amorphous, and nanocrystalline structure is the dominant reason for excellent corrosion resistance. At the same time, high content of doping elements also enables the formation of strong passivation layers.
- V. Irradiation resistance: Recent results have proved that effective self-healing mechanisms can be designed in HEAs. The particle irradiation could cause atomic displacements, which induces the irradiation defects, such as vacancies and interstitials, and also is accompanied by thermal spikes. For HEAs, the possibility of vacancy-interstitial recombination is higher than in traditional alloys due to complex interactions between atoms. And also, high levels of atomic-level stress in HEAs destabilize the solid solution and facilitate atomic remake to eliminate defects. This part will be discussed in detail in subsequent chapters.

2.2 Key research topics

For the property of HEAs, besides the current efforts on breaking the trade-off between the strength and ductility, we would like to propose several trade-offs between the mechanical properties and the physical properties, such as the deformability and soft magnetic properties, conductivity, and strength. Generally, the functional properties are available from traditional materials. However, traditional materials usually fail to provide a well-service under extreme conditions due to the destabilization of mechanical properties. In this case, outstanding mechanical also is a major boost for developing functional HEAs. Hence, we predict that developing HEAs with unique physical properties is a key research topic for future development. There are also other attractive properties, such as irradiation resistance and self-sharpening

properties. In subsequent chapters, we will discuss these performances and related mechanisms in detail.

3. Soft-magnetic and mechanical properties

The performance of the soft magnetic material directly affects the transformer loss rate. Traditional soft magnetic materials, such as steel, Fe-Co alloys, and silicon steels, are often limited in their applications to the brittleness and poor deformability of the alloys. For soft-magnetic materials, it is very important to seek the balance between the magnetic properties and mechanical properties. However, this breakthrough is difficult to achieve in traditional materials, which generally have a relatively high degree of structural order, thereby showing poor deformability. In contrast, the excellent mechanical properties over a wide temperature range guarantee a well-service of HEAs under extreme environments. Moreover, high-entropy soft magnetic materials are expected to break the trade-off between power and frequency, as shown in **Figure 4**. For example, the conventional silicon steel is especially suitable for using in conditions of high power and low frequency. Once silicon steel is used at high frequencies, losses will increase dramatically. On the contrary, the amorphous alloys and ferrite generally possess low coercivity and exhibit lower losses at high frequencies, which give rise to the application of high-frequency transformers. Here, high-entropy soft-magnetic alloys show great advantages in filling the gap between high power/low frequency and low power/high frequency.

As we discussed in the previous chapter, HEAs have good mechanical properties, flexible deformability and excellent thermal stability, which is one of the most important properties for promising soft-magnetic materials. Many efforts have proved that HEAs also show acceptable soft magnetic properties. The promising soft-magnetic materials should have high-electrical resistivity, high-saturation magnetization, and low coercivity. As shown in **Figure 5**, the soft-magnetic HEAs are mainly located in

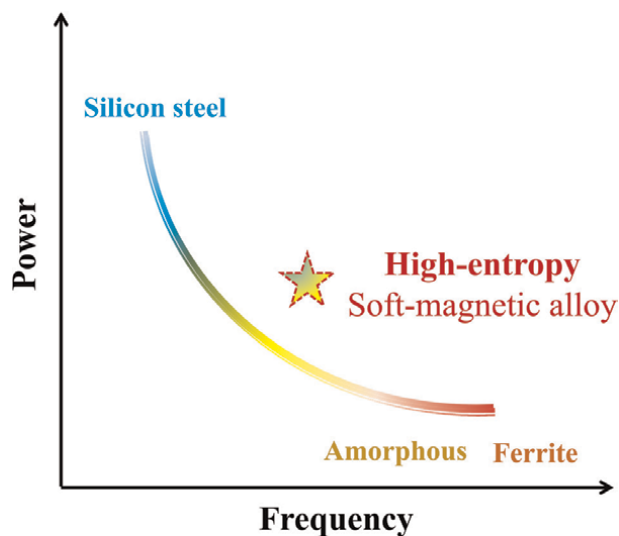


Figure 4. General relationship of power to frequent for common magnetic materials.

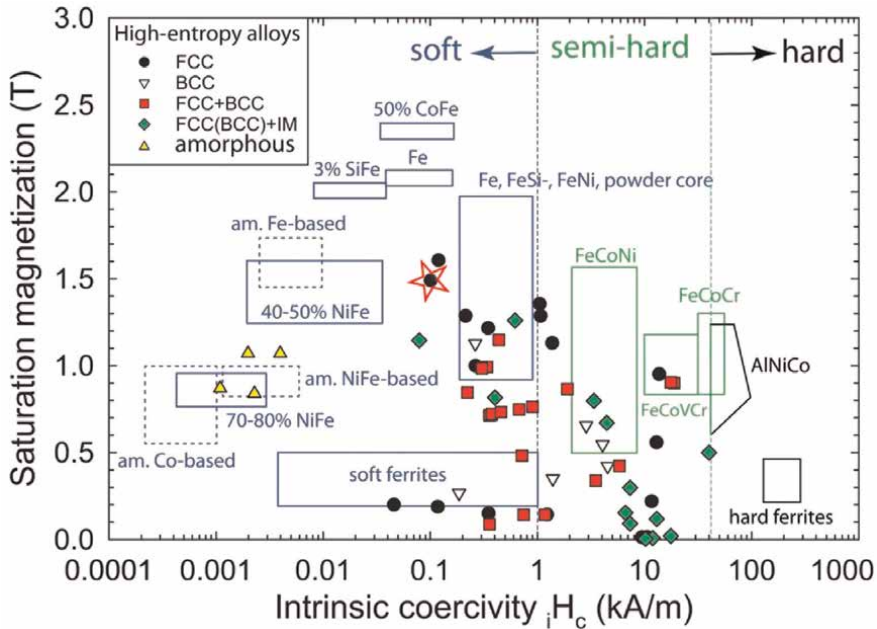


Figure 5. Saturation magnetization versus coercivity of HEAs compared with major conventional soft and semi-hard magnetic materials [10].

the region of soft and semi-hard regions, and the properties of partial alloys are accepted by the soft-magnetic materials [10].

In addition, HEAs generally possess higher electrical resistivity in comparison with traditional alloys due to large lattice distortion. Chou et al. [11] have investigated the electrical resistivity of CoCrFeNiAl_x alloy. Results showed that the resistivity of this series of HEAs is higher, second only to that of bulk amorphous alloys, and the resistivity increases with the increase of temperature, showing a linear relationship with temperature. Currently, many efforts have been conducted to improve the comprehensive soft-magnetic properties of HEAs. Zuo and co-workers [12] have designed a system of CoFeMnNi-X ($X=\text{Al, Cr, Ga, and Sn}$) magnetic alloys. The hysteresis loops of these HEAs are shown in **Figure 6**. Ordered phases form by adding Al/Ga/Sn to the FCC-structured CoFeMnNi alloy. This phase transition leads to the significant enhancement of the saturation magnetization. Especially for CoFeMnNiAl alloy, the alloy has M_s of $147.86 \text{ Am}^2/\text{kg}$.

Moreover, Zuo and co-workers have tried to optimize soft magnetic properties by changing the fabrication process [13]. They found that the HEAs fabricated by directional solidification process showed a lower coercivity. The coercivity value of $\text{FeCoNiAl}_{0.2}\text{Si}_{0.2}$ alloy manufactured by directionally solidified is reduced to 315 A/m , which is much lower than the as-cast alloy with 1400 A/m . Results prove that the chemical short-range order in HEAs significantly changes the local environment of atomic, which further reduces the average magnetic moment of magnetic atoms. Zhang and co-workers have also investigated the magnetic properties and mechanical properties of Fe-Co-Ni-Al-Si HEAs [14]. The alloy shows pretty good mechanical properties and deformability. As shown in **Figure 7**, the alloy was fabricated by vacuum magnetic suspension melting, and also can be conducted by cold-rolling to

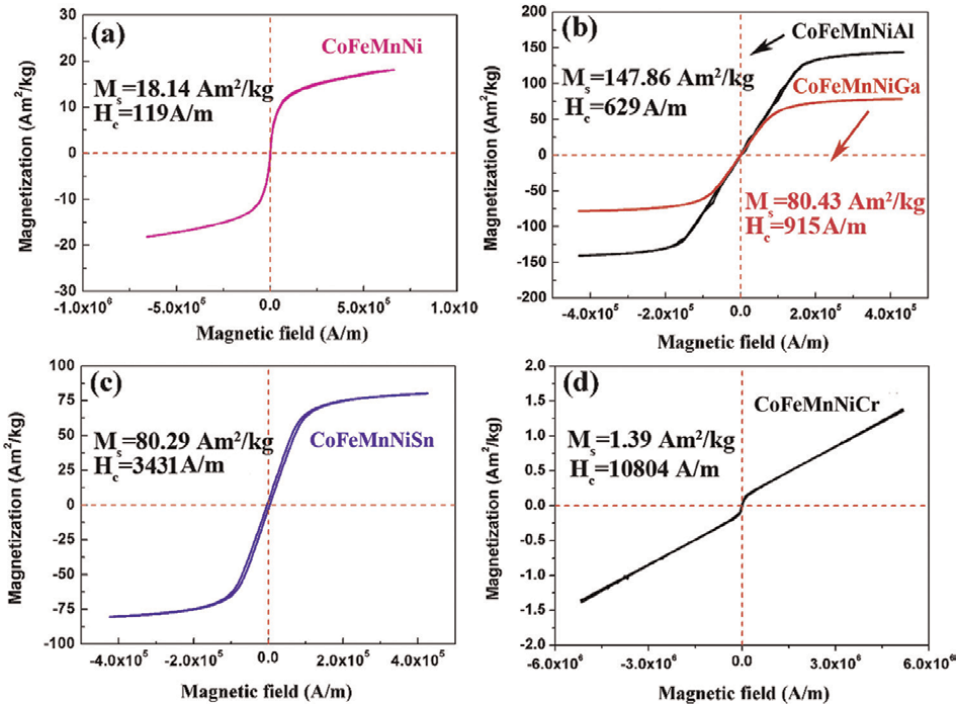


Figure 6. Hysteresis loops of (a) CoFeMnNiMn, (b) CoFeMnNiAl and CoFeMnNiGa, (c) CoFeMnNiSn, and (d) CoFeMnNiCr alloys at room temperature [12].

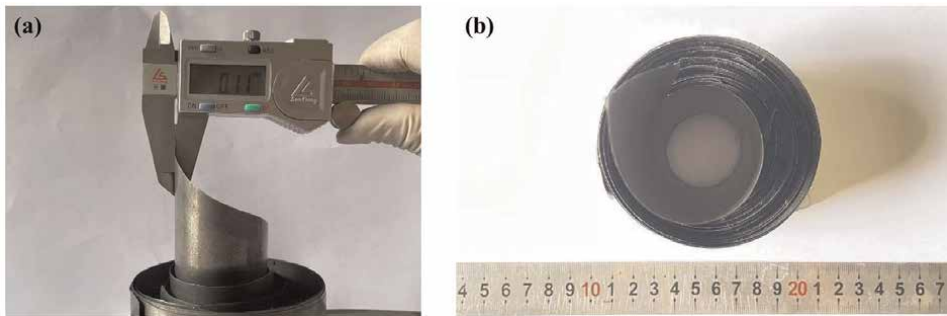


Figure 7. The macroscopic appearance of $(Fe_{0.3}Co_{0.5}Ni_{0.2})_{95}(Al_{1/3}Si_{2/3})_5$ cold-rolled sheet.

form the sheet. The alloy after annealing exhibits a tensile yield strength of 235 MPa, an ultimate tensile strength of 572 MPa, and an elongation of 38%. The superior ductility of HEAs provides the possibility of preparing thin plates, which can effectively reduce eddy current losses of magnetic devices.

4. Conductivity and strength

Generally, high-purity materials have high conductivity, and the higher the purity, the higher the electrical conductivity accordingly. Also, it is well known that the

higher the purity of the material, the lower the strength. However, due to low strength of high-purity materials, they cannot meet the requirements of industrial applications. In this case, increasing the strength of alloy without significantly reducing the electrical conductivity is essential. There are many methods to strengthen materials, for example:

(i) Fine grain strengthening: Fine grains can be obtained through plastic deformation or other methods, which improves the strength but also hinders the electron transport; (ii) Solid solution strengthening: Solid solution treatment causes the crystal lattice distortion, which enhances the scattering of electrons, thus making the movement of electrons difficult; (iii) Second phase strengthening (precipitation strengthening): The second phase precipitated from the alloy matrix will hinder the movement of dislocations, which can improve the strength of the alloy, but at the same time, it will also block electrons, which will hinder the transmission of electrons; and (iv) Phase transformation strengthening: The lattice is strongly distorted, and the resistance increases sharply. Obviously, these strengthening methods reduce the conductivity. The current research work demonstrates the possibility of breaking the balance between conductivity and strength in the design of HEAs.

Excellent mechanical performance of HEAs is a basic guarantee for using as conductivity materials. Moreover, there have been HEA superconductors discovered to date, which seem to offer some interesting properties. Guo et al. [15] reported the observation of extraordinarily robust zero-resistance superconductivity in the pressurized $(\text{TaNb})_{0.67}(\text{HfZrTi})_{0.33}$ HEAs with a bcc phase structure. The transition to superconductivity (T_C) increases from an initial temperature of 7.7 K at ambient pressure to 10 K at ~ 60 GPa, and then slowly decreases to 9 K by 190.6 GPa, a pressure that falls within that of the outer core of the earth. High-pressure resistance measurements were performed for four samples that were cut from the material used as the standard for the superconductivity at ambient pressure. The electrical resistance measurements for these samples were performed between 4 and 300 K. They inferred that the continuous existence of the zero-resistance superconductivity from 1 atm up to such a high pressure requires a special combination of electronic and mechanical characteristics. The HEAs superconductor thus may have a bright future for applications under extreme conditions, and also poses a challenge for understanding the underlying quantum physics.

Vrtnik and co-workers [16] designed Ta-Nb-Hf-Zr-Ti HEAs with a structure varying between a homogeneous random solid solution and a partially ordered nanostructure in the form of a three-dimensional grid of short-range ordered atomic clusters enriched in Zr and Hf and investigated the superconducting behaviors. The superconducting transition temperatures T_C of Ta-Nb-Hf-Zr-Ti HEAs are scattered in the range between 5.0 and 7.3 K and this scatter could be related to the degree of structural and chemical inhomogeneity of the samples. They demonstrated the important fact that the formation, stability, and structure of a regular (non-ideal) HEA mixture is determined by both, the minimization of the mixing enthalpy that favors local atomic ordering and the maximization of the mixing entropy that favors a random solid solution. The actual equilibrium state achieved during long-time thermal annealing via the atomic diffusion is generally partially ordered, and the resulting nanostructure is a sensitive function of the number of components constituting the HEA, their concentrations, and the differences in the atomic radii and the annealing temperature and time. This nanostructure essentially determines the electronic properties of HEA materials.

5. Irradiation and self-healing

The unexpected stability of phase structure and mechanical performances in extreme environments makes HEAs attractive candidates for irradiation-resistant materials. It is well known that particle irradiation could cause atomic displacements, which induces the irradiation defects, such as vacancies and interstitials. In contrast with the traditional alloys, the integrated experiment and modeling work indicate that HEAs show a lower volume swelling rate and defect density, which may be attributed to the effective self-healing mechanisms of HEAs under irradiation conditions [6]. The possible self-healing mechanisms of HEAs can be concluded from three aspects, as shown in **Figure 8** [6].

Unlike interstitial atoms in conventional alloys, which migrate in the direction of the Burgers vector in a long-range one-dimensional mode, interstitial atoms and clusters in HEAs have short-range three-dimensional (3D) motion. The short-range 3D motion of interstitial clusters gives rise to the recombination of vacancy-interstitial, thereby reducing the defects in alloys, as shown in **Figure 8-I**. In other words, the chemical disorder and compositional complexity of HEAs promote the novel short-range 3D migration paths, which facilitate the disappearance of radiation damage, and improve the radiation tolerance. High atomic-level stresses caused by mixing of elements with different atomic sizes are the reason for self-healing mechanism in HEAs. Higher atomic-level stresses destabilize the solid solution, which will facilitate amorphization of alloys during irradiation process. In this case, the thermal spikes caused by particle irradiation will bring local melting and recrystallization, which promote the orderliness of the alloy, and further reduce the density of defects, as shown in **Figure 8-II**. Moreover, simulation results show that the electron mean free path decreases significantly with the increase of the number of component elements. In this case, the consumption efficiency in HEAs is lower than that in conventional alloys. This action can help to prolong thermal spike and significantly promote the defect recovery of HEAs.

Nagase and co-workers [17] have investigated the irradiation behavior of CoCrCuFeNi multicomponent nano-crystalline HEAs. A fine-grained fcc single phase was obtained in the sputtered specimens. The fcc solid solution showed high phase

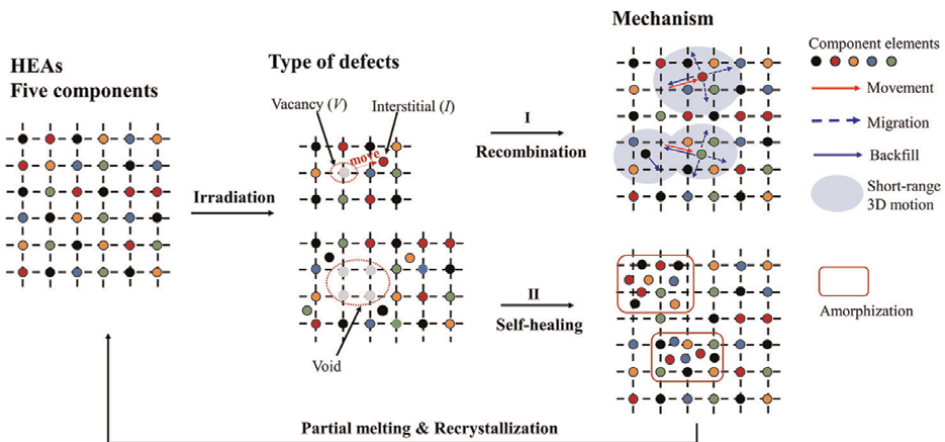


Figure 8. Schematic diagram for the self-healing mechanism of irradiation resistance HEAs [6].

stability against irradiation over a wide temperature range from 298 to 773 K and remained as the main constituent phase even when the samples were irradiated up to 40 displacement per atom (dpa). Moreover, they found that the irradiation did not seem to induce grain coarsening. Jin et al. [18] have investigated the effects of compositional complexity on the ion-irradiation-induced swelling and hardening in Ni-containing HEAs. They designed four alloys with different component numbers, including Ni, NiCo, NiCoCr, and NiCoFeCrMn alloys. It is reported that the irradiation resistance at the temperature of 500 °C is improved by controlling the number and, especially, the type of alloying elements. Alloying with Fe and Mn has a stronger influence on swelling reduction than does alloying with Co and Cr. The quinary alloy NiCoFeCrMn, with known excellent mechanical properties, has shown 40 times higher swelling tolerance than nickel.

Briefly, the recent progress in HEAs demonstrates the possibility of obtaining high radiation tolerance through unique damage self-healing mechanisms. It is desirable to design high-performance HEAs for serving as irradiation resistance materials.

6. Serration behaviors and self-sharpening

Serration behaviors in plastically deforming solids are related to avalanches of deformation processes. In the stress-strain curves, the serration characteristics are visible as stress drops or strain jumps. In fact, similar serration characteristics are ubiquitous in many structural and functional materials [19], such as amorphous materials, high-entropy alloys (HEAs), superalloys, ordered intermetallic, shape-memory alloys (SMAs), electrochemical noise, carbon steels, twinning-induced plasticity steels, phase transformation-induced plasticity steels, Al-Mg alloys, nanomaterials, magnetic functional materials, and so on.

The serration behaviors are produced by the material under the action of the external field present a disordered distribution in time and space, which is closely related to the rheological structural unit of the material. The zigzag rheological phenomenon of materials in the process of plastic deformation objectively reflects some characteristics of its deformation mechanism, such as the interaction of interstitial solute atoms or replacement solute atoms and dislocations, local shear instability, grain boundary migration, and twinning. At the same time, the rheological characteristics of sawtooth are affected by many factors (such as external factors including temperature, strain rate, and heat treatment process; and internal factors including composition, grain morphology, size, and phase composition of the material).

“Self-sharpening,” the capability of a material maintaining its acute head shape during penetration, is a highly required attribute of materials in armor piercing. Liu and co-workers [20] firstly reported the self-sharpening behavior of HEAs in a composition of WFeNiCo. It was observed that the remnant of 93 W penetrator has suffered severe plastic deformation and exhibits an obvious mushroom-like head. In contrast, the remnant of WFeNiMo penetrator maintains an acute head shape, demonstrating a conspicuous self-sharpening ability, which is responsible for the improved penetration performance of WFeNiMo penetrators. In comparison with conventional single-principal-element tungsten alloys where precipitated phases are strictly suppressed, they found that the new tungsten HEA by chemical disordered design promotes precipitation of rhombohedral μ phase, which can trigger dynamic recrystallization softening mediated shear banding and give rise to the prominent self-sharpening behaviors. They proved that inhomogeneous deformation and relatively higher strain

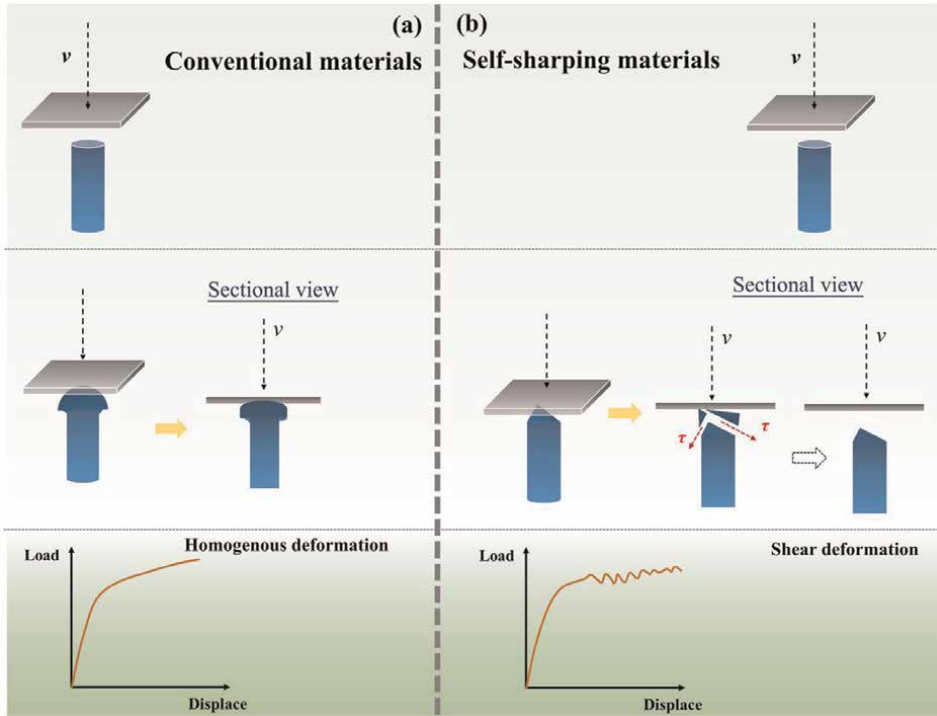


Figure 9. Deformation diagram of conventional materials and self-sharpening materials.

gradients caused by precipitates stimulate dynamic recrystallization and lead to shear band formation.

In this case, the inhomogeneous deformation is a key issue for self-sharpening behaviors, and the serration is an important reflection of inhomogeneous deformation, as shown in **Figure 9**. Hence, we infer that there should be a correlation between serration behavior and self-sharpening behavior, which is expected to shed light on the origin of self-sharpening and might open new opportunities for developing high-performance penetrator materials.

7. Strength-ductility trade-off

As an emerging material system, unique characteristics of HEAs in dynamics, thermodynamics, and structure have aroused great interest in potential structural materials. Considerate efforts have been focused on the mechanical properties and related mechanisms of HEAs. As we all know, most metallurgical mechanisms for increasing strength lead to ductility loss. One of the most exciting breakthroughs of HEAs is breaking the trade-off of strength and ductility. It can be attributed to several mechanisms as follows:

(1) Concentrated solid-solution structure: Causing significant solid solution strengthening effect. (2) Severe lattice distortion: A core effect in the design of HEAs, it has been proved that can effectively improve both yield stress and its sensitivity to grain size. In this case, fine grain strengthening effect plays a more positive role in

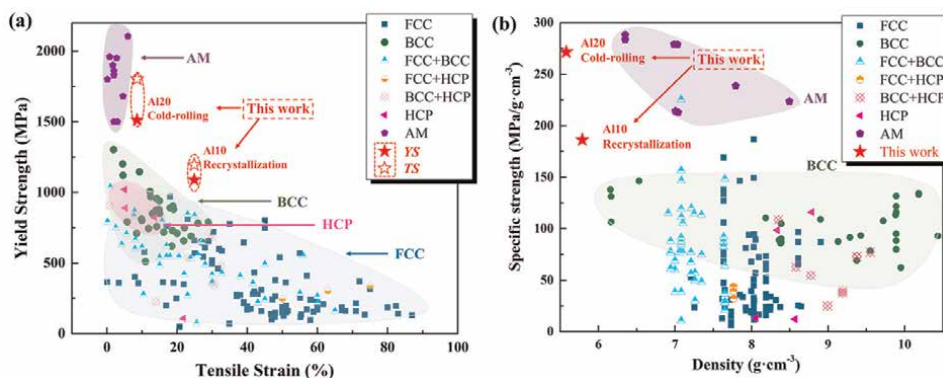


Figure 10. Comparison of the Zr-Ti-Nb-Al HEAs with existing HEAs and amorphous alloys. (a) Maps of yield strength versus tensile strain of HEAs reported previously at room temperature [Abbreviation: Yield strength (YS), Tensile strength (TS), Amorphous alloy (AM)]. (b) Maps of specific strength versus density of HEAs reported previously at room temperature [22].

HEAs, which improves the strength as well as optimizes the deformation stability. (3) Tailoring the stability of the constituent phases in HEAs in the wide compositional space: such as designing nanoprecipitates, phase transformation, twinning, and regulating the chemical short-order.

There are many salient works that have developed HEAs possess high strength, as well as good ductility, which show great application potential in new generation of structural materials. Li and co-workers [21] have reported that $\text{Fe}_{80-x}\text{Mn}_x\text{Co}_{10}\text{Cr}_{10}$ (at. %) alloy systems successfully overcome the strength-ductility trade-off by regulating metastable phase. Transformation-induced plasticity and dual-phase strengthening are two key contributions to such a breakthrough. In the $\text{Fe}_{80-x}\text{Mn}_x\text{Co}_{10}\text{Cr}_{10}$ HEA, two contributions lead to enhanced trans-grain and inter-grain slip resistance, and hence, increased strength. The increased strain hardening capacity that is enabled by dislocation hardening of the stable phase and transformation-induced hardening of the metastable phase produces increased ductility.

The high strength is a typical advantage of body-centered-cubic HEAs (BCC-HEAs). However, brittleness and weak strain-hardening ability are still their Achilles' heel. Developing ultra-strong and ductile BCC-HEAs are highly desirable but extremely challenging. Yan and co-workers [22] have reported a $(\text{Zr}_{0.5}\text{Ti}_{0.35}\text{Nb}_{0.15})_{100-x}\text{Al}_x$ ($x=10$ and 20 at. %) HEAs, which show extraordinary strength (~ 1.2 to 1.8 GPa) together with good tensile ductility ($\sim 8\%$ to 25%) at room temperature. Ultrahigh strength and excellent tensile ductility are record-high values over existing BCC-HEAs, as shown in **Figure 10**. Remarkably, relatively low densities of less than 6 g/cm^3 are exhibited in these alloys. They demonstrated that inducing nanoprecipitates and diversifying dislocation motion modes are the key factors to achieving such a remarkable breakthrough.

8. Conclusion

The unique characteristics of HEAs in dynamics, thermodynamics, and structure have aroused great interest in the new generation of structural and functional

materials. The ability of HEAs to be designed with unique properties in an unlimited space of alloy compositions is encouraging. In the past two decades, many salient efforts have been conducted to explore unique and useful properties of HEAs. Many attractive properties that break the limits of traditional materials are reported. It is desirable that the development of HEAs can shed light on the novel alloy design concept and open new opportunities for developing next-generation structural and functional materials.

Acknowledgements

Y. Z. acknowledges support from (1) Guangdong Basic and Applied Basic Research Foundation (2019B1515120020); and (2) Creative Research Groups of China (No. 51921001).

The authorship criteria are listed in our Authorship Policy: <https://www.intechopen.com/page/authorship-policy>.

Conflict of interest


The authors declare no conflict of interest.

Author details

Yong Zhang* and Xuehui Yan
State Key Laboratory of Advanced Metals and Materials, University of Science and Technology Beijing (USTB), Beijing, China

*Address all correspondence to: drzhangy@ustb.edu.cn

IntechOpen

© 2022 The Author(s). Licensee IntechOpen. This chapter is distributed under the terms of the Creative Commons Attribution License (<http://creativecommons.org/licenses/by/3.0>), which permits unrestricted use, distribution, and reproduction in any medium, provided the original work is properly cited. 

References

- [1] Yan XH, Liaw PK, Zhang Y. Order and disorder in amorphous and high-entropy materials. *Metallurgical and Materials Transactions A*. 2021;**52**(6): 2111-2122. DOI: 10.1007/s11661-021-06250-4
- [2] Zhang Y, Lu ZP, Ma SG, et al. Guidelines in predicting phase formation of high-entropy alloys. *Mrs Communications*. 2014;**4**(02):57-62. DOI: 10.1557/mrc.2014.11
- [3] Yong Z, Zuo TT, Zhi T, et al. Microstructures and properties of high-entropy alloys. *Progress in Materials Science*. 2014;**61**(8):1-93. DOI: 10.1016/j.pmatsci.2013.10.001
- [4] Zhang WR, Liaw PK, Zhang Y. Science and technology in high-entropy alloys. *Science China Materials*. 2018;**61**(1):2-22. DOI: 10.1007/s40843-017-9195-8
- [5] Yan XH, Zhang Y, Zou Y. Properties and processing technologies of high-entropy alloys. *Materials Futures*. 2022;**1**: 022002. DOI: 10.1088/2752-5724/ac5e0c
- [6] Yan XH, Zhang Y. Functional properties and promising applications of high entropy alloys. *Scripta Materialia*. 2020;**187**:188-193. DOI: 10.1016/j.scriptamat.2020.06.017
- [7] Naeem M, He H, Harjo S, et al. Extremely high dislocation density and deformation pathway of CrMnFeCoNi high entropy alloy at ultralow temperature. *Scripta Materialia*. 2020;**188**:21-25. DOI: 10.1016/j.scriptamat.2020.07.004
- [8] Liu J, Guo X, Lin Q, et al. Excellent ductility and serration feature of metastable CoCrFeNi high-entropy alloy at extremely low temperatures. *Science China Materials*. 2019;**62**(6):853-863. DOI: 10.1007/s40843-018-9373-y
- [9] Li DY, Li C, Feng T, et al. High-entropy Al_{0.3}CoCrFeNi alloy fibers with high tensile strength and ductility at ambient and cryogenic temperatures. *Acta Materialia*. 2017;**123**:285-294. DOI: 10.1016/j.actamat.2016.10.038
- [10] Gao MC, Miracle DB, Maurice D, et al. High-entropy functional materials. *Journal of Materials Research*. 2018;**33**(19):3138-3155. DOI: 10.1557/jmr.2018.323
- [11] Chou HP, Chang YS, Chen SK, et al. Microstructure, thermophysical and electrical properties in Al_xCoCrFeNi (0 ≤ x ≤ 2) high-entropy alloys. *Materials Science and Engineering B*. 2009;**163**(3): 184-189. DOI: 10.1016/j.mseb.2009.05.024
- [12] Zuo TT, Gao MC, Ouyang L, et al. Tailoring magnetic behavior of CoFeMnNi_x (X= Al, Cr, Ga, and Sn) high entropy alloys by metal doping. *Acta Materialia*. 2017;**130**:10-18. DOI: 10.1016/j.actamat.2017.03.013
- [13] Zuo TT, Yang X, Liaw PK, et al. Influence of Bridgman solidification on microstructures and magnetic behaviors of a non-equiatomic FeCoNiAlSi high-entropy alloy. *Intermetallics*. 2015;**67**: 171-176. DOI: 10.1016/j.intermet.2015.08.014
- [14] Zhang Y, Zhang M, Li D, et al. Compositional design of soft magnetic high entropy alloys by minimizing magnetostriction coefficient in (Fe_{0.3}Co_{0.5}Ni_{0.2})_{100-x}(Al_{1/3}Si_{2/3})_x system. *Meta*. 2019;**9**(3):328. DOI: 10.3390/met9030382
- [15] Guo J, Wang H, Rohr FV, et al. Robust zero resistance in a

- superconducting high-entropy alloy at pressures up to 190 GPa[J]. Proceedings of the National Academy of Sciences. 2017;**114**(50):13144-13147. DOI: 10.1073/pnas.1716981114
- [16] Vrtnik S, Koželj P, Meden A, et al. Superconductivity in thermally annealed Ta-Nb-Hf-Zr-Ti high-entropy alloys. *Journal of Alloys and Compounds*. 2017; **695**:3530-3540. DOI: 10.1016/j.jallcom.2016.11.417
- [17] Nagase T, Rack PD, Noh JH, et al. In-situ TEM observation of structural changes in nano-crystalline CoCrCuFeNi multicomponent high-entropy alloy (HEA) under fast electron irradiation by high voltage electron microscopy (HVEM). *Intermetallics*. 2015;**59**:32-42. DOI: 10.1016/j.intermet.2014.12.007
- [18] Jin K, Lu C, Wang LM, et al. Effects of compositional complexity on the ion-irradiation induced swelling and hardening in Ni-containing equiatomic alloys. *Scripta Materialia*. 2016;**119**: 65-70. DOI: 10.1016/j.scriptamat.2016.03.030
- [19] Zhang Y, Liu JP, Chen SY, et al. Serration and noise behaviors in materials. *Progress in Materials Science*. 2017;**90**:358-460. DOI: 10.1016/j.pmatsci.2017.06.004
- [20] Liu XF, Tian ZL, Zhang XF, et al. “Self-sharpening” tungsten high-entropy alloy. *Acta Materialia*. 2020;**186**:257-266. DOI: 10.1016/j.actamat.2020.01.005
- [21] Li ZM, Pradeep KG, Deng Y, et al. Metastable high-entropy dual-phase alloys overcome the strength–ductility trade-off. *Nature*. 2016;**534**(7606): 227-230. DOI: 10.1038/nature17981
- [22] Yan XH, Liaw PK, Zhang Y. Ultrastrong and ductile BCC high-entropy alloys with low-density via dislocation regulation and nanoprecipitates. *Journal of Materials Science and Technology*. 2022;**110**: 109-116. DOI: 10.1016/j.jmst.2021.08.034

Chapter 4

Solid Solution Strengthening in High-Entropy Alloys

Ibrahim Ondicho, Benard Alunda and Kahinga Kamau

Abstract

This book chapter discusses solid solution strengthening (SSS) as one of the main hardening mechanisms in high-entropy alloys (HEAs) that form basis as one of its core effects (lattice distortion). The various techniques used to quantify SSS and the role of different substitutional and interstitial elements/atoms in improving the strength of HEAs are outlined in detail. This review provides a good assessment on ways to enhance the mechanical properties of HEAs to suit the extreme demands of modern engineering applications. Based on theoretical modeling and experimental validation, Al and Nb provide superior substitutional SSS in face-centered cubic and body-centered cubic crystal structures, while carbon has a 50% more effect on improving the mechanical properties of HEAs than in stainless and twinning-induced plasticity steels. Moreover, a detailed description of the application of machine learning in design of HEAs shows that trial and error can be eliminated in identifying HEAs with exceptional yield strength. The atomic size difference should be used to evaluate the lattice distortion effect.

Keywords: high-entropy alloys, solid solution strengthening, lattice distortion, interstitials

1. Introduction

For decades since the Iron Age, many engineering applications have relied upon metallic materials that are designed on the basis of one principal element. Their physical properties of the matrix are enhanced by introducing small quantities of alloying elements. However, with the increment of complex engineering systems operating in extreme conditions, the need for materials with excellent mechanical properties has also increased exponentially. For instance, even though austenitic stainless steels have been successfully used as a structural material in a nuclear reactor core, irradiation embrittlement, irradiation-induced stress corrosion cracking and low fatigue life limits their extensive application in design of future nuclear reactors [1]. The aforementioned challenges among others require new materials that withstand the physical demands of their application environments that cannot be harnessed from the current traditional alloys. Recently, a new alloy design approach, which utilizes more principal elements in a metallic alloy was proposed by Yeh et al. [2, 3] and Cantor et al. [4]. These alloys, which were christened as high-entropy alloys (HEAs), consist of five or more principal elements with a concentrate range of 5–35 at. %.

These alloys have been reported to possess some excellent physical and mechanical properties compared to the conventional alloys [5–7]. This makes them suitable candidates for structural applications such as chemical and nuclear reactors, which have highly corrosive and extreme temperatures, aircraft engine turbines, hydrogen storage facilities, where creep strength and resistance to hydrogen embrittlement are key design considerations [8–11].

It is noteworthy that the strengthening mechanisms in HEAs are not any different from the ones observed in conventional alloys although the activation pathways and their contribution to strengthening can be different. These strengthening mechanisms include solid solution strengthening (SSS), grain boundary (GB) strengthening, dislocation strengthening (DS), precipitation hardening (PH), transformation-induced plasticity (TRIP), twinning-induced plasticity (TWIP), and composite microstructures (CM) [12–19]. Among these strengthening mechanisms, SSS is the only inherent hardening mechanism courtesy of the high atomic size mismatch in the crystal structure inducing lattice distortion, which is enlisted as one of the core effects of HEAs. Consequently, SSS forms the basis upon which other strengthening mechanisms are built on, hence, warranting in-depth review on the recent advances as new HEAs are designed. Therefore, this chapter discusses the SSS mechanism in HEAs spanning from the theoretical and analytical method to experimental techniques used in screening of this hardening mechanism.

2. Solid solution strengthening mechanism in high-entropy alloys

In conventional alloys, solid solution strengthening can be achieved by substitution or interstitial atoms of alloying elements (**Figure 1**). In the former, solute atoms replace solvent atoms in the crystal structure while in the latter, the smaller interstitial atoms such as carbon, nitrogen and boron, tend to dissolve into the interstitial spaces within the atoms of the solvent element. Both substitutional and interstitial SS strengthening induces a local lattice distortion as shown in **Figure 2a**. The stress fields caused by both substitutional and interstitial atoms coupled with the local lattice distortion impede dislocation motion and make it difficult for the introduction of new dislocations into the crystal structure during plastic deformation. Therefore, it requires higher stresses to introduce and induce dislocation motion past the strain fields and the solvent atoms. It is important to note that lattice distortion is localized in

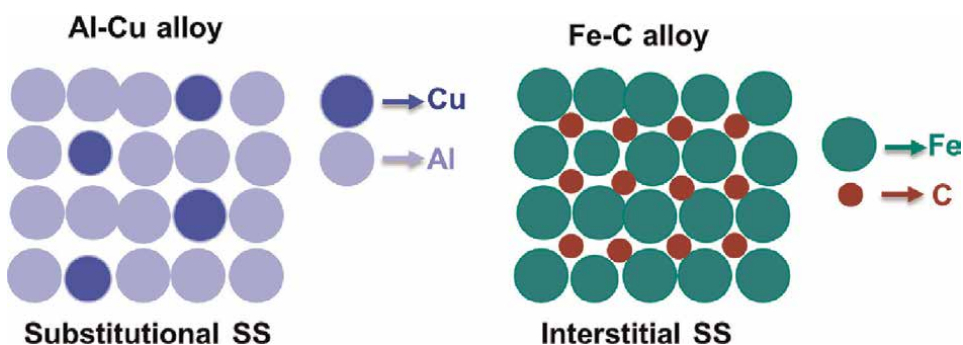


Figure 1. Schematic drawing of substitutional and interstitial solid solution strengthening in conventional alloys.

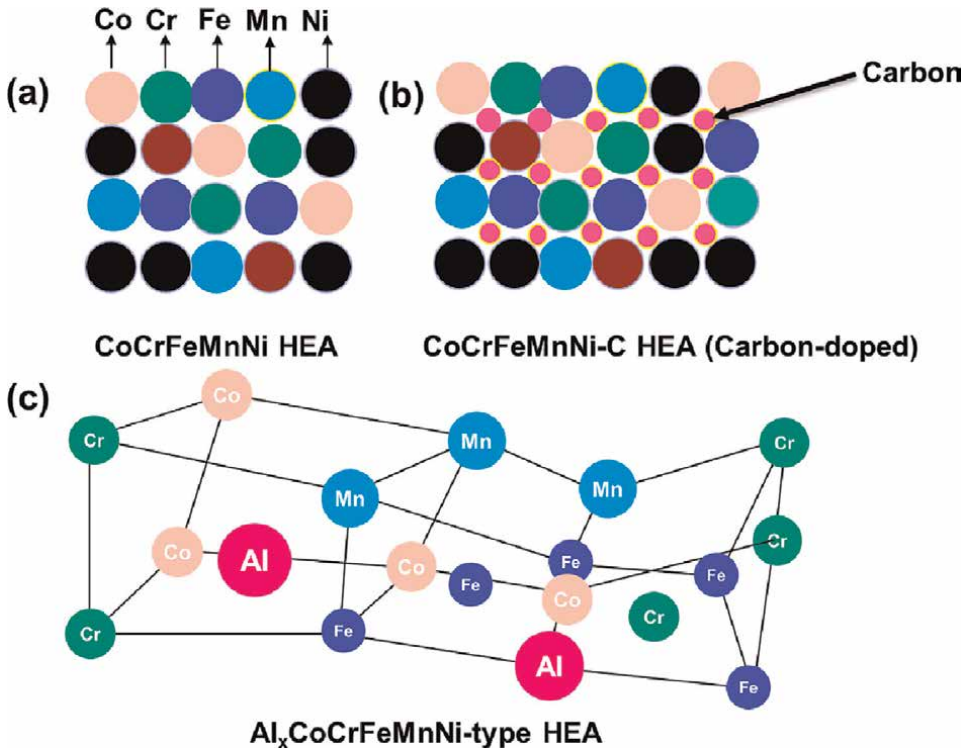


Figure 2. Schematic diagram of (a) CoCrFeMnNi equiatomic high-entropy alloy crystal structure (b) carbon-doped CoCrFeMnNi high entropy alloy, and (c) severely distorted crystal structure of a typical Al_xCoCrFeMnNi high-entropy alloy.

conventional alloys as compared to global distorted crystal lattice in HEAs as shown in **Figure 2b**.

2.1 Estimating solid solution strengthening in high-entropy alloys

2.1.1 Theoretical models

Labusch et al. [20] developed a model that describes the SS hardening in conventional multicomponent alloys by considering the impact of frictional effect caused by the continuous interaction of the solute and solvent atoms on the dislocation motion as in the Fleischer model [21]. According to this model, the effect of solute atoms acting as blocking barriers is negligible compared to the frictional effect. The Labusch model ascribes SS hardening of an alloy to its elastic mismatch and atomic size misfit [22].

$$\Delta \sigma_{ss} = B_i X_i^{2/3} \tag{1}$$

where the parameters B_i and ϵ_i can be expressed as:

$$B_i = 3\mu\epsilon_i^{4/3}Z; \quad \epsilon_i = \left(n_i^{1/2} + \alpha^2\delta_i^2\right)^{1/2} \tag{2}$$

where X_i is the solute content and B_i is a constant that depends on the alloy shear modulus, mismatch parameter and a fitting constant Z as shown in Eq. (2): The mismatch parameter is a convolution of the elastic misfit and the atomic size misfit, which can be described by Eq. (3):

$$n'_i = \frac{n_i}{1 + 0.5|n_i|}; \quad n_i = \frac{d\mu}{dX_i} \frac{1}{\mu}; \quad \delta_i = \frac{da}{dX_i} \frac{1}{a} \quad (3)$$

where a is the lattice parameter and α being the paramter that accounts for difference in interacting forces between edge and screw dislocations. For the screw dislocations the acceptable value is $3 < \alpha < 16$ while for the edge dislocations $\alpha > 16$.

The lack of a reference atom in HEAs, especially in equiatomic or near equiatomic alloys, complicates the direct application of the Labusch model in evaluating SS hardening in HEAs. Therefore, Toda-Caraballo et al. proposed another theoretical model based on the Gypen and Deruyttere's model [23] to calculate SS hardening in HEA by taking into account the average interatomic distance S_{ij} and average lattice constant:

$$S_{ij} = \frac{S_{ii}^2 K_i X_i + S_{jj}^2 K_j X_j}{S_{ii} K_i X_i + S_{jj} K_j X_j} \quad (4)$$

where s_{ii} is the atomic size of pure elements, K_i is the bulk modulus of pure elements and x_i is the concentration of the elements. The average lattice constant of the alloy, a , is calculated as:

$$a = f \sum_{ij} S_{ij} X_i X_j \quad (5)$$

where f is a constant depending on the crystal structure assuming a rigid sphere model (e.g., $f = p/2$ for FCC).

The above approach was adopted for HEAs due to their unique design in which five or more principal elements are involved in equiatomic or close to equiatomic compositions. Therefore, it is difficult to distinguish between the solvent and solute atoms since there is no reference atom and the entire crystal lattice is severely distorted as shown in **Figure 2b**. As a result, the Labusch model cannot be directly implemented in HEAs since it becomes difficult to determine the average lattice parameter theoretically. Toda-Caraballo compared predicted and experimental lattice parameters and an overestimation in bcc HEAs and underestimation in fcc HEAs was observed. A corrective multiplicative factor A was included and Eq. (3) can re-written as:

$$a^{ave} = s^{ave} f_p A \quad (6)$$

where $A = 0.98$ for bcc and $A = 1.01$ for fcc HEAs. The other parameters remained the same as expressed in the Labusch model [22]. Furthermore, the calculated misfit of CrFeNbV equiatomic HEA shows that the model can be used to track the change in the interatomic spacing. It was found that this change obeys is linear and can easily be regarded as an extension of the Vegard's law. The effect of different elements on the SS hardening of HEAs was mapped out by evaluating the average interatomic spacing as their atomic concentration is varied. For instance, both theoretically and experimentally, it was established that addition of Cr enhances the strength of CoFeNi by increasing its interatomic spacing while addition of Fe softens CoCrNi [22]. Okamoto

et al. used root-mean-square atomic displacements X-ray diffraction (XRD) and first-principles calculation to predict the strength of the equiatomic CoCrFeMnNi HEA, which can scaled to its MEA subsets (i.e CrMnCoNi, CoCrNi, FeCoNi, MnFeCoNi, MnCoNi, MnFeNi, and CrFeCoNi). It was established that the MSAD increases as the atomic number of pure elements decreases. Moreover, the lattice distortion depends on both the atomic size of the pure element and the surrounding atom in HEAs. For instance, Mn has a MSAD of 60.9 pm² in CrMnFeNi quaternary alloy compared to 26.2 pm² in MnFeCoNi HEA. Therefore, the choice of elements has a great influence in lattice distortion of HEAs [24]. Moon et al. [25] utilized a geometrical model to evaluate SSS in a single crystal of CoCrFeMnNi HEA based on the intrinsic residual strain criterion proposed by Ye et al. [26] in conjunction with lattice friction stress. It was empirically established that there is an exponential increase of the normalized intrinsic yield strength (σ_o/E) with an increasing residual mean strain (RMS) and Eq. (7):

$$\frac{\sigma_o}{E} = Y_o + A \cdot \exp\left(B \cdot \sqrt{\langle \varepsilon^2 \rangle}\right) \quad (7)$$

where ε^2 is the RMS and Y_o , A , and B are fitting parameters. The values of aforementioned parameters were found to be 27.81, 35.57, and 202.28, respectively, using a minimization function of experimental and calculated yield stress values, $f = \sigma_{experimental} - \sigma_{calculated} \rightarrow \min$ [25]. The comparison of the experimental and calculated data is shown in **Figure 3b**.

Ultimately, it was elucidated that there was an exponential increment of the intrinsic yield strength (i.e. lattice friction) with an increasing residual strain. In addition, the CoCrFeMnNi, which has a higher RMS residual strain than the quaternary CoCrFeNi HEA, was reported to have a 14.3% higher in intrinsic yield strength. This enhanced solid solution strengthening was ascribed to the presence of Mn atoms, which tend to enhance mean-square atomic displacements (MSADs) as confirmed theoretically and experimentally by Okamoto et al. [24].

2.1.2 Machine learning

Machine learning (ML) is a subset of involves using computer algorithms to study the available data and statistics and ultimately improving the performance or the output of the systems. ML has been successfully used to accurately predict phase stability in HEAs [31–33]. Recently, Wen et al. [34] recently demonstrated that ML is able to identify the underlying factors that contribute to SSS. It was established that the electronegativity difference between local interacting atoms plays a dominant role in SSS of HEAs by inducing variation of the atomic level pressure or stresses, which determines the bonding strength of element. The superior SSS in HEAs is ascribed to the greater driving force that is required to induce an electronic rearrangement [35]. Therefore, the authors proposed a model based on the electronegativity difference in predicting HEAs with superior SSS.

$$\Delta \sigma = \xi \cdot Z \cdot G \cdot \delta Xr \dots\dots\dots (8)$$

Based on this model, it was established that Mn and Cu had no profound influence on the SSS when added in a CoCrFeNi matrix while refractory elements such as Hf, Zr, Nb, and Mo showed a remarkable contribution to the SSS effect in both CoCrFeNi

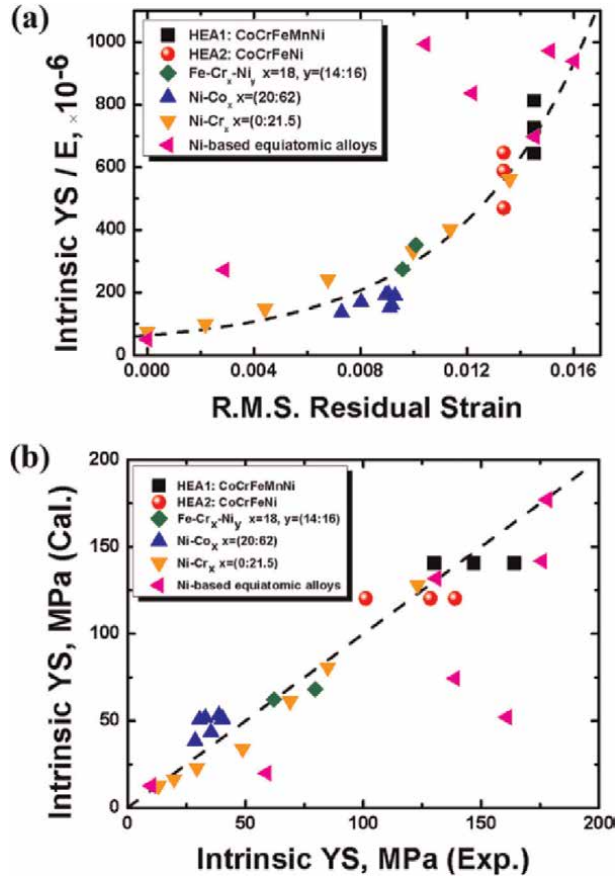


Figure 3. (a) Relationship between intrinsic yield strength (YS) normalized by the elastic modulus and the RMS residual strain for low to high entropy alloys and (b) comparison of the calculated and experimental data. Adopted from Moon et al. [25]. The other experimental data was referenced from [27–30].

and CoMnFeNi base matrix. It was further elucidated that a higher Co and Cr content with a decreased amount of Mn enhances SSS, which is consistent with the observations made by Toda Caraballo [22].

Huang et al. [36] also utilized ML to model SSS in HEA using atomic environment and interactions as the input parameters. The developed ML model was used to predict hardness of single solid solution HEAs by combining the critical theoretical SSS descriptors such as shear modulus, atomic size mismatch, bulk modulus and phase stability descriptors such as mixing enthalpy, mixing entropy, and a phase stability descriptor, Pauling electronegativities, valence electron concentration (VEC) and melting temperature. In this study, Random Forest (RF) was selected as the best algorithm for hardness prediction over the other four commonly used algorithms (Multilayer Perceptron, LibSVM, Bagging, and k-Nearest Neighbor). RF was adopted based on its high correlation coefficients (CC), low mean absolute error (MAE) and root mean squared error (RMSE).

Previously, Ding et al. [37] proposed that competition between lattice strains and concentration differences give rise to a strong local concentration fluctuations in CrFeCoNiPd HEA, which induces a strong resistance to dislocation glide. Based on the

local chemical environment, Huang et al. [36] proposed a modified physical model for SSS by adding the charge transfer (dQ) between atoms to the Varvenne and Maresca-Curtin models. This charge transfer induces atomic-level pressure (DP_{solute}) fluctuations, which dominates the SSS of several Cantor based HEAs [35]. According to the Varvenne model, the yield strength and atomic-level pressures have the following relationship $\sigma_{\text{SSS}} \propto \Delta P_{\text{solute}}^{4/3}$ and the first ionization energy (E_I^{1st}) is used to estimate the charge transfer. Based on the aforementioned parameters, the following equation was proposed to quantify the correlation between dQ factor and σ_{SSS} .

$$\begin{aligned} \sigma_{\text{SSS}} &= M \times 0.051\alpha^{-\frac{1}{3}}G \left(\frac{1+\nu}{1-\nu}\right)^{\frac{4}{3}} f_1(\omega_c) \times m_o (E_I^{1st})^{-\frac{4}{3}} \\ &= m_\nu \times m_o (E_I^{1st})^{-\frac{4}{3}} \end{aligned} \quad (9)$$

where M denotes the Taylor factor, α and ν are line tension parameter and Poisson's ratio, respectively, G is the shear modulus, $f_1(\omega_c)$ is the minimized core coefficient, m_o is the transfer coefficient between dQ and σ_{SSS} and all the material constants are merged and termed as m_ν . The results of fitting as shown in **Figure 4a**, indicate that σ_{SSS} has a linear relationship with the dQ factor. A total of 556 as-cast alloys were screened using the developed ML-SSS model for single phase solid solution (FCC/BCC) and hardness prediction in HEA compositional space [36]. Two HEA families CrMoNbTi and FeNiCuCo with a dominant BCC- and FCC-single phase solid solution, were adopted for alloy design and experimental validation with a compositional variation of between 5 and 35% of each element. Interestingly, the predicted and experimental hardness of SPSS-HEAs from the five equiatomic and non-equiatomic exhibited an excellent agreement as shown in **Figure 4b** and **c** for FeNiCuCo (FCC) and CrMoNbTi (BCC) HEAs, respectively. Moreover, in this study it was demonstrated that some non-equiatomic HEAs (FCC or BCC) have superior hardness compared to their equiatomic counterparts. For instance, $\text{Fe}_{32}\text{Ni}_{12}\text{Cu}_{27}\text{Co}_{29}$ HEA has a 236 HV while $\text{Fe}_{25}\text{Ni}_{25}\text{Cu}_{25}\text{Co}_{25}$ HEA has 184 HV for the FCC family and $\text{Cr}_{18}\text{Mo}_{32}\text{Nb}_{35}\text{Ti}_{15}$ has 607 HV while $\text{Cr}_{25}\text{Mo}_{25}\text{Nb}_{25}\text{Ti}_{25}$ has hardness value of 558 HV for the BCC family based on the experimental results. Therefore, this shows that the developed ML-SSS model is able to accurately screen a large compositional space of HEAs and identify alloys with superior mechanical properties.

2.1.3 Experimental techniques

XRD and Hall-Petch relationship are some of the experimental techniques that have been used to experimentally mapping out SSS in HEAs [38–40]. In XRD, the

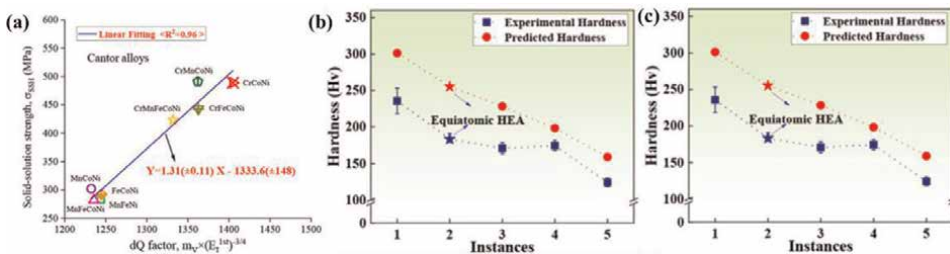


Figure 4. (a) Charge transfer part versus experimentally measured solid solution strengths σ_{SSS} of cantor alloys. The predicted and experimental hardness of (b) FeNiCuCo and (c) CrMoNbTi high entropy alloys.

change in lattice constant due to the large atomic size misfit experienced in HEAs as a result of having more principal elements with different atomic sizes has been observed in many HEA systems. Macro- or micro-chemical inhomogeneity can lead to a change in lattice parameter in HEAs, which causes a proportional change of 2θ in XRD diffractograms according to the classical Bragg's law ($n\lambda = 2d\sin\theta$). From the Bragg's law, an obvious indication of SSS is the shift of peaks to lower 2θ angles in HEA possessing high degree of SS hardening compared to the reference alloy [41]. This is due to the change in the average lattice parameter of HEAs caused by high atomic size misfit [42]. Addition of Al either as a principal or as alloying element has been used to induce substantial lattice distortion in HEAs systems due to its large atomic size [43]. Wang et al. [43] studied the effect of Al addition in the crystal structure evolution of $Al_xCoCrFeNi$ HEA system and established that fcc solution is formed when <11 at.% of Al is used while bcc is stabilized when Al content is >18.4 at.%. A careful observation of XRD peaks $(200)_{fcc}$ and $(200)_{bcc}$ for $Al_0 - Al_7$ and $Al_{0.7} - Al_{2.0}$ respectively, shows a peak shift to lower 2θ angles with increasing Al content due to the expansion of the d-spacing of both fcc and bcc phases as shown in **Figure 5a** and **b**. A proportional increase of the lattice constant values for both fcc and bcc values is observed as Al content is increased as shown in **Figure 5c**. Changes in the lattice constant and Vickers hardness exhibit different behaviors. Addition of $Al_{0.1}$ to the base system (CoCrFeNi) induces substantial change in lattice constant while a gradual increase is observed between $Al_{0.2} - Al_{0.5}$ in the fcc region. However, there is minimal change in hardness between $Al_0 - Al_{0.4}$ while a drastic change is observed in the alloy with $Al_{0.4}$ content, which is in the boundary of single-phase fcc and fcc + bcc regions. Therefore, this infers that substantial SSS is achieved when the Al content is above $x = 0.5$ (11 at.%). $Al_{0.9}$ alloy (bcc) has the highest hardness value of all the alloys with a bcc phase although it has the least lattice constant. $Al_{2.0}$ alloy has the highest lattice constant. Chen et al. [44] observed a similar shift of peaks with the addition of different amounts of Nb and Cr to the base of MoCrTiAl bcc HEA as shown in **Figure 6**. Addition of Nb to MoCrTiAl as shown in **Figure 6b** and **c**, induces a slight peak shift to lower 2θ angles signifying a proportional expansion of d-spacing and eventual increase of the lattice constant. It is interesting to note that replacing Cr with Nb induces a larger peak shift to lower 2θ angles than when Nb content is less. Therefore, it is reasonable to deduce that Nb has a superior SSS ability compared to Cr in both fcc- and bcc-based HEAs [22, 44]. However, Cr was reported to be a superior SSS element in CoFeNi fcc compared to Co, Fe, Ni elements [45]. Moreover, the sensitivity of change in lattice spacing in higher 2θ values can be observed in **Figure 4**, where peak shift is higher compared to that at lower 2θ values. It is important for the readers to examine carefully the accuracy of lattice parameter values reported in literature when describing SSS behavior of HEAs even though the trend may remain unchanged in some cases. The authors [43, 44] have used an extrapolation function $\frac{1}{2}(\cot^2 \theta + \cot \theta \cdot \cos \theta)$ according to Nelson-Riley [46], to calculate accurate lattice parameter values, which are extrapolated back to $\theta = 90^\circ$, where inherent systematic errors of diffractometers are minimized instead of using single peak such as ref. [45] or all peaks without extracting systematic errors [47].

The yield strength (YS) of metals and alloys is related to grain size by the classical Hall-Petch equation [48, 49]:

$$\sigma_y = \sigma_0 + \frac{K}{\sqrt{d}} \quad (10)$$

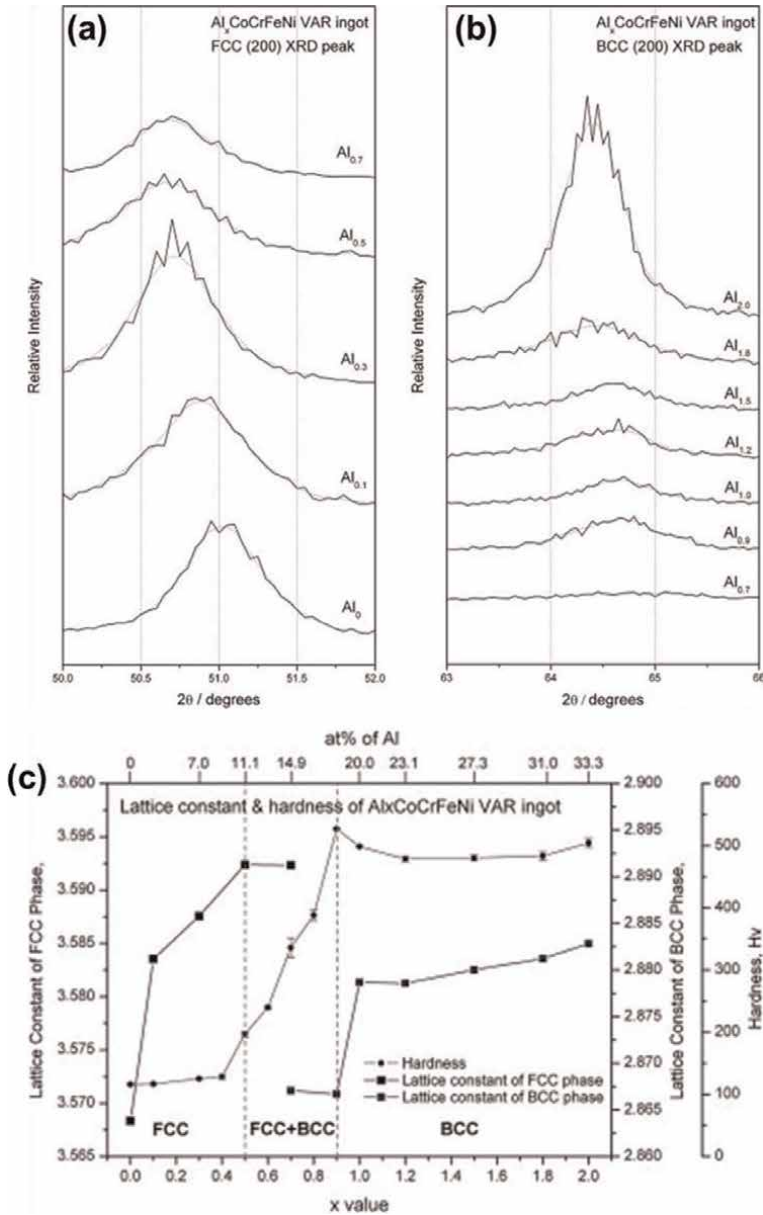


Figure 5. XRD patterns showing peak shift of 200 peaks of Al₀ – Al₇ and Al_{0.7} – Al_{2.0} for (a) fcc and (b) bcc phases, respectively. (c) Lattice constant and hardness of the Al_xCoCrFeNi alloys as functions of Al content. Symbol (▲) and symbol (■) denote lattice constants of FCC and BCC phases, respectively. Symbol (●) denotes hardness. Adopted from reference [43].

where σ_y is the YS, σ_o is the friction stress (which is defined as the flow stress required to move dislocations within the grain matrix without the effect of grain boundaries), K is a constant, which depends on the ability of the grain boundaries to resist transmission of dislocations from one grain to the adjacent grain, and d is the mean grain size. To evaluate SSS, first term on the right-hand side of Eq. (4) (friction

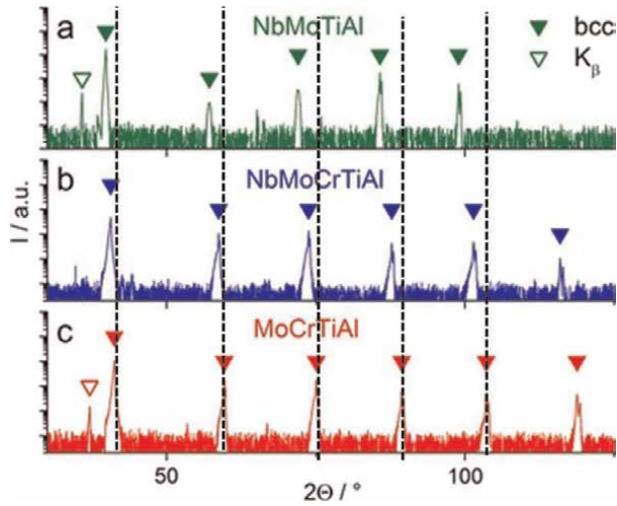


Figure 6. XRD patterns with logarithmic intensity scale of alloys with equiatomic composition in homogenized condition: (a) NbMoTiAl annealed at 1500°C, (b) NbMoCrTiAl annealed at 1300°C, and (c) MoCrTiAl annealed at 1200°C, each for 20 h. peaks arising from residual Cu-K β radiation are indicated by open triangles. The dotted lines are used to indicate peak shifts with the change of alloying elements (Nb and Cr). Data is adopted from ref. [44].

stress), will be considered. Friction stress is affected by solutes and any second phases present in the grain matrix. To effectively and accurately determine the effect of SSS on the mechanical properties of HEAs, the friction stress values of single-phase fcc alloys were compared as shown in **Figure 7**. Yoshida et al. [39] utilized the theoretical models of Toda-Caraballo et al. to predict SSS in HEAs with a single-phase fcc and compared the results with trends of their respective friction stress values obtained from the Hall-Petch equation. The theoretical model is used to predict the atomic size misfit HEA, where lattice distortion and eventual SSS is expected to be high in HEAs

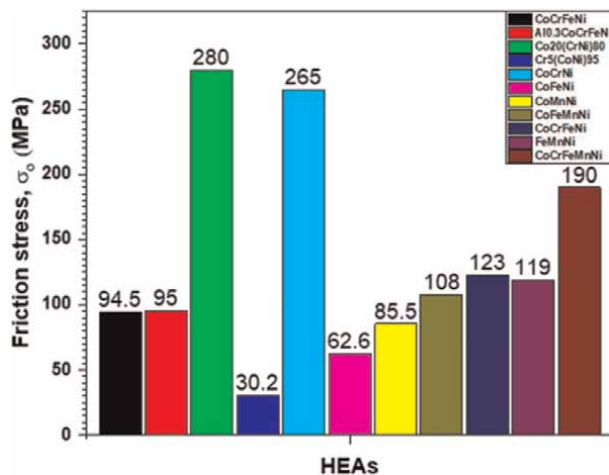


Figure 7. Friction stress of various HEAs with single-phase fcc obtained from the Hall-Petch relationship using tensile yield stress. Data extracted from Refs. [39, 40].

with large atomic size misfit especially in those alloys with Cr, Mn, Nb and Al as constituent elements [22, 39, 40, 43, 47]. Theoretically, it was established that $\text{Cr}_{20}(\text{CrNi})_{80}$ MEA has the largest atomic size misfit; hence, its crystal structure is severely distorted with a potential of having SSS as one of the main contributing mechanisms towards its overall YS. Further experimental investigation using the Hall-Petch equation, accurately validated the theoretical prediction by showing that indeed $\text{Cr}_{20}(\text{CrNi})_{80}$ MEA had the highest friction stress compared to other HEAs and MEAs under study. This is despite this alloy having a non-equiatom composition and three constituent elements. Surprisingly, its friction stress (280 MPa) was even higher than that of CoCrNi MEA (265 MPa) previously reported by [40] and the quinary equiatom CoCrFeMnNi HEA (194 MPa) [50] as shown in **Figure 7**. A recent study by Ondicho et al. [51] reported a continuous decrement of friction stress as the amount of Fe is increased in the equiatom CoCrFeMnNi HEA as the other four elements remain in equiatom composition. This increment of Fe weakens both SSS and GB strengthening because of monotonic decrease of friction stress and Hall-Petch coefficient. This phenomenon elucidates on the critical role the type and amount of constituent elements plays in SSS of HEAs. Therefore, simple stress-strain curves from tensile test can be effectively used to quickly check and pick HEAs with superior SSS without computational-intensive theoretical models. In addition, it provides an opportunity to extract GB strengthening data concurrently instead of separate evaluation as is in the case of computational models. It is important to note that an increase in SSS does not guarantee a proportional improvement of the GB strengthening [39, 40].

2.1.4 Interstitial atoms

Interstitial atoms have successfully used in conventional alloys such as steels, to enhance by both SSS and precipitation of carbides and nitrides (as discussed in Section 2.4). Similarly, as illustrated in **Figure 2b**, carbon and nitrogen have been employed in HEAs to improve their mechanical properties. Stepanov et al. [52] investigated microstructure evolution and mechanical properties of CoCrFeNiMn-1(at.%)C after cold rolling and annealing between 800°C and 100°C. They established that the as-cast specimen had a fcc phase with a lattice parameter of 0.3595 nm, which is slightly higher than that of carbon-free CoCrFeMnNi (0.3593 nm) [53]. This increment of lattice parameter was attributed to the dissolved carbon. The friction stress of this alloy as obtained from the Hall-Petch relationship was reported to be 288.15 MPa, which is higher than 125 MPa reported by Otto et al. [12] for undoped CoCrFeMnNi. This increment of the lattice resistance to dislocation by more than two-fold can be attributed to the dissolved carbon, which induces lattice dilation of the crystal lattice as evidenced by an increase of the lattice parameter. This phenomenon is in agreement with the linear dependence of strength in stainless steels and TWIP steels, where 1 at.% of C induces 76.6 MPa and 42 MPa of strength, respectively. However, in CoCrFeMnNi HEA system, 1 at.% C induces approximately ~160 MPa of strength, indicating that carbon has a superior influence on the strength of HEAs than in steels [54]. In addition, a systematic addition of carbon up to 0.25 wt.% in CoCrFeMnNi HEA induced a proportional increase of lattice parameter from 0.3593 nm for undoped alloy to 0.3602 nm for the CoCrFeMnNi-C_{0.25} in the as-solidified state [53]. Annealing heat treatment for between 600°C and 800°C of the as-solidified HEAs induces a decrease of the lattice parameter but increases again at 1000°C and 1200°C as shown in **Figure 8** below.

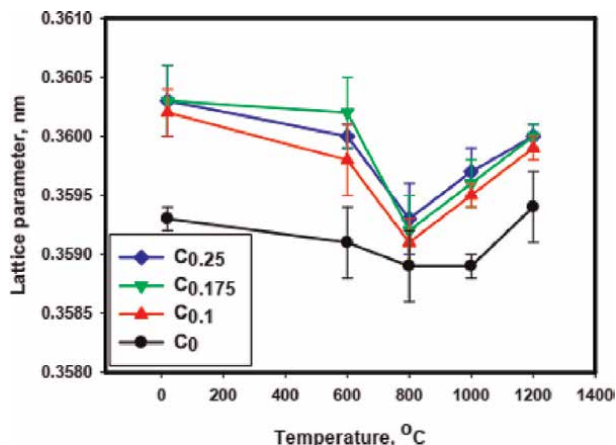


Figure 8. Dependence of lattice parameter of the CoCrFeNiMnCx ($x = 0; 0.1; 0.175; 0.25$) alloys on annealing temperature. Reprinted from Ref. [53].

3. Conclusion

It is evident that solid solution plays a critical role in the hardening of HEAs and the following conclusions can be inferred:

- i. The distortion of the crystal lattice strongly determines the degree of SSS in HEAs. And that the choice of elements has a great influence on the degree of lattice distortion which largely depends the atomic size of pure elements and the surrounding atom in HEAs. Based on the average interatomic spacing, it was Cr tends to enhance the strength of HEAs while Fe tends to have a softening effect as confirmed by both theoretical and experimental methods
- ii. HEAs with high residual mean strain tend to have a high intrinsic yield strength. The presence of some atoms such as Mn in CoCrFeMnNi HEA increases its strength by 14.3% compared to its quaternary subset CoCrFeNi because of the significant enhancement of the MSADs.
- iii. An integration of machine learning into alloy design provides a quicker pathway to screening a large compositional HEA space and identifying alloys with superior mechanical properties. For instance, it was predicted and verified experimentally using a modified ML-SSS model that non-equiatomic $\text{Fe}_{32}\text{Ni}_{12}\text{Cu}_{27}\text{Co}_{29}$ and $\text{Cr}_{18}\text{Mo}_{32}\text{Nb}_{35}\text{Ti}_{15}$ HEAs with FCC and BCC crystal structures, respectively, have higher hardness compared to their equiatomic counterparts.
- iv. In substitutional SS hardening, Al has been proven to be a strong SSS agent in fcc based HEAs. it is noteworthy that Al content more than ~ 11 at.% in $\text{Al}_x\text{CoCrFeNi}$ HEA system transforms the crystal structure from FCC to FCC + BCC and finally to fully BCC phase. This transformation is ascribed to the need for the FCC crystal structure to ‘shed off’ the excess energy from the distorted crystal lattice. Additionally, Nb has superior SSS ability both in FCC and BCC-based HEAs.

- v. Carbon can be used to improve the already available substitutional SSS in HEAs as it is the case in stainless steels. In fact, 1% C induces ~ 160 MPa of strength in equiatomic CoCrFeMnNi HEA compared to the 76.6 MPa in stainless steels and 42 MPa in TWIP steels.

Acknowledgements

The research was supported by the Kenyan German Centre for Mining, Environmental Engineering and Resource Management (CEMEREM) based at Taita Taveta University.

Author details

Ibrahim Ondicho^{1*}, Benard Alunda² and Kahinga Kamau³


1 Department of Mechanical Engineering, Dedan Kimathi University of Technology, Nyeri, Kenya

2 School of Mines and Engineering, Taita Taveta University, Voi, Kenya

3 Department of Chemistry, Jomo Kenyatta University of Agriculture and Technology, Nairobi, Kenya

*Address all correspondence to: ibrahim.ondicho@dkut.ac.ke

IntechOpen

© 2022 The Author(s). Licensee IntechOpen. This chapter is distributed under the terms of the Creative Commons Attribution License (<http://creativecommons.org/licenses/by/3.0>), which permits unrestricted use, distribution, and reproduction in any medium, provided the original work is properly cited. 

References

- [1] Kohyama A, Grossbeck ML, Piatti G. The application of austenitic stainless steels in advanced fusion systems: Current limitations and future prospects. *Journal of Nuclear Materials*. 1992;**191–194**(1992):37-44. DOI: 10.1016/S0022-3115(09)80008-1
- [2] Yeh JW. Recent progress in high-entropy alloys. *Annales de Chimie Science des Matériaux*. 2006;**31**(6): 633-648. DOI: 10.3166/acsm.31.633-648
- [3] Yeh JW. Alloy design strategies and future trends in high-entropy alloys. *JOM*. 2013;**65**(12):1759-1771. DOI: 10.1007/s11837-013-0761-6
- [4] Cantor B, Chang ITH, Knight P, Vincent AJB. Microstructural development in equiatomic multicomponent alloys. *Materials Science and Engineering A*. 2004;**375–377**:213-218. DOI: 10.1016/j.msea.2003.10.257
- [5] El-Atwani O et al. Outstanding radiation resistance of tungsten-based high-entropy alloys. *Science Advances*. 2019;**5**(3):eaav2002. DOI: 10.1126/sciadv.aav2002
- [6] He JY et al. A precipitation-hardened high-entropy alloy with outstanding tensile properties. *Acta Materialia*. 2016;**102**:187-196. DOI: 10.1016/j.actamat.2015.08.076
- [7] Tong Y et al. Outstanding tensile properties of a precipitation-strengthened FeCoNiCrTi_{0.2} high-entropy alloy at room and cryogenic temperatures. *Acta Materialia*. 2019;**165**: 228-240. DOI: 10.1016/j.actamat.2018.11.049
- [8] Xu S et al. Effect of oxygen content in 400 °C super-heated steam on the corrosion resistance of Zr-xSn-0.35Fe-0.15Cr-0.15 Nb alloys. *Corrosion Science*. 2022;**198**:110135. DOI: 10.1016/j.corsci.2022.110135
- [9] Wang Q et al. CoCrFeNiMo_{0.2} high entropy alloy by laser melting deposition: Prospective material for low temperature and corrosion resistant applications. *Intermetallics*. 2020;**119**:106727. DOI: 10.1016/j.intermet.2020.106727
- [10] Wu Y et al. Effect of high temperature molten salt corrosion on the microstructure of a Co-Mo-Cr-Si wear resistant alloy. *Materials Characterization*. 2021;**179**:111377. DOI: 10.1016/j.matchar.2021.111377
- [11] Shree Meenakshi K, Ananda Kumar S. Corrosion resistant behaviour of titanium – Molybdenum alloy in sulphuric acid environment. *Materials Today Proceedings*. 2022;**65**:3282-3287. DOI: 10.1016/j.matpr.2022.05.389
- [12] Otto F, Dlouhý A, Somsen C, Bei H, Eggeler G, George EP. The influences of temperature and microstructure on the tensile properties of a CoCrFeMnNi high-entropy alloy. *Acta Materialia*. 2013;**61**(15):5743-5755. DOI: 10.1016/j.actamat.2013.06.018
- [13] An XL et al. Hall-Petch relationship and corrosion behavior of cold-rolled CoNiFe medium entropy alloy. *Journal of Alloys and Compounds*. 2019;**807**:151698. DOI: 10.1016/j.jallcom.2019.151698
- [14] Liu WH et al. Ductile CoCrFeNiMo x high entropy alloys strengthened by hard intermetallic phases. *Acta Materialia*. 2016;**116**:332-342. DOI: 10.1016/j.actamat.2016.06.063
- [15] Li C, Li JC, Zhao M, Jiang Q. Effect of alloying elements on microstructure

and properties of multiprincipal elements high-entropy alloys. *Journal of Alloys and Compounds*. 2009;**475**: 752-757. DOI: 10.1016/j.jallcom.2008.07.124

[16] Wu Z, Parish CM, Bei H. Nano-twin mediated plasticity in carbon-containing FeNiCoCrMn high entropy alloys. *Journal of Alloys and Compounds*. 2015; **647**:815-822. DOI: 10.1016/j.jallcom.2015.05.224

[17] Li Z, Pradeep KG, Deng Y, Raabe D, Tasan CC. Metastable high-entropy dual-phase alloys overcome the strength-ductility trade-off. *Nature*. 2016; **534**(7606):227-230. DOI: 10.1038/nature17981

[18] Sabzi HE, Zarei Hanzaki A, Abedi HR, Soltani R, Mateo A, Roa JJ. The effects of bimodal grain size distributions on the work hardening behavior of a TRansformation-TWinning induced plasticity steel. *Materials Science and Engineering A*. 2016;**678**:23-32. DOI: 10.1016/j.msea.2016.09.085

[19] Sabzi HE et al. *Ab initio* assisted design of quinary dual-phase high-entropy alloys with transformation-induced plasticity. *Materials Science and Engineering A*. 2019;**636**:262-270. DOI: 10.1016/j.msea.2015.03.109

[20] Labusch R. A statistical theory of solid solution hardening. *Physica Status Solidi B: Basic Solid State Physics*. 1970; **41**(2):659-669. DOI: 10.1002/pssb.19700410221

[21] Fleischer RL. Substitutional solution hardening. *Acta Metallurgica*. 1963; **11**(3):203-209. DOI: 10.1016/0001-6160(63)90213-X

[22] Toda-Caraballo I, Rivera-Díaz-del-Castillo PEJ. Modelling solid solution

hardening in high entropy alloys. *Acta Materialia*. 2015;**85**:14-23. DOI: 10.1016/j.actamat.2014.11.014

[23] Gypen LA, Deruyttere A. Multi-component solid solution hardening. *Journal of Materials Science*. 1977;**12**(5): 1034-1038. DOI: 10.1007/BF00540988

[24] Okamoto NL, Yuge K, Tanaka K, Inui H, George EP. Atomic displacement in the CrMnFeCoNi high-entropy alloy – A scaling factor to predict solid solution strengthening. *AIP Advances*. 2016; **6**(12):125008. DOI: 10.1063/1.4971371

[25] Moon J et al. Mechanical behavior and solid solution strengthening model for face-centered cubic single crystalline and polycrystalline high-entropy alloys. *Intermetallics*. 2018;**98**:89-94. DOI: 10.1016/j.intermet.2018.04.022

[26] Ye YF, Liu CT, Yang Y. A geometric model for intrinsic residual strain and phase stability in high entropy alloys. *Acta Materialia*. 2015;**94**:152-161. DOI: 10.1016/j.actamat.2015.04.051

[27] Zhao YY, Nieh TG. Correlation between lattice distortion and friction stress in Ni-based equiatomic alloys. *Intermetallics*. 2017;**86**:45-50. DOI: 10.1016/j.intermet.2017.03.011

[28] Wu Z, Bei H, Pharr GM, George EP. Temperature dependence of the mechanical properties of equiatomic solid solution alloys with face-centered cubic crystal structures. *Acta Materialia*. 2014;**81**:428-441. DOI: 10.1016/j.actamat.2014.08.026

[29] Kako K, Kawakami E, Ohta J, Mayuzumi M. Effects of various alloying elements on tensile properties of high-purity Fe-18Cr-(14-16)Ni alloys at room temperature. *Materials Transactions*. 2002;**43**(2):155-162. DOI: 10.2320/matertrans.43.155

- [30] Van Drunen G, Saimoto S. The growth of Ni and Ni-Co single crystals. *Journal of Crystal Growth*. 1971;**11**(2):151-156. DOI: 10.1016/0022-0248(71)90179-5
- [31] Risal S, Zhu W, Guillen P, Sun L. Improving phase prediction accuracy for high entropy alloys with machine learning. *Computational Materials Science*. 2021;**192**:110389. DOI: 10.1016/j.commatsci.2021.110389
- [32] Zeng Y, Man M, Bai K, Zhang Y-W. Revealing high-fidelity phase selection rules for high entropy alloys: A combined CALPHAD and machine learning study. *Materials and Design*. 2021;**202**:109532. DOI: 10.1016/j.matdes.2021.109532
- [33] Li R, Xie L, Wang WY, Liaw PK, Zhang Y. High-throughput calculations for high-entropy alloys: A brief review. *Front. Mater*. 2020;**7**:290. DOI: 10.3389/fmats.2020.00290
- [34] Wen C et al. Modeling solid solution strengthening in high entropy alloys using machine learning. *Acta Materialia*. 2021;**212**:116917. DOI: 10.1016/j.actamat.2021.116917
- [35] Oh HS et al. Engineering atomic-level complexity in high-entropy and complex concentrated alloys. *Nature Communications*. 2019;**10**(1):Art. no. 1. DOI: 10.1038/s41467-019-10012-7
- [36] Huang X, Jin C, Zhang C, Zhang H, Fu H. Machine learning assisted modelling and design of solid solution hardened high entropy alloys. *Materials and Design*. 2021;**211**:110177. DOI: 10.1016/j.matdes.2021.110177
- [37] Ding Q et al. Tuning element distribution, structure and properties by composition in high-entropy alloys. *Nature*. 2019;**574**(7777):223-227. DOI: 10.1038/s41586-019-1617-1
- [38] Zhang F et al. Chemical complexity induced local structural distortion in NiCoFeMnCr high-entropy alloy. *Materials Research Letters*. 2018;**6**(8):450-455. DOI: 10.1080/21663831.2018.1478332
- [39] Yoshida S, Ikeuchi T, Bhattacharjee T, Bai Y, Shibata A, Tsuji N. Effect of elemental combination on friction stress and Hall-Petch relationship in face-centered cubic high/medium entropy alloys. *Acta Materialia*. 2019;**171**:201-215. DOI: 10.1016/j.actamat.2019.04.017
- [40] Yoshida S, Bhattacharjee T, Bai Y, Tsuji N. Friction stress and Hall-Petch relationship in CoCrNi equi-atomic medium entropy alloy processed by severe plastic deformation and subsequent annealing. *Scripta Materialia*. 2017;**134**:33-36. DOI: 10.1016/j.scriptamat.2017.02.042
- [41] He Q, Yang Y. On lattice distortion in high entropy alloys. *Frontiers in Materials*. 2018;**5**:42. DOI: 10.3389/fmats.2018.00042
- [42] Tian F. A review of solid-solution models of high-entropy alloys based on *ab initio* calculations. *Frontiers in Materials*. 2017;**4**:36. DOI: 10.3389/fmats.2017.00036
- [43] Wang W-R, Wang W-L, Wang S-C, Tsai Y-C, Lai C-H, Yeh J-W. Effects of Al addition on the microstructure and mechanical property of Al_xCoCrFeNi high-entropy alloys. *Intermetallics*. 2012;**26**:44-51. DOI: 10.1016/j.intermet.2012.03.005
- [44] Chen H et al. Contribution of lattice distortion to solid solution strengthening in a series of refractory high entropy alloys. *Metallurgical and Materials Transactions A: Physical Metallurgy and Materials Science*. 2018;**49**(3):772-781. DOI: 10.1007/s11661-017-4386-1

- [45] Wang Z et al. Quantitative determination of the lattice constant in high entropy alloys. *Scripta Materialia*. 2019;**162**:468-471. DOI: 10.1016/j.scriptamat.2018.12.022
- [46] Nelson JB, Riley DP. An experimental investigation of extrapolation methods in the derivation of accurate unit-cell dimensions of crystals. *Proceedings of the Physical Society*. 1945;**57**(3):160-177. DOI: 10.1088/0959-5309/57/3/302
- [47] Agustianingrum MP, Yoshida S, Tsuji N, Park N. Effect of aluminum addition on solid solution strengthening in CoCrNi medium-entropy alloy. *Journal of Alloys and Compounds*. 2019; **781**:866-872. DOI: 10.1016/j.jallcom.2018.12.065
- [48] Hall EO. The deformation and ageing of mild steel: III discussion of results. *Proceedings of the Physical Society. Section B*. 1951;**64**(9):747-753. DOI: 10.1088/0370-1301/64/9/303
- [49] N. J. Petch. The Cleavage Strength of Polycrystals. 1953. Available from: <https://www.scinapse.io/papers/517706> [Accessed: May 25, 2021]
- [50] Sun SJ et al. Enhanced strength and ductility of bulk CoCrFeMnNi high entropy alloy having fully recrystallized ultrafine-grained structure. *Materials and Design*. 2017;**133**:122-127. DOI: 10.1016/j.matdes.2017.07.054
- [51] Ondicho I, Alunda B, Park N. Effect of Fe on the Hall-Petch relationship of (CoCrMnNi)_{100-x}Fe_x medium-and high-entropy alloys. *Intermetallics*. 2021; **136**:107239. DOI: 10.1016/j.intermet.2021.107239
- [52] Stepanov ND et al. Effect of thermomechanical processing on microstructure and mechanical properties of the carbon-containing CoCrFeNiMn high entropy alloy. *Journal of Alloys and Compounds*. 2017;**693**:394-405. DOI: 10.1016/j.jallcom.2016.09.208
- [53] Stepanov ND, Yurchenko NY, Tikhonovsky MA, Salishchev GA. Effect of carbon content and annealing on structure and hardness of the CoCrFeNiMn-based high entropy alloys. *Journal of Alloys and Compounds*. 2016; **687**:59-71. DOI: 10.1016/j.jallcom.2016.06.103
- [54] Bouaziz O, Zurob H, Chehab B, Embury JD, Allain S, Huang M. Effect of chemical composition on work hardening of Fe—Mn—C TWIP steels. *Materials Science and Technology*. 2011; **27**(3):707-709. DOI: 10.1179/026708309X12535382371852

Section 2

Processing

Proposition of a Growth Law as a Function of Solidification Parameters for Monotectic Alloy Systems

Adrina Silva, José Braga, Paulo Monteiro Jr, Cassio Silva, Camila Konno, Thiago Costa and Emmanuelle Feitosa

Abstract

Monotectic alloys show promising applications in wear-resistant automotive components, once these systems have remarkable self-lubricating properties that are of great interest for using in bearings. Much research has been devoted to better comprehend monotectic reactions. Some studies assume that the interphase spacing evolution in monotectic alloys follows the classical relationship used for eutectics or the dendritic growth relationship; however, some studies reported that the growth laws seem not to be valid for some cases. Because of that, obtaining single mathematical expressions that allow describing the development of solidification structures as a function of thermal parameters is very important. Based on the above, this chapter proposes a systematic analysis of the monotectic growth laws proposed in the literature and suggests exclusive growth laws as a function of solidification parameter for monotectic alloys solidified under different heat extracting configurations.

Keywords: mathematical expressions, solidification structures, interphase spacings, low miscibility

1. Introduction

Monotectic alloys have limited solubility in the liquid state as a determining characteristic. Some of these alloys are of unique importance, such as aluminum alloys dispersed with lead, bismuth, and indium, used as self-lubricating automotive components [1–3]. Bismuth, lead, and indium dispersed in the aluminum matrix have a low melting point and remain dispersed in the matrix, which reduces the hardness of the material but can improve the performance in service against adhesive and abrasive wear since they can flow easily in conditions of slipping, like on components that are in a relative motion [4, 5]. The sum of these characteristics results in a favorable tribological behavior. According to [6, 7], Al-Bi alloys are potential substitutes for materials containing lead additions.

Among the bearing alloys used today in the automotive industry, bronze with irregularly distributed lead stands out. The cars of the future require a bearing material with lower coefficients of friction and wear, besides being able to sustain higher dynamic pressures compared with those offered by bronze-lead alloys [8]. In addition, recent investigations have pointed to the possibility of manufacturing porous aluminum with deep pores using monotectic alloys and electrochemical attack, since with this method it is possible to produce anisotropic porous media with pore sizes between 5 μm and 20 μm , smaller than those obtained by classical procedures for manufacturing porous materials [9, 10].

In monotectic alloys, the immiscibility of the elements tends to give rise two very distinct phases during solidification. Normally the structure of this material is formed by a soft constituent (in smaller content) dispersed in the matrix of the constituent with greater resistance [11]. This low miscibility maybe caused by the atomic size mismatch, which makes that each element diffuses differently and leads to unique microstructure, and the great wear resistance property in monotectic alloys is seen as a characteristic of high-entropy alloys (HEAs). Recently, HEAs have drawn enormous attention in diverse fields because of their distinctive concept and unique properties [12, 13].

Due to their interesting peculiarities, important studies have been developed in the last three decades to improve understanding about the phenomena involved in the formation of the monotectic alloys [7, 8, 14–21]. It is extremely important to understand the process of formation and development of these structures to control the properties of the final product, for example, recently, due to the potential application in tribological systems, some authors have developed studies with the purpose of verifying the influence of monotectic structures on micro-abrasive wear resistance [11, 22].

Interphase spacing is the commonly investigated microstructural parameter, with the attempt to obtain mathematical expressions that allow to describe the development of solidification structures as a function of solidification thermal parameters such temperature gradient or growth rate, but some other parameters, such particles' diameters were also analyzed.

In analyzing the monotectic reaction, [14] found that the development of many monotectic alloys during directional solidification is in accordance with a relationship between interphase spacing (λ) and growth rate (v). This relationship, given by $\lambda^2 v = C$, where C is a constant, is the same that governs the development of regular eutectics, according to studies by [23]. The monotectic systems can be separated into two categories, i.e., those that are in accordance with the model cited with acceptable agreement and those that respect the power-function relationship but with exponents different from that proposed by [14]. Furthermore, in many studies where values for C have been determined, the solidification conditions are not transient [8, 14, 17, 24, 25], which tends to distance the conditions of these experiments from those occurring in industrial processes.

Calberg and Bergman [15] have found that the relationship of growth to some irregular monotectic structures is like the relationship governing dendritic growth, given by $\lambda \cdot v^a \cdot G^b = C$, where v is the growth rate, C is a constant for both cases, G is the temperature gradient, and a and b are constants.

Yang and Liu [17] analyzed the particle diameter of hypermonotectic alloys and found results that lead to power-type functions, however, with different exponents from those proposed ever, with different exponents from those proposed for the quantification of interphase spacings.

Silva et al. [6, 7, 18, 26–29] tried to evaluate the microstructural behavior of hypomonotectic and hypermonotectic alloys solidified in devices with upward and downward configurations. They found that the alloys that showed cellular configuration presented mathematical expressions correlating cellular spacing with growth rate in agreement with the one found and merged in the literature, $\lambda_1 = C \cdot v^{-1,1}$, where v is the growth rate and C is a constant [30–33]. In addition, the alloys solidified in an upward device and exhibited particle morphology, presented mathematical expressions congruent to the one for regular eutectic alloys. On the other hand, some alloys solidified in a downward setup, and the ones that presented fibrous morphologies did not fit in any expression, as well as alloys' particle diameters. The relationship governing dendritic growth could represent all the upward solidification microstructures. The results of particle diameters found also obey power-type functions, as suggested by Yang et al., but with different exponents.

Freitas [34], when analyzing the behavior of monotectic and hypermonotectic alloys, found power-type functions to quantify the interphase spacing and particle diameter with growth velocity, all different from the laws proposed previously. Costa et al. [31], who studied ternary monotectic alloys, but with a microstructure of particles and pearl strands, presented mathematical expressions to correlate interphase spacings with the velocity of the type, $\lambda = C \cdot v^{-1,1}$, for cell growth and potency-like functions, but with different exponents, to analyze the diameter of the particles.

There is no agreement as to the validity of these growth laws to characterize the growth of monotectic systems. The vast majority of these studies are based on the use of solidification devices of the Bridgman type that impose a stationary regime of heat extraction [35], with few evaluating solidification processes of monotectic alloys under transient conditions, considering the effects of the flow of particles rich in solute in the remaining liquid volume, and correlating the measured thermal solidification parameters with the monotectic structures got, which brings the experiences closer to the industrial reality [28, 36]. There are also few studies that analyze the influence of the growth direction on the interphase spacings and on the dimensions of bismuth, lead, and indium particles [37]. The use of the relationships of [23] may not be valid under certain conditions, as verified by [29], in the case of downward directional solidification. Moreover, the relationship proposed by [15] for dendritic growth cannot be suitable to be employed in the case of downward directional solidification where the heat transfer can occur not only by conduction but also by convection.

Researchers often aim to study whether there is some association between two observed variables and to estimate the strength of this relationship. These research objectives can be quantitatively addressed by correlation analysis, which provides information about not only the strength but also the direction of a relationship. The two most used correlation coefficients in medical research, the Pearson coefficient, and the Spearman coefficient. With Pearson coefficient, two typical properties of the bivariate normal distribution can be relatively easily assessed, and researchers should check approximate compliance of their data. The correlation coefficient is sometimes criticized as having no obvious intrinsic interpretation, and researchers sometimes report the square of the correlation coefficient. This R^2 is termed the “coefficient of determination.” It can be interpreted as the proportion of variance in one variable that is accounted for by the other [38, 39].

With so many results already found, both for the same and different alloys and under different solidification conditions, with all of them establishing power-type laws as a proposition, it is understood to be a good alternative to organizing the results

and performing visual and statistical analysis. To evaluate a possible correlation between several experiments performed and get standardized laws of monotectic growth that can make physical sense and thus specifically characterize monotectic growth, with its particularities of solidification process and microstructural morphologies, besides being able to predict this growth and be able to set solidification parameters that result in certain microstructural behavior.

Based on this consideration, this research aims to analyze statistically and physically various results to get a monotectic growth law as a function of position and growth rate for directionally solidified systems under transient heat extraction conditions, with expectations to be extended for all types of solidification.

2. Experimental procedure

In the present work, some results were analyzed: the ones of the works by [40, 41] concerning the vertical, upward, and downward solidification of monotectic alloys of the Al-Bi, Al-Pb, and Al-In system, by [34] regarding the upward vertical solidification of monotectic alloys of the Al-Bi and Al-Pb system and by [42], whose summaries of materials and methods are described in this work; however, details are found in the former literature.

Directional solidification devices, in which heat is extracted only through a water-cooled side, promoting vertical upward and downward and horizontal solidification, were used in the experiments permitting a wide range of cooling rates to be attained along the length of the castings.

The alloys detailed in **Table 1** were prepared using alloying elements in a fixed proportion, which were melted in a refractory crucible in a muffle furnace. The

Type of solidification device—author	Alloy composition	Temperature (°C)		
		T_L ou T_M	T_P	ΔT_p (%)
Upward-Silva et al. [41]	Al-3.2wt.%Bi	658	690	5
Upward-Freitas et al. [5]	Al-3.2wt.%Bi	658	690.9	5
Downward-Silva et al. [41]	Al-3.2wt.%Bi	658	690	5
Upward-Silva et al. [7]	Al-5.0wt.%Bi	708.6	744	5
Upward-Silva et al. [7]	Al-7.0wt.%Bi	750	788	5
Upward-Silva et al. [19]	Al-0.9wt.%Pb	659.6	692	≈5
Downward-Silva et al. [28]	Al-0.9wt.%Pb	659.6	692	≈5
Upward-Silva et al. [19]	Al-1.2wt.%Pb	659	692	≈5
Downward-Silva et al. [28]	Al-1.2wt.%Pb	659	692	≈5
Horizontal-Konno [40]	Al-1.2wt.%Pb	659	692	≈5
Upward-Silva et al. [34]	Al-2.1wt.%Pb	720.6	798	10
Upward-Freitas [33]	Al-2.5wt.%Pb	745	782.25	5
Upward-Silva et al. [27]	Al-5.5wt.%In	652.2	671	3

Table 1.

Experiments performed with alloys of the Al-Bi, Al-Pb, and Al-In systems: T_M , monotectic temperature at equilibrium; T_L , liquidus line temperature; T_P , pouring temperature; ΔT_p , percentage of overheating of the liquidus line.

molten alloy was then poured into the casting chamber of the directional solidification apparatus. The melt temperature was parameterized in ΔT_V above the *liquidus* temperature of each alloy at the beginning of each experiment, according to **Table 1**. Approaching the parameterized melt temperature, the electric heaters were disconnected and at the same time the controlled water flow was initiated, permitting the onset of solidification. Continuous temperature measurements in the castings were monitored during solidification via the output of a bank of fine type K, placed in the geometrical center of the molds' cavities along their length. All the thermocouples were connected by coaxial cables to a data logger interfaced with a computer, capable of automatically record temperature data.

The ingots were subsequently sectioned along their vertical axis, ground, and etched with an acid solution to reveal the macrostructure (Poulton's reagent: 5 mL H₂O; 5 mL of hydrofluoric acid (HF) 48%; 30 mL of nitric acid (HNO₃) 65%; 60 mL of hydrochloric acid (HCl) 37%). The microstructural characterizations of the directionally solidified (DS) alloy castings were performed by extracting samples at different sections along the length of the castings. The samples were polished with SiC papers, finely polished with diamond paste, and then etched with an acid solution to reveal the microstructure (hydrofluoric acid (HF)). The examinations of the microstructures were performed using an optical metallurgical microscope. The interphase spacings (λ) were measured from the optical images of the solidified samples. They were measured along the casting longitudinal section by averaging the horizontal distance between the droplets, fibers, and/or strings of pearls, adopting as reference the center of each morphology. The evolution of the particles size (droplet diameter: d) along the casting lengths was also determined. A scanning electron microscope equipped with an energy-dispersive spectrometer complemented the microstructural characterization.

Table 1 presents: the list of directional solidification experiments performed with the device used, alloy composition, liquidus temperatures (hypomonotectic and hypermonotectic alloys) or monotectic temperature at equilibrium (T_L or T_M , respectively), and pouring temperature (T_P) along with the percentage of *liquidus* temperature super-heat ($\Delta T_V\%$). **Figure 1** shows some typical microstructures obtained from the monotectic solidification processes: droplets, fibers, and strings of pearls.

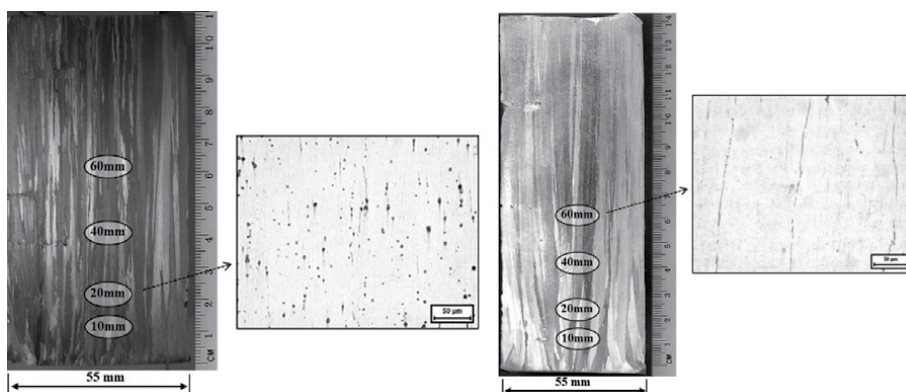


Figure 1. Macrostructure and longitudinal microstructure of the Al-2.5wt.%Pb and Al-3.2wt.%Bi alloys, respectively, solidified in a vertical upward device [14].

To get a result as a function of position, all points from the experimental results by [34, 40, 41] were used for interphase spacings and particle diameters for each position, and the results were dimensionless by dividing each point by the value of spacing or average diameter for each structure observed, i.e., for an ingot in which a structure of particles from 0 mm to 40 mm and fibers from 60 mm to 90 mm was found, and calling λ_i the value of the spacing for a position i in this structure, it is seen that:

- λ_{MED} for droplets morphology = λ_{20} [μm]
- value of dimensionlessization for a position i in this structure = λ_i/λ_{20} dimensionless
- λ_{MED} for fibrous morphology = λ_{75} [μm]
- value of dimensionlessization for a position i in this structure = λ_i/λ_{75} dimensionless

Dimensionlessization is of fundamental importance in physical analyses because of the significant reduction in experimental effort to establish the relationship between two variables, besides producing a better approximation than the variables themselves.

After dimensionlessization, all points were plotted as a function of position, also calculating the coefficient of determination (R^2), which is one way to assess the quality of the model's fit.

In statistics, simple linear regression is a linear regression model with a single explanatory variable. That is, it concerns two-dimensional sample points with one independent variable and one dependent variable (conventionally, the x and y coordinates in a Cartesian coordinate system) and finds a linear function (a non-vertical straight line) that, as accurately as possible, predicts the dependent variable values as a function of the independent variables. The adjective simple refers to the fact that the outcome variable is related to a single predictor [43, 44].

It is common to make the additional stipulation that the ordinary least squares (OLS) method should be used: the accuracy of each predicted value is measured by its squared residual (vertical distance between the point of the dataset and the fitted line), and the goal is to make the sum of these squared deviations as small as possible. Other regression methods that can be used in place of ordinary least squares include least absolute deviations (minimizing the sum of absolute values of residuals) and the Theil-Sen estimator (which chooses a line whose slope is the median of the slopes determined by pairs of sample points).

Consider the model function

$$y = \alpha + \beta x \tag{1}$$

which describes a line with slope β and y -intercept α . In general, such a relationship may not hold exactly for the largely unobserved population of values of the independent and dependent variables; it can be called the unobserved deviations from the above equation the errors. Suppose it is observed n data pairs and call them $\{(x_i, y_i), i = 1, \dots, n\}$. The underlying relationship between y_i and x_i involving this error term ε_i can be described by

$$y_i = \alpha + \beta x_i + \varepsilon_i \tag{2}$$

This relationship between the true (but unobserved) underlying parameters α and β and the data points is called a linear regression model.

The goal is to find estimated values $\hat{\alpha}$ and $\hat{\beta}$ for the parameters α and β , which would provide the "best" fit in some sense for the data points. On the case of this work, the "best" fit will be understood as in the least-squares approach: a line that minimizes the sum of squared residuals $\hat{\epsilon}_i$ (differences between actual and predicted values of the dependent variable y), each of which is given by, for any candidate parameter values α and β ,

$$\hat{\epsilon}_i = y - \hat{\beta}x \quad (3)$$

In other words, $\hat{\alpha}$ and $\hat{\beta}$ solve the following minimization problem:

$$\text{Find } \min_{\alpha, \beta} Q(\alpha, \beta) \text{ for } Q(\alpha, \beta) = \sum_{i=1}^n \hat{\epsilon}_i^2 + \sum_{i=1}^n (y_i - \alpha - \beta x_i)^2 \quad (4)$$

By expanding to get a quadratic expression in α and β , α and β values can be derived to minimize the objective function Q (these minimizing values are denoted $\hat{\alpha}$ and $\hat{\beta}$ [6]:

$$\hat{\alpha} = y_i - \alpha - \beta x_i \quad (5)$$

$$\hat{\beta} = \frac{\sum_{i=1}^n (x_i - \underline{x})(y_i - \underline{y})}{\sum_{i=1}^n (x_i - \underline{x})^2} = \frac{\text{Cov}(x, y)}{\text{Var}(x)} = r_{xy} \frac{\delta_y}{\delta_x} \quad (6)$$

where \underline{x} and \underline{y} are the average of the x_i and y_i , respectively; r_{xy} is the sample correlation coefficient between x and y ; δ_x and δ_y are the uncorrected sample standard deviations of x and y ; and Var and Cov are the sample variance and sample covariance, respectively.

Substituting the above expressions for $\hat{\alpha}$ and $\hat{\beta}$ into

$$f = \hat{\alpha} + \hat{\beta}x \quad (7)$$

yields

$$\frac{f - \underline{y}}{\delta_y} = r_{xy} \frac{x - \underline{x}}{\delta_x} \quad (8)$$

This shows that r_{xy} is the slope of the regression line of the standardized data points (and that this line passes through the origin).

Generalizing the \underline{x} notation, a horizontal bar can be written over an expression to indicate the average value of that expression over the set of samples. For example:

$$\underline{xy} = \frac{1}{n} \sum_{i=1}^n x_i y_i \quad (9)$$

This notation allows a concise formula for r_{xy} :

$$r_{xy} = \frac{\underline{xy} - \underline{x}\underline{y}}{\sqrt{(\underline{x}^2 - \underline{x}^2)(\underline{y}^2 - \underline{y}^2)}} \quad (10)$$

The coefficient of determination (Pearson product-moment correlation coefficient, or “Pearson’s correlation coefficient,” commonly called simply “the correlation coefficient” – “R squared”) is equal to r^2_{xy} when the model is linear with a single independent variable, and it is the most familiar measure of dependence between two quantities [45].

There is a corollary of the Cauchy-Schwarz inequality that the absolute value of the Pearson correlation coefficient is not bigger than 1. The correlation coefficient is +1 in the case of a perfect direct (increasing) linear relationship (correlation), -1 in the case of a perfect decreasing (inverse) linear relationship (anticorrelation), and some value in the open interval (-1,1) in all other cases, indicating the degree of linear dependence between the variables. As it approaches zero there is less of a relationship (closer to uncorrelated). The closer the coefficient is to either -1 or 1, the stronger the correlation between the variables, although there is a detailed table of the representativeness of the values, in module, as shown in **Table 2** [46].

The R^2 is, therefore, a descriptive measure of the goodness of fit got. It refers to how the amount of variability in the data that is explained by the fitted regression model. However, the value of the coefficient of determination depends on the number of observations (n), increasing when n decreases. If $n = 2$, always $R^2 = 1$.

R^2 should be used with caution, as it is always possible to make it larger by adding enough terms to the model. Thus, if, for example, there are no repeated data (over one y value for the same x a polynomial of degree (n - 1)), it will give a perfect fit ($R^2 = 1$) for n data. When there are repeated values, it will never be equal to 1, as the model cannot explain the variability, because of pure error.

Although R^2 increases with the addition of terms to the model, this does not mean that the new model is superior to the previous one. Unless the new model's residual sum of squares is reduced to an amount equal to the original residual mean square, the new model will have a larger residual mean square than the original because of the loss of 1 degree of freedom. This new model could be worse than the previous one.

The magnitude of R^2 also depends on the amplitude of variation of the regressor variable (x). R^2 will increase with greater amplitude of variation of the x's and decrease otherwise. It can be shown that

$$E[R^2] \cong \frac{\hat{\beta}_1^2 \sum_{i=1}^n (x_i - \bar{x})^2}{\hat{\beta}_1^2 \sum_{i=1}^n (x_i - \bar{x})^2 + \sigma^2} \tag{11}$$

Thus, a big value of R^2 may be large simply because x has varied by a very large amplitude. R^2 may be small because the amplitude of the x's was too small to

Value	Representativeness
0.9 and beyond	Very strong correlation
Between 0.7 and 0.9	Strong correlation
Between 0.3 and 0.7	Moderate correlation
Between 0 and 0.3	Weak correlation
0	Negligible correlation

Table 2. Interpretation of the correlation coefficient values, in module.

allow a relationship with y to be detected. In general, R^2 does not measure the magnitude of the slope of the line. A big value of R^2 does not mean a steeper line. It does not consider the model's lack of fit; it may be large, even if y and x are nonlinearly related [47, 48]. Hence, although R^2 values were used as an adjustment basis in this work, which is widely accepted in the literature [34, 36, 40, 49], this should not be considered alone, but always combined with other diagnoses of the model.

Although the establishment of a single morphology versus position relationship for aluminum-based monotectic alloys directionally solidified is of great importance, it is known the thermal parameters have a considerable influence on the development of the solidification structures. Therefore, it is interesting that a relationship in function, e.g., of the growth rate could be established for these alloys. In addition, if the solidification processes were performed again and the growth rate values at each ingot position were different from those resulting from the original experiment, the interphase spacing values at each position would also be different compared to the results of the original experiment, which emphasizes the importance of obtaining the growth laws of microstructural parameters as a function of the solidification thermal parameters.

In this way, following the same methodology used for the analysis of the interphase spacings and droplets diameters with positions from metal/mold interface, the ordered pairs of the curves that relate the interphase spacing and the droplet diameters with the corresponding growth rates obtained in the studies were used [6, 7, 20, 28, 29, 34, 36, 40]. Again, the values of interphase spacing, and droplet diameters used in the present analysis were dimensionless.

With the dimensionless points of all the data collected and plotted, it was observed that the points of a single experiment were quite parallel to the points of the other ones, which led to the proposition of a function that translated and could represent the growth of each microstructure. Once again, a statistical analysis by simple linear regression was used since this is the most suitable tool for continuous input-output values and represents the situation in question [50].

Konno [42] studied the behavior of an Al-1.2wt.%Pb alloy solidified in a horizontal directional device. It is the only study performed in horizontal direction of these type of alloys, and Konno et al. [21], who analyzed the influence of the directionality of heat extraction on the morphology of the Al-1.2wt.% Pb alloy, found that horizontal solidification has sufficient convective movements to break the fiber formation and generate a morphology of only irregularly distributed particles; however, it has higher cooling rates than the solidification performed in a descending device, resulting in an interesting and differentiated behavior of the solidification process. Thus, a comparison of the growth law as a function of speed for this alloy was carried out separately, to ratify the accuracy of the proposed expressions.

3. Results and discussion

The graph in **Figure 2** presents the values of interphase spacing and particle diameter (when applicable), respectively, as a function of position for all monotectic structures analyzed. Where different morphologies occurred in the same ingot, this was divided according to the type of morphology found (globular or fibrous). In these cases, the position adopted as a reference for nondimensionalization was the average

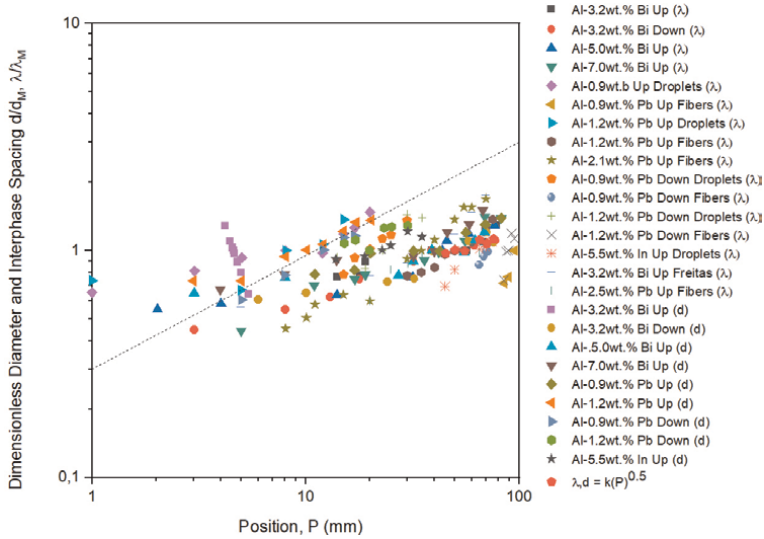


Figure 2. Globular and fibrous interphase spacings and particle diameter (in which particles occurred) as a function of position for all studied alloys.

position of each structure. As it can be seen, there was a collapse between all the results got for both cases, which means that a single law of growth can be established, $\lambda = k.(P)^{0.5}$. It is observed, besides the collapsed points, that the curves tend to a certain parallelism between them, a fact used to find the value of k that best represents each of the experimental situations got. The collapse between the points is best visualized in a log-log scale, which can reduce data dispersion and, therefore, present better quality in relation to the linear scale for this case.

Table 3 presents the condensed k values got for the best determination coefficients found for each case, separated by alloy. By observing the tables, it is noted that no coefficient of determination was in the range considered being of weak intensity (0–0.3), with most being between moderate intensity (0.3–0.7) and some between strong intensity (above 0.7), which is considered a satisfactory result considering the number of experiments analyzed. The lower values of determination coefficients were found for the downward experiments, which could be justified because of the intense convective flow that occurs on these cases. Even so, the results are acceptable both by visual analysis and by the values of the coefficient of determination.

It was also noted that the k values, both for fibers and for particles, are between 0.1 and 0.19, except for lead particles, which all found k values beyond those mentioned above, which are even higher when considering the results got in experiments with upward configuration (k ranging from 0.32 to 0.33). In addition, it could be seen that the values of k , when observed in experiments with the occurrence of particles, are quite close in certain situations, which leads to the elaboration of **Table 4**, which shows the new values of k got for each situation, evidencing that for these cases a single function can be established to represent the evolution of the spacings and diameters of the particles as a function of the position from the metal/mold interface in each system, except for the Al-Pb alloy, where the upward solidification cases differ from downward.

Alloy	Type of solidification device	Structure, parameter	k	R ²
Al-3.2wt.%Bi	Upward and Downward	Droplet, interphase spacing, diameter	0.14–0.16	0.48–0.81
Al-5.0wt.%Bi	Upward	Droplet, interphase spacing, diameter	0.15–0.17	0.60–0.70
Al-7.0wt.%Bi	Upward	Droplet, interphase spacing, diameter	0.16	0.67–0.83
Al-0.9wt.%Pb	Upward and Downward	Droplet, fiber, interphase spacing, diameter	0.10–0.33	0.35–0.71
Al-1.2wt.%Pb	Upward and Downward	Droplet, fiber, interphase spacing, diameter	0.11–0.33	0.36–0.77
Al-2.1wt.%Pb	Upward-Silva et al. [34]	Fiber, interphase spacing	0.19	0.84
Al-2.5wt.%Pb	Upward-Freitas [33]	Fiber, interphase spacing	0.15	0.62
Al-5.5wt.%In	Upward-Silva et al. [27]	Droplet, interphase spacing, diameter	0.12–0.13	0.50–0.66

Table 3. Values of the constant *k* got and respective correlation coefficients for the spacing/diameter versus position function found for the experiments carried out with the alloys of the Al-Bi, Al-Pb, and Al-In systems.

Alloy	Type of solidification device	Function	R ²
Al-Bi	Upward and Downward	$\lambda = 0.15.(P)^{0.5}$	0.48–0.82
Al-Pb	Upward	$\lambda = 0.33.(P)^{0.5}$	0.54–0.67
	Downward	$\lambda = 0.23.(P)^{0.5}$	0.37–0.71
Al-In	Upward	$\lambda = 0.13.(P)^{0.5}$	0.33–0.65

Table 4. Adjusted values of the function got and respective correlation coefficients for the spacing/diameter versus position function found for the experiments carried out with the alloys of the Al-Bi, Al-Pb, and Al-In systems.

Figure 3 highlights the behavior of the solidification processes of the ingots, highlighting the morphology got in each alloy system and emphasizing the behavior of the spacing and particle diameters that resulted in the proposed law.

The graph in **Figure 4** shows the values of the interphase spacings and the droplet diameters, respectively, as a function of the growth rate, for all monotectic structures analyzed. A parallel behavior is observed between the resulting curves of the experiments. Thus, the growth law $\lambda = k (v)^{-2.1}$ could be established.

Table 5 presents the condensed values of *k* obtained for the best coefficient of determination found in each case, separated by alloy and morphology. Observing the tables, it could be noted that no coefficient of determination was in the range considered of weak effect (under 0.3), being the majority in the range of moderate effect (0.3–0.7) and some in the strong effect range (above 0.7), which is considered a satisfactory result considering the number of experiments analyzed. Once again, the lower values of determination coefficients were found for the downward experiments, which could be justified because of the intense convective flow that occurs on these cases and for fibrous morphologies, which are more irregular.

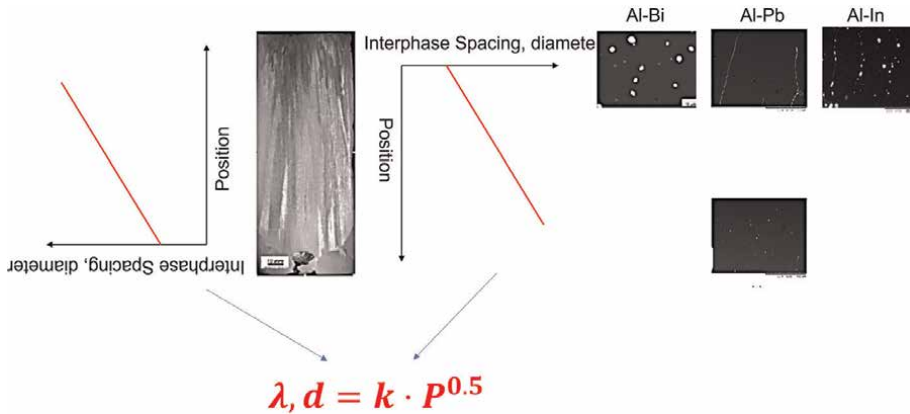


Figure 3. Schematic representation of the behavior of solidified alloys, which resulted in the proposed law.

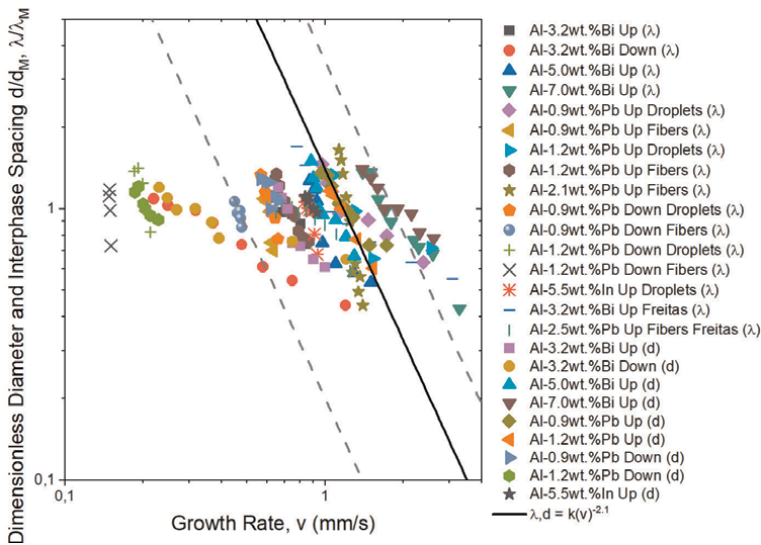


Figure 4. Evolution of droplet diameters and interphase spacings of the droplet and fiber structures as a function of growth rate for all analyzed alloys.

Considering that the results were more acceptable for the formulation of a growth law as a function of position for monotectic alloys and the position from the metal/mold interface of the ingots is directly related to the cooling rate of the alloys, a growth law as a function of the cooling rate can be quite adequate, a parameter that has not yet been directly considered in the formulations of monotectic growth laws. Even so, the results are acceptable both by visual analysis and by the values of the coefficient of determination.

When droplets occur, the values of k obtained for both spacing and diameter are remarkably close (except for the Al-3.2 wt.%Bi alloy solidified in the upward vertical device). This indicates that they can be represented by a single function.

Table 6 shows the new values of k obtained for each situation, including for the situation where more discrepant k values were obtained, showing that, when droplet

Alloy	Type of solidification device	Structure, parameter	k	R ²
Al-3.2wt.%Bi	Upward and downward	Droplet, interphase spacing, diameter	0.07–1.89	0.30–0.78
Al-5.0wt.%Bi	Upward	Droplet, interphase spacing, diameter	0.92–1.10	0.74–0.75
Al-7.0wt.%Bi	Upward	Droplet, interphase spacing, diameter	3.10–3.20	0.56–0.76
Al-0.9wt.%Pb	Upward and downward	Droplet, fiber, interphase spacing, diameter	0.20–1.40	0.33–0.73
Al-1.2wt.%Pb	Upward and downward	Droplet, fiber, interphase spacing, diameter	0.02–1.60	0.34–0.85
Al-2.1wt.%Pb	Upward	Fiber, interphase spacing	1.80	0.33
Al-2.5wt.%Pb	Upward	Fiber, interphase spacing	0.54	0.30
Al-5.5wt.%In	Upward	Droplet, interphase spacing, diameter	0.72–0.80	0.56–0.63

Table 5. Values of the constant k obtained and the respective coefficients of determination for the interphase spacing/droplet diameter as a function of the growth rate found for the experiments performed with the alloys of the Al-Bi, Al-Pb, and Al-In systems.

structure occur, a single function can be established in each experiment to represent the correlation between spacing and diameter with growth rate. No other correlation between k values was observed.

As well as in the previous analysis, **Figure 5** highlights the behavior of the solidification processes of the ingots, highlighting the morphology got in each alloy system and emphasizing the behavior of the spacing and particle diameters that resulted in the proposed law.

In their results, [20] was able to correlate the results obtained for the evolution of the interphase spacing to the growth rate with the relation proposed by [23], $\lambda = C \cdot (v)^{-0.5}$, only for occurrence of the droplet structure. The relationship proposed by [15], $\lambda = C \cdot G^a \cdot v^b$, was valid for cases of occurrence of fiber and droplet morphologies; however, that study is limited to cases of solidification in the upward vertical device.

In the other cases, different power functions were obtained $\lambda = a \cdot (V)^{-b}$, with b reaching the following values: -2.2 for the occurrence of fibers in the upward vertical solidification [20]; -2 and -6.5 for the occurrence of droplets and fibers in the downward vertical solidification, respectively [29].

The results show that, contrary to what some authors have assumed [4, 14, 17, 24, 51] the growth of a monotectic alloy is not like eutectic, because although two phases grow side by side simultaneously, the thermocapillary effect acts in some cases, making the law proposed by [23] not valid. In their studies, [14] had already shown this fact when they developed their model for monotectic behavior, as well as [52], also in the development of their model.

Silva et al. [6] found power-type functions to evaluate the evolution of the particle diameter as a function of the solidification growth rate but with different exponent values as following: -0.4 for the solidification of Al-3.2% Bi alloy in a downward vertical device and -1.5 for the same alloy solidified in an upward vertical device. Silva et al. [7, 20, 36] also found power-type functions to express the particle

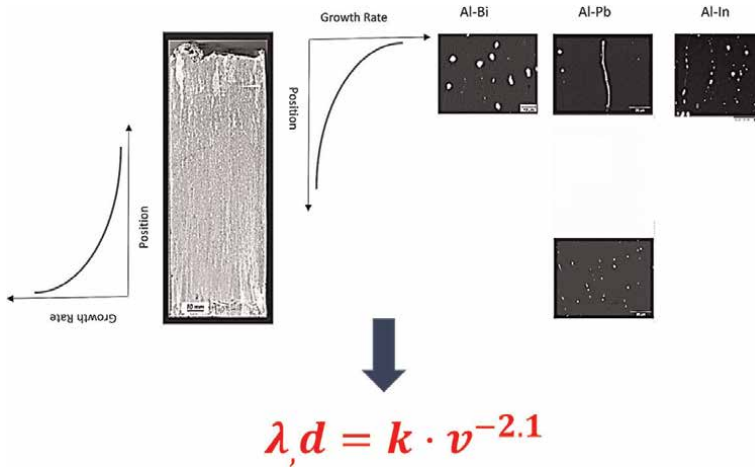


Figure 5. Schematic representation of the behavior of solidified alloys, which resulted in the second proposed law.

Alloy	Type of solidification device	k	R ² (λ)	R ² (d)
Al-3.2wt.%Bi	Upward	0.65	0.39	0.39
Al-3.2wt.%Bi	Downward	0.07	0.34	0.30
Al-5.0wt.%Bi	Upward	1.01	0.72	0.74
Al-7.0wt.%Bi	Upward	3.15	0.75	0.55
Al-0.9wt.%Pb	Upward	1.40	0.57	0.73
Al-0.9wt.%Pb	Downward	0.40	0.65	0.49
Al-1.2wt.%Pb	Upward	1.45	0.46	0.72
Al-1.2wt.%Pb	Downward	0.04	0.57	0.46
Al-5.5wt.%In	Upward	0.76	0.52	0.47

Table 6. Adjusted values of the constant *k* obtained and the respective coefficients of determination for the interphase spacing/droplet diameter as a function of the growth rate found for the experiments performed with Al-Bi, Al-Pb, and Al-In system alloys when the droplet morphology occurs.

diameter as a function of growth rate of many alloys from monotectic systems and a single exponent value, -1.5 , was found for all alloys solidified in an upward vertical device.

According to the obtained results in this study, it is possible to establish a single law for growth for monotectic structures, which ratifies the growth mechanism proposed by [52]. These authors have developed a model based on the approximation of Hunt and Jackson for eutectics systems, which emphasize that as one of the phases concomitantly growing is a liquid, convection must have prominent role in total mass transport above the monotectic interface. Thus, the shape of the interface is particularly important for the flow field and the concentration field in front of the phase boundaries and, therefore, cannot assume a planar solidification front without surface convection.

The growth law proposed in this study ($\lambda = k \cdot (V)^{-2.1}$) was applied to the data obtained by [42]. The value found for *k* was 25. The coefficient of determination, $R^2 =$

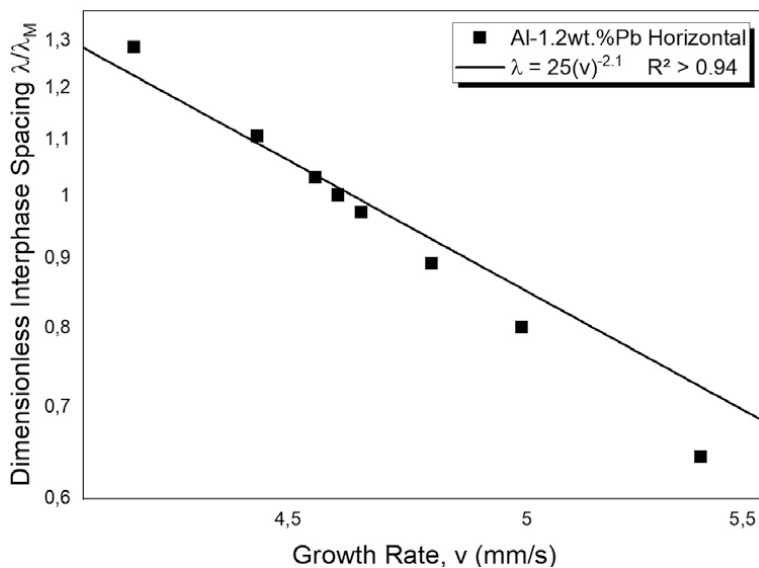


Figure 6. Evolution of interphase spacing of the droplet structure as a function of growth rate for Al –1.2 wt.% Pb alloy solidified under transient conditions in a horizontal directional device.

0.94, was in the very strong intensity range (above 0.9), showing that the law proposed in this work can also be applied to the growth of binary monotectic alloys solidified in horizontal devices (**Figure 6**). The K value extremely higher than the ones found for other heat extraction configurations ratifies the evidence of a strong flow convection on this type of device.

From the results of this analysis, it was observed that growth based on the solidification growth rate leads to a single growth law, $\lambda = k \cdot v^{-2.1}$, and it is supposed that the analysis of the growth for monotectic systems can be extended for different situations, as for solidification experiments in steady state, for example.

4. Conclusions

Based on the results of the investigations carried out throughout this work, added to the comparisons made, and having as reference the other studies in the literature on the subject, the following major conclusions are derived from the present study:

1. When taking the values of spacing versus position and diameter versus position for the alloys studied, a single experimental law could be proposed, as $\lambda = k \cdot (P)^{0.5}$, with no coefficient of determination found in the range considered as “weak intensity,” which is satisfactory, given the number of experiments analyzed.
2. When the values of λ and d versus v for the alloys studied were taken, a single experimental law could be established, in the form $\lambda = k (v)^{-2.1}$. Again, no coefficient of determination was found in the range considered as “weak effect,” which is considered satisfactory considering the number of experiments analyzed. For this case, it has been found that both spacings and droplet diameters can be represented by a single function.

3. The growth of a monotectic alloy is not analogous to the eutectic one, because although two phases grow side by side simultaneously, the thermocapillary effect acts in some cases, making the law proposed by Hunt and Jackson not valid for monotectic growth.
4. The proposed law was found to be applicable on monotectic horizontal transient solidification allowing to suppose that the function may be valid for the analysis of the growth for monotectic alloys for different situations, such as solidification experiments in steady state, for example.
5. Obtaining a single law of growth for all cases shows that the mechanism of formation and growth of structures in monotectic systems appears to be the set between the effects of Marangoni thermosolutal convection and coupled repulsive diffusion, regardless of morphology and/or of the solidification front.

Acknowledgements

The authors acknowledge the financial support provided by UFPA (Federal University of Pará), CAPES (Coordination of Superior Level Staff Improvement), and CNPq (The Brazilian Research Council), Brazil, grant 400634/2016-3.

Author details

Adrina Silva^{1*}, José Braga², Paulo Monteiro Jr³, Cassio Silva⁴, Camila Konno⁴, Thiago Costa⁵ and Emmanuelle Feitosa⁶

1 Federal University of Pará, Belém, Brazil

2 Federal Institute of Amazonas, Manaus, Brazil

3 Federal University of Uberlândia, Uberlândia, Brazil


4 State University of Campinas, Campinas, Brazil

5 Federal Institute of Pará, Belém, Brazil

6 Federal University of South and Southeast of Pará, Marabá, Brazil

*Address all correspondence to: mariaestillac@gmail.com

IntechOpen

© 2022 The Author(s). Licensee IntechOpen. This chapter is distributed under the terms of the Creative Commons Attribution License (<http://creativecommons.org/licenses/by/3.0>), which permits unrestricted use, distribution, and reproduction in any medium, provided the original work is properly cited. 

References

- [1] Ratke L, Diefenbach S, Drees S, Alkemper J, Prinz B, Romero A, et al. Multi-droplet marangoni motion in immiscible Al-Si-Bi alloys—Results of a d-2 experiment. *Advanced Space Research*. 1995;**16**(7):185-190. DOI: 10.1016/0273-1177(95)00157-a
- [2] Phanikumar G, Dutta P, Galun R, Chattopadhyay K. Microstructural evolution during remelting of laser surface alloyed hyper-monotectic al-bi alloy. *Materials Science and Engineering A*. 2004;**371**:91-102. DOI: 10.1016/j.msea.2003.09.071
- [3] Wang N, Wei B. Phase separation and structural evolution of undercooled Fe-Sn monotectic alloy. *Materials Science and Engineering A*. 2003;**345**:145-154. DOI: 10.1016/S0921-5093(02)00471-9
- [4] Ratke L, Muller A. On the destabilisation of fibrous growth in monotectic alloys. *Scripta Materialia*. 2005;**54**:1217-1220. DOI: 10.1016/j.scriptamat.2005.07.044
- [5] Es F, Ap S, Je S, Lc C, Garcia A. Inter-relation of microstructural features and dry sliding wear behavior of monotectic Al–Bi and Al–Pb alloys. *Tribology Letters*. 2014;**55**(1): 111-120. DOI: 10.1007/s11249-014-0338-8
- [6] Silva A, Spinelli J, Garcia A. Microstructural evolution during upward and downward transient directional solidification of hypomonotectic and monotectic Al–Bi alloys. *Journal of Alloys and Compounds*. 2009;**480**(2):485-493. DOI: 10.1016/j.jallcom.2009.01.105
- [7] Silva AP, Spinelli JE, Mangelinck-Noël N, Garcia A. Microstructural development during transient directional solidification of hypermonotectic Al–Bi alloys. *Materials & Design*. 2010;**31**:4584-4591. DOI: 10.1016/j.matdes.2010.05.046
- [8] Ratke L. Theoretical considerations and experiments on microstructural stability regimes in monotectic alloys. *Materials Science and Engineering A*. 2005;**413-414**:504-508. DOI: 10.1016/j.msea.2005.08.195
- [9] Yasuda H, Ohnaka I, Fujimoto S, Sugiyama A, Hayashi Y, Yamamoto M, et al. Fabrication of porous aluminum with deep pores by using Al-In monotectic solidification and electrochemical etching. *Materials Letters*. 2004;**58**:911-915. DOI: 10.1016/j.matlet.2003.07.032
- [10] Yasuda H, Ohnaka I, Fujimoto S, Takezawa N, Tsuchiyama A, Nakano T, et al. Fabrication of aligned pores in aluminum by electrochemical dissolution of monotectic alloys solidified under a magnetic field. *Scripta Materialia*. 2006;**54**:527-532. DOI: 10.1016/j.scriptamat.2005.10.059
- [11] Costa T, Dias M, Freitas E, Casteletti L, Garcia A. The effect of microstructure length scale on dry sliding wear behaviour of monotectic Al-Bi-Sn alloys. *Journal of Alloys and Compounds*. 2016;**689**: 767-776. DOI: 10.1016/j.jallcom.2016.08.051
- [12] Wang X, Guo W, Fu Y. High-entropy alloys: Emerging materials for advanced functional applications. *Journal of Materials Chemistry A*. 2021;**9**:663-701. DOI: 10.1039/D0TA09601F
- [13] Zhang Y. *High-Entropy Materials*. [S.L.]: Springer; 2019

- [14] Grugel R, Hellawell A. Alloy solidification in systems containing a liquid miscibility gap. *Metallurgical Transactions A*. 1981;**1981**(12A): 669-681. DOI: doi.org/10.1007/BF02649742
- [15] Carlberg T, Bergman A. On the formation of irregular monotectic structures. *Scripta Metallurgica*. 1985;**19**: 333-336. DOI: 10.1016/0036-9748(85)90325-4
- [16] Kaukler W, Rosemberger F, Curreri P. In situ studies of precipitate formation in Al-Pb monotectic solidification by X-ray transmission microscopy. *Metallurgical and Materials Transactions A*. 1997;**28**:1705-1710. DOI: 10.1007/s11661-997-0262-8
- [17] Yang S, Liu W. Effects of transverse magnetic field during directional solidification of monotectic Al-6,5wt%Bi alloy. *Journal of Materials Science*. 2001; **36**:5351-5355. DOI: 10.1023/A:1012467817033
- [18] An J, Shen X, Lu Y, Liu YB. Microstructure and tribological properties of Al-Pb alloy modified by high current pulsed electron beam. *Wear*. 2006;**261**:208-215. DOI: 10.1016/j.wear.2005.09.014
- [19] Ozawa S, Motegi T. Solidification of hyper-monotectic Al-Pb alloy under microgravity using a 1000-m drop shaft. *Materials Letters*. 2004;**58**: 2548-2552. DOI: 10.1016/j.matlet.2004.03.027
- [20] Silva A, Garcia A, Spinelli J. Microstructure morphologies during the transient solidification of hypomonotectic and monotectic Al-Pb alloys. *Journal of Alloys and Compounds*. 2011;**509**:10098-10104. DOI: 10.1016/j.jallcom.2011.08.049
- [21] Konno C, Vasconcelos A, Barros A, Silva A, Rocha O, Spinelli J. Analysis of the microstructural evolution during the transient upward, downward and horizontal directional solidification of the Al-1.2wt%Pb Monotectic Alloy. *Materials Science Forum (Online)*. 2016; **896**:429-434. DOI: 10.4028/www.scientific.net/MSF.869.429
- [22] Freitas E, Spinelli J, Casteletti L, Garcia A. Microstructure-wear behavior correlation on a directionally solidified Al-In monotectic alloy. *Tribology International*. 2013;**66**:182-186. DOI: 10.1016/j.triboint.2013.05.009
- [23] Hunt J, Jackson K. Binary eutectic solidification. *Transactions of the Metallurgical Society of AIME*. 1967;**236**: 1129-1142
- [24] Derby B, Favier J. A criterion for the determination of monotectic structure. *Acta Metallurgica, Elmsford*. 1983;**31**: 1123-1130. DOI: 10.1016/0001-6160(83)90208-0
- [25] Kamio A, Tezuka H, Kumai S, Takahashi T. Unidirectional solidification structure of Al-In monotectic alloys. *Transactions of the Japan Institute of Metals*. 1984;**25**: 569-574. DOI: 10.2320/matertrans1960.25.569
- [26] Silva A, Spinelli J, Garcia A. Thermal parameters and microstructure during transient directional solidification of a monotectic Al-Bi alloy. *Journal of Alloys and Compounds*. 2009;**475**:347-351. DOI: 10.1016/j.jallcom.2008.07.021
- [27] Silva A, Goulart P, Spinelli J, Garcia A. Microstructural evolution during the directional transient solidification of a hypomonotectic Al-0.9wt%Pb Alloy. *Materials Science Forum (Online)*. 2012;**730-732**:829-834.

DOI: 10.4028/www.scientific.net/
MSF.730-732.829

[28] Silva A, Goulart P, Garcia A, Spinelli J. Microstructural development during transient directional solidification of a hypomonotectic Al-In alloy. *Philosophical Magazine Letters (Print)*. 2012;**92**:442-450. DOI: 10.1080/09500839.2012.685962

[29] Silva A, Freitas E, Spinelli J, Garcia A, Goulart P. On the growth of the minority phase during downward transient directional solidification of hypomonotectic and monotectic Al-Pb alloys. *Journal of Materials Science*. 2012; **47**:5581-5589. DOI: doi.org/10.1007/s10853-012-6450-y

[30] Rocha O, Costa T, Dias M, Garcia A. Cellular/dendritic transition, dendritic growth and microhardness in directionally solidified monophasic Sn-2%Sb alloy. *Transactions of Nonferrous Metals Society of China*. 2018;**28**: 1679-1686. DOI: 10.1016/S1003-6326(18)64811-3

[31] Costa T, Freitas E, Dias M, Brito C, Cheung N, Garcia A. Monotectic Al-Bi-Sn alloys directionally solidified: Effects of Bi content, growth rate and cooling rate on the microstructural evolution and hardness. *Journal of Alloys and Compounds*. 2015;**653**: 243-254. DOI: 10.1016/j.jallcom.2015.09.009

[32] Dias M, Costa T, Rocha O, Spinelli J, Cheung N, Garcia A. Interconnection of thermal parameters, microstructure and mechanical properties in directionally solidified Sn-Sb lead-free solder alloys. *Materials Characterization*. 2015;**106**: 52-61. DOI: 10.1016/j.matchar.2015.05.015

[33] Goulart P, Cheung N, Garcia A. The effects of cell spacing and distribution of

intermetallic fibers on the mechanical properties of hypoeutectic Al Fe alloys. *Materials Chemistry and Physics*. 2010; **119**:272-278. DOI: 10.1016/j.matchemphys.2009.08.063

[34] Freitas E. Desenvolvimento de Correlações entre Microestruturas de Solidificação e Resistências ao Desgaste e à Corrosão. [doctoral thesis]. Campinas: State University of Campinas; 2013

[35] Wang S, Zang Y. Shear-band spacing controlled by Bridgman solidification in Dendrite/BMG composites. *Science in China Series G: Physics, Mechanics, and Astronomy*. 2009;**52**(10):1632-1636. DOI: 10.1007/s11433-009-0237-4

[36] Silva A, Garcia A, Spinelli J. Microstructural morphologies and experimental growth laws during solidification of monotectic and hypermonotectic Al-Pb alloys. *Journal of Materials Science & Technology*. 2014; **30**(4):401-407. DOI: 10.1016/j.jmst.2013.10.027

[37] Braga F, Silva A, Silva A, Spinelli J, Garcia A. Lei de crescimento de parâmetro microestrutural para ligas monotéticas à base de alumínio. *Semina. Ciências Exatas e Tecnológicas (Online)*. 2016;**37**:35. DOI: 10.5433/1679-0375.2016v37n1p35

[38] Rodgers J, Nicewander A. Thirteen ways to look at the correlation coefficient. *The American Statistician*. 1988;**42**(1):59-66. DOI: 10.1080/00031305.1988.10475524

[39] Schober P, Boer C, Schwarte A. Correlation coefficients. *Anesthesia & Analgesia*. 2018;**126**(5):1763-1768. DOI: 10.1213/ANE.0000000000002864

[40] Silva A. Solidificação transitória de ligas dos sistemas monotéticos Al-Bi,

- Al-Pb e Al-In [doctoral thesis].
Campinas: State University of Campinas;
2011
- [41] Silva A. Solidificação transitória de ligas hipomonotética e monotéticas do sistema Al-Bi [master's thesis].
Campinas: State University of Campinas;
2008
- [42] Konno C. Caracterização da liga monotética al-1,2%Pb solidificada em regime transitório: propriedades microestruturais, microdureza e usinabilidade [master's thesis]. Belém: Federal University of Pará; 2015
- [43] Kenney J, Keeping E. Mathematics of Statistics, Pt. 1. 3rd ed. Princeton: Van Nostrand; 1962. pp. 252–285
- [44] Seltman J. Experimental Design and Analysis (PDF). 2018. p. 227
- [45] Rodgers J, Nicewander W. The American Statistician. 1988;42(1):59-66
- [46] Dowdy S, Wearden S. Statistics for Research. Wiley; 1983. ISBN 0-471-08602-9. p. 230
- [47] Fonseca J, Martins G. Curso de estatística. 4ª ed. São Paulo: Atlas; 1993
- [48] Wonnacott T, Wonnacott, J. Introductory Statistics. New York. John Wiley & Sons; 1990
- [49] Santos W, Brito C, Quaresma J, Spinelli J, Garcia A. Plate-like cell growth during directional solidification of a Zn-20wt.%Sn high-temperature lead-free solder alloy. Materials Science and Engineering B. 2014;182:29-36. DOI: 10.1016/j.mseb.2013.11.016
- [50] Reis E. Estatística Descritiva. 2ª ed. Lisboa: Edições Sílabo; 1994
- [51] Chadwick G. Monotectic solidification. British Journal of Applied Physics, London. 1965;16:1095-1097
- [52] Stocker C, Ratke L. A new Jackson-Hunt model for monotectic composite growth. Journal of Crystal Growth, Amsterdam. 1999;203:582-593

High Entropy Thin Films by Magnetron Sputtering: Deposition, Properties and Applications

Mohamed El Garah, Frederic Schuster and Frederic Sanchette

Abstract

Surface coating is of a great interest to increase the performances of the materials and extend its lifetime. High entropy films (HEFs) become the hot spot for developing surface engineering applications due to their good performances. They are reported to have superior properties such as good corrosion, wear resistance and excellent high temperature oxidation. Various deposition techniques have been exploited to fabricate HEFs such as laser cladding, spraying, sputter deposition and electrochemical deposition. These techniques are known to be an easy process to achieve a rapid quenching. Magnetron sputtering is seen as the most efficient methods to deposit the HEFs. Different gas can be used to prepare the ceramic materials. Besides, the deposition parameters reveal a strong influence on the physicochemical properties of HEFs. Working pressure, substrate temperature, bias voltage and gas mixture flow ratios have been reported to influence the morphology, microstructure, and functional properties of HEFs. The chapter overviews the development of the recent HEFs prepared by magnetron sputtering technique. First, it describes the principal of the technique. Then, it reports the classes of HEFs followed by the effect of the deposition parameters on their different properties. Applications have been developed using some HEFs for biomaterials and machining process.

Keywords: high entropy films, magnetron sputtering, corrosion, oxidation

1. Introduction

Conventional alloys are usually based on one main element. To improve the structural and functional properties of the alloy, other elements can be added. However, this strategy leads to the formation of several phases. Indeed, physical metallurgy and phase diagrams show that multifunctional alloys can develop dozens of structures with several phases. Structurally, they can be fragile, and scientifically their analysis will be difficult. On the other hand, high entropy alloys (HEAs) [1, 2] are characterized by high mixing entropy. Therefore, they have become primordial structures for developing potential applications tanks to their superior properties.

HEAs materials are characterized by four effects: high entropy, severe lattice distortion, slow scattering and the cocktail effect. They are detailed in the reference [3]. Excellent properties of HEAs have been reported such as outstanding thermal stability [4], good wear resistance [5], good corrosion resistance [6] and best oxidation resistance [7].

On the other hand, the surface is seen as an important component of the material for developing industrial applications. It can be easily modified and adapted to improve the performance of the materials according to demanding conditions. Thus, the quality of the material surface has a significant impact on its lifetime. Thin films are found in many applications with improved surface properties for high-performance materials. For example, tools used in machining are often coated with protective and hard thin films to achieve high mechanical properties and better wear resistance [8–10]. Better physical properties such as a good oxidation resistance are also required for aerospace and automotive applications. Protective films can also be found in biomedical applications such as bio-implants [11, 12]. Review articles have been reported on the effect of process parameters on the phase structure of HEFs with also a discussion on the preparation process and the functional properties of the films [13]. Others have been focused on the development of HEAs/HEFs operating in extreme conditions and other characteristics [14–16].

Magnetron sputtering is a widely used technique to deposit thin films. It is used in several industrial applications. This technology has been continuously developed to improve the target utilization and increase the deposition rates by reducing operating costs. Preparing high entropy films (HEFs) by this technique is of considerable interest to provide coatings with superior properties. To this end, several research works report on the development of coatings with improved performances but with low-cost materials. Conventional hard coatings, such as traditional nitrides and carbides, have shown the potential to increase wear resistance. However, these traditional materials seem to not meet the current needs. For example, some traditional nitrides have a limited oxidation resistance. Recently, HEFs have shown much improved performances. A comparison of different alloys is presented in the reference [17] where the oxidation resistance of an HEF reaches 1300°C. (AlCrNbTaTi)N HEF shows an oxidation resistance at 850°C for 100 hours [18] which is better than various traditional nitrides. Many HEFs, prepared by magnetron sputtering technique, revealed other excellent performances [19–22].

By using magnetron sputtering technique, various deposition parameters are exploited to control the properties of HEFs. Among these parameters, we find gas flow rate, substrate temperature, working pressure, and bias voltage. The chapter overviews magnetron sputtering process, the classes of different HEFs and it shed light on the effect of the different parameters on the properties of HEFs. Applications of some HEFs are also presented.

2. Magnetron sputtering deposition

There are several ways to prepare thin films. The most common methods used in research laboratories and in industry are PVD and CVD techniques. Among the PVD procedures, magnetron sputtering shows several advantages. It offers the possibility to obtain a stoichiometry like that of the used target. The quenching rate is high (10^9 K/s) leading to the formation of solid solutions. In the following paragraph, the process of the magnetron sputtering will be briefly introduced.

2.1 Direct current magnetron sputtering (DCMS) deposition

The synthesis of coatings by using magnetron sputtering technique can be done in three steps. In the first step, an atomic vapor is created by extracting the atoms from the target thanks to applied potential difference between the target and the reactor walls. Then this vapor is transferred to the substrate in a rarefied atmosphere of chemically neutral gas. In the last step, the atomic vapor condenses into the substrate surface allowing the germination process and consequently the growth of the film.

This basic process is limited by various effects like low deposition rate, low ionization coefficient in the plasma, and a substrate heat. To circumvent these limitations, a magnetron dispositive is integrated into the process. The magnets are placed behind the cathode. They generate a magnetic field parallel to the surface of the target, perpendicular to the electric field. The electrons emitted by the cathode and present in the gas and are trapped by the field lines (**Figure 1**). The probability that an electron meets argon is so high. The ion bombardment of the target results in a higher sputtering rate and the deposition rate increases.

2.2 High power impulse magnetron sputtering (HiPIMS) deposition

The difference between the High Power Impulse Magnetron Sputtering (HiPIMS) and DCMS is the use of high power densities. HiPIMS is a recent advance in sputtering process using magnetron sputtering with a high voltage power source. High voltage with short duration is used to generate high-density plasma resulting in high degree of ionization of the coating material. HiPIMS, has various advantages. The highly energetic ions, produced by high voltage, result in denser film compared to that deposited by conventional techniques. HiPIMS bombards the sample with high-energy gas ions that can remove oxides and therefore clean the surface. This can improve the adhesion of the coating to the surface. A description of plasma process using HiPIMS can be found in Anders's tutorial [23].

Few studies have been reported in the literature on using HiPIMS to prepare the HEFs. The papers revealed the formation of dense microstructures of the films compared to that obtained by DCMS process. The change of the microstructure

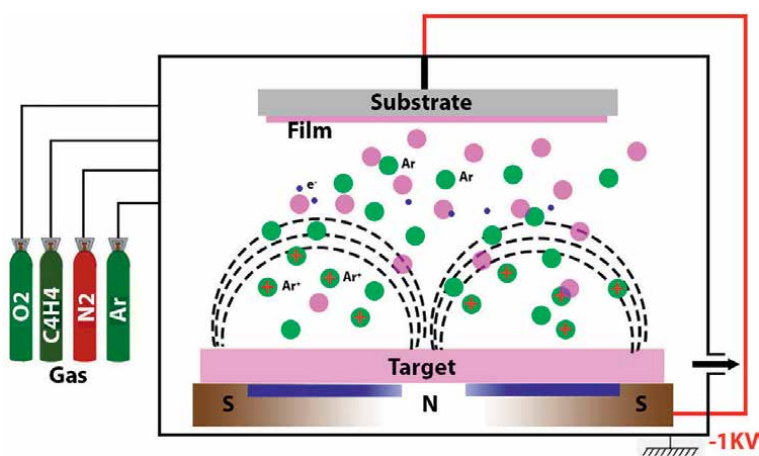


Figure 1.
Magnetron sputtering process.

strongly influences the mechanical and electrochemical performances of HEFS. For example, Bachani and co-workers [24] investigated (TiZrNbTaFe)N using HiPIMS process and found that the film containing 32 at.% of nitrogen exhibits a very dense microstructure compared to others. Its hardness is improved (36.2 GPa). The corrosion resistance is increased, according to the variation of the nitrogen content, due to the densification of the films. CuNiTiNbCr dual-phases were formed at different working pressures as reported by Li and co-workers [25]. AlCrTiVZr HEFs have been studied under the effect of nitrogen. Due to its densification, the nitride obtained at 12 sccm presents a hardness of 41.8 GPa which is the super-hard film compared to others. **Figure 2** presents SEM images showing the difference in the morphology of (AlCrNbSiTiV)N films obtained by both processes DCMS (**Figure 2a,b**) and HiPIMS (**Figure 2c,d**) [26].

3. HEFs classes

HEFs can be classified into three categories: metallics, ceramics and composites films as presented in **Figure 3**.

Metallic HEFs: they consist basically of Cantor-based elements. They are mostly composed of transition elements such as Al, Cr, Fe, Ti, Mo, etc. Refractory elements are also used to develop coatings for high-temperature applications. The refractory elements, such as Hf, Ta, Nb, V, W, etc have much higher melting point. These materials are classified into HfNbTaZr, CrMoNbTa [27].

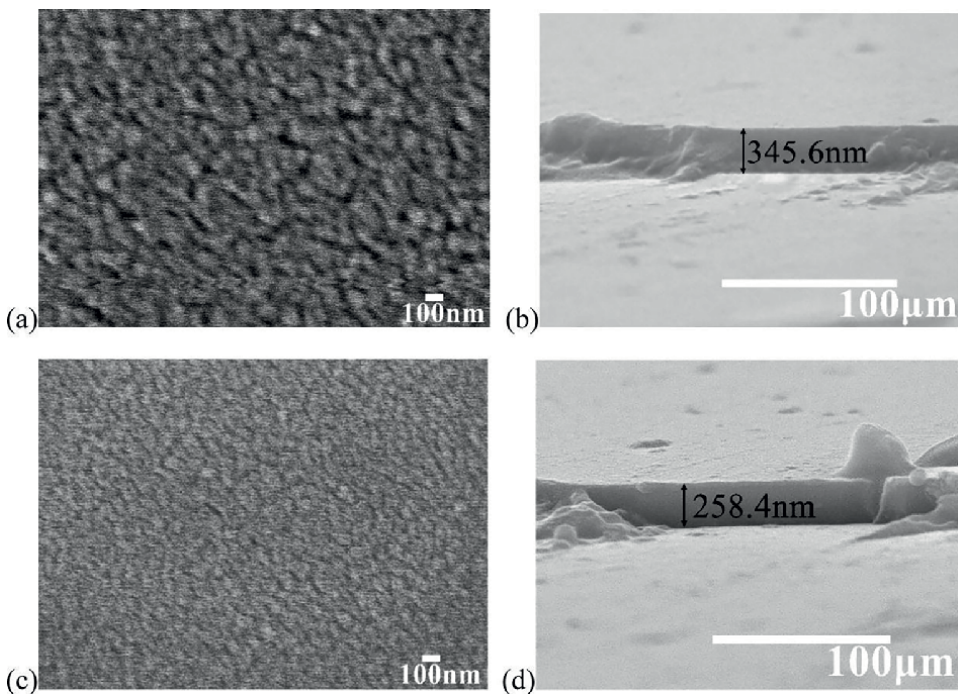


Figure 2. SEM images showing the surfaces and cross-sectional microstructure of (AlCrNbSiTiV)N deposition using DCMS (a,b) and HiPIMS (c,d). The figure is reproduced with permission of [26].

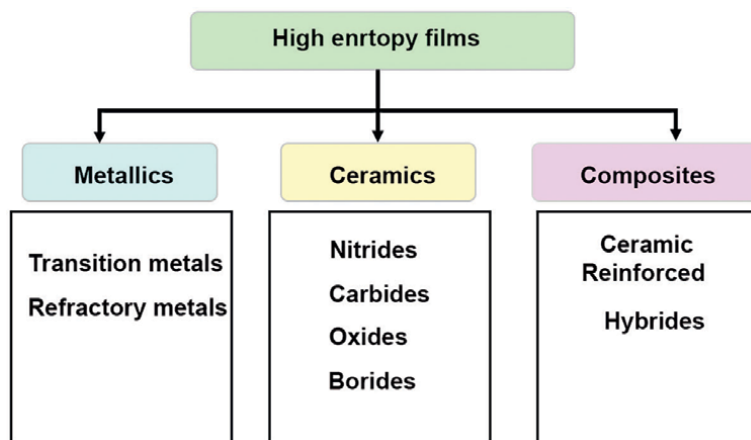


Figure 3.
Classes of HEFs.

Ceramic HEFs: consist of nitrides, carbides, oxides and borides. These materials can be deposited on substrates by using reactive mode (introduction of gas). Solid solutions are reported and strong nitride-, carbide-, oxide-forming elements like Zr, Cr, Si and Ti are used. These ceramics exhibit superior properties such as high oxidation resistance, good corrosion resistance and high tribological performances.

Composite HEFs: These materials can be prepared by reinforcing the film matrix with ceramics. Various ceramics like WC, TiC, NbC, and others have been used as reinforcements to improve the properties of HEFs. Metallic reinforcements have been also used. For example, Tian and co-workers [28] prepared a compact ACoCrniFeTi/Ni coating with Ni splats uniformly distributed in the matrix (ACoCrniFeTi). Due to this reinforcement, the results reveal an improvement in its tensile test compared to that of the matrix alone.

4. Properties of HEFs

4.1 Morphology and structural of HEFs

DCMS was largely used to prepare the HEFs under different conditions. The most-reported films have three different morphologies, columnar, dendrite-like and fibrous-like. The deposition parameters are reported to have a strong influence on the HEFs morphology. The mobility of particles into the surface of the substrate is the main reason of resulted morphology of the films. Studies have reported the effect of gas mixture on the films properties. Nitrogen, carbon and oxygen are used to form high entropy ceramics. For example, AlCrNbYZr exhibits dendrite-like morphology. By adding the nitrogen (AlCrNbYZr)N films reveal V-shaped columnar morphology. Zhang et al. [29] studied the effect of nitrogen on CrNbTiAlV films. Smooth surface and dense cross-sectional morphology are observed in the metallic film (CrNbTiAlV). With addition of the nitrogen, (CrNbTiAl)N gradually changes into columnar morphology. Some carbides show a different trend. Jhong et al. [21] studied CrNbSiTaZr as a function of CH₄ flow rate. They show that all films exhibit smooth surface and featureless cross-sectional morphology. The mobility of the atoms on

the surface can be the main reason for the formation of dense structures. Oxygen gas also influences the morphology of HEFs. In the case of AlCoCrCu0.5FeNi, the films exhibit agglomerated grains at a low oxygen flow rate. However, as the oxygen flow increases the grains become equiaxed with a size of 35 nm.

The morphology of HEFs can be also influenced by other parameters like the pressure and the bias voltage. AlCrTiWNbT shows a columnar morphology when the bias voltage changes from -50V to -100V but at -150V fine spaced striation lines are formed of the film [30]. Fine fibers morphology is formed for CrNbSiTiZr at -50V which is transformed to compact at -200V [31].

For the structure, the prepared HEFs by magnetron sputtering are reported to have amorphous or crystalline structure. The most crystalline structures exhibit fcc solid solution. The structure can change under the effect of various parameters such as the high entropy and the atomic mismatch. The high entropy promotes the formation of the solid solution instead of metallics compounds. However, if the difference in atomic mismatch is enough, the film remains amorphous. In the case of HEFs by magnetron sputtering, three different structures are reported: amorphous, fcc and bcc. AlCoCrNi [32], NbTiAlSiZr [33] and FeCoNiCuVZrAl [34] HEFs exhibit an amorphous structure which remains unchangeable even after adding the nitrogen. On the other hand, other studies revealed the phase transformation from amorphous to crystalline structure upon increasing the nitrogen contents in the films. Cheng et al. [22] examined the effect of nitrogen on AlCrMoTaTiZr by varying its flow rate from 0% to 50%. The percentage of the flow rate is calculated according to argon quantity by the followed formula $R_N = N_2 / (Ar + N_2)$. The results show that the film exhibits an amorphous structure at $R_N = 0\%$. However, when the nitrogen flow increases fcc-single phases structures are formed as is presented the **Figure 4**.

The nitrogen atoms are adsorbed in interstitial sites leading to the formation of nitrides. The interaction between the nitrogen and the elements varies along with the periodic table. Group 4–6 are strong nitride former while metals in group 7–11 are weakly nitride former. This interaction has a mix of ionic, metallic and covalent bonding. The reported HEFs nitrides have NaCl-type structure as mentioned above. Because of the similarities of the structure between different standard nitrides, extended homogeneity regions for solid solutions can be obtained.

Among other ceramics, carbides can be also prepared. Up to now, they have not been widely investigated like the nitrides. Most references focus on the use of strong carbide forming metals. Kuang et al. have investigated the tribological properties of CrNbTiMoZr carbide films [35]. Kao and co-workers studied the effect of carbon content on the mechanical and electrochemical properties of CrNbSiTaZr films [36]. There is also others few studied on the same subject [21, 37]. **Figure 5** shows XRD diffractograms of (CrNbSiTiZr)_x films as a function of CH₄ rate flow. In the case of carbides, textured solid solutions are also formed. (111), (200), (220) and (311) peaks of the prepared films reveal the formation of fcc NaCl-type structure (**Figure 5**).

4.2 Surface chemistry of HEFs

X-ray photoelectron spectroscopy (XPS) is a powerful technique to provide information on the composition and the chemical binding between the elements. Up to date, few XPS analysis are reported on HEFs studies. More efforts are needed to provide more information on the binding nature and the compound of different elements constituting HEFs.

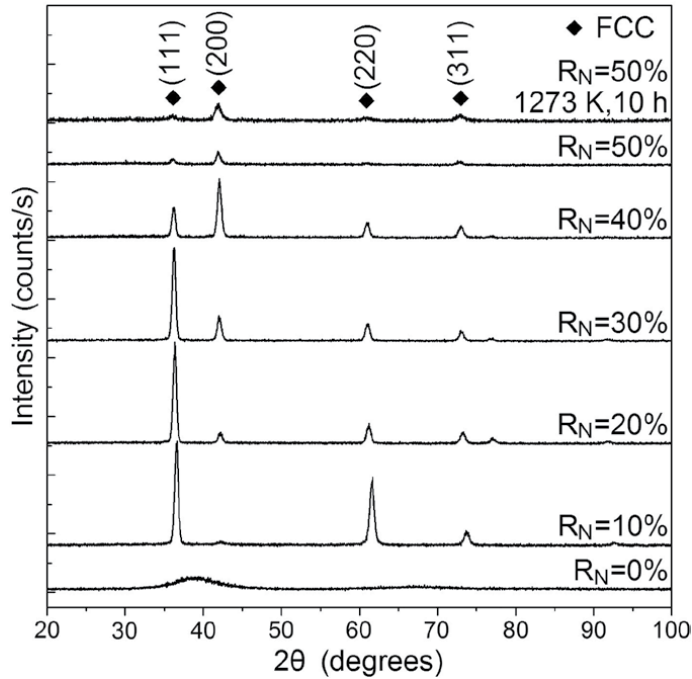


Figure 4. X-ray diffractogramme of $(AlCrMoTaTiZr)N$ as function of nitrogen flow rate (N_2). The figure is reproduced with permission of [22].

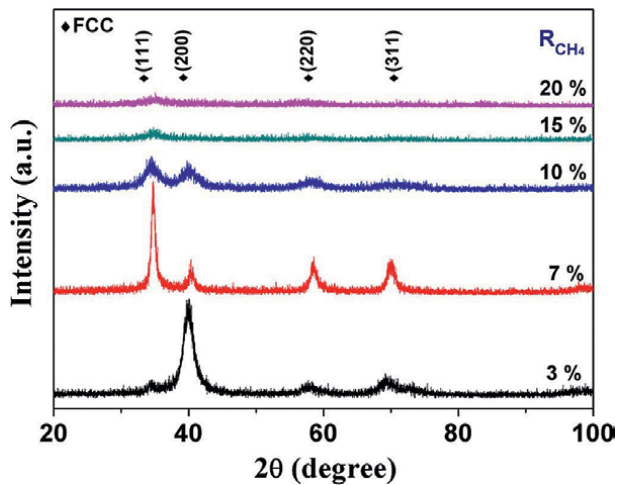


Figure 5. X-ray diffractogramme of $(CrNbSiTiZr)C_x$ as function of nitrogen flow rate (N_2). The figure is reproduced with permission of [21].

Khan et al. [38] examined $AlCoCrCu_{0.5}FeNi$ nitride films by XPS. They showed that the porosity of films grows with a higher nitrogen flow fraction facilitating than the atmospheric oxidation. XPS analysis confirmed the formation of protective oxides AlO_3 , CrO_3 and nitrides AlN and CrN on the films surfaces [38].

Khan and co-workers [38] used XPS to determine the oxidation states of AlCoCrCu_{0.5}FeNi HEFs. The films were deposited at various nitrogen flow rates. The results revealed the formation of both nitrides and oxides on the surface of the films. At higher nitrogen flow, binary oxides Al₂O₃ and Cr₂O₃ were formed together with nitrides AlN and CrN on the films surfaces. Feng and coworkers [39] studied (ZrNbTaTiW)N HEFs and reported by XPS the formation of a mixture of metallic (Nb, W, Ta), nitride (ZrN, TiN, TaN) and oxide ZO₂.

Our group studied the nitridation effect on AlTiTaZrHf, prepared by the magnetron sputtering technique [40]. All the elements are nitride after adding the nitrogen. As the nitrogen flow rate increases, the nitride content changes according to the affinity of each element. The atomic percentage is estimated according to XPS analysis and is presented for each individual element in **Figure 6**. Both metal Ta and Hf show a quick increase of nitridation followed by quasi-stable evolution when $R_{N_2} = N_2 / (N_2 + Ar)$ increases from 0 to 50%. Al and Zr elements show a weak increase of nitridation followed by quasi-stable evolution when R_{N_2} continues to grow. However, Ti reveals a quasi-stable formation of nitride even though R_{N_2} increases (**Figure 6**). The results demonstrate that all the elements are nitride during the deposition leading to the formation of high entropy nitride films.

4.3 Mechanical properties

The mechanical properties have been investigated for large amounts of HEFs and the results revealed an improvement in the materials' performances. Indeed, good hardness and wear resistance make the HEFs as well as their nitrides promising candidates for cutting tools for example. HEFs prepared by the magnetron sputtering

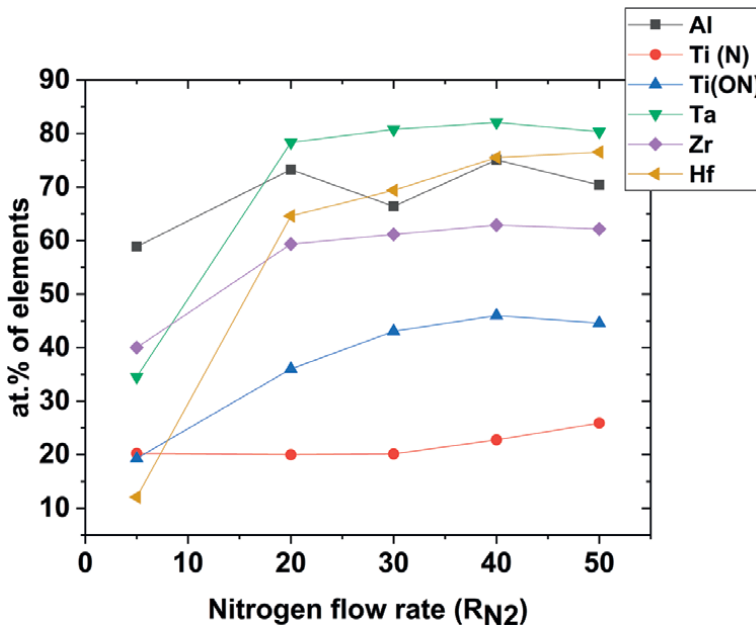


Figure 6. Atomic percentage of individual elements, Al, Ti, Ta, Zr, and Hf as a function of nitrogen flow rate $R_{N_2} = N_2 / (N_2 + Ar)$ during the preparation of AlTiTaZrHf(-N) HEFs. The curves are presented according to XPS analysis.

technique showed that the mechanical properties are influenced by various deposition parameters. For example, Yu and co-workers [31] studied CrNbSiTiZr by changing the substrate bias voltage. The results showed that the hardness increased at a maximum of 12.4 ± 0.3 GPa with -50 V bias followed by a decrease to 9.8 ± 0.2 GPa when the bias is -200 V. Young's modulus shows the same trend by increasing at 187.7 ± 3.3 GPa for -100 V and a decreasing to 162.3 ± 3.7 GPa for -200 V. The working pressure is also another parameter influencing the mechanical properties of HFEs. Kim and co-workers [32] reported high mechanical properties of AlCoCrNi films obtained with a pressure of 1.33×10^{-1} Pa. Indeed, at low pressure (1.33 Pa), the hardness is measured at 8.9 ± 0.9 GPa and the modulus at 142 ± 11 GPa. However, when the pressure reaches 1.33×10^{-1} Pa, the hardness increase to 16.8 ± 0.5 GPa and the modulus to 243 ± 39 GPa.

The nitrides show an increasing of mechanical properties as the nitrogen flow rate increases followed by a decrease as the flow continues to increase. This trend is seen for various high entropy nitrides [29, 41–44]. An example is presented in **Figure 7a**. (AlCrMoTaTiZr)N HEFs, obtained with 40% nitrogen flow ratio, is the hardest film compared to others with a hardness of 40 GPa with Young's modulus higher than 370 GPa. Residual stresses have been also studied and their evolution is depending on the nitrogen content. Zhang and co-workers [29] investigated the residual stress of (CrNbTiAlV)N HEFs at different nitrogen flows. The result is presented in **Figure 7b**. The metallic film has the lowest value of -2.35 GPa while a maximum (-6.55 GPa) is obtained for the nitride at 38 sccm.

In the case of oxides, as the oxygen flow rate increases the microstructure became dense and consequently the mechanical properties are improved. At a high flow rate, these properties degrade. The hardness of AlCoCrCu_{0.5}FeNi reaches the maximum (11.3 ± 0.9 GPa) at 25% of O₂ and decreases as the flow continues to increase.

Other results show that this trend is not always true. Khan and co-workers [45] reported no change in the mechanical properties by studying AlCoCrCu_{0.5}FeNi films. These later are prepared as a function of the working pressure. Their hardness was measured at 13 GPa while Young's modulus was evaluated at 204 GPa and no change was revealed as the pressure increased.

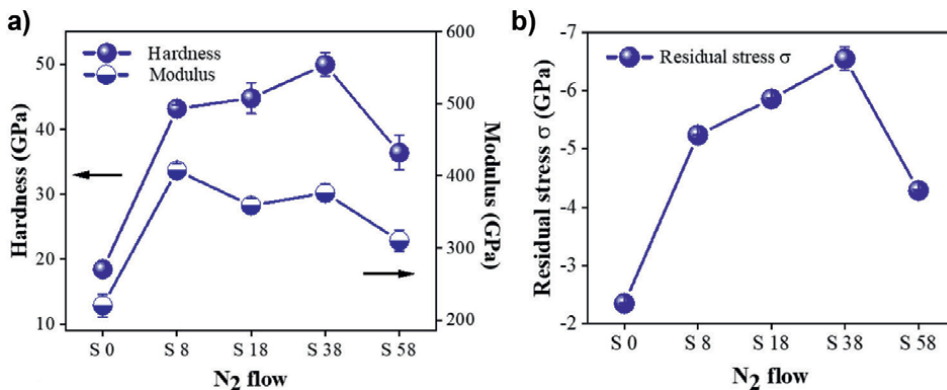


Figure 7. Hardness (a) and Residual stress (b) of (CrNbTiAlV)Nx films deposited under different nitrogen flows. Figure reproduced with permission from [29].

4.4 Tribological performances

The change in microstructure could be the result of several factors such as preferential orientation and variation in crystallite size. These phenomena improve the tribological performance of HEFs. The presence of defects can also prevent plastic flow during deformation in the material that can change its hardness. The change in the hardness will lead to a change in its tribological properties.

The tribological performance of (AlCrNbSiTiMo)N has been studied by Lo and co-workers [46] at ambient temperature and after annealing at 700°C. The results showed a decrease in the friction coefficient, especially after annealing. This reduction difference in the coefficient of friction was measured at 0.2. At room temperature, the coefficient was 0.68 ± 0.09 while after annealing at 700°C it became 0.48 ± 0.08 as shown in **Figure 8**. The result revealed an improved wear resistance due to the formation of MoO₃ after annealing, which acts as a lubricating effect.

By changing the content of the elements, the tribological properties can be improved. For example, the effect of Al was studied by Cui and co-workers [47] on FeCoCrNiMnAl_x alloy. As the Al content increases, the friction coefficient of these films decreases. On the other hand, the incorporation of carbon, producing a lubricating effect can also reduce the friction coefficient [35].

4.5 Corrosion

Corrosion is described as a physical-chemical interaction between a metal and its environment leading to changes in its properties and significant degradation of its function. Developing corrosion-resistant materials is a necessary need to resolve the issue and improve their performance. Due to the elevated entropy, HEFs form solid solutions rather than intermetallic compounds. This makes the materials with best functional properties. The corrosion of HEFs has been mostly studied in nitric acid, salt (NaCl) and in HCl. It has been reported that Cr, Ni, Co and Ti elements can improve the corrosion resistance in acid solution. Mo element could inhibit pitting corrosion in a solution containing Cl. Such phenomena have been carried out for

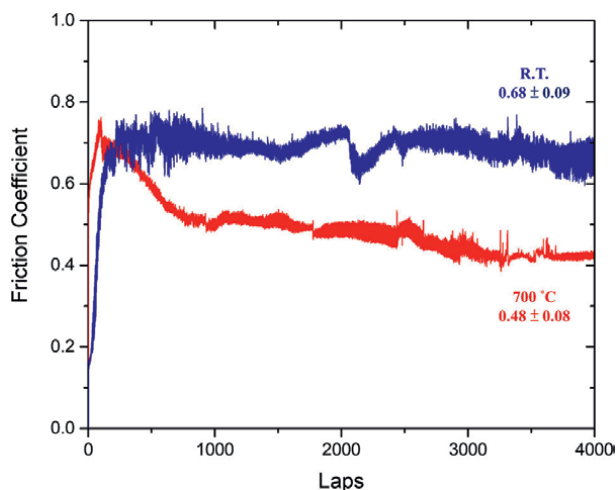


Figure 8. Friction Coefficient of the AlCrNbSiTiMoN coatings. Figure reproduced with permission from [46].

HEFs prepared by magnetron sputtering. The results revealed that these properties are influenced by different deposition parameters. To carry out the electrochemical measurements of the films, potentiodynamic polarization tests are used. The parameters include corrosion potential (E_{corr}), pitting potential (E_{pit}) and corrosion-current density (I_{corr}). This later can be used to estimate the corrosion rate as described by the equation below [48]:

$$\text{Corroion rate} \left(\frac{\text{mm}}{\text{year}} \right) = 3.27 \times 10^{-3} \times \frac{I_{\text{corr}}}{\rho} \times EW \quad (1)$$

Where ρ is the density of the alloys (g/cm^3), I_{corr} ($\mu\text{A/cm}^2$) and EW present the equivalent weight given by:

$$EW = \left(\sum \frac{n_i f_i}{W_i} \right)^{-1} \quad (2)$$

n_i , f_i and W_i are the i th elements, the masse fraction and the atomic weight of i th element in the alloy respectively.

Anti-corrosion performance of (CrNbTaTiW)C has been studied by Malinovskis and co-workers [19] in HCl solution with a concentration of 1M. The results revealed that the carbides showed the best corrosion resistance compared to that Stainless Steel. Gao and co-workers [49] performed a deposition of (CoCrFeNiAl_{0.3}) on silicon by using magnetron sputtering. The films show better corrosion resistance compared to austenitic 304L stainless steel. Wang and a coworker [50] studied corrosion behavior of AlCoFeNiTiZr HEFs in NaCl solution. Three coatings, (Fe-Co-Ni)₂₅(Al-Ti-Zr)₇₅, (Fe-Co-Ni)₂₀(Al-Ti-Zr)₈₀, (Fe-Co-Ni)₁₅(Al-Ti-Zr)₈₅ have been tested. According to the reported results, (Fe-Co-Ni)₂₅(Al-Ti-Zr)₇₅ exhibits the lowest I_{corr} and the highest E_{corr} revealing its best corrosion resistance compared to other films. Wang and co-worker [37] investigated the electrochemical properties of (CrNbSiTiZr)C in a 3.5 wt% NaCl solution. **Figure 9** presented the potentiodynamic polarization curves of the film. The result is compared to that of 304L stainless steel (SS). The study reported that (CrNbSiTiZr)C shows a E_{corr} of -189 mV and I_{corr} of $0.0026 \mu\text{A/cm}^2$. E_{corr} is higher and I_{corr} is smaller than that of 304L SS ($E_{\text{corr}} = -319$ mV; $I_{\text{corr}} = 0.13 \mu\text{A/cm}^2$). Th result then reveal that (CrNbSiTiZr)C exhibits a higher corrosion resistance compared to that of 304L SS.

The change in composition (variation in the elements contents) influences the microstructure. Therefore, the change of the microstructure will improve the functional properties such as corrosion resistance. Wang and co-workers [50] reported an improved corrosion resistance of (Fe-Co-Ni)_x(Al-Ti-Zr)_{100-x} as a result of the increase in Fe-Co-Ni content. As a result, (FeCoNi)₂₅(AlTiZr)₇₅ showed a better corrosion performance. The addition of Al in the refractory HEF films VNbMoTaW was beneficial in terms of increasing the corrosion resistance. With 2.37 at.% of Al present in the alloy, excellent corrosion resistance was measured compared to 304 stainless steels in 0.5M of H₂SO₄ [51]. However, increasing the Al content can have a negative effect on the quality of the film. Indeed, at high Al content porous oxides can be formed and the pores can easily facilitate the diffusion of acid. As a result, the corrosion resistance decreases.

Other deposition parameters strongly influence the anticorrosion performance of HEFs. Kao and co-workers [36] reported an improved corrosion resistance of

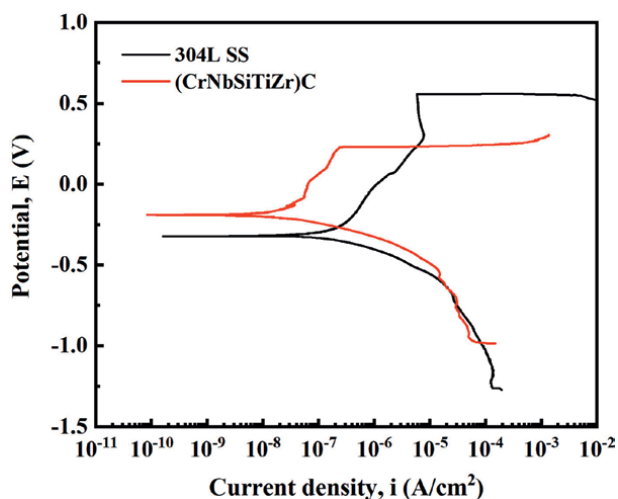


Figure 9. Potentiodynamic curve of (CrNbSiTiZr)C in 3.5 wt% NaCl solution. Figure reproduced with permission from [37].

CrNbSiTaZr films. The films were prepared in a C_2H_2 containing environment. Varying the bias voltage can also change the properties of the films. Von Fieandt and co-workers [52] showed a better corrosion resistance of $(AlCrNbYZr)N_x$ films compared to stainless steel. The electrochemical measurements were done in HCl by changing the polarization voltage and the temperature.

4.6 High temperature oxidation

Various HEFs have been prepared to investigate their high-temperature oxidation behavior. $(Al_{0.34}Cr_{0.22}Nb_{0.11}Si_{0.11}Ti_{0.22})_{50}N_{50}$ HEFs have been annealed at $900^\circ C$ for 50 hours [17]. Two different oxides were formed: $\alpha-Al_2O_3$ and rutile- TiO_2 . The dense Al_2O_3 formed on the top layer of the films was a key reason to improve their oxidation resistance. Compared to traditional films TiN and TiAlN prepared under the same conditions, $(Al_{0.34}Cr_{0.22}Nb_{0.11}Si_{0.11}Ti_{0.22})_{50}N_{50}$ HEFs reveal the best oxidation resistance and can be potential candidates for developing high-temperature applications. The element content is one of the influencing parameters that can improve the oxidation resistance of the films. Indeed, Al and Si can lead to the formation of dense $\alpha-Al_2O_3$ and $\alpha-SiO_2$ layers on HEFs at high temperature which improves their oxidation resistance. The oxidation behavior of $(AlCrNbTaTi)N$ films, in air as a function of Si concentration, was reported by Kretschmer and co-workers [18]. The films were annealed at $850^\circ C$ for 100 hours. Without Si, the oxide thickness of the film is important (2700 nm), however when Si was added the oxide thickness was measured at 280 nm. This means that Si forms a dense layer on the surface during the oxidation preventing then the diffusion of the oxygen in the film.

Tsai and co-workers [53] reported the same trend of Si effect. **Figure 10** shows the variation of the oxide thickness formed according to Si content in the films. As Si content increases, the thickness of oxide layer decreases revealing a good oxidation resistance at high temperature.

In the case of HfNbTaTiZr film HEFs, it was shown that oxygen reacted with all elements forming oxide nanoclusters. XPS was used to analyze the oxidation behavior

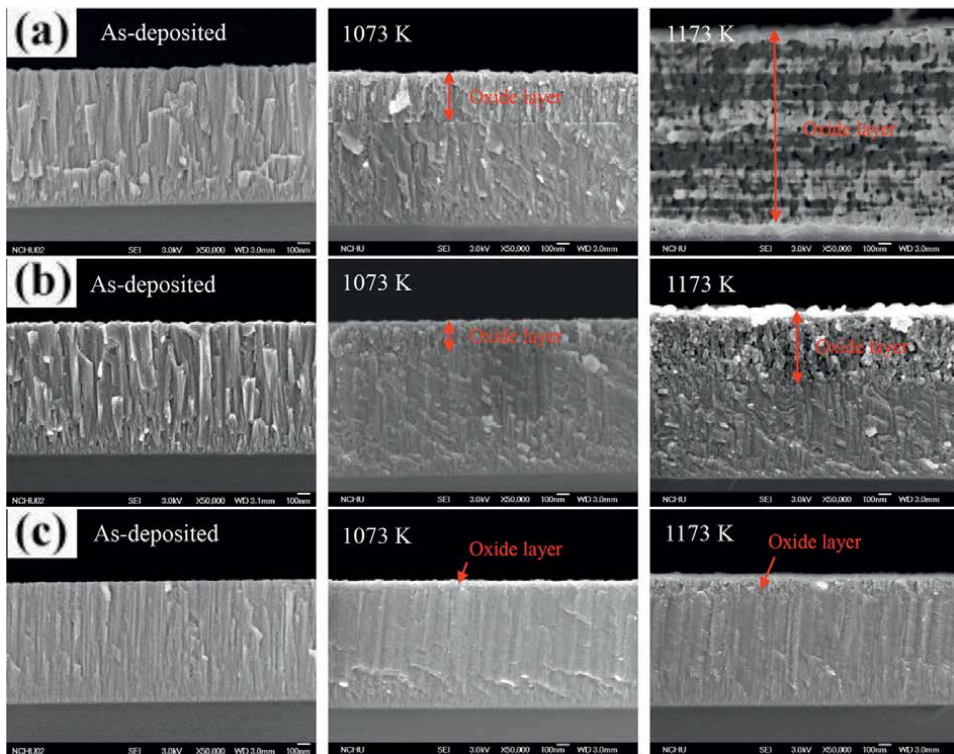


Figure 10. Cross-sectional SEM micrographs of the (AlCrMoTaTi)N HEFs with (a) 0 at.%, (b) 2.77 at.%, and (c) 7.51 at.% of Si coatings after annealing at different temperature in air. Figure reproduced with permission from [53].

and the results revealed 66 at.% of oxygen content where no oxide was determined by other techniques like SEM, TEM and X-ray diffraction [54]. The oxygen was found to preferentially bind to Ti, Zr and Hf rather than other elements.

5. Applications

HEFs deposited by magnetron sputtering techniques have been exploited to develop some applications. They can serve as surface protective materials. Among the different applications, materials for biomedical and for machining will be presented in this section.

5.1 Biomedical application

Various scientific research has been focused on coatings to improve the performance of implants and prostheses. Compared to traditional coatings using this field, HEFs become the hot spot in surface engineering development. Two films, (HfNbTaTiZr)N and (HfNbTaTiZr)C, have been prepared by magnetron sputtering technique [55]. The corrosion property of these films was simulated in body fluid. The results have revealed a very small ratio of dead cells that were observed for both (HfNbTaTiZr)N and (HfNbTaTiZr)C HEFs. Si was used to improve the

biocompatibility of the materials. Valdescu and co-workers [11] have replaced Ta with Si in the case of (TiZrNbTaHf)C. Considering the role of electrostatic interactions between the biomaterial surface and the cells, the authors examined the effects of surface charge (characterized by electrical potential and work function) on the biocompatibility property. A low electrical potential and high work function of (TiZrNbSiHf)C film was obtained revealing that this film exhibits best biocompatibility.

5.2 Machining application

The dry machining process is seen as the best alternative to replace the oils in the industry. Because the oils have a negative impact on both operator health and the ecology. An environmental transition is, therefore, necessary to develop clean processes. HEFs are now interesting materials where scientific efforts are underway to improve the performance of cutting tools. thermal and machining properties of $(Al_{0.34}Cr_{0.22}Nb_{0.11}Si_{0.11}Ti_{0.22})_{50}N_{50}$ HEF, have been examined by Shen and co-workers [56]. The cutting performances of the films are better as the milling was operating at a high temperature. Due to its superior properties like high hardness, good thermal stability and outstanding oxidation resistance, the HEF shows great potential to be exploited in machining applications. The study reported that, after 900 m of cutting, the wear depth is 226, 202, 184, and 175 μm for uncoated, TiN, TiAlN and $(Al_{0.34}Cr_{0.22}Nb_{0.11}Si_{0.11}Ti_{0.22})_{50}N_{50}$ HEF respectively.

6. Conclusion

The chapter reports and discusses briefly various properties of HEFs fabricated by magnetron sputtering. Intensive scientific efforts have been paid to this area for improving the materials surfaces and developing innovant materials. The preparation of the films is performed according to various deposition parameters.

Two processes are reported, standard direct current magnetron sputtering (DCMS) and high power impulse magnetron sputtering (HiPIMS) that are used to prepare HEFs in different environments. HiPIMS process led to the formation of denser microstructure compared to that with DCMS. Substrate bias voltage, working pressure, gas flow rate as deposition parameters, all are discussed and revealed that they strongly influence the physico-chemical properties of HEFs. Amorphous to crystalline structure of the most prepared HEFs transition took place upon introduction of gas like N_2 or CH_4 or O_2 .

Two functional properties, electrochemical (corrosion) and physical (oxidation) are reported and discussed. Th both properties have been reported to be influenced by different deposition parameters. The preparation of dense films prevents acid attack and improve corrosion resistance. The formation of some oxide layers such as $\alpha-Al_2O_3$ and $\alpha-SiO_2$ on the top film surface plays a great role in protecting the materials from oxidation at high temperature.

Some HEFs are exploited to develop application in the various materials field. Examples are reported on biomaterials and machining processes showing the best performances of the films compared to traditional coatings.

The prepared HEFs revealed enhanced surface protection ability. Even with the promising performances that possess the HEFs, more efforts are needed to develop a deep understanding of this class of materials. The complexity of the materials

increases with the number of possible combinations of elements. Traditional metallurgy cannot meet the requirements of quick results, which requires a lot of time depending on the combinations. Advanced characterization techniques are needed which must be combined with theoretical simulation to solve this type of problem. Artificial intelligence can also be added to the knowledge of traditional metallurgy to define new approaches for studying innovative HEFs.

Acknowledgements

Authors ME, FS and FSC thank the Université de Technologie de Troyes (UTT) and Commissariat à l'Energie Atomique et aux énergies alternatives (CEA) Saclay.

Conflict of interest

The authors declare no conflict of interest.

Author details

Mohamed El Garah^{1,2*}, Frederic Schuster³ and Frederic Sanchette^{1,2}

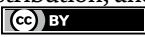
1 LASMIS, Laboratoire des Systèmes Mécaniques et d'Ingénierie Simultanée, Antenne de Nogent-52, Pôle Technologique de Sud-Champagne, Nogent, France

2 LRC CEA-LASMIS, Nogent International Center for CVD Innovation (NICCI), Pôle Technologique de Sud-Champagne, Nogent, France

3 Commissariat à l'Energie Atomique et aux énergies alternatives (CEA) Saclay, Gif-sur Yvette, France

*Address all correspondence to: mohamed.el_garah@utt.fr

IntechOpen

© 2022 The Author(s). Licensee IntechOpen. This chapter is distributed under the terms of the Creative Commons Attribution License (<http://creativecommons.org/licenses/by/3.0>), which permits unrestricted use, distribution, and reproduction in any medium, provided the original work is properly cited. 

References

- [1] Yeh JW, Chen SK, Lin SJ, Gan JY, Chin TS, Shun TT, et al. Nanostructured high-entropy alloys with multiple principal elements: Novel alloy design concepts and outcomes. *Advanced Engineering Materials*. 2004;**6**:299-303
- [2] Cantor B, Chang I, Knight P, Vincent A. Microstructural development in equiatomic multicomponent alloys. *Materials Science and Engineering: A*. 2004;**375**:213-218
- [3] Jien-Wei Y. Recent progress in high entropy alloys. *Annales de Chimie Science des Matériaux*. 2006;**31**:633-648
- [4] Wu Y, Cai Y, Wang T, Si J, Zhu J, Wang Y, et al. A refractory Hf₂₅Nb₂₅Ti₂₅Zr₂₅ high-entropy alloy with excellent structural stability and tensile properties. *Materials Letters*. 2014;**130**:277-280
- [5] Chuang M-H, Tsai M-H, Wang W-R, Lin S-J, Yeh J-W. Microstructure and wear behavior of Al_xCo₁₋₅CrFeNi₁₋₅Ti high-entropy alloys. *Acta Materialia*. 2011;**59**:6308-6317
- [6] Chen Y, Hong U, Shih H, Yeh J, Duval T. Electrochemical kinetics of the high entropy alloys in aqueous environments – A comparison with type 304 stainless steel. *Corrosion Science*. 2005;**47**:2679-2699
- [7] Ouyang D, Chen Z-j, Yu H-b, Chan K, Liu L. Oxidation behavior of the Ti₃₈V₁₅Nb₂₃Hf₂₄ refractory high-entropy alloy at elevated temperatures. *Corrosion Science*. 2022;**198**:110153
- [8] Guo F, Li K, Huang X, Xie Z, Gong F. Understanding the wear failure mechanism of TiAlSiCN nanocomposite coating at evaluated temperatures. *Tribology International*. 2021;**154**:106716
- [9] Bagdasaryan A, Pshyk A, Coy L, Kempniński M, Pogrebnjak A, Beresnev V, et al. Structural and mechanical characterization of (TiZrNbHfTa) N/WN multilayered nitride coatings. *Materials Letters*. 2018;**229**:364-367
- [10] Lu X, Zhang C, Wang C, Cao X, Ma R, Sui X, et al. Investigation of (CrAlTiNbV) N_x high-entropy nitride coatings via tailoring nitrogen flow rate for anti-wear applications in aviation lubricant. *Applied Surface Science*. 2021;**557**:149813
- [11] Vladescu A, Titorencu I, Dekhtyar Y, Jinga V, Pruna V, Balaceanu M, et al. In vitro biocompatibility of Si alloyed multi-principal element carbide coatings. *PLoS One*. 2016;**11**:e0161151
- [12] Codescu MM, Vladescu A, Geanta V, Voiculescu I, Pana I, Dinu M, et al. Zn based hydroxyapatite based coatings deposited on a novel FeMoTaTiZr high entropy alloy used for bone implants. *Surfaces and Interfaces*. 2022;**28**:101591
- [13] Yan X, Zhang Y. High-entropy films and compositional gradient materials. *Surface Technology*. 2019;**48**:98
- [14] Sharma A. High entropy alloy coatings and technology. *Coatings*. 2021;**11**:372
- [15] Duchaniya RK, Pandel U, Rao P. Coatings based on high entropy alloys: An overview. *Materials Today: Proceedings*. 2021;**44**:4467-4473
- [16] Li W, Liu P, Liaw PK. Microstructures and properties of high-entropy alloy

- films and coatings: A review. *Materials Research Letters*. 2018;**6**:199-229
- [17] Shen W, Tsai M, Tsai K, Juan C, Tsai C, Yeh J, et al. Superior oxidation resistance of (Al_{0.34}Cr_{0.22}Nb_{0.11}Si_{0.11}Ti_{0.22})_{50N50} high-entropy nitride. *Journal of the Electrochemical Society*. 2013;**160**:C531
- [18] Kretschmer A, Kirnbauer A, Moraes V, Primetzhofner D, Yalamanchili K, Rudigier H, et al. Improving phase stability, hardness, and oxidation resistance of reactively magnetron sputtered (Al, Cr, Nb, Ta, Ti) N thin films by Si-alloying. *Surface and Coatings Technology*. 2021;**416**:127162
- [19] Malinovskis P, Fritze S, Riekehr L, von Fieandt L, Cedervall J, Rehnlund D, et al. Synthesis and characterization of multicomponent (CrNbTaTiW) C films for increased hardness and corrosion resistance. *Materials & Design*. 2018;**149**:51-62
- [20] Liang S-C, Chang Z-C, Tsai D-C, Lin Y-C, Sung H-S, Deng M-J, et al. Effects of substrate temperature on the structure and mechanical properties of (TiVCrZrHf) N coatings. *Applied Surface Science*. 2011;**257**:7709-7713
- [21] Jhong Y-S, Huang C-W, Lin S-J. Effects of CH₄ flow ratio on the structure and properties of reactively sputtered (CrNbSiTiZr) C_x coatings. *Materials Chemistry and Physics*. 2018;**210**:348-352
- [22] Cheng K-H, Lai C-H, Lin S-J, Yeh J-W. Structural and mechanical properties of multi-element (AlCrMoTaTiZr) N_x coatings by reactive magnetron sputtering. *Thin Solid Films*. 2011;**519**:3185-3190
- [23] Anders A. Tutorial: Reactive high power impulse magnetron sputtering (R-HiPIMS). *Journal of Applied Physics*. 2017;**121**:171101
- [24] Bachani SK, Wang C-J, Lou B-S, Chang L-C, Lee J-W. Fabrication of TiZrNbTaFeN high-entropy alloys coatings by HiPIMS: Effect of nitrogen flow rate on the microstructural development, mechanical and tribological performance, electrical properties and corrosion characteristics. *Journal of Alloys and Compounds*. 2021;**873**:159605
- [25] Li Y, Wang C, Ma D, Zeng X, Liu M, Jiang X, et al. Nano dual-phase CuNiTiNbCr high entropy alloy films produced by high-power pulsed magnetron sputtering. *Surface and Coatings Technology*. 2021;**420**:127325
- [26] Chang K-S, Chen K-T, Hsu C-Y, Hong P-D. Growth (AlCrNbSiTiV) N thin films on the interrupted turning and properties using DCMS and HIPIMS system. *Applied Surface Science*. 2018;**440**:1-7
- [27] Miracle DB, Senkov ON. A critical review of high entropy alloys and related concepts. *Acta Materialia*. 2017;**122**:448-511
- [28] Tian L, Feng Z, Xiong W. Microstructure, microhardness, and wear resistance of AlCoCrFeNiTi/Ni₆₀ coating by plasma spraying. *Coatings*. 2018;**8**:112
- [29] Zhang C, Lu X, Wang C, Sui X, Wang Y, Zhou H, et al. Tailoring the microstructure, mechanical and tribocorrosion performance of (CrNbTiAlV) N_x high-entropy nitride films by controlling nitrogen flow. *Journal of Materials Science & Technology*. 2022;**107**:172-182
- [30] Zhao F, Song Z, Zhang G, Hou X, Deng D. Effects of substrate bias on

structure and mechanical properties of AlCrTiWNbTa coatings. *Surface Engineering*. 2013;**29**:778-782

[31] Yu X, Wang J, Wang L, Huang W. Fabrication and characterization of CrNbSiTiZr high-entropy alloy films by radio-frequency magnetron sputtering via tuning substrate bias. *Surface and Coatings Technology*. 2021;**412**:127074

[32] Kim YS, Park HJ, Lim KS, Hong SH, Kim KB. Structural and mechanical properties of AlCoCrNi high entropy nitride films: Influence of process pressure. *Coatings*. 2020;**10**:10

[33] Xing Q, Wang H, Chen M, Chen Z, Li R, Jin P, et al. Mechanical properties and corrosion resistance of NbTiAlSiZrNx high-entropy films prepared by RF magnetron sputtering. *Entropy*. 2019;**21**:396

[34] Liu L, Zhu J, Hou C, Li J, Jiang Q. Dense and smooth amorphous films of multicomponent FeCoNiCuVZrAl high-entropy alloy deposited by direct current magnetron sputtering. *Materials & Design*. 2013;**46**:675-679

[35] Kuang S, Wang J, Wang L, Huang W, Zhou Z. Improvement of the mechanical and the tribological properties of CrNbTiMoZr coatings through the incorporation of carbon and the adjustment of the substrate bias voltage. *Surface and Coatings Technology*. 2021;**412**:127064

[36] Kao W, Su Y, Horng J, Wu H. Effects of carbon doping on mechanical, tribological, structural, anti-corrosion and anti-glass-sticking properties of CrNbSiTaZr high entropy alloy coatings. *Thin Solid Films*. 2021;**717**:138448

[37] Wang J, Zhang H, Yu X, Wang L, Huang W, Lu Z. Insight into the structure and tribological and

corrosion performance of high entropy (CrNbSiTiZr) C films: First-principles and experimental study. *Surface and Coatings Technology*. 2021;**421**:127468

[38] Khan NA, Akhavan B, Zhou C, Zhou H, Chang L, Wang Y, et al. High entropy nitride (HEN) thin films of AlCoCrCu0.5FeNi deposited by reactive magnetron sputtering. *Surface and Coatings Technology*. 2020;**402**:126327

[39] Feng X, Tang G, Ma X, Sun M, Wang L. Characteristics of multi-element (ZrTaNbTiW) N films prepared by magnetron sputtering and plasma based ion implantation. *Nuclear Instruments and Methods in Physics Research Section B: Beam Interactions with Materials and Atoms*. 2013;**301**:29-35

[40] El Garah M, Touaibia DE, Achache S, Michau A, Sviridova E, Postnikov PS, et al. Effect of nitrogen content on structural and mechanical properties of AlTiZrTaHf(-N) high entropy films deposited by reactive magnetron sputtering. *Surface and Coatings Technology*. 2022;**432**:128051

[41] Li H, Jiang N, Li J, Huang J, Kong J, Xiong D. Hard and tough (NbTaMoW) Nx high entropy nitride films with sub-stoichiometric nitrogen. *Journal of Alloys and Compounds*. 2021;**889**:161713

[42] Chen R, Cai Z, Pu J, Lu Z, Chen S, Zheng S, et al. Effects of nitriding on the microstructure and properties of VAlTiCrMo high-entropy alloy coatings by sputtering technique. *Journal of Alloys and Compounds*. 2020;**827**:153836

[43] Chen L, Li W, Liu P, Zhang K, Ma F, Chen X, et al. Microstructure and mechanical properties of (AlCrTiZrV) Nx high-entropy alloy nitride films by reactive magnetron sputtering. *Vacuum*. 2020;**181**:109706

- [44] Cui P, Li W, Liu P, Zhang K, Ma F, Chen X, et al. Effects of nitrogen content on microstructures and mechanical properties of (AlCrTiZrHf) N high-entropy alloy nitride films. *Journal of Alloys and Compounds*. 2020;**834**:155063
- [45] Khan NA, Akhavan B, Zhou H, Chang L, Wang Y, Sun L, et al. High entropy alloy thin films of AlCoCrCu₀.5FeNi with controlled microstructure. *Applied Surface Science*. 2019;**495**:143560
- [46] Lo W-L, Hsu S-Y, Lin Y-C, Tsai S-Y, Lai Y-T, Duh J-G. Improvement of high entropy alloy nitride coatings (AlCrNbSiTiMo) N on mechanical and high temperature tribological properties by tuning substrate bias. *Surface and Coatings Technology*. 2020;**401**:126247
- [47] Cui Y, Shen J, Manladan SM, Geng K, Hu S. Wear resistance of FeCoCrNiMnAlx high-entropy alloy coatings at high temperature. *Applied Surface Science*. 2020;**512**:145736
- [48] Shi Y, Yang B, Liaw PK. Corrosion-resistant high-entropy alloys: A review. *Metals*. 2017;**7**:43
- [49] Gao L, Liao W, Zhang H, Surjadi JU, Sun D, Lu Y. Microstructure, mechanical and corrosion behaviors of CoCrFeNiAl_{0.3} high entropy alloy (HEA) films. *Coatings*. 2017;**7**:156
- [50] Wang H-D, Liu J-N, Xing Z-G, Ma G-Z, Cui X-F, Jin G, et al. Microstructure and corrosion behaviour of AlCoFeNiTiZr high-entropy alloy films. *Surface Engineering*. 2020;**36**:78-85
- [51] Bachani SK, Wang C-J, Lou B-S, Chang L-C, Lee J-W. Microstructural characterization, mechanical property and corrosion behavior of VNbMoTaWAl refractory high entropy alloy coatings: Effect of Al content. *Surface and Coatings Technology*. 2020;**403**:126351
- [52] von Fieandt K, Paschalidou E-M, Srinath A, Soucek P, Riekehr L, Nyholm L, et al. Multi-component (Al, Cr, Nb, Y, Zr) N thin films by reactive magnetron sputter deposition for increased hardness and corrosion resistance. *Thin Solid Films*. 2020;**693**:137685
- [53] Tsai D-C, Deng M-J, Chang Z-C, Kuo B-H, Chen E-C, Chang S-Y, et al. Oxidation resistance and characterization of (AlCrMoTaTi)-Six-N coating deposited via magnetron sputtering. *Journal of Alloys and Compounds*. 2015;**647**:179-188
- [54] Hruška P, Lukáč F, Cichoň S, Vondráček M, Čížek J, Fekete L, et al. Oxidation of amorphous HfNbTaTiZr high entropy alloy thin films prepared by DC magnetron sputtering. *Journal of Alloys and Compounds*. 2021;**869**:157978
- [55] Braic V, Balaceanu M, Braic M, Vladescu A, Panseri S, Russo A. Characterization of multi-principal-element (TiZrNbHfTa) N and (TiZrNbHfTa) C coatings for biomedical applications. *Journal of the Mechanical Behavior of Biomedical Materials*. 2012;**10**:197-205
- [56] Shen W-J, Tsai M-H, Yeh J-W. Machining performance of sputter-deposited (Al_{0.34}Cr_{0.22}Nb_{0.11}Si_{0.11}Ti_{0.22})_{50N50} high-entropy nitride coatings. *Coatings*. 2015;**5**:312-325

Optimization of Retained Austenite and Corrosion Properties on EN-31 Bearing Steel by Cryogenic Treatment Process

Shunmuga Priyan Murugan

Abstract

In this work, the percentage of retained austenite and corrosion rate presented on EN 31 bearing steel was identified by which cryogenic treatment processes. Further investigation carried out the possible mechanism brought in by which treatment has significantly improving the properties of the EN-31 bearing steel. The hardness values of CHT and DCT were compared by using the microstructure view of the CHT and DCT samples. The optimised cryotreated samples were prepared for metallographic examination as per ASTM E3-01. Then, the specimen were subjected to factor level settings such as cooling rate, soaking period, soaking temperature and tempering temperature at various conditions. Moreover, the precipitation of fine carbides and the transformation of retained austenite to martensite showed considerable variations in the hardness of the optimised DCT samples compared with the CHT samples. The mean hardness value of this sample is 861 HV and 19.20%, 847 HV and 17.25%, 838 HV and 17.10%, 857 HV and 18.40%, 790 HV and 13.45% improvement in the hardness compared with CHT.

Keywords: cryogenic treatment, EN 31 steel, retained austenite, corrosion, optimization

1. Introduction

EN-31 Bearing steel is a chromium-alloy steel, which is suitable for most applications such as bearing, plunger, barrel, etc. According to Ashish Bhateja et al. [1], the effect on the hardness of three sample grades of steel i.e. EN31, EN-8 and D3 after heat treatment processes such as annealing, normalising, hardening and tempering were conducted. According to their study after annealing specimen of EN31 it becomes softer than untreated specimen. After normalising hardness is more as compared to untreated specimen. Amey et al. [2], studied the effect of heat treatment on the degree of distortion due to phase transformation on 100Cr6 material. It was inferred that cooling rate plays a major role in decreasing distortion. It also

suggested that the presence of retained austenite, in the large amount, on the material can lead to distortion/.failure of the component. Sri Siva et al. [3], conducted a study to examine the effect of cryogenic treatment on the enhancement of wear resistance of 100Cr6 bearing steel. The study also aims to reveal the underlying mechanisms responsible for the enhancement of wear resistance by deep cryogenic treatment. It was found that the wear resistance was increased by 37% due to DCT when compared with that of conventional heat treatment (CHT). However, DCT may also be employed due to the increased benefits reported in terms of wear resistance and compressive residual stress compared with SCT. The presence of dimples and fractured surface are more in conventional heat treatment than the cryogenic treatment reported by Bensely et al. [4]. Author reported the carbon clusters increases during the heat treatment the carbide resulted improving wear resistance in the steels by Huang et al. [5]. Joseph Vimal et al. [6], conducted a Deep cryogenic treatment improves wear resistance of EN-31 steel. The bearing steel was selected and cryogenically treated to improve the physical properties of EN-31 steel. Before treatment EN-31 steel hardness is 18HRC hardness of untreated material is less. After done the heat treatments the hardness of the specimen is improved. Das et al. [7], the amount of carbide was decided the properties such as mechanical and wear resistance on D2 steel and also the carbide precipitation employed the behaviour of the steel materials. Harish et al. [8], conducted a comparative study of EN-31 bearing steel samples after CHT, SCT and DCT. The study reveals the presence of equi axed dimples and flat facets in the SCT specimen, micro cracks and wide ranged dimples in DCT specimen with respect to CHT samples. Hao-huai Liu et al. [9], investigated the characterisation on CrMnB high-chromium cast iron with the help of optical microscopy (OM), scanning electron microscopy (SEM) and X-ray diffraction (XRD), which can be improved due to the precipitation of carbides, the martensite transformation, and a refined microstructure resulting from cryogenic treatment [10]. The refrigeration of metals to improve their performance was generally classified as either shallow cryogenic treatment, sometimes referred to as subzero treatment, or deep cryogenic treatment (DCT) based on the treatment temperature. Fadare et al. [11], conducted an Effect of heat treatment on mechanical properties and micro structure of NST 37-2 steel. This study based upon the empirical study which means it is derived from experiment and observation rather than theory. The heat treatment operation is controlled heating and cooling rates but also determine microstructure and the grain size. The main aim of heat treatment is control the properties of a metal or alloy through the alternation of structure of metal or alloy. Harish S et al. [12], conducted a Micro structural study of cryogenically treated EN-31 bearing steel. The bearing steel was selected and cryogenically treated to improve the physical properties of EN-31 bearing steel. Before treatment EN-31 hardness is 18HRC hardness of untreated material is less. After done the heat treatments the hardness of the specimen is improved. Vadivel and Rangasamy [13], conducted Performance analysis of cryogenically treated coated carbide inserts. This performance analysis is produce micro structural view of two or more carbides. Images of micro structure taken at 50× magnification shows lot difference between conventional heat treatment and cryogenic treatment. Especially around the grain boundaries the fine precipitates carbides of size 0.1–0.3 micron. Based on the above literature survey, it was observed that the mechanical properties like hardness for the bearing steels. This paper has been carried out to study the effect and microstructure analysis of various heat treatments and cold treatment on EN-31 bearing steel and its influence on hardness of bearing steel.

2. Experimental investigation

2.1 Chemical composition

The optical emission spectroscopy (OES) was used to identify the chemical composition of the material. Moreover, the chemical composition was employed by using the spark analyser software to determining the weight percentage of the elements from the sample. Normally, the size of the specimen sized as per the standard used for the test is cylindrical, 20 mm in diameter and 10 mm in height. From the test which was identified the quantitative elements from the samples in ambient condition by optical spectrometer mentioned in the **Table 1**.

2.2 Experimental procedure

EN-31 bearing steel samples was machined as per ASTM standards for various mechanical tests. The experimental procedure adopted in the present work is shown in **Figure 1**. According to the flow chart, the composition of the raw material was analysed in optical emission spectroscopy (OES). The material considered for the study was obtained in the form of 6 mm diameter rod. The test was carried out separately for different treatments. Then the sample was subjected to conventional heat treatment and deep cryogenic treatment as per orthogonal array. Followed by the thermal treatment hardness test and microstructural study has been carried out. Finally the comparison of microstructure and the influence of the microstructure the hardness were studied.

2.3 Conventional heat treatment

The Conventional Heat treatment (CHT) was given to the EN31 bearing steel specimens as per the procedure prescribed in the ASM standards. The materials were subjected to hardening (austenitizing) at 850°C for 1 hour, followed by an oil quench, and tempered immediately after quenching at 200°C for 2 hours. The process graph for conventional heat treatment is shown in **Figures 2** and **3** respectively.

Figure 2 represented the procedure of conventional heat treatment on martensitic steels has employed at various heat treatment process starting from desired temperature at 850°C. The following quenching medium such as air, oil and water involve the martensitic steel which was decided the properties of steels behaviour. Moreover, the properties of steel tempered depend on the rapid cooling with various time and temperatures. The martensite steel surface became soft and ductile nature due to spheroidite dispersed present in materials during cryogenic treatment conditions. Most of the applications of steel materials resulted either pearlitic and bainitic nature during the production in lower cost. The EN 31 steels must tempered at microstructure of martensitic due to their significant brittleness. The microstructure and mechanical

Element	C	Mn	Si	S	P	Cr
Range (%)	0.95–1.10	0.25–0.40	0.15–0.35	<0.03	<0.03	1.40–1.70

Table 1.
Chemical composition of EN-31 bearing steel.

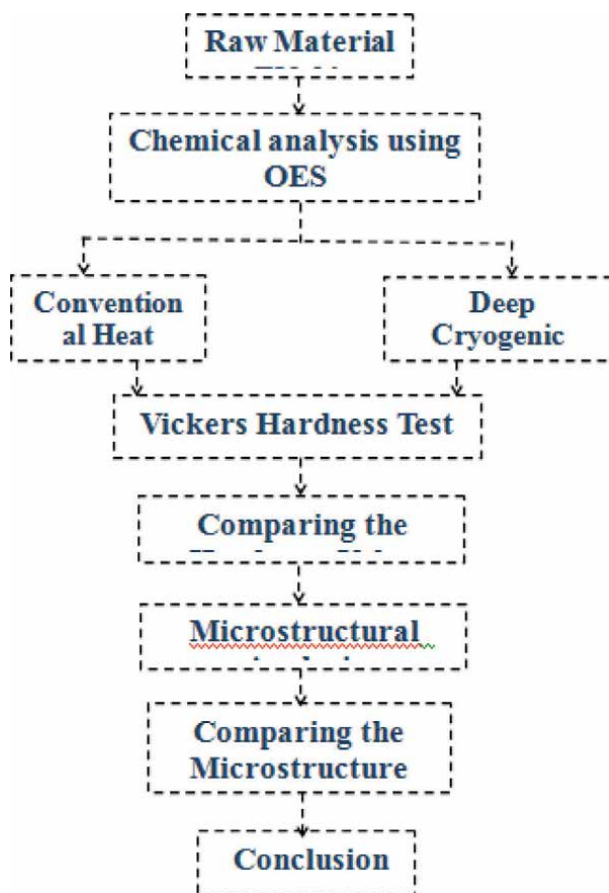


Figure 1.
Experimental procedure.

properties which are decided based on the elevated treatment and also being getting the retained of carbide in the materials. The samples revealed various microstructures such as Pearlite, Bainite and Martensite was decided the properties during the heat treatment process. The following heat treatment Annealing, Normalising, Quench Hardening, Tempering, and Austempering often used to change the properties of steels surface significantly. Moreover, the surface resulted solid strengthening also being desired the properties of the materials.

2.4 Deep cryogenic treatment

Deep cryogenic treatment was performed as per the factor level setting of the taguchi's OA. The chemical composition of the material should be confirmed by optical emission spectroscopy. Then the samples for mechanical testing were as machined as per the ASTM standard and the machined samples were subjected to hardening at 850°C for 1 hour, followed by a rapid oil quench, and treated in an A.C.I.CP-200vi cryogenic treatment processor (Applied Cryogenic Inc., Burlington, MA, USA) as required for the Taguchi orthogonal array. The cryogenic processor consists of a treatment chamber, which is connected to a liquid nitrogen tank through an insulated

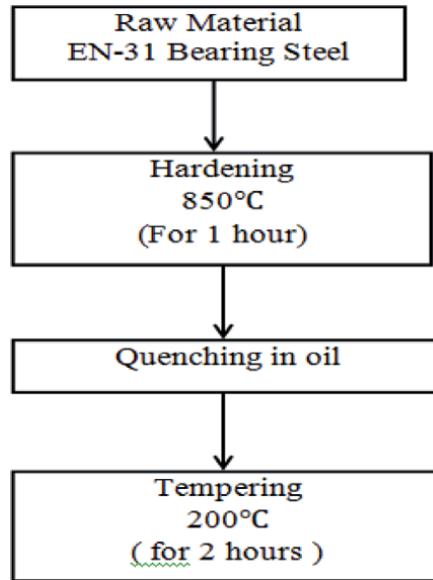


Figure 2.
Process chart for conventional heat treatment.

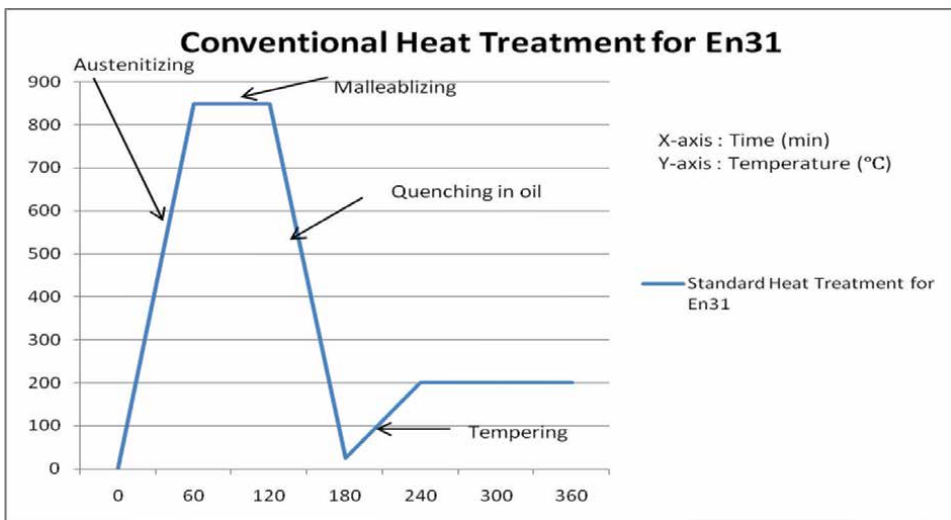


Figure 3.
Process graph for conventional heat treatment.

hose. The thermocouple inside the chamber senses the temperature, and accordingly the proportional –integral-derivative (PID) temperature controller operates the solenoid valve to regulate the liquid nitrogen flow. The liquid nitrogen passes through the spiral heat exchanger and enters the duct leading to the bottom of the chamber as nitrogen gas. The blower at the top of the chamber sucks the gas coming out at the bottom and makes it circulate inside the chamber. The programmable temperature controller of the cryogenic processor is used to set the cryogenic treatment parameters, as per the Taguchi orthogonal array. Following DCT, the samples were prepared

for 2 h and the performance characteristics of the samples were evaluated by conducting a reciprocating hardness test. At the time of the experiment, as per the Taguchi factor-level settings, three replications were performed for each test. The cryogenic processor consists of a treatment chamber, which is connected to a liquid nitrogen tank through an insulated hose. The thermocouple inside the chamber senses the temperature, and accordingly the proportional-integral-derivative (PID) temperature controller operates the solenoid valve to regulate the liquid nitrogen flow. The liquid nitrogen passes through the spiral heat exchanger and enters the duct leading to the bottom of the chamber as nitrogen gas. The blower at the top of the chamber sucks the gas coming out at the bottom and makes it circulate inside the chamber. The programmable temperature controller of the cryogenic processor is used to set the cryogenic treatment parameters, as per the Taguchi orthogonal array. Following DCT, the samples were prepared for 2 h and the performance characteristics of the samples were evaluated by conducting a reciprocating hardness test. At the time of the experiment, as per the Taguchi factor-level settings, three replications were performed for each test. DCT Process factors and their levels were shown in the **Tables 2 and 3**.

2.5 Specimen preparation and microstructure analysis

When grinding manually, the specimen should be a moved back and forth across the paper to allow for even wear. Between grinding steps, the specimen should be rotated 45O-90O. The moulded specimens were first polished using emery paper of grits 80, 120, 200, 600, 800 and followed by polishing using on a rotating linen disc,

Symbol	Factors	Level 1	Level 2	Level 3
A	Cooling rate (°C/min)	1	1.5	2
B	Soaking temperature (°C)	-130	-150	-185
C	Soaking period (hr.)	24	36	48
D	Tempering temperature (°C)	150	200	250

Table 2.
DCT Process factors and their levels.

Exp. No	Cooling rate (A) (°C/min)	Soaking temperature (B) (°C)	Soaking period (C) (hr.)	Tempering temperature (D) (°C)
1	1	-130	24	150
2	1	-150	36	200
3	1	-185	48	250
4	1.5	-130	36	250
5	1.5	-150	48	150
6	1.5	-185	24	200
7	2	-130	48	200
8	2	-150	24	250
9	2	-185	36	150

Table 3.
Orthogonal array.

and finished on a velvet cloth using alumina powder and water as a coolant. After polishing, the moulded samples were subjected to microstructure analysis. A microstructural study was conducted to explain the improvement in hardness of EN-31 bearing steel subjected to CHT and DCT. The samples were prepared as per the ASTM E3-01 for metallographic examination. These samples were etched with 2 vol% Nital and dried in air. The etched samples were examined using Metallurgical microscope at 50× magnification to study the changes in hardness. High resolution digital micrographs were taken randomly at different regions of the specimens.

3. Results and discussion

3.1 Chemical composition

The measured values of the sample were tabulated in the **Table 4**. The result of the chemical analysis confirms the chemical composition of EN-31 bearing steel.

With the above results of chemical composition it is proved that the selected material is EN-31 alloy bearing steel, according to BS 450 ASTM standard.

3.2 Vickers's hardness test

The result obtained from the Vickers's hardness of the EN-31 alloy bearing steels is given as below in the **Table 5**. From the results of Vickers hardness test, the hardness value of Conventional Heat Treatment sample is compared to the hardness value of

Element	C	Mn	Si	S	Ph	Cr
Measured value (%)	0.97	0.27	0.28	0.002	0.006	1.43

Table 4.
 Chemical composition of EN-31 Bearing steel.

Process	Exp. No	Vicker's hardness			Mean
		Y1	Y2	Y3	
CHT	1	698	696	706	700
DCT	1	866	853	854	858
	2	850	845	843	846
	3	864	854	864	861
	4	851	839	850	847
	5	838	837	840	838
	6	804	802	800	802
	7	850	857	863	857
	8	784	786	799	790
	9	846	864	846	850

Table 5.
 Hardness values of EN-31 bearing steel.

Deep Cryogenic Treatment samples using orthogonal array. It is significantly increase in the hardness of DCT sample. It is clear from the table that the raw material has the lower hardness.

The DCT samples have the highest hardness when compared to SCT and CHT samples. DCT followed by tempering improves the hardness by 14% and sub-zero treatment followed by tempering improves hardness by 13% when compared to the CHT. The untemper structure has the highest hardness in all the cases but the material is more brittle due to presence of untemper martensite which is seen in the microstructure. Martensite is a highly supersaturated solid solution of carbon in iron. Hence, tempering should be done to reduce the brittleness by scarifying some hardness and tensile strength to relieve internal stresses and to increase toughness and ductility. It results in a desired combination of hardness, ductility, toughness and structural stability. During tempering, marten site rejects carbon in the form of finely divided carbide phases. The end result of tempering is a fine dispersion of carbides in the iron matrix, which bears little structural similarity to the original as-quenched martensite.

3.3 Microstructure analysis

A microstructural investigation was carried out to identifying the possible mechanism brought in by the thermal treatment in improving the hardness of the EN-31 bearing steel. The hardness values of CHT and DCT were compared by using the microstructure view of the CHT and DCT samples. The micrograph view of the CHT sample is given in below **Figure 4**. The CHT sample was prepared for metallographic examination as per ASTM E3-01. The specimen was investigated using a Metallographic microscope at 50X magnification to study the changes influence the hardness. The CHT sample exhibited non-uniform distribution of large, elongated carbides on the tempered martensite matrix and a notable amount of retained austenite in the specimen. The mean hardness value of CHT sample is 700 HV. The optimised cryotreated samples were prepared for metallographic examination as per ASTM E3-01. Then the specimen were subjected to factor level setting like cooling rate, soaking period, soaking temperature and tempering temperature for experiment-1 in OA table. After the specimens were investigated using a Metallurgical microscope at 50× magnification to study the changes that influence the hardness. The micrograph of the optimised DCT samples shown given below. The micrograph of the optimised DCT sample-01 revealed a marked reduction in the amount of retained austenite and an increase in the amount of fine secondary carbides. At cryogenic temperature, the amount of retained austenite decreased, resulting in a greater amount of tempered martensite; the increased amount of martensite led to more uniform distribution of fine carbides throughout the structure. The precipitation of fine carbides and the transformation of retained austenite to martensite showed considerable variations in the hardness of the optimised DCT sample-01 compared to the CHT samples. The mean hardness value of this sample is 858 HV and 18.43% improvement in the hardness compared to CHT. The micrograph of the optimised DCT samples shown given below. The optimised cryotreated samples were prepared for metallographic examination as per ASTM E3-01. Then the specimen were subjected to factor level setting like cooling rate, soaking period, soaking temperature and tempering temperature for experiment-2 in OA table. After, the specimens were investigated using a Metallurgical microscope at 50× magnification to study the

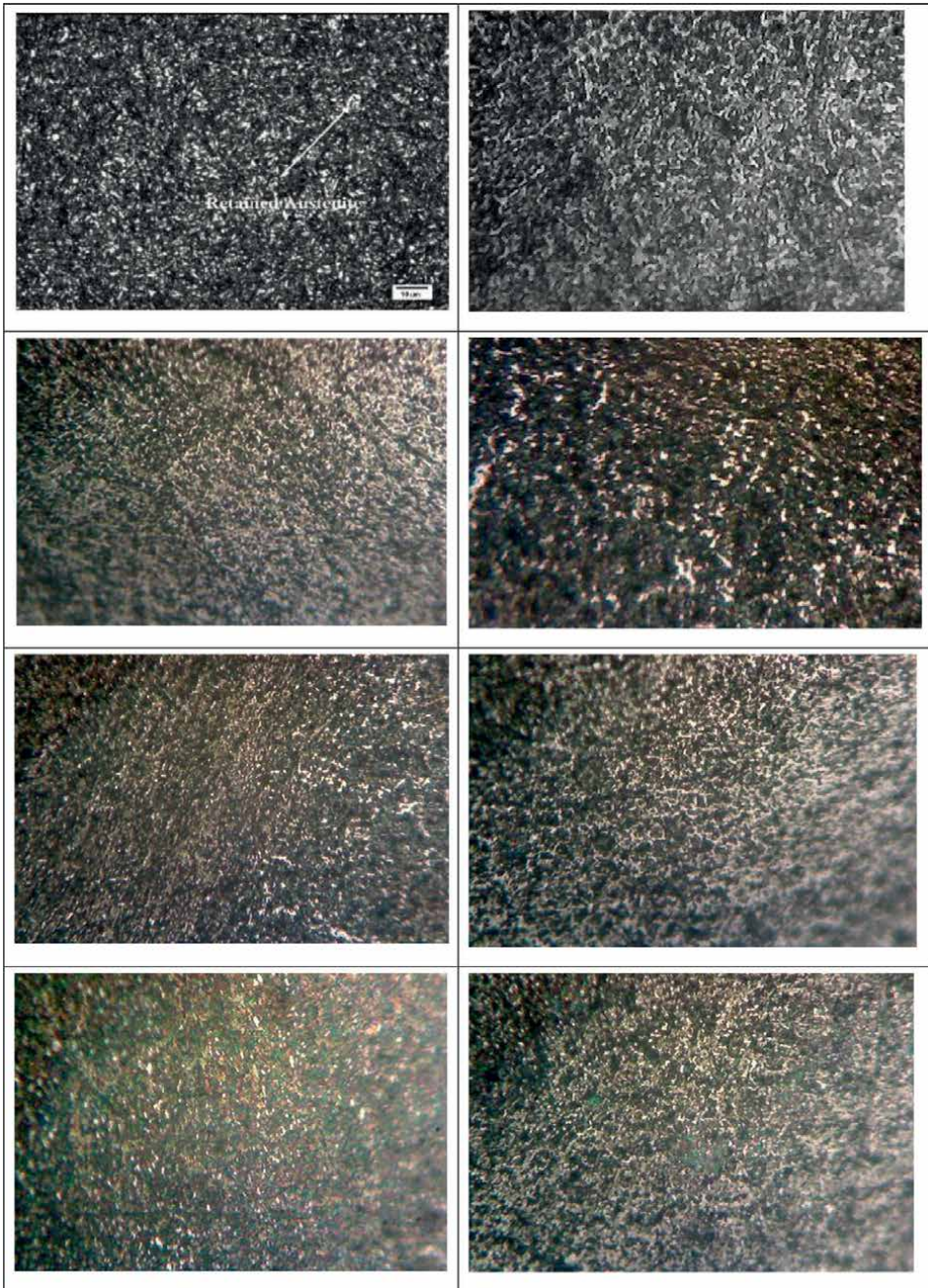


Figure 4.
Microstructure of the optimised DCT sample at 50× magnification.

changes that influence the hardness. The CHT sample exhibited non-uniform distribution of large, elongated carbides on the tempered martensite matrix and a notable amount of retained austenite in the specimen. The mean hardness value of CHT sample is 700 HV.

The optimised cryotreated samples were prepared for metallographic examination as per ASTM E3-01. Then the specimen were subjected to factor level setting like cooling rate, soaking period, soaking temperature and tempering temperature for experiment-1 in OA table. After the specimens were investigated using a Metallurgical microscope at 50× magnification to study the changes that influence the hardness. The micrographs of the optimised DCT sample-01 were shown in below. The SEM micrograph images found the wear debris of the CHT samples as shown in Figure has large platelets and flake shaped particles worn out and further determined the particle size which is comparatively smaller than the optimised DCT samples. The SEM micrographs were seen the worn morphology DCT samples considerably smoother than that of the CHT samples at significant loading conditions. Further it shows the SEM images more delamination lips and small considerably cracks could be seen in the CHT samples than the DCT samples. The precipitation of fine carbides and the transformation of retained austenite to martensite showed considerable variations in the hardness of the optimised DCT sample-01 compared to the CHT samples. The mean hardness value of this sample is 858 HV and 18.43% improvement in the hardness compared to CHT.

The micrographs of the optimised DCT sample-02 were shown in below. The optimised cryotreated samples were prepared for metallographic examination as per ASTM E3-01. Then the specimen were subjected to factor level setting like cooling rate, soaking period, soaking temperature and tempering temperature for experiment-2 in OA table. After, the specimens were investigated using a Metallurgical microscope at 50X magnification to study the changes that influence the hardness. The mean hardness value of this sample is 46 and 17.23% improvement in the hardness compared to CHT. The micrograph of the optimised DCT samples was shown in below. The optimised cryotreated samples were prepared for metallographic examination as per ASTM E3-01. Then the specimen were subjected to factor level setting like cooling rate, soaking period, soaking temperature and tempering temperature for experiment-3 in OA table. After the specimens were investigated using a Metallurgical microscope at 50× magnification to study the changes that influence the hardness. The DCT samples examined the surface after the heat treatment revealed the carbides produce good mechanical properties which is the help of secondary carbides. Sometimes the surface was marked as a condition is homogeneity; it may be resulted in better surface during the treatment process. From the micrograph of the optimised DCT sample which was observed the fine secondary carbides in martensitic steels. The optimised DCT sample-03 compared to the CHT samples. The mean hardness value of this sample is 861 HV and 19.20% improvement in the hardness compared to CHT. The optimised cryotreated samples were prepared for metallographic examination as per ASTM E3-01. Then the specimen were subjected to factor level setting like cooling rate, soaking period, soaking temperature and tempering temperature for experiment in OA table. After the specimens were investigated using a Metallurgical microscope at 50X magnification to study the changes that influence the hardness. The micrograph of the optimised DCT sample revealed a marked reduction in the amount of retained austenite and an increase in the amount of fine secondary carbides. At cryogenic temperature, the amount of retained austenite decreased, resulting in a greater amount of tempered martensite; the increased amount of martensite led to more uniform distribution of fine carbides throughout the structure. The micrograph of the optimised DCT sample retained carbide dispersed on homogenous condition of the microstructure.

Moreover, the optimised DCT sample-7 compared to the CHT samples which is resulting the better hardness due to the transformation of retained austenite to martensite. The mean hardness value of this sample is 857 HV and 18.40% improvement in the hardness compared to CHT. The optimised DCT sample-08 compared to the CHT samples. The mean hardness value of this sample is 790 HV and 13.45% improvement in the hardness compared to CHT. The micrograph of the optimised DCT sample estimated the percentage of retained austenite fine secondary carbides. During the cryogenic temperature resulted fine carbides in the form of closed packed and hardened. Some sample of DCT has revealed carbides presented in homogeneity structure during the treatment process. Moreover, the carbides which are employed better mechanical properties due to the solid precipitation. The transformation of retained austenite to martensite due to precipitate the fine carbides in the surface of DCT samples significantly. Finally, the hardness of the optimised DCT sample-09 compared to the CHT samples. The mean hardness value of this sample is 850 HV and 17.54% improvement in the hardness compared to CHT.

3.4 Corrosion behaviour

Figure 5 shows the potentiodynamic polarisation curves for the bulk of the CHT and DCT samples in 1 M Na_2CO_3 solution. It can be noted that the DCT show lower I_{corr} than the CHT and SCT (I_{corr} for DCT is about one order the magnitude lower than that of CHT) indicating more general corrosion resistance. In this experiments were taken three samples showing the passive state conditions. The Figure resulted the current has moving the positive terminal is to identify the low corrosion tendency in martensite samples in the same potential. Moreover, the corrosion peak identified all three samples at passivation behaviour in a slow manner.

Sometimes the increasing the anodic scan limit to 2 V (versus Ag/AgCl₂ basic line) and breakdown potential is observed at almost the same potential (about 0.75 V). Normally the alkali media were resulted the properties of low corrosion resistance of martensite materials at conventional treatment especially for the deep cryogenic treatment (DCT). However, it seems the samples of CHT and DCT the passivation layer forms at slower rate than in the case of the SCT as observed with the lower corrosion currents.

For the En 52 valve steel material, the potential of the DCT specimen shows -0.485 mV and the CHT specimen shows -0.54 mV at the initial condition. The potential of the CHT specimen decreases continuously and reaches a stable value, and for the DCT specimen the potential decreases up to around 1300 sec and increases to some extent and gets stable at the end. The increase in the potential for the DCT specimen is due to the repassivation effect; this may be due to the presence of more chromium carbides in the martensitic structure. From **Figure 6** the initial potential for the 21-4 N valve steel at the CHT condition is -0.195 mV and at the DCT it shows a value of -0.205 mV. The potential value for both the specimen decreases continuously with time and the DCT specimen reaches a stable value at the end; the potential of the CHT specimen increases after around 1500 sec and reaches a stable condition. The higher potential value in the OCP curve indicates the higher corrosion resistance of the En 52 DCT and 21-4 N CHT specimen. The polarisation curves for the CHT and optimised DCT specimens of both the materials are shown in **Figures 6** and **7**. The corrosion potential E_{corr} and corrosion current I_{corr} are determined by the Tafel extrapolation method, by carrying out scans in both the positive and negative directions.

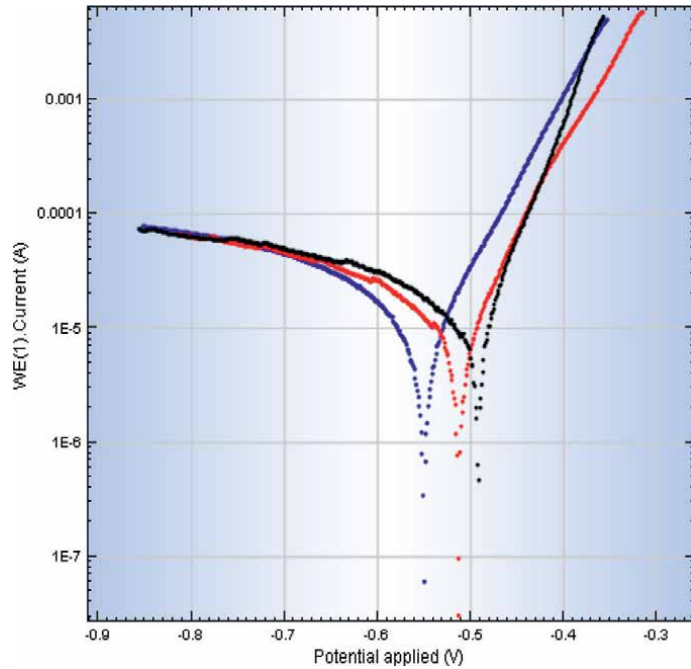


Figure 5.
Polarisation curves recorded in 1 M Na₂CO₃ solution at 10 mv/s for the Bulk of CHT and DCT samples.

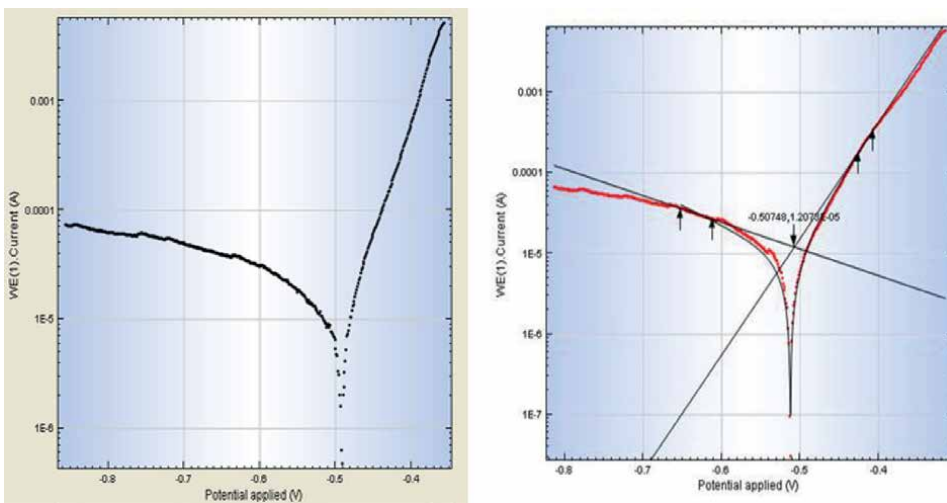


Figure 6.
Normal corrosion tafel plot for DCT samples.

4. Conclusion

The hardness of the EN-31 bearing steel almost varied after both CHT and DCT which is evident from the mean VICKERS'S hardness test. The microstructural analysis reveals that the precipitation of fine carbides and transformation of the retained austenite to martensite enhanced the hardness. The hardness of the DCT samples is

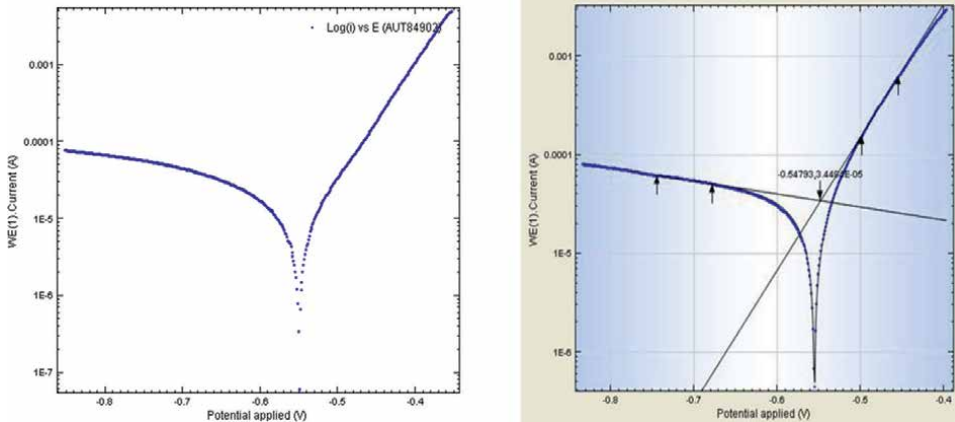


Figure 7.
Normal corrosion Tafel plot for CHT samples.


higher than the CHT. The Images of microstructure were taken at 50X magnification source lot of differences between CHT and DCT. Fine carbides are found in that treatment CHT and DCT. It was very fining nature with reasonable hardness. The DCT seems to offer higher corrosion resistance than CHT samples.

Author details

Shunmuga Priyan Murugan
Department of Mechanical Engineering, Loyola Institute of Technology and Science,
Kanya Kumari, Tamil Nadu, India

*Address all correspondence to: iampriyan25@gmail.com

IntechOpen

© 2022 The Author(s). Licensee IntechOpen. This chapter is distributed under the terms of the Creative Commons Attribution License (<http://creativecommons.org/licenses/by/3.0>), which permits unrestricted use, distribution, and reproduction in any medium, provided the original work is properly cited. 

References

- [1] Ashish Bhateja AV. Study the effect on the hardness of three sample grades of tool steel i.e. EN-31, EN-8 and D3 after heat treatment processes such as annealing, normalizing and hardening & tempering. *The International Journal of Engineering and Science*. 2010;**1**(2):253-259
- [2] Amey CM, Huang H, Rivera-Diaz-del-Castillo PEJ. Distortion in 100Cr6 and nanostructured bainite. *Materials & Design*. 2009;**35**:66-71
- [3] Sri Siva R, Mohan Lal D, Arockia Jaswin M. Optimization cryogenic treatment process for 100Cr6 bearing steel using the Grey-Taguchi method. *Tribology Transaction*. 2012;**55**(6):854-862
- [4] Bensley A, Senthilkumar A, Mohanlal D, Nagarajan G, Rajadurai A. Effect of cryogenic treatment on tensile behaviour of case carburized steel-15M17. *Materials Characterization*. 2010;**58**:485-491
- [5] Huang JY, Zhu YT, Liao XZ, Beyerlein IJ, Bourke MA, Mitchell TE. Microstructure of cryogenic treated M2 tool steel. *Material Science and Engineering*. 2011;**120**:450-455
- [6] Joseph Vimal A, Bensley A, Mohan Lal D, Srinivasan K. Deep cryogenic treatment improves wear resistance of En 31 steel. *Materials and Manufacturing Processes*. 2010;**23**(3-4):369-376
- [7] Das D, Dutta AK, Ray KK. Optimization of the duration of cryogenic processing to maximize wear resistance of AISI D2 steel. *Cryogenics*. 2009;**49**(5):176-184
- [8] Harish S, Bensley A, Mohan Lal D, Rajadurai A, Gyongyver LB. Microstructure study of cryogenically treated En 31 bearing steel. *Journal of Material Processing Technology*. 2010;**209**(9):3351-3357
- [9] Liu H, Wang J, Hongshan Y, Shen B. Effects of cryogenic treatment on microstructure and abrasion resistance of CrMnB high-chromium castiron subjected to sub critical treatment. *Materials Science and Engineering A*. 2010;**478**(1-2):324-328
- [10] Vimal J, Bensley A, Mohan Lal D, Srinivasan K. Deep cryogenic treatment improves wear resistance of En 31 steel. *Materials and Manufacturing Processes*. 2009;**23**(4):369-376
- [11] Fadare DA, Fadara TG, Akanbi OY. Effect of heat treatment on mechanical properties and microstructure of NST 37-2 steel. *Journal of Minerals and Materials Characterization and Engineering*. 2008;**10**(3):299-308
- [12] Harish S, Bensley A, Mohan Lal D, Rajadurai A, Gyongyver LB. Microstructure study of cryogenically treated En 31 bearing steel. *Journal of Material Processing Technology*. 2011;**209**(9):3351-3357
- [13] Vadivel K, Rangasamy R. Performance analysis of cryogenically treated coated carbide inserts. *International Journal of Advanced Manufacturing Technology*. 2011;**42**(3):222-232

Section 3

Modelling and Calculations

Simulation and Calculation for Predicting Structures and Properties of High-Entropy Alloys

Yong Zhang and Yuanying Yue

Abstract

High-entropy alloys (HEAs) have attracted the attention of scholars due to their outstanding properties such as excellent fracture, and irradiation resistance for various applications. However, the complex composition space hinders the exploration of new HEAs. The traditional experimental trial-and-error method has a long periodicity and is difficult to understand the complexity of the structural characteristics of HEAs. With the rise of the “Materials Genome Initiative”, simulation methods play an important role in accelerating the development of new materials and speeding up the design process of new HEAs. In this chapter, some of the multi-scale simulation methods, such as density functional theory (DFT) calculations and molecular dynamics (MD) methods, used in designing HEAs and predicting their properties are reviewed. The advantages and limitations of these methods are discussed, and the role of computational simulation methods in guiding experiments is illustrated. This study aims to promote the rapid development of computational simulation methods in HEAs.

Keywords: high-entropy alloys, simulation and calculation, density functional theory calculations, molecular dynamics, phases, properties

1. Introduction

Metal materials play an essential role in aerospace, transportation, national defense equipment, and other important areas of the national economy, and the development of science and technology has put forward higher requirements for new metal materials. Traditional alloys such as aluminum alloys [1, 2] and magnesium alloys [3] are mainly based on 1 or 2 elements, and the properties are changed or optimized by adding small amounts of other elements. The traditional alloy preparation technique and its performance have become mature and stable after years of research and development, and new alloys are urgently required to alleviate the bottleneck. In 2004, high-entropy alloys (HEAs) were first proposed [4, 5], breaking away from the traditional alloy single-element-based design concept. Because of their excellent properties and wide potential for application, HEAs have gained considerable attention in recent years and have become a hot field of research in materials science. HEAs are new multi-principal metallic materials with a predominantly configurational

entropy. In HEAs, there is a wide variety of primary elements, and no element dominates, so the mixing entropy value is high. According to Boltzmann hypothesis, the mixing entropy ΔS_{mix} of n-component alloys is

$$\Delta S_{mix} = -R \sum_i C_i \ln C_i \quad (1)$$

where R is gas constant, C_i is the i^{th} element molar fraction.

The thermophysical parameter calculation is based on the ‘‘Hume-Rothery criterion.’’ This rule is extended to the field of HEAs, and a variety of related parameters are proposed for predicted phase formation, which may not be applicable to all HEAs. Zhang et al. [6] summarized the factors of the atomic-size difference, δ , and the enthalpy of mixing, ΔH_{mix} , of the multi-component alloys:

$$\delta = \sqrt{\sum_{i=1}^N x_i \left(1 - x_i / \sum_{j=1}^N x_j r_j \right)^2} \quad (2)$$

$$\Delta H_{mix} = \sum_{i \neq j} 4x_i x_j \Delta H_{ij} \quad (3)$$

where N is the number of the elements in HEAs, x_i or x_j is the atomic percentage of the i^{th} or j^{th} component, r_j is the atomic radius of the j^{th} component, and ΔH_{mix} is the mixing enthalpy for i and j element.

Subsequently, to further understand the connection between ΔH_{mix} and ΔS_{mix} , Zhang and Yang [7] proposed a new parameter, Ω , defined by:

$$\Omega = T_m \Delta S_{mix} / |\Delta H_{mix}| \quad (4)$$

where T_m is the melting temperature of the N -component alloy. Zhang et al. [8] summarized the published HEAs and suggested a phase-formation rule using the δ and Ω with $\Omega \geq 1.1$ and $\delta \leq 6.6\%$ as shown in **Figure 1**. The Ω criterion enables simple

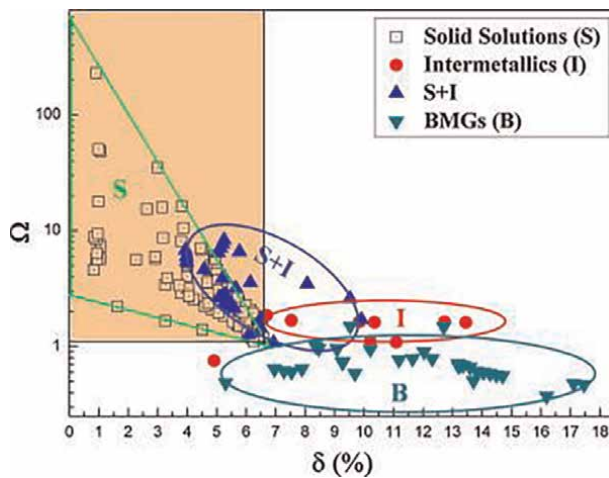


Figure 1. The relationship between parameters δ and Ω for multi-component alloys [7]. Copyright © 2011 Elsevier.

and convenient phase structure prediction by combining the parameters that affect HEAs: size difference, mixing enthalpy, and mixing entropy. However, the FCC-type phase-forming δ shows a significant overlap with that of the BCC-type phase, which means new rules or parameters need to be considered for the phase formation.

Since FCC and BCC phases overlap, from the perspective of alloy design, Guo et al. [9] proposed the valence electron concentration (VEC) to determine the formation of FCC or BCC solid solution in HEAs.

$$VEC = \sum_{i=1}^n c_i (VEC)_i \quad (5)$$

where c_i and VEC_i are the atomic percentage and VEC of the i^{th} component.

The analysis of experimental data leads to the following conclusions: BCC structure of HEA is easier to predict than FCC structure; $VEC < 6.8$ will form BCC structure solid solution; if $6.8 < VEC < 7.8$, FCC + BCC structure solid solution will be formed; $VEC > 7.8$, FCC structure solid solution will be formed. Therefore, it is the potential to separate FCC and BCC phases by the VEC criterion, but it is not probable to determine whether there is intermetallic compound formation. The above parameters that emerged during the development of HEAs are important conclusions for researchers in their quest to accelerate alloy development. The prediction of thermodynamic parameters improves the research efficiency and gives strong theoretical headings for the experiment, thus reducing waste. Due to the huge composition space of HEAs, these parameter judgments cannot satisfy every possible composition, and therefore, researchers are eager to have dependable databases and high-performance calculations in order to increase the efficiency of alloy design.

It has been particularly notable that the Materials Genome Initiative (MGI) was announced in 2011 to accelerate the pace of materials discovery, design, and implementation through the integration of experimentation, theory, and computation in a highly integrated, high-throughput manner [10]. By integrating both computational and experimental data, as well as high-throughput computations and multi-scale simulations, this project aims to change the research and design culture of materials and advance material development methods and approaches [11]. MGI project has contributed to the development of HEAs. Even though predictive computational modeling of HEAs is challenging primarily due to the complex multi-component system and disordered solid-solution structure, HEAs are challenging systems to model. Although computational modeling of HEAs is becoming increasingly popular as a tool for studying the structure (including defects, dislocation), thermodynamics, kinetics, and mechanical properties [12]. In the material simulation, we can simulate the material from various scales, and qualitatively as well as quantitatively describe the characteristics of the material and promote our understanding of it from multiple perspectives. For materials with different scale-space, there are corresponding material calculation methods, including the first-principles density functional theory (DFT), molecular dynamics (MD), the calculation of phase diagram (CALPHAD), and high-throughput methods [13–20]. Hence, from the microscopic to the macroscopic scale, this chapter reviews the limitations and potentials of different simulation methods by summarizing in a targeted manner the characteristics and application areas of different simulation methods. It also looks at database-driven machine learning, as well as the use of multi-scale simulation methods in the future to aid in the design, development, and performance tuning of new HEAs.

2. DFT calculations

In comparison with other computational techniques, first-principles calculations are an effective method for predicting the physical and structural properties of materials. It is calculated only by parameters such as the number of atoms inherent to the material. The essence is to obtain the various properties of the material by solving the Schrödinger equation. However, the state of motion of an electron corresponds to a Schrödinger equation, which can be solved for simple single-electron systems and is hard to solve for complex multi-electron systems. Kohn and Sham [21] considered that the particle density function of a multi-particle system can be achieved by a simple single-particle wave equation, and the Kohn-Sham equation [22] is self-consistent. Scientists usually use scientific approximations to simplify the Schrödinger equation to reach an exact solution. One of the most widely used first-principles calculations based on DFT [23]. The DFT calculation process converts the multi-electron problem into a single-electron problem by describing the physical properties of the electron density of states. DFT calculations usually include only fundamental physical constants such as speed of light, Planck's constant, electron, and charge mass as input parameters [24]. Solving the Schrödinger equation is an iterative process, given an initial electron number density iteration to determine if it converges, to obtain the total energy. Then calculate fundamental material properties such as lattice constants, elastic constants, stacking fault energies, vacancy formation energies and migration barriers, and cohesive energies as a function of composition and crystal structure [25, 26]. The first-principles approach referred here deals with the DFT. Although the DFT simplifies the Schrödinger equation, the computation process is still challenging because HEAs have multiple principal components. Thus, special quasi-random structure (SQS) modeling, coherent potential approximation (CPA), and virtual crystal approximation (VCA) calculations are used for the DFT calculation of HEA [16, 27]. Common software used for DFT calculations is VASP (Vienna Ab Initio Simulation Package, Vienna, Austria) [28], CASTEP (Cambridge Sequential Total Energy Package) [29], and SIESTA [30].

2.1 Modeling methods

2.1.1 VCA

The VCA is based on the mean-field theory. Commonly, atomic potentials representing atoms of two or more elements are averaged. This is an oversimplified approach to substitutional solid solutions [31]. As there is no need to construct a supercell, the calculation time can be reduced considerably. In most cases, the VCA can be applied and are effective when the alloying elements are neighbors on the periodic table [27, 32] (i.e. TiVNbMo [33]). Nonetheless, it remains to be seen whether the VCA can be applied to other HEAs. The VCA was used to investigate the effect of alloying elements on phase stability, elastic and thermodynamic properties of random Nb-Ti-V-Zr HEAs. Liao et al. [32] found that the lattice constant, elastic constant, and thermal expansion coefficient of NbTiVZr were in agreement with other calculations and experiments, confirming that the VCA scheme was suitable for random Nb-Ti-V-Zr systems. A similar study was conducted by Chen et al. [14] which focused on the phase structure, elastic constants, and thermodynamic properties of Ti_xVNbMo refractory high entropy alloy (RHEA) by the VCA in conjunction with the equation of state (EOS) equilibrium equation of state and the quasi-harmonic

Deby-Grüneisen model. Researchers are involved in the exploration of new HEA systems suitable for use in the VCA. Gao et al. [14] explored the elastic constants and elastic properties of VMoNbTaWM_x (M = Cr, Ti) RHEA by using the first principle and VCA method. In addition, they found that, when Cr content was raised, the bulk modulus B, Young's modulus E, and the shear modulus G increased, while the Pugh ratio B/G and Poisson's ratio ν fluctuated to some extent. Among them, VMoNbTaWCr_{1.75} had the highest plasticity and VMoNbTaWCr₂ had the highest strength, respectively. It is important to note that VCA is computationally compact, highly efficient, and easy to model, yet the influence of the environment on the system is ignored, thereby resulting in a somewhat limited application.

2.1.2 CPA

The CPA rests on the assumption that the alloy may be replaced by an ordered effective medium, which is self-consistent in its parameters. The single-site approximation is applied to the impurity problem, which is a description of a single impurity embedded in an effective medium and no extra information is given about the individual potential and charge density beyond the sphere or polyhedron around the impurity. The CPA relies on two main approximations. One is to presume that the local potentials (P_A, P_B, P_C, P_D, P_E) around an atom from the alloy are the same, resulting in the disregard of local environment effects. Accordingly, a similar approximation can be made by replacing the system with a monoatomic medium described by the site-independent coherent potential \tilde{P} , as shown in **Figure 2** [27].

CPA has proven to be a very successful and popular technique that has been used extensively in the calculation of total energy, density of states, conductivity, and other electronic structure properties of random alloys [20]. The Exact Muffin-Tin Orbital (EMTO) in conjunction with the CPA method is demonstrated to be effective for a series of HEA systems including refractory HEAs [34] and HEA systems

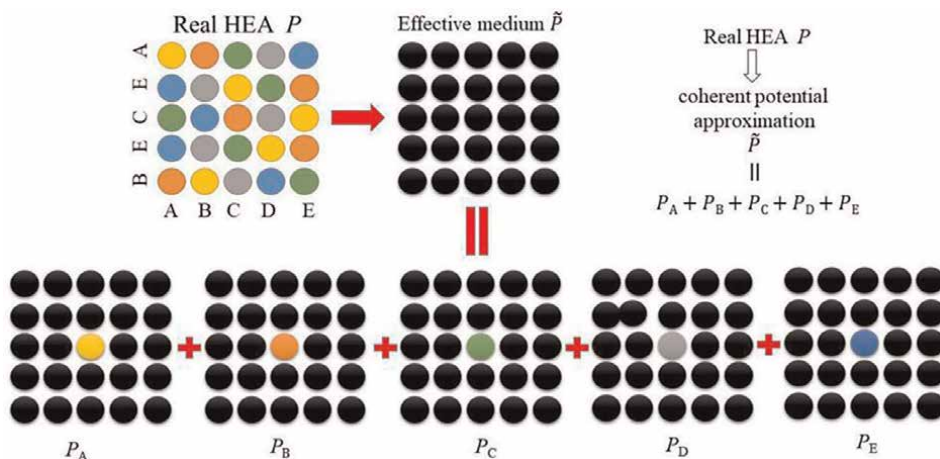


Figure 2. Two-dimensional illustration of the CPA for the equimolar ABCDE HEAs (HEAs). The symbol P represents the real alloy potential, \tilde{P} for coherent potential, $P_A, P_B, P_C, P_D,$ and P_E are the potentials of the alloying elements [27]. © 2017 Tian.

composed of transition metals [35]. Niu et al. [35] calculated ΔH_{mix} , lattice parameter (a_0), bulk modulus (B), and shear modulus (G) by the exact EMTO-CPA for over 2700 compositions of the NiFeCrCo alloy as a single-phase solid solution in paramagnetic state. An application of the CPA method is a mean-field approximation that is computationally small and, therefore, has an advantageous efficiency. The application can describe phenomena such as magnetic disorder and lattice vibrations. Rao et al. [36] studied the abnormal magnetic behavior of FeNiCoMnCu HEAs using DFT implemented in the EMTO-CPA formalism. Cu played a significant role in stabilizing the ferromagnetic order of Fe, they found. The calculated magnetization and Curie temperatures of alloys closely match the experimental results. Furthermore, comparing SQS with CPA, where there were no convergence problems, the results were very similar. It is important to emphasize that the difficulties associated with treating different magnetic states in the supercell approach further emphasize the advantages of the EMTO-CPA method for the present study. Through the Korringa-Kohn-Rostoker (KKR-CPA) method, Cieslak et al. [37] calculated total energy electronic accounting for chemical disorder effects of high entropy $\text{Cr}_x\text{AlFeCoNi}$ alloys ($x = 0, 0.5, 1.0, 1.5$). Singh et al. [38] examined the total energy of $\text{Ti}_{0.25}\text{CrFeNiAl}_x$ and found increasing Al stabilized the BCC phase and the FCC phase became stable above %65-Al. However, there are also certain disadvantages associated with the CPA method. The first problem is that the effective atom is fiction, and the resulting uniformity of the environment is not correct. Second, since all surrounding lattice sites are identically occupied, each atom is in a position of high symmetry, i.e. there is no force that would normally cause it to move from its own lattice site, thus, there is no lattice distortion [39].

2.1.3 SQS

SQS is a special periodic structure that is constructed using a small number of atoms per unit cell. The correlation functions within the first few nearest-neighbor shells are designed to approach the periodic functions of a random alloy to ensure that periodicity errors occur only among more distant neighbors. An SQS can be considered to be the best unit cell possible representing random alloys since interactions between distant neighbors generally contribute less to the system energy than interactions between near neighbors [40]. There are two approaches to generate SQSs. One is to generate exhaustively all possible combinations of supercells for a given cell size, and then select the one that best mimics the correlation functions of the random alloy. The second method involves performing Monte Carlo simulations to locate the optimal SQS. The two methods have been, respectively, realized in the *gensqs* and *mcsqs* codes within the Alloy Theoretic Automated Toolkit (ATAT) developed by Axel van de Walle and coworkers [41, 42]. While the *gensqs* code can only be used to generate smaller SQS, the *mcsqs* code [43] is more powerful and can be used to produce large SQS containing hundreds of atoms per unit cell. The SQS method combined with VASP software can be used to calculate properties such as lattice constants, layer misalignment energy, phase stability, elastic constants, magnetic properties, and electronic density of states of HEAs. According to Zhang et al. [44], stacking fault energies (SFEs) were computed in FCC and HCP HEAs utilizing the first-principles method combined with the SQS technique, revealing the mechanism for the formation of stacking faults and nanodiamonds. According to their findings, the negative SFEs are related to the energetic preference for HCP stacking and the metastability of FCC structures at low temperatures. During the past decade, a series of ferromagnetic

HEAs systems such as Fe-Co-Ni-Al-Si, Fe-Co-Ni-Mn-Al, Fe-Co-Ni-Mn-Ga, Fe-Co-Ni-Cr-Si, Fe-Co-Ni-Mn-Si, and Fe-Co-Ni-Cu-Si. have been reported [45–47]. As well, non-ferromagnetic elements can significantly influence the magnetic properties of HEAs [36]. The importance of understanding the influences of non-ferromagnetic elements on the magnetic behavior of HEAs cannot be overstated. This can be achieved by using a first-principle method in conjunction with the SQS technique. Zuo et al. [19] used the SQS approach to create the structures of CoFeMnNi, CoFeMnNiCr, and CoFeMnNiAl.

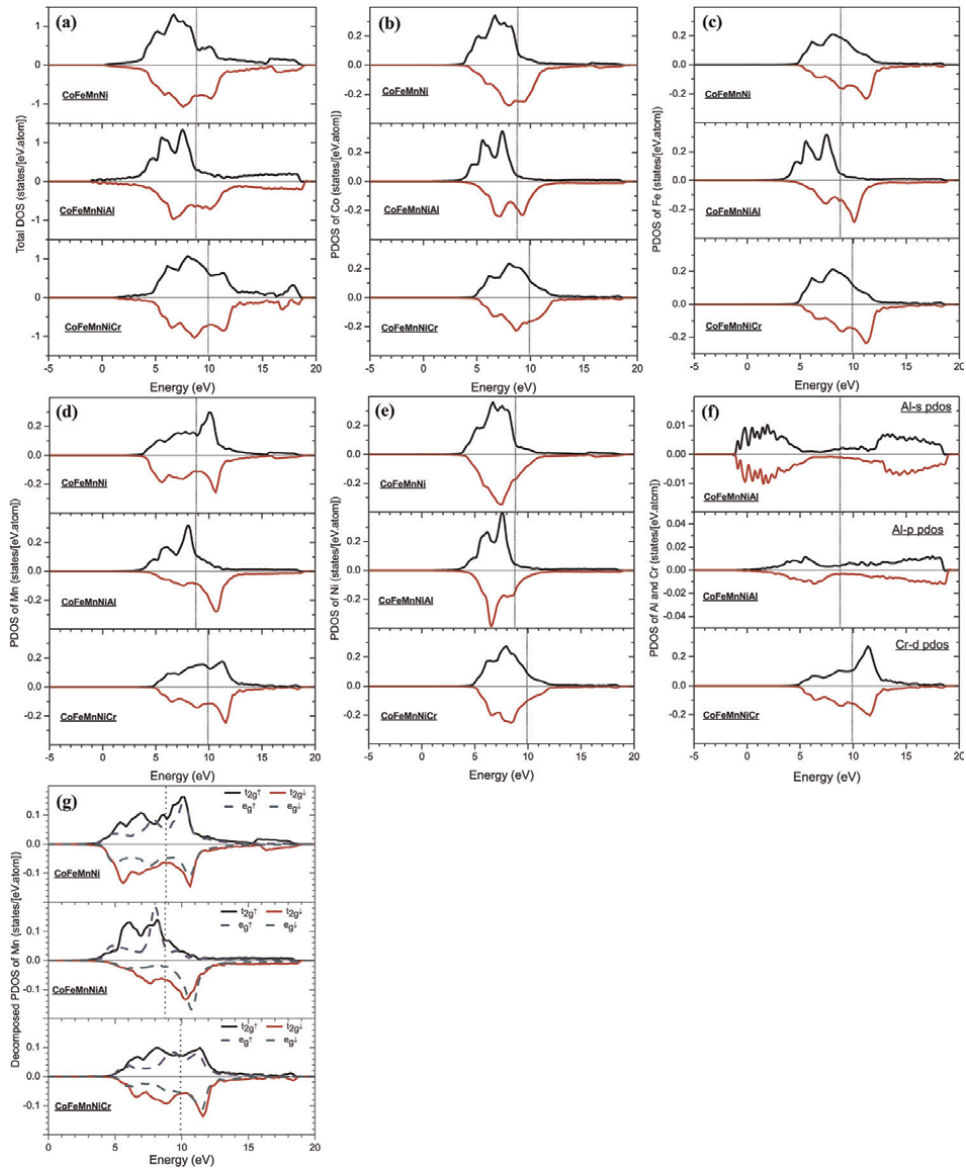


Figure 3. (a) Spin-polarized total DOS; (b) Co d partial DOS; (c) Fe d partial DOS; (d) Mn d partial DOS; (e) Ni d partial DOS; and (f) Al s, p and Cr d partial DOS for the FCC CoFeMnNi, FCC CoFeMnNiCr, and BCC CoFeMnNiAl from DFT calculations at zero temperature; and (g) Mn d-orbital decomposed partial DOS. The vertical dotted lines indicate the Fermi level [48]. © 2017 Acta Materialia Inc.

and CoFeMnNiAl, with the DFT calculations conducted at 0 K through the VASP. The DFT calculations on the electronic and magnetic structures reveal that the anti-ferromagnetism of Mn atoms in CoFeMnNi is suppressed especially in the CoFeMnNiAl HEAs, because Al changes the Fermi level and itinerant electron-spin coupling that leads to ferromagnetism as illustrated in **Figure 3**. Furthermore, Wei et al. [19] investigated the mechanism of the magnetic behavior of FeCoNiSi_{0.2}M_{0.2} (M = Cr, Mn) HEAs using first-principles calculations combined with the SQS method. It was found that doping the Mn resulted in a reduction in the number of spin-down electrons, which ultimately led to the transition of the Mn from an anti-ferromagnetic to ferrimagnetic state. SQS method may also be used for investigating short-range order effects in the chemical environment.

The SQS method can obtain a more realistic disordered distribution of HEAs and to consider the influence of the local atomic environment within the alloy matrix on the physical and chemical properties of the alloy. However, the complexity of the constituent elements of HEAs leads to the construction of SQS supercells considering more correlation functions among the principal elements, which has some influence on the efficiency and accuracy of the calculation. Therefore, how to reduce the difficulty of supercell construction is also a pressing issue for researchers to address.

3. MD calculations

Molecular dynamics (MD) methods rely heavily on Newtonian mechanics to calculate the properties and structure of molecules at the molecular level by simulating molecular motion. It is derived from samples that originate from a whole system made up of different states of the molecular system. The configuration of the system is then derived using calculation. Since computer computing power has increased rapidly, the research system of the MD method has also progressed to a larger spatial and temporal scale. A gap exists between the mechanical property values derived from simulation and the actual macroscopic mechanical properties of materials. However, this does not hinder the systematic study of the microstructural evolution of materials using MD methods. The main software groups currently used for molecular dynamics simulations are Lammps [49], Gromacs, Amber, Material studio, etc. Constructing models is the basis of molecular dynamics studies, and models are generally constructed by the random occupation of lattice sites by constituent atoms. Potential functions describe interatomic interactions, and the accuracy of the MD simulation results is dependent on the potential function describing the interatomic interactions. The main potential functions commonly used are Lennard-Jones (L-J) potential, Embedded atom method (EAM) potential, and Average-atom potential [50–52]. Currently, the most extensive description of interatomic interactions in HEAs is the EAM potential, which compensates for the shortcomings of the pair potential by forming a many-body potential function. Nevertheless, the EAM potential does not consider the covalent bond directionality. Based on this, the researchers also proposed the modified embedded-atom method (MEAM) potential and the EAM-Morse potential [53, 54], etc.

Qi et al. [55] used the MD method with MEAM potential to simulate the microstructure evolution and mechanical properties of CoCrFeMnNi HEAs under nano scratching. Several new behaviors were found in HEAs, such as twin boundary migration and dislocation locks. In HEAs, MD methods have been applied to mechanical properties, irradiation damage, thermal stability, and film growth by studying the microstructure evolution of the alloy and its mechanism. Jiang et al. [56] used MD

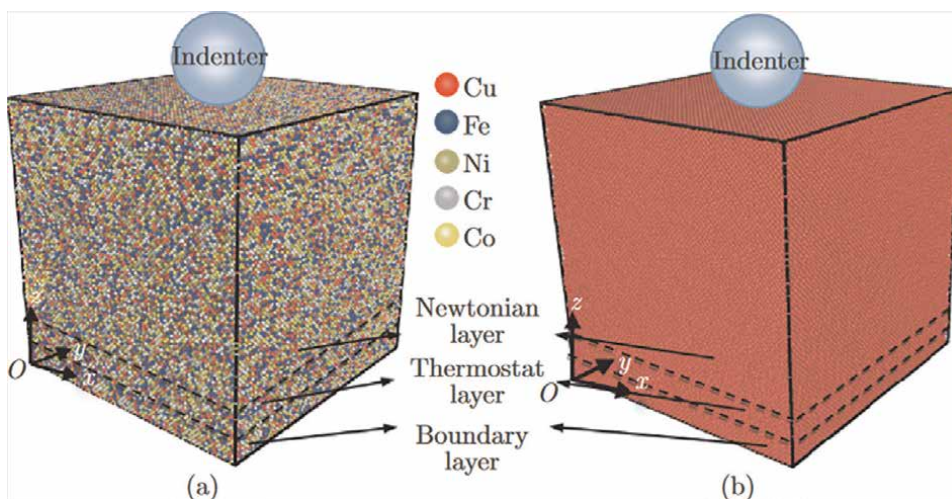


Figure 4. Nanoindentation models of (a) the single crystal HEA, and (b) Cu [57].

simulations combined with EAM potential to study microstructural evolution and mechanical properties of $\text{Al}_x\text{CoCrFeNi}$ HEAs under uniaxial tension. Higher aluminum content was found to deteriorate Young's modulus, yield stress, and yield strain of $\text{Al}_x\text{CoCrFeNi}$ HEAs. However, the dislocation density declined with increasing temperature. The high Al concentration suppressed the decrease of tensile properties with increasing temperature. Nanoindentation experiments utilize an indenter of a specific shape to apply a load to the surface of a material in a vertical direction and through computer control of the variation in load, determine the depth of the indentation in real-time. To gain a better understanding of the surface properties of HEAs, it is imperative to learn more about the deformation mechanism of indentation; however, due to the limitations of instruments and means of observation, experiments generally yield load-displacement curves, elastic moduli, hardness, and other macroscopic properties, and the microstructure and deformation mechanism cannot be examined at the nanoscale. MD simulation has proved to be a useful tool for analyzing and predicting the evolution of tissue and mechanical properties of HEAs under indentation. Therefore, more MD research on nanoindentation has been conducted. Based on MD simulations, LUO et al. [57] constructed the nanoindentation models of single-crystal FeCoCrNiCu HEA and Cu as shown in **Figure 4**. MD models included (i) FeCoCrNiCu HEA workpiece + virtual indenter and (ii) Cu workpiece + virtual indenter. Compared to Cu, the FeCoCrNiCu HEA exhibited a high dislocation density and high loading force during indentation. These findings indicated that the HEA had high strength.

HEA coatings have attracted more and more attention from researchers, especially HEA hard coatings, which can be used for cutting tools used in harsh environments, etc., to significantly improve their service life. This suggests that the exploration of HEA high wear-resistant coatings has a high prospect of application. The growth mode of thin films influences their structure and properties, so molecular dynamics simulations of thin film growth can be used to study the mechanism of film growth. Xie et al. [17] studied AlCoCrCuFeNi HEA coatings. **Figure 5** showed the deposition of HEA coatings on Si(100) substrate. The atoms in $\text{Al}_2\text{Co}_9\text{Cr}_{32}\text{Cu}_{39}\text{Fe}_{12}\text{Ni}_6$ and $\text{Al}_3\text{Co}_{26}\text{Cr}_{15}\text{Cu}_{18}\text{Fe}_{20}\text{Ni}_{18}$ were arranged in a crystalline structure, while $\text{Al}_{39}\text{Co}_{10}\text{Cr}_{14}\text{Cu}_{18}\text{Fe}_{13}\text{Ni}_6$ formed an

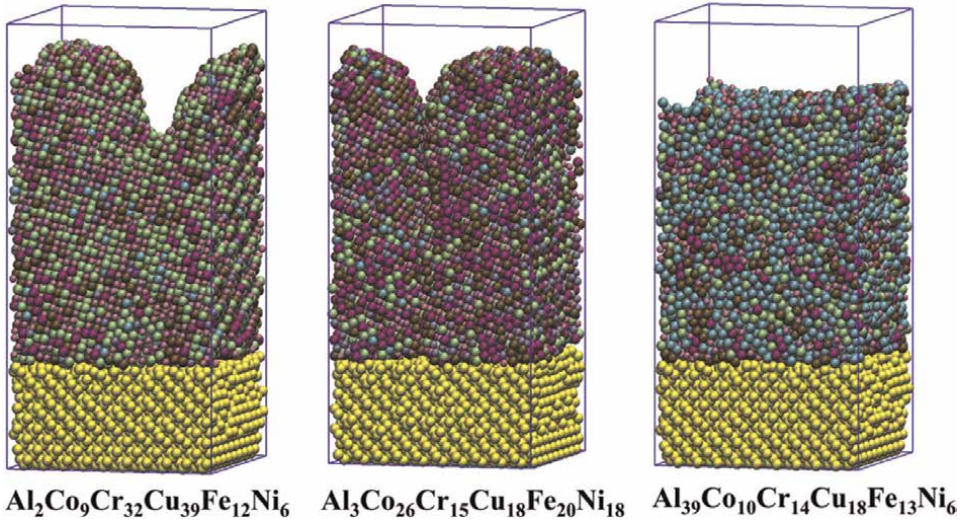


Figure 5.
 HEA films deposited on Si(100) substrate [17]. Copyright © 2015 Elsevier.

amorphous structure over the entire thickness. The simulation results show that the differences in the number of elements and atomic sizes have a significant effect on the atomic configuration, and a tendency to develop from solid solution to bulk amorphous is predicted by calculating the parameters of the HEAs.

4. CALPHAD methods

In terms of phase diagrams, they are a geometric representation of a system in equilibrium and thus serve as the basis for the study of solidification, phase transformation, crystal growth, and solid-phase transformation. Traditional phase diagrams such as binary or ternary phase diagrams can rely on experimental determination but for multivariate systems, the experimental approach is not desirable. To overcome the obstacles, CALPHAD methods based on thermodynamic theory and thermodynamic databases are created. CALPHAD methods estimate the Gibbs free energy of each phase, such as solid solution (SS) phase, intermetallic compound (IM), etc., by calculating the mixing enthalpy and the conformational entropy. It is now possible to develop new materials on a more reliable basis. **Figure 6** shows the steps of the HEAs design using CALPHAD methods [15]. HEAs can be developed from these thermodynamic models directly or HEA databases can be created from the models specifically for HEAs. Once the parameters have been optimized, the relevant thermodynamic information can then be derived, such as the composition of each phase, phase ratio, activity, and mixing enthalpy. Several companies offer databases and associated software tools, notably PANDAT, FactSage, and Thermo-Calc [58], each of which has developed databases geared toward the study of HEAs. The main thermodynamic databases that have been developed for HEAs are PanHEA [59, 60] and TCHEA [13, 58] etc.

Because of their high hardness and excellent wear resistance, light-weight HEAs are suitable as protective coatings for machine components and tools [61]. Sanchez

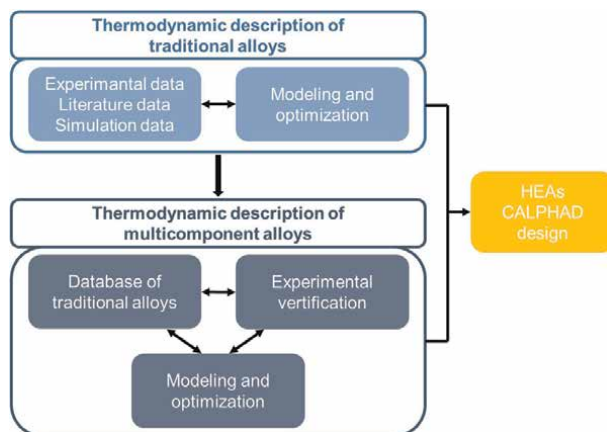


Figure 6.
The steps of HEAs compositional design using CALPHAD [15]. © 2020 Li, Xie, Wang, Liaw, and Zhang.

et al. [62] designed low-density and inexpensive $\text{Al}_{40}\text{Cu}_{15}\text{Cr}_{15}\text{Fe}_{15}\text{Si}_{15}$, $\text{Al}_{65}\text{Cu}_5\text{Cr}_5\text{Si}_{15}\text{Mn}_5\text{Ti}_5$, and $\text{Al}_{60}\text{Cu}_{10}\text{Fe}_{10}\text{Cr}_5\text{Mn}_5\text{Ni}_5\text{Mg}_5$ alloys by the CALPHAD method in conjunction with thermodynamic database TCAL5. CALPHAD thermodynamic modeling was successful in predicting the constituent phases, which were in close agreement with experimental results. But there remains a gap between Thermo-Calc calculations and the experimental results. Overall, this database has been proven to be an appropriate technique for designing Al-based HEAs. The growth of microelectronics has highlighted the importance of silicide materials - high entropy silicides (HES) [63, 64] that are especially promising due to their potential for use in microelectronics. ThermoCalc Software equipped with the TCHEA3 HEA thermodynamic database was used for complex HES compositions with targeted phase stability by Vyatskikh et al. [65]. Two single-phase HES materials were identified, the ternary $(\text{CrMoTa})\text{Si}_2$ and quinary $(\text{CrMoTaVNb})\text{Si}_2$. Both materials were identified using the CALPHAD method. It could be decided that both the ternary and quinary alloys were predicted to exhibit a single phase with a C40 hexagonal crystal structure.

Therefore, we conclude that the CALPHAD methodology is capable of formulating compositionally complex, HEA systems, and overcoming obstacles associated with certain experiments (such as high-temperature and high-pressure environments). To realize the rapid scientific design of materials, it is possible to use the component that is easy to calibrate by experiment to predict the component that is difficult to calibrate. Still, the non-equilibrium solidification structures observed in experiments and the CALPHAD calculations based on equilibrium have some differences.

5. Machine learning

Considering the complex elemental composition of HEAs, the use of an empirical “trial and error” material design paradigm may result in significant time and cost overruns, and thus a new material development paradigm is urgently required to guide the design of HEAs. Computing power and the development of computing platforms have led to an increase in computational materials science that has promoted the development of materials research and development from a trial-and-error

mode to a computation-driven process. As of late, the importance of MGI has resulted in the development of big data on materials and the full application of artificial intelligence to the development of HEAs. Among them, machine learning models such as support vector machine (SVM), principal component analysis (PCA), and cluster analysis play an important role in the construction and screening of HEA features and the prediction and classification of phase structures, and the prediction of HEA properties can be performed with the help of artificial neural networks, linear regression, and logistic regression. At the same time, active learning strategies based on Bayesian optimization and genetic algorithms are applied to the inverse optimization design of HEAs, which makes them have better comprehensive performance. Zhang et al. [66] used atomic radius, melting temperature, mixing entropy, and empirical parameters of HEA phase formation as features, and established a high-precision HEA phase classification model using a combination of genetic algorithm screening material features and machine learning models. Based on 322 data samples of cast HEAs, Li and Guo [67] built a support vector machine classification model by screening five material factors: VEC, δ , melting temperature (T_m), ΔS_{mix} , and ΔH_{mix} as features by sequential selection method, and the model achieved more than 90% accuracy in classifying HEAs as BCC single-phase, FCC single-phase and non-forming single-phase solid solution. Huang et al. [68] developed K-nearest neighbor (KNN), SVM, and artificial neural network (ANN) classification models based on 401 HEA data samples featuring VEC, electronegativity difference $\Delta\chi$, δ , ΔS_{mix} , and ΔH_{mix} . And then the prediction of whether the HEA formed SS, IM, and mixed SS and IM (SS + IM). The prediction accuracies of the three models obtained from cross-validation for the three classifications were 68.6%, 64.3%, and 74.3%, respectively. The reason for the low classification accuracy was found to be the unclear interphase boundary between SS and SS + IM by the self-organizing mapping (SOM) neural network. Then, the binary classification models of SS and IM, SS + IM and IM, SS and SS + IM were developed using multi-layer feed-forward neural network (MLFFNN) with classification accuracies of 86.7%, 94.3%, and 78.9%, respectively. Zhao et al. [69] applied machine learning to combine elemental characteristics with long-term ordering and established 87% of prediction accuracy. A deep neural network classification model for HEAs was developed by Lee et al. [70]. To compensate for the lack of experimental data, additional HEA data were generated using a conditional generative adversarial network (GAN), which improved the classification accuracy from 84.75% to 93.17%, exceeding the prediction accuracy of previous literature. Machine learning is generally based on big data, and data mining and cleaning are difficult. The quality of data will also directly determine the accuracy of prediction. Therefore, is it possible to make accurate predictions based on high-quality and relatively small data sets? A bilinear log model based on 21 HEA compositions was proposed by Steingrimsón et al. [71], and the break temperature, T_{break} , was introduced to predict the ultimate strength of temperature-dependent body-centered-cubic HEAs. They derived the ultimate strength as a function of composition and temperature by using **Figure 7** at high temperatures and defined the key T_{break} for optimizing the high temperature properties of the alloys.

HEAs experimental data has increased dramatically over the past two decades, and ML provides a means to utilize this information. In particular, ML in HEAs is currently focused on the prediction of phases, and there are 13 commonly used criteria as shown in **Table 1** [72]. In the future, a focus of machine learning will be to identify new unified criteria for phase formation in HEAs. Combined with simulation methods and machine learning already can accelerate the compositions

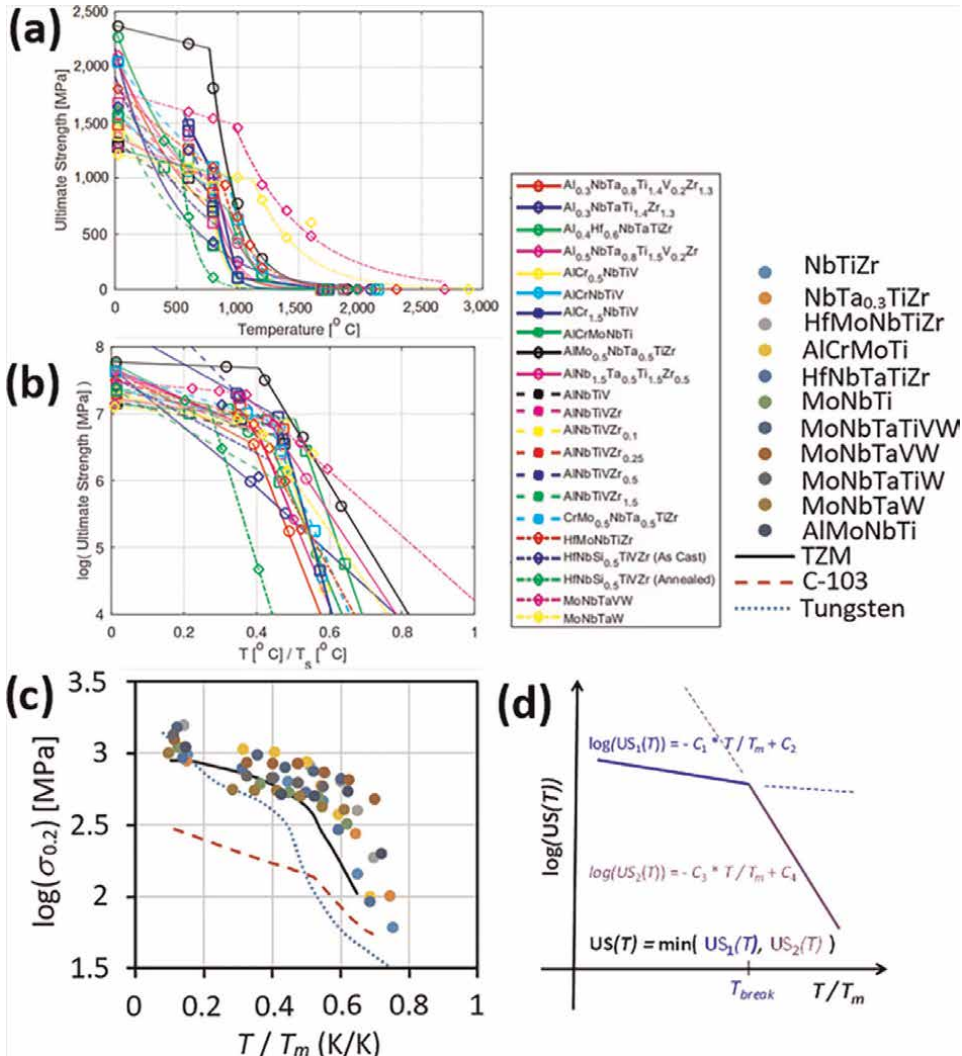


Figure 7. Identification of compositions with the ability to retain strengths at high temperatures [71].

Parameters	Formula
Mean atom radius	$a = \sum_{i=1}^n c_i r_i$
Atomic size difference	$\delta = \sqrt{\sum_{i=1}^n c_i \left(1 - \frac{r_i}{a}\right)^2}$
Average of the melting points of constituent elements	$T_m = \sum_{i=1}^n c_i T_{mi}$
Standard deviation of melting temperature	$\sigma_T = \sqrt{\sum_{i=1}^n c_i \left(1 - \frac{T_i}{T_m}\right)^2}$
Average mixing enthalpy	$\Delta H_{mix} = 4 \sum_{i \neq j} c_i c_j H_{ij}$
Standard deviation of mixing enthalpy	$\sigma_{\Delta H} = \sqrt{\sum_{i \neq j} c_i c_j (H_{ij} - \Delta H_{mix})^2}$

Parameters	Formula
Ideal mixing entropy	$S_{id} = -k_B \sum_{i=1}^n c_i \ln c_i$
Electronegativity	$\chi = \sum_{i=1}^n c_i \chi_i$
Standard deviation of electronegativity	$\Delta\chi = \sqrt{\sum_{i=1}^n c_i (\chi_i - \chi)^2}$
Average VEC	$VEC = \sum_{i=1}^n c_i VEC_i$
Standard deviation of VEC	$\sigma_{VEC} = \sqrt{\sum_{i=1}^n c_i (VEC_i - VEC)^2}$
Mean bulk modulus	$K = \sum_{i=1}^n c_i K_i$
Standard deviation of bulk modulus	$\sigma_K = \sqrt{\sum_{i=1}^n c_i (K_i - K)^2}$

Table 1.
The 13 design parameters and the corresponding formula [72].

and procedures of HEAs compositions and procedures. ML will play an important role in addressing challenges that are too difficult for relationships among phases/structures, the processing structure-property, the microstructure, and the performance of materials.

6. Conclusions

As computers have developed rapidly, materials have faced new challenges and opportunities. Developing new alloys is no longer a time-consuming and laborious trial-and-error process, but rather a method for efficiently exploring alloys using computations. Contrary to conventional alloys, HEAs are positioned in the center of the phase diagram. Many primary elements indicate a large composition space, which presents both impediments and challenges for the development. A number of HEAs are studied including RHEAs, light-weight HEAs, and others, all of which have great industrial applications. Based on the proposed simulations and calculations, researchers can target the exploration of alloy compositions based on properties in order to develop new HEAs. The focus of this chapter is on reviewing the simulation tools at different scales and summarizing cutting-edge research. The use of alloy design calculations based on DFT or MD calculations of alloy properties and multi-component phase diagrams calculated by CALPHAD is an effective method for saving time and reducing costs. However, the multi-element (more than 5) and microstructure (solid solution) of HEAs make the calculation process more complex and time-consuming than that of conventional alloys. In addition, there is a gap between the phase composition of HEAs determined by the experimental method and that predicted by the CALPHAD method. Therefore, combining more than two computational methods is a focus for future simulations. An example is the combination of DFT and CALPHAD methods. CALPHAD is often limited in scope due to the lack of reliable data. DFT method can calculate various thermodynamic properties, such as formation energy, heat of formation, etc. to supplement the data to provide support for phase diagrams. Last, it is also vital that a robust and comprehensive database be established for HEAs through the MGI project.

Acknowledgements

Yong Zhang acknowledges support from (1) Guangdong Basic and Applied Basic Research Foundation (2019B1515120020); and (2) Creative Research Groups of China (No.51921001).

Conflict of interest


The authors declare no conflict of interest.

Author details

Yong Zhang* and Yuanying Yue
State Key Laboratory of Advanced Metals and Materials, University of Science and Technology Beijing (USTB), Beijing, China

*Address all correspondence to: drzhangy@ustb.edu.cn

IntechOpen

© 2022 The Author(s). Licensee IntechOpen. This chapter is distributed under the terms of the Creative Commons Attribution License (<http://creativecommons.org/licenses/by/3.0>), which permits unrestricted use, distribution, and reproduction in any medium, provided the original work is properly cited. 

References

- [1] Viana F, Pinto AMP, Santos HMC, et al. Retrogression and re-ageing of 7075 aluminium alloy: Microstructural characterization. *Journal of Materials Processing Technology*. 1999;**92–93**: 54-59. DOI: 10.1016/S0924-0136(99)00219-8
- [2] Joel J, Anthony XM. Aluminium alloy composites and its machinability studies; A review. *Materials Today: Proceedings*. 2018;**5**:13556-13562. DOI: 10.1016/j.matpr.2018.02.351
- [3] Luo AA. Recent magnesium alloy development for elevated temperature applications. *International Materials Reviews*. 2004;**49**:13-30. DOI: 10.1179/095066004225010497
- [4] Cantor B, Chang ITH, Knight P, et al. Microstructural development in equiatomic multicomponent alloys. *Materials Science and Engineering A*. 2004;**375–377**:213-218. DOI: 10.1016/j.msea.2003.10.257
- [5] Yeh J-W, Chen S-K, Lin S-J, et al. Nanostructured high-entropy alloys with multiple principal elements: Novel alloy design concepts and outcomes. *Advanced Engineering Materials*. 2004; **6**:299-303. DOI: 10.1002/adem.200300567
- [6] Zhang Y, Zhou YJ, Lin JP, et al. Solid-solution phase formation rules for multi-component alloys. *Advanced Engineering Materials*. 2008; **10**:534-538. DOI: 10.1002/adem.200700240
- [7] Yang X, Zhang Y. Prediction of high-entropy stabilized solid-solution in multi-component alloys. *Materials Chemistry and Physics*. 2012;**132**: 233-238. DOI: 10.1016/j.matchemphys.2011.11.021
- [8] Gao MC, Yeh J-W, Liaw PK, et al., editors. *High-Entropy Alloys*. Cham: Springer International Publishing; 2016. DOI: 10.1007/978-3-319-27013-5
- [9] Guo S, Ng C, Lu J, et al. Effect of valence electron concentration on stability of FCC or BCC phase in high entropy alloys. *Journal of Applied Physics*. 2011;**109**:103505. DOI: 10.1063/1.3587228
- [10] de Pablo JJ, Jones B, Kovacs CL, et al. The materials genome initiative, the interplay of experiment, theory and computation. *Current Opinion in Solid State and Materials Science*. 2014;**18**: 99-117. DOI: 10.1016/j.cossms.2014.02.003
- [11] Green ML, Choi CL, Hattrick-Simpers JR, et al. Fulfilling the promise of the materials genome initiative with high-throughput experimental methodologies. *Applied Physics Reviews*. 2017;**4**:011105. DOI: 10.1063/1.4977487
- [12] Mishin Y, Asta M, Li J. Atomistic modeling of interfaces and their impact on microstructure and properties. *Acta Materialia*. 2010;**58**:1117-1151. DOI: 10.1016/j.actamat.2009.10.049
- [13] Chen H-L, Mao H, Chen Q. Database development and Calphad calculations for high entropy alloys: Challenges, strategies, and tips. *Materials Chemistry and Physics*. 2018;**210**:279-290. DOI: 10.1016/j.matchemphys.2017.07.082
- [14] Chen L, Hao X, Wang Y, et al. First-principles calculation of the effect of Ti content on the structure and properties of TiVNbMo refractory high-entropy alloy. *Materials Research Express*. 2020; **7**:106516. DOI: 10.1088/2053-1591/abbf11

- [15] Li R, Xie L, Wang WY, et al. High-throughput calculations for high-entropy alloys: A brief review. *Frontiers in Materials*. 2020;**7**:290. DOI: 10.3389/fmats.2020.00290
- [16] Ge H, Tian F. A review of ab initio calculation on lattice distortion in high-entropy alloys. *JOM*. 2019;**71**: 4225-4237. DOI: 10.1007/s11837-019-03777-1
- [17] Xie L, Brault P, Thomann A-L, et al. Molecular dynamics simulation of Al-Co-Cr-Cu-Fe-Ni high entropy alloy thin film growth. *Intermetallics*. 2016;**68**: 78-86. DOI: 10.1016/j.intermet.2015.09.008
- [18] Yao Y, Dong Q, Brozena A, et al. High-entropy nanoparticles: Synthesis-structure-property relationships and data-driven discovery. *Science*. 2022; **376**:eabn3103. DOI: 10.1126/science.abn3103
- [19] Wei P, Fan Y, Zhang W, et al. Understanding magnetic behaviors of FeCoNiSi_{0.2}M_{0.2} (M=Cr, Mn) high entropy alloys via first-principle calculation. *Journal of Magnetism and Magnetic Materials*. 2021;**519**:167432. DOI: 10.1016/j.jmmm.2020.167432
- [20] Raghuraman V, Wang Y, Widom M. An investigation of high entropy alloy conductivity using first-principles calculations. *Applied Physics Letters*. 2021;**119**:121903. DOI: 10.1063/5.0065239
- [21] Hohenberg P, Kohn W. Inhomogeneous electron gas. *Physics Review*. 1964;**136**:B864-B871. DOI: 10.1103/PhysRev.136.B864
- [22] Ryabinkin IG, Kohut SV, Staroverov VN. Reduction of electronic wave functions to Kohn-sham effective potentials. *Physical Review Letters*. 2015;**115**:083001. DOI: 10.1103/PhysRevLett.115.083001
- [23] Snyder JC, Rupp M, Hansen K, et al. Finding density functionals with machine learning. *Physical Review Letters*. 2012;**108**:253002. DOI: 10.1103/PhysRevLett.108.253002
- [24] Curtarolo S, Hart GLW, Nardelli MB, et al. The high-throughput highway to computational materials design. *Nature Materials*. 2013;**12**: 191-201. DOI: 10.1038/nmat3568
- [25] George EP, Curtin WA, Tasan CC. High entropy alloys: A focused review of mechanical properties and deformation mechanisms. *Acta Materialia*. 2020;**188**: 435-474. DOI: 10.1016/j.actamat.2019.12.015
- [26] Kresse G, Furthmüller J. Efficient iterative schemes for ab initio total-energy calculations using a plane-wave basis set. *Physical Review B: Condensed Matter*. 1996;**54**:11169-11186. DOI: 10.1103/physrevb.54.11169
- [27] Tian F. A review of solid-solution models of high-entropy alloys based on ab initio calculations. *Frontiers in Materials*. 2017;**4**:36. DOI: 10.3389/fmats.2017.00036
- [28] Kresse G, Hafner J. Ab initio molecular dynamics for liquid metals. *Physical Review B*. 1993;**47**:558-561. DOI: 10.1103/PhysRevB.47.558
- [29] Clark SJ, Segall MD, Pickard CJ, et al. First principles methods using CASTEP. *Zeitschrift für Kristallographie—Crystalline Materials*. 2005;**220**:567-570. DOI: 10.1524/zkri.220.5.567.65075
- [30] Soler JM, Artacho E, Gale JD, et al. The SIESTA method for abinitio order-N materials simulation. *Journal of Physics:*

- Condensed Matter. 2002;**14**:2745-2779. DOI: 10.1088/0953-8984/14/11/302
- [31] Wang S, Xiong J, Li D, et al. Comparison of two calculation models for high entropy alloys: Virtual crystal approximation and special quasi-random structure. *Materials Letters*. 2021;**282**: 128754. DOI: 10.1016/j.matlet.2020.128754
- [32] Liao M, Liu Y, Min L, et al. Alloying effect on phase stability, elastic and thermodynamic properties of Nb-Ti-V-Zr high entropy alloy. *Intermetallics*. 2018;**101**:152-164. DOI: 10.1016/j.intermet.2018.08.003
- [33] Tian F, Wang D, Shen J, et al. An ab initio investigation of ideal tensile and shear strength of TiVNbMo high-entropy alloy. *Materials Letters*. 2016; **166**:271-275. DOI: 10.1016/j.matlet.2015.12.064
- [34] Ge H. Elastic and thermal properties of refractory high-entropy alloys from first-principles calculations. *Computational Materials Science*. 2017; **128**:185-190. DOI: 10.1016/j.commatsci.2016.11.035
- [35] Niu C, Zaddach AJ, Koch CC, et al. First principles exploration of near-equiatom NiFeCrCo high entropy alloys. *Journal of Alloys and Compounds*. 2016;**672**:510-520. DOI: 10.1016/j.jallcom.2016.02.108
- [36] Rao Z, Dutta B, Körmann F, et al. Unveiling the mechanism of abnormal magnetic behavior of FeNiCoMnCu high-entropy alloys through a joint experimental-theoretical study. *Physical Review Materials*. 2020;**4**:014402. DOI: 10.1103/PhysRevMaterials.4.014402
- [37] Cieslak J, Tobola J, Przewoznik J, et al. Multi-phase nature of sintered vs. arc-melted CrxAlFeCoNi high entropy alloys—Experimental and theoretical study. *Journal of Alloys and Compounds*. 2019;**801**:511-519. DOI: 10.1016/j.jallcom.2019.06.121
- [38] Singh P. First-principles prediction of incipient order in arbitrary high-entropy alloys: Exemplified in Ti_{0.25}CrFeNiAl_x. *Acta Materialia*. 2020; **189**:248-254. DOI: 10.1016/j.actamat.2020.02.063
- [39] Widom M. Modeling the structure and thermodynamics of high-entropy alloys. *Journal of Materials Research*. 2018;**33**:2881-2898. DOI: 10.1557/jmr.2018.222
- [40] Gao MC, Niu C, Jiang C, et al. Applications of special quasi-random structures to high-entropy alloys. In: Gao MC, Yeh J-W, Liaw PK, et al., editors. *High-Entropy Alloys: Fundamentals and Applications*. Cham: Springer International Publishing; 2016. pp. 333-368. DOI: 10.1007/978-3-319-27013-5_10
- [41] van de Walle A, Asta M, Ceder G. The alloy theoretic automated toolkit: A user guide. *Calphad*. 2002;**26**:539-553. DOI: 10.1016/S0364-5916(02)80006-2
- [42] van de Walle A. Multicomponent multisublattice alloys, nonconfigurational entropy and other additions to the alloy theoretic automated toolkit. *Calphad*. 2009;**33**: 266-278. DOI: 10.1016/j.calphad.2008.12.005
- [43] van de Walle A, Tiwary P, de Jong M, et al. Efficient stochastic generation of special quasirandom structures. *Calphad*. 2013;**42**:13-18. DOI: 10.1016/j.calphad.2013.06.006
- [44] Zhang YH, Zhuang Y, Hu A, et al. The origin of negative stacking fault energies and nano-twin formation in

face-centered cubic high entropy alloys. *Scripta Materialia*. 2017;**130**:96-99. DOI: 10.1016/j.scriptamat.2016.11.014

[45] Chen C, Zhang H, Fan Y, et al. Improvement of corrosion resistance and magnetic properties of FeCoNiAl_{0.2}Si_{0.2} high entropy alloy via rapid-solidification. *Intermetallics*. 2020;**122**:106778. DOI: 10.1016/j.intermet.2020.106778

[46] Wang X, Guo W, Fu Y. High-entropy alloys: Emerging materials for advanced functional applications. *Journal of Materials Chemistry A*. 2021;**9**:663-701. DOI: 10.1039/D0TA09601F

[47] Chen C, Zhang H, Hu S, et al. Influences of laser surface melting on microstructure, mechanical properties and corrosion resistance of dual-phase Cr-Fe-Co-Ni-Al high entropy alloys. *Journal of Alloys and Compounds*. 2020;**826**:154100. DOI: 10.1016/j.jallcom.2020.154100

[48] Zuo T, Gao MC, Ouyang L, et al. Tailoring magnetic behavior of CoFeMnNi_X (X = Al, Cr, Ga, and Sn) high entropy alloys by metal doping. *Acta Materialia*. 2017;**130**:10-18. DOI: 10.1016/j.actamat.2017.03.013

[49] Plimpton S. Fast parallel algorithms for short-range molecular dynamics. *Journal of Computational Physics*. 1995;**117**:1-19. DOI: 10.1006/jcph.1995.1039

[50] Kulakova L, Arampatzis G, Angelikopoulos P, et al. Data driven inference for the repulsive exponent of the Lennard-Jones potential in molecular dynamics simulations. *Scientific Reports*. 2017;**7**:16576. DOI: 10.1038/s41598-017-16314-4

[51] Kang H, Zhang Y, Yang M. Molecular dynamics simulation of thermal conductivity of Cu-Ar nanofluid

using EAM potential for Cu-Cu interactions. *Applied Physics A: Materials Science & Processing*. 2011;**103**:1001. DOI: 10.1007/s00339-011-6379-z

[52] Varvenne C, Luque A, Nöhning WG, et al. Average-atom interatomic potential for random alloys. *Physical Review B*. 2016;**93**:104201. DOI: 10.1103/PhysRevB.93.104201

[53] Ding S, Li Y, Luo Y, et al. Modified embedded-atom interatomic potential parameters of the Ti-Cr binary and Ti-Cr-N ternary systems. *Frontiers in Chemistry*. 2021;**9**:773015. DOI: 10.3389/fchem.2021.773015

[54] Oluwajobi A, Chen X. The effect of interatomic potentials on the molecular dynamics simulation of nanometric machining. *International Journal of Automation and Computing*. 2011;**8**:326-332. DOI: 10.1007/s11633-011-0588-y

[55] Qi Y, He T, Xu H, et al. Effects of microstructure and temperature on the mechanical properties of nanocrystalline CoCrFeMnNi high entropy alloy under nanoscratching using molecular dynamics simulation. *Journal of Alloys and Compounds*. 2021;**871**:159516. DOI: 10.1016/j.jallcom.2021.159516

[56] Jiang J, Chen P, Qiu J, et al. Microstructural evolution and mechanical properties of Al_xCoCrFeNi high-entropy alloys under uniaxial tension: A molecular dynamics simulations study. *Materials Today Communications*. 2021;**28**:102525. DOI: 10.1016/j.mtcomm.2021.102525

[57] Luo G, Li L, Fang Q, et al. Microstructural evolution and mechanical properties of FeCoCrNiCu high entropy alloys: A microstructure-based constitutive model and a molecular dynamics simulation study.

- Applied Mathematics and Mechanics. 2021;**42**:1109-1122. DOI: 10.1007/s10483-021-2756-9
- [58] Mao H, Chen H-L, Chen Q. TCHEA1: A thermodynamic database not limited for “high entropy” alloys. *Journal of Phase Equilibria and Diffusion*. 2017;**38**:353-368. DOI: 10.1007/s11669-017-0570-7
- [59] Gao MC, Zhang C, Gao P, et al. Thermodynamics of concentrated solid solution alloys. *Current Opinion in Solid State and Materials Science*. 2017;**21**: 238-251. DOI: 10.1016/j.cossms.2017.08.001
- [60] Zhang C, Zhang F, Diao H, et al. Understanding phase stability of Al-Co-Cr-Fe-Ni high entropy alloys. *Materials & Design*. 2016;**109**:425-433. DOI: 10.1016/j.matdes.2016.07.073
- [61] Kumar A, Gupta M. An insight into evolution of light weight high entropy alloys: A review. *Metals*. 2016;**6**:199. DOI: 10.3390/met6090199
- [62] Sanchez JM, Vicario I, Albizuri J, et al. Phase prediction, microstructure and high hardness of novel light-weight high entropy alloys. *Journal of Materials Research and Technology*. 2019;**8**:795-803. DOI: 10.1016/j.jmrt.2018.06.010
- [63] Liu D, Huang Y, Liu L, et al. A novel of MSi₂ high-entropy silicide: Be expected to improve mechanical properties of MoSi₂. *Materials Letters*. 2020;**268**:127629. DOI: 10.1016/j.matlet.2020.127629
- [64] Gild J, Braun J, Kaufmann K, et al. A high-entropy silicide: (Mo_{0.2}Nb_{0.2}Ta_{0.2}Ti_{0.2}W_{0.2})Si₂. *Journal of Materiomics*. 2019;**5**:337-343. DOI: 10.1016/j.jmat.2019.03.002
- [65] Vyatskikh AL, MacDonald BE, Dupuy AD, et al. High entropy silicides: CALPHAD-guided prediction and thin film fabrication. *Scripta Materialia*. 2021;**201**:113914. DOI: 10.1016/j.scriptamat.2021.113914
- [66] Zhang Y, Wen C, Wang C, et al. Phase prediction in high entropy alloys with a rational selection of materials descriptors and machine learning models. *Acta Materialia*. 2020;**185**:528-539. DOI: 10.1016/j.actamat.2019.11.067
- [67] Li Y, Guo W. Machine-learning model for predicting phase formations of high-entropy alloys. *Physical Review Materials*. 2019;**3**:095005. DOI: 10.1103/PhysRevMaterials.3.095005
- [68] Huang W, Martin P, Zhuang HL. Machine-learning phase prediction of high-entropy alloys. *Acta Materialia*. 2019;**169**:225-236. DOI: 10.1016/j.actamat.2019.03.012
- [69] Zhao DQ, Pan SP, Zhang Y, et al. Structure prediction in high-entropy alloys with machine learning. *Applied Physics Letters*. 2021;**118**:231904. DOI: 10.1063/5.0051307
- [70] Lee SY, Byeon S, Kim HS, et al. Deep learning-based phase prediction of high-entropy alloys: Optimization, generation, and explanation. *Materials & Design*. 2021;**197**:109260. DOI: 10.1016/j.matdes.2020.109260
- [71] Steingrimsson B, Fan X, Yang X, et al. Predicting temperature-dependent ultimate strengths of body-centered-cubic (BCC) high-entropy alloys. *npj Computational Materials*. 2021;**7**:1-10. DOI: 10.1038/s41524-021-00623-4
- [72] Zhou Z, Zhou Y, He Q, et al. Machine learning guided appraisal and exploration of phase design for high entropy alloys. *npj Computational Materials*. 2019;**5**:1-9. DOI: 10.1038/s41524-019-0265-1

Chapter 9

CALPHAD as a Toolbox to Facilitate the Development of HEAs

Wei Wang and Zhou Li

Abstract

This chapter would be a comprehensive review of the successful application of the CALPHAD method in the research and development of high-entropy alloys (HEAs) in recent years. The structure of this chapter is obedient to the conventional framework in materials science, and several topics would be covered, including composition and structure design, heat treatment and solidification processing, and some properties and performances, such as mechanical and electrochemical corrosion behaviors and high-temperature oxidation characteristics. A conclusion and outlook of the CALPHAD method are also provided at the end of this chapter. Hope this chapter could offer a thermodynamic and kinetic perspective for facilitating the field of HEA research and inspire other researchers to contribute more valuable ideas and works.

Keywords: high-entropy alloys, CALPHAD, materials design, processing optimization, mechanical properties, electrochemical corrosion, high-temperature oxidation

1. Introduction

The concept of high-entropy alloys (HEAs), where the configurational entropy plays a significant role, is closely related to the content of thermodynamics. As a phenomenological methodology of computational thermodynamics, CALPHAD could be the most direct tool for the design of HEAs [1]. CALPHAD stands for the abbreviation of CALculation of PHase Diagram, which is a computational approach proposed in the early 1970s to bridge the gap between the theoretical calculations and the experimental phase equilibrium information [2]. The Gibbs energy function occupies the core of the CALPHAD method. Thermodynamic properties of the materials could be described by the Gibbs energy of each phase. The phase diagrams are constructed by minimizing the total Gibbs energy of the system. The model parameters of Gibbs energy, which is the main constitute of the CALPHAD databases, are assessed by fitting the input data via CALPHAD-based software, such as Thermo-Calc [3], Pandat [4], and FactSage [5]. The experimental results would be the first choice for the input, and the first-principle calculations would be a good complement wherever there is a lack of experimental input [6]. The Gibbs energy of an element can be written as follows [7]:

$$G_i^0 - H_i^{SER} = a + bT + cT \ln(T) + dT^2 + dT^{-1} + fT^3 + \dots \quad (1)$$

where H_i^{SER} represents the enthalpy of the pure element i in its reference state standard element reference (SER). This reference state is defined as the most stable state of the pure element at 298.15 K and 1 bar. Coefficients a, b, c, d, \dots are the parameters to be optimized.

To deal with the case containing more elements, several models were proposed to describe the atomic interactions, such as compound energy formalism (CEF) [8], cluster variation method [9], quasi-chemical model [10], and so on. In this chapter, the compound energy formalism (CEF) as the most widely used model was introduced. In the CEF, the structure of a phase is considered to be constituted by a set of sublattices represented by the formula $(A, C)_x(B, D)_y$, with A, C mixing on the first sublattice and B, D occupying the second one [6].

$$G_m^\alpha = Srf G_m + T^{cfg} S_m + Phy G_m + Ex G_m \\ = \sum P_{I_0}(Y) G_{end}^\circ + RT \sum \sum n^s y_j^s \ln(y_j^s) + Phy G_m + \sum P_{I_1}(Y) L_{I_1} + \sum P_{I_2}(Y) L_{I_2} \dots \quad (2)$$

$Srf G_m$ is named ‘‘surface of reference,’’ which is a linear combination of the Gibbs energy of end-members. $^{cfg} S_m$ denotes the configurational entropy of the phase, considering the ideal mixing only. The sum of $Srf G_m$ and $T^{cfg} S_m$ is the so-called ideal solution model. $^{Phy} G_m$ describes the physical effect (usually the magnetic effect), which was treated separately. $^{Ex} G_m$ represents the excess Gibbs energy describing the interactions between the constituents in different sublattices. $P_{I_0}(Y)$ refers to the product of site fraction in I_0 , which means an array of zeroth order including only one constituent in each sublattice. $P_{I_n}(Y)$ corresponds to the n th-order array, which contains n extra constituents in sublattices 1, 2, \dots , $n - 1$. n^s is the number of sites in sublattice s and y_j^s is the site fraction of element j in sublattices. L denotes the interaction parameter, which is a Redlich-Kister polynomial.

One of the aims of the CALPHAD method is to develop the reliable databases for the users of interest. The descriptions of stable binaries and ternaries are the building blocks for the multicomponent CALPHAD databases. The CALPHAD method uses extrapolation to extend the range from these stable constituent lower systems to the unstable region and higher order systems. The semiempirical nature and the unique structure of the database (**Figure 1**) make CALPHAD an accurate and self-consistent technique and gain the popularity in the research of structural materials [11]. Therefore, the CALPHAD has been considered as an important part of the Integrated Computational Materials Engineering (ICME) and Materials Genome Initiative (MGI) [12].

With the combination of thermodynamic and kinetic databases, the CALPHAD method could not only depict the characteristics of thermodynamics (phase diagrams and thermophysical properties) but also simulate the kinetic process (precipitation and diffusion) by solving the diffusion equations numerically. The following sections will show how the CALPHAD method serves as a powerful toolbox to facilitate the development of the HEAs.

2. Thermodynamic calculations in the composition and phase design of HEAs

The emergence of the HEA provides a new alloying strategy for the materials scientists. Different from the conventional way of adding a handful of alloying

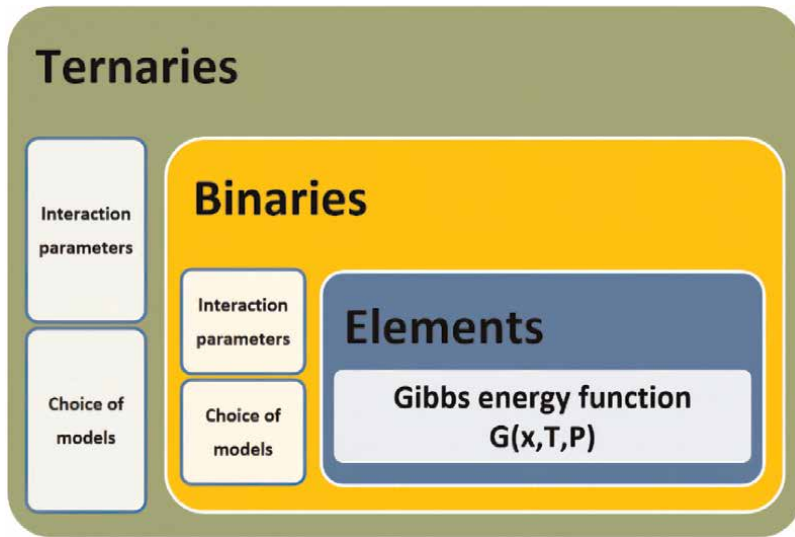


Figure 1.
The structure of the CALPHAD thermodynamic databases.

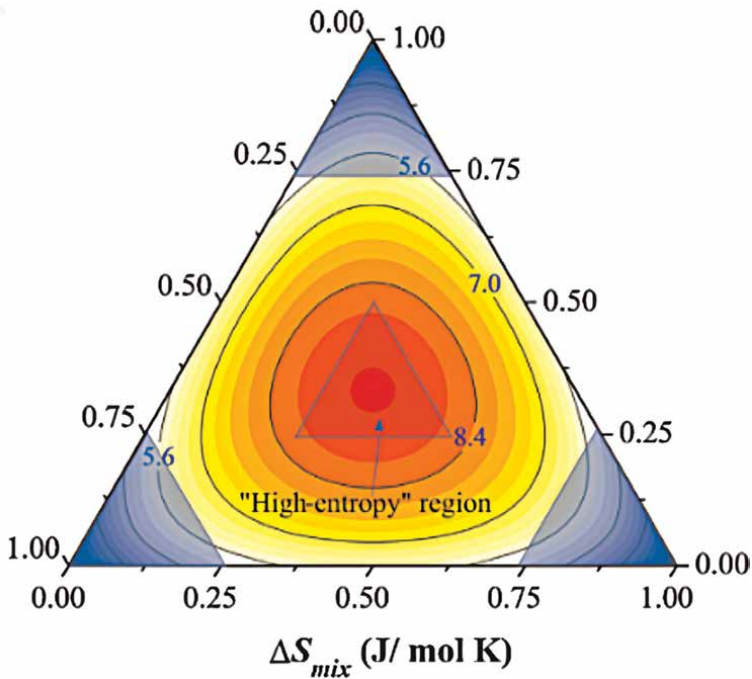


Figure 2.
The contour map of entropy of mixing on an illustrated ternary alloy. The blue regions represent the conventional alloys with only one principal element and the bright area indicates the high-entropy region [13].

elements to a primary one, the HEA creates a mixture of the multiple principle elements with (near) equiatomic concentration [13, 14]. The most intuitive representation of this strategy would be the composition map of the phase diagram (**Figure 2**). The conventional alloys locate at the corner regions (blue region), and the HEAs

occupy the central region of the phase diagram. Therefore, the name of “central alloys” is perhaps a good choice to eliminate the ambiguity caused by the confusing use of “high-entropy alloys,” “medium-entropy alloys,” “complex concentrated alloys (CCAs),” “multiprincipal element alloys (MPEAs),” etc. Its vastness of the composition space and the complex combination of elements open the possibilities of discovering novel alloys with exceptional properties [15]. Meanwhile, it is a more challenging task of the HEA design to find the desired point in this composition sea. As the sole technique of visualizing the phase diagram directly, the CALPHAD method that is expert in the composition and phase design for the multicomponent systems could serve as an equipped ship for the HEA researchers. Hundreds of published works have applied the CALPHAD method in the phase prediction of HEAs [16, 17]. In this section, the advantage and limitations of the CALPHAD method will be discussed with several examples.

2.1 Application of CALPHAD databases in the HEA design

Phase diagrams have been considered as the road map for the research of materials science, which act as a guiding role to design the experiments and understand the behavior of the materials. As mentioned above, the accuracy of the calculated phase diagram depends on the reliability of the CALPHAD databases. Owing to the lack of specific HEA databases, the early works usually uses the Ni-base and, sometimes, the Fe-base databases to explore the alloy composition of the desired phase. Choi et al. [18] used the TCFE2000 database [19] to design a new face-centered cubic (FCC) phase HEA with nonequiatomic composition. **Figure 3** shows that the prepared samples fall well on the FCC single-phase region, which verifies the validity of the

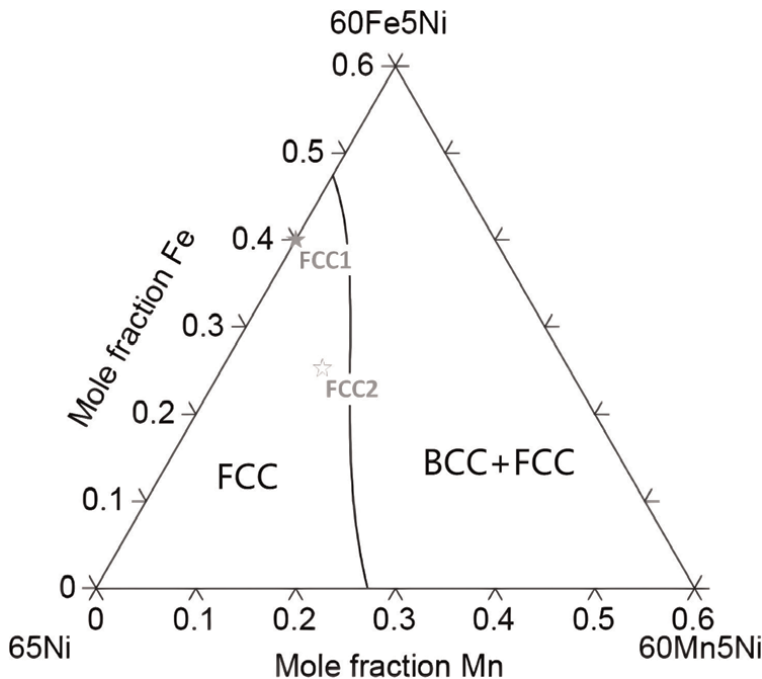


Figure 3. Calculated FCC phase region of 10Co-15Cr-10 V-65 (Fe, Mn, Ni) [18].

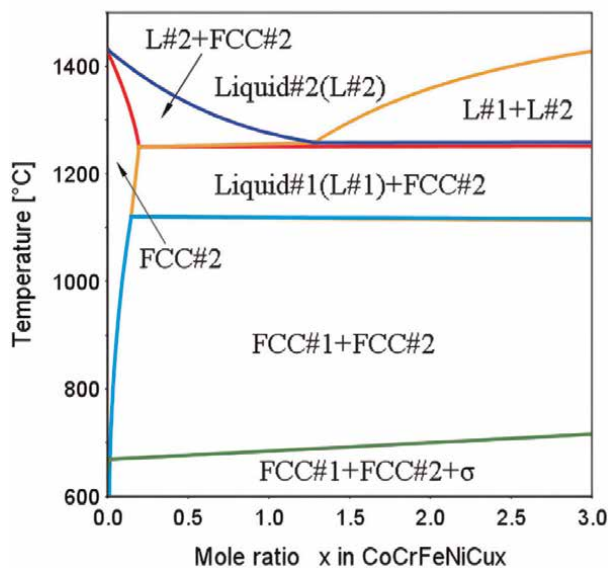


Figure 4.
Pseudobinary phase diagram of CoCrFeNiCux [20].

CALPHAD calculation. Zhang et al. [20] employed the Thermo-Calc software [3] with database TCNI8 [19] to calculate the phase diagram of the CoCrFeNi-based HEAs. In **Figure 4**, the pseudobinary phase diagram of CrCoFeNi-Cux was calculated to show the alloying effect of Cu on the phase stability of the HEA. Miscibility gaps of FCC and liquid phase begin to form with the increasing Cu content. This calculated result has been experimentally confirmed by the work of Wu et al. [21]. Butler et al. [22] studied the phase stability of AlNiCoCrFe alloy using the CALPHAD approach. **Figure 5d** shows their prediction on the phase fractions of the Al15 HEA calculated by using the TCNI8 database. They found that the predicted phase stability was generally in agreement with the experimental measurements except the FCC phase. These findings indicate that the CALPHAD could be a powerful tool for the design of HEAs, but the quality of the databases needs to be improved. Therefore, the specific thermodynamic databases, TCHEA [23] and PanHEA [24], have been tailored in recent years to accelerate the development of HEAs. Feng et al. [25] extensively investigated the phase stability of the lightweight HEAs using both the experimental and computational methods. They calculated the phase fraction of each in Al1.5CrFeMnTi alloy (**Figure 6a**) and the isopleth of Al1.5CrFeMnTix (**Figure 6b**) using Pandat software with the PanHEA database. A reasonable agreement has been reported between the experimentally determined and predicted compositions. One of the disagreements is that the nanosized L21 phase was experimentally observed at higher annealing temperature than the predicted one. MacDonald et al. [26] thoroughly discussed the FCC phase decomposition of the equiatomic CoCuFeMnNi alloy with the aid of the CALPHAD method. They performed the calculation on the equilibrium step diagram of CoCuFeMnNi alloy at the temperature range from 400 to 1600°C employing the Thermo-Calc software with database TCHEA3 and compared the experimentally observed compositions of three phases with the CALPHAD-predicted ones at 500°C. It can be seen in **Figure 7** that the composition predicted by CALPHAD reasonably agrees with the measured ones except the case in the Cu-rich FCC phase. Although the

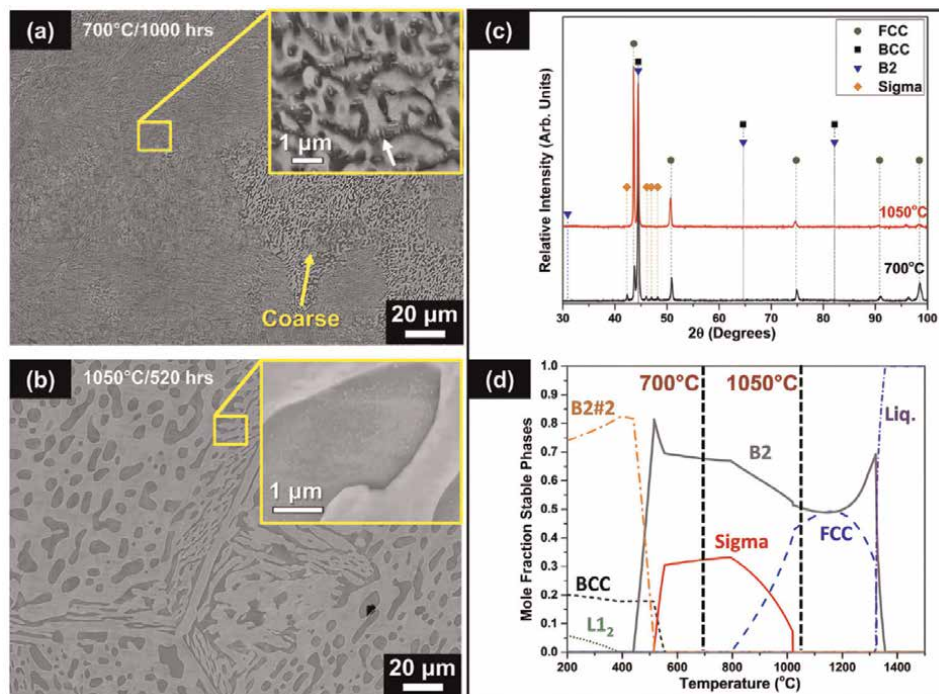


Figure 5. BSE image of Al₁₅ HEA heated treating at (a) 700°C and (b) 1050°C, (c) XRD spectra of Al₁₅ HEA, and (d) calculated phase fractions for the Al₁₅ HEA [22].

CALPHAD has been successfully applied to the phase and composition design of HEAs, its power has not been fully explored due to the imperfection of the databases. The difficulties of developing a high-quality HEA database could be attributed to several reasons. As we noted earlier, the traditional alloy databases were developed based on the binaries and ternaries with only one principal component, while the HEAs focus on the central regions of the alloy systems. Therefore, one of the difficulties is that there is lack of experimental data on this region as the input for the CALPHAD assessment [27]. Another thing that should be noted is that the ternary interaction could be significant at the highly concentrated region, so all the ternaries should be carefully evaluated [28]. Those barriers will burden the workload of assessment exponentially and make it almost a “mission impossible” to develop a perfect HEA database in a short term [27].

2.2 High-throughput CALPHAD (HT-CALPHAD) calculations for the HEA design

Alternatively, the high-throughput CALPHAD method and the machine learning (ML) models provide us a promising way of accelerating the design of advanced HEAs. Feng et al. [29] utilized the CALPHAD-based high-throughput calculation to screen the optimal composition of the lightweight HEAs. The vast composition space has been narrowed to a small range by meeting the criteria on phase fraction and temperature, with eight candidate alloys surviving out finally (**Figure 8**). In **Figure 8b–e**, region 1 meets only one criterion, region 2 meets two of criteria, and

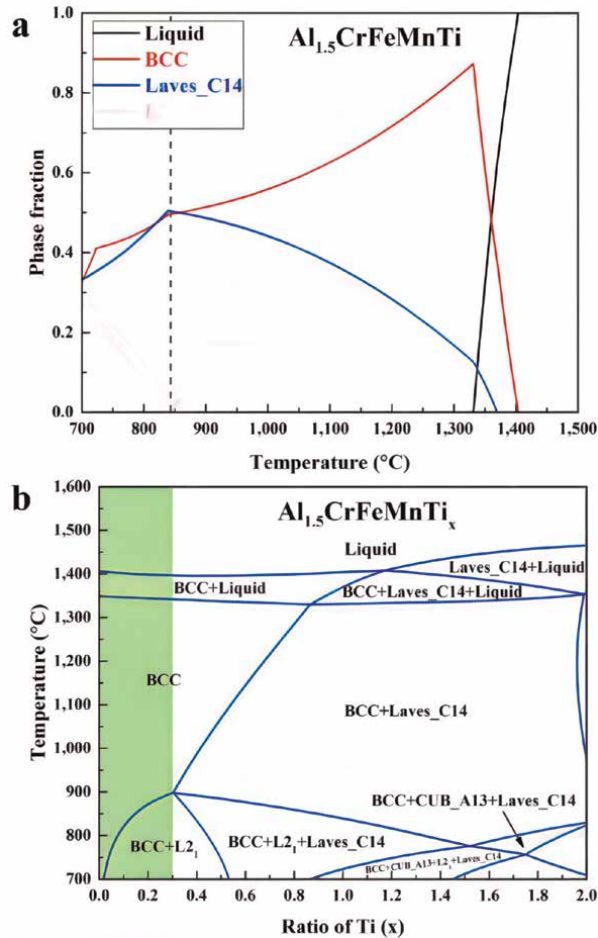


Figure 6. Calculated phase diagram of the (a) alloy $Al_{1.5}CrFeMnTi$ and (b) isopleth of $Al_{1.5}CrFeMnTi_x$ [25].

region 3 meets three. This approach significantly reduces the cost of experimental work. Zeng et al. [30] proposed several phase selection rules by combining the machine learning method and the CALPHAD calculations. The flowchart of this chapter is summarized in **Figure 9**. More than 300,000 of entries of phase equilibrium information were generated by the CALPHAD method. Then, the XGBoost method was employed to explore five most important features to depict the composition space spanned by the generated data. Based on the trained ML model, five-phase selection rules were established, which provides an efficient approach of designing a single-phase HEA. The CALPHAD method has accumulated tons of high-quality phase equilibria and thermochemical data in decades, which would be a valuable resource for the machine learning models. At the same time, ML could help CALPHAD extend its application and establish the structure–property connection quantitatively. A recent review of the HT-CALPHAD method could be found in [31].

Besides, thermodynamic analysis on the phase stability of single solid solution (SSS) phases in HEA has also been extensively studied by using the CALPHAD method [14, 32]. Unexpectedly, the configurational entropy does not play the

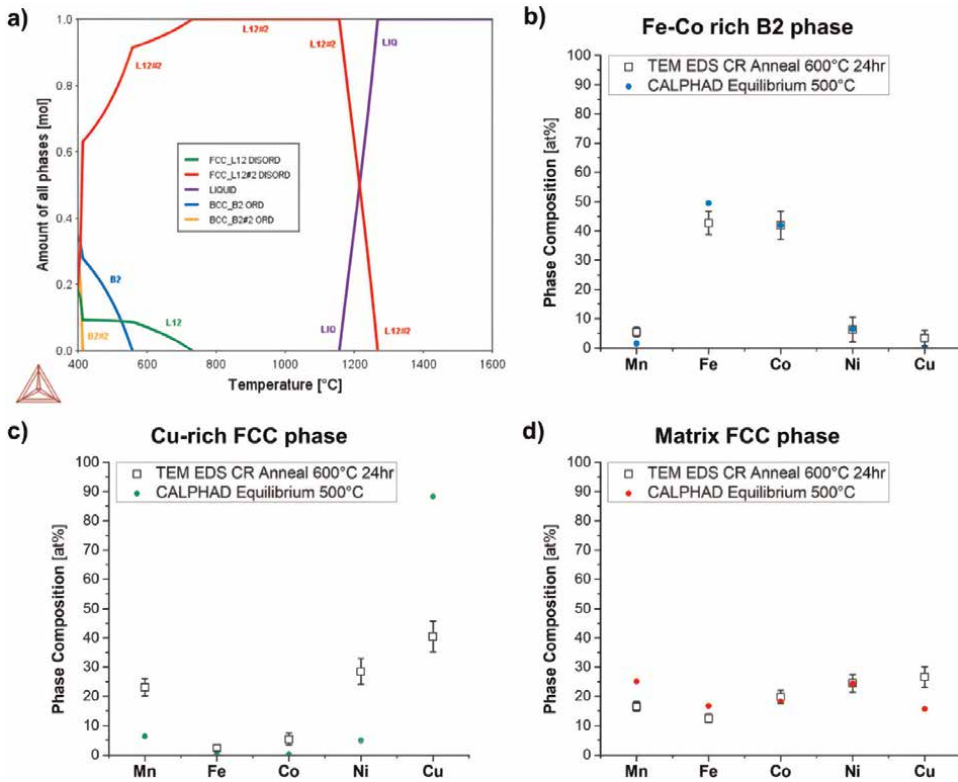


Figure 7. (a) Calculated equilibrium step diagram of the CoCuFeMnNi alloy from 400–1600°C compared with experimentally measured phase composition from STEM EDS, (b) Fe-Co rich B2 phase, (c) Cu-rich FCC phase, and (d) the matrix FCC phase [26].

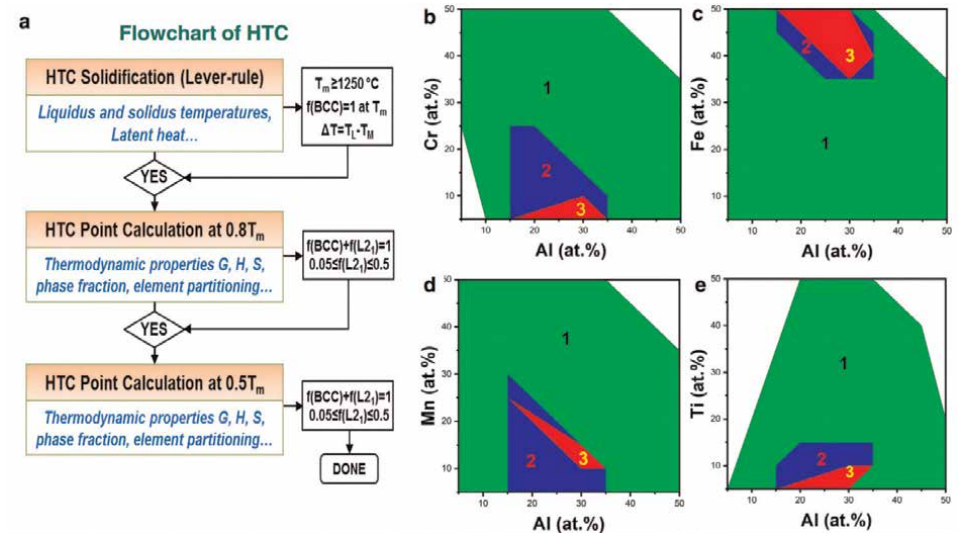


Figure 8. (a) Flowchart of the HT-CALPHAD, (b) Al-Cr projection, (c) Al-Fe projection, (d) Al-Mn projection, and (e) Al-Ti projection [29].

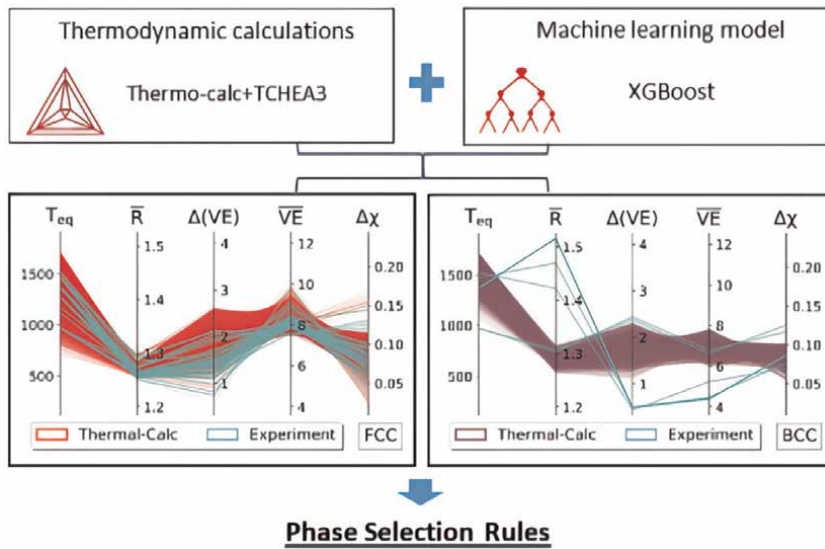


Figure 9.
The road map for the discovery of phase selection rules [30].

dominant role in many cases [1]. Other entropic contribution and enthalpy should also be valued in the analysis because the phase stability of the SSS depends on the Gibbs energy ($G = H - TS$) of its competing intermetallic phases [14, 15]. A widely accepted framework of this analysis is needed for further research.

3. CALPHAD-based prediction in processing optimization

3.1 Heat treatment processing optimization

Known as the idiom “the refined steel, softly winds fingers,” the condensed words were refined as the most significant information about heat treatment in the present perspective. For metallic materials, heat treatment represents some thermal as well as thermochemical processes to bring a series of complicated transformations in physical metallurgy, mechanical, and corrosion resistance performances. Therefore, to understand heat treatment, it is necessary to study the thermal phenomena, microstructure, phase stability/transformation, properties, and so on. As a kind of promising material, HEAs like other ferrous and nonferrous alloys, heat treatment is also an important process for improving formability, machinability, strength, and ductility.

As the name implies, the CALPHAD method is a technique of calculation for phase diagram initially. Therefore, in the field of the phase diagram, the CALPHAD method is inherently associated with a unique advantage in comparison with other techniques. One of the most important advantages of the CALPHAD method is to predict high-order thermodynamic information via extrapolation from the corresponding low-order subsystems. To realize the CALPHAD method, it is required to combine both computational platforms and some thermodynamic and mobility databases, and so on. Some commercial software is available to perform various calculation and simulation, including Thermo-Calc software (also add-on diffusion and precipitation module,

Dictra & TC-Prisma) [3, 19], Pandat [33], and FactSage [34]. Some commercial databases also need to be matched in these software to provide various thermodynamic and mobility information, including TCHEA5 and MOBHEA2 [35], PanHEA_TH, PanHEA_MB, and PanHEA_MV [36]. The continuous update databases, which contained dozens of elements and hundreds of subsystems, provide a set of self-consistent thermodynamic and kinetic parameters to assist a high-quality prediction. With the development of thermodynamic and kinetic modeling, the CALPHAD method has played a more and more important role in materials design, processing optimization, phase transformation, mechanical and corrosion behavior investigations, and so on.

In this section, some CALPHAD-based research on the heat treatment of HEAs was collected to aim at highlighting the significant role of the CALPHAD method in the thermodynamic, kinetic, and precipitation predictions, which are the three main parts of this section.

3.1.1 Thermodynamic analysis of heat treatment

The phase diagram is one of the most important components in the field of materials science and technology, obviously in the field of heat treatment. Thus, the CALPHAD method has an inherent advantage due to the technique that was initially originated to couple the phase diagrams and thermochemistry, especially due to the extrapolation characteristic. For “multiprincipal element alloy (MPEA)” [37, 38] or “complex concentrated alloy (CCA)” [39] systems, the extrapolation characteristic from the known low-order subsystems to the unknown high-order HEAs system becomes an outstanding superiority of the CALPHAD method, particularly in comparison with the conventional one or two principal metallic materials. To complete a high-quality thermodynamic prediction needs an important prerequisite, i.e., a set of critical, reliable, and self-consistent thermodynamic modeling, especially in the whole composition and at a wide temperature range, due to the equiatomic or near-equiatomic composition region of the HEA system.

The application of the CALPHAD-based thermodynamic analysis in heat treatment will be introduced as follows.

The equilibrium mapping and stepping calculations of the phase diagram, viz., calculated isothermal/isoplethal sections and calculated equilibrium phase fraction at various temperatures, are two major applications in materials design and also in heat treatment optimization. The basic investigation approach is to study from the subsystems (i.e., binary and ternary) to the multicomponent HEA systems; some examples for determining the temperature of annealing heat treatment for a proposed alloy are shown in (**Figures 10** and **11**) [27, 40, 41].

For casting, a low liquidus temperature and a narrow window between liquidus temperature (T_{liquidus}) and solidus temperature (T_{solidus}) are desirable [42]. However, for high-temperature alloys (i.e., superalloys) and high-temperature HEAs (also known as high-entropy superalloys (HESA) [1]), a higher T_{liquidus} and T_{solidus} and also a narrow window between the two temperatures are beneficial. For homogenization heat treatment, a wide temperature range of the one-phase region at high temperature (i.e., high-temperature solid solution phase) is preferable (**Figure 10**). Meanwhile, for precipitation heat treatment, a wider window in-between T_{solidus} and the solvus temperature of the precipitation phase (T_{solvus}) is favorable. Therefore, in certain or designed compositions for an HEA system, these typical temperatures of heat treatment can be predicted by using the

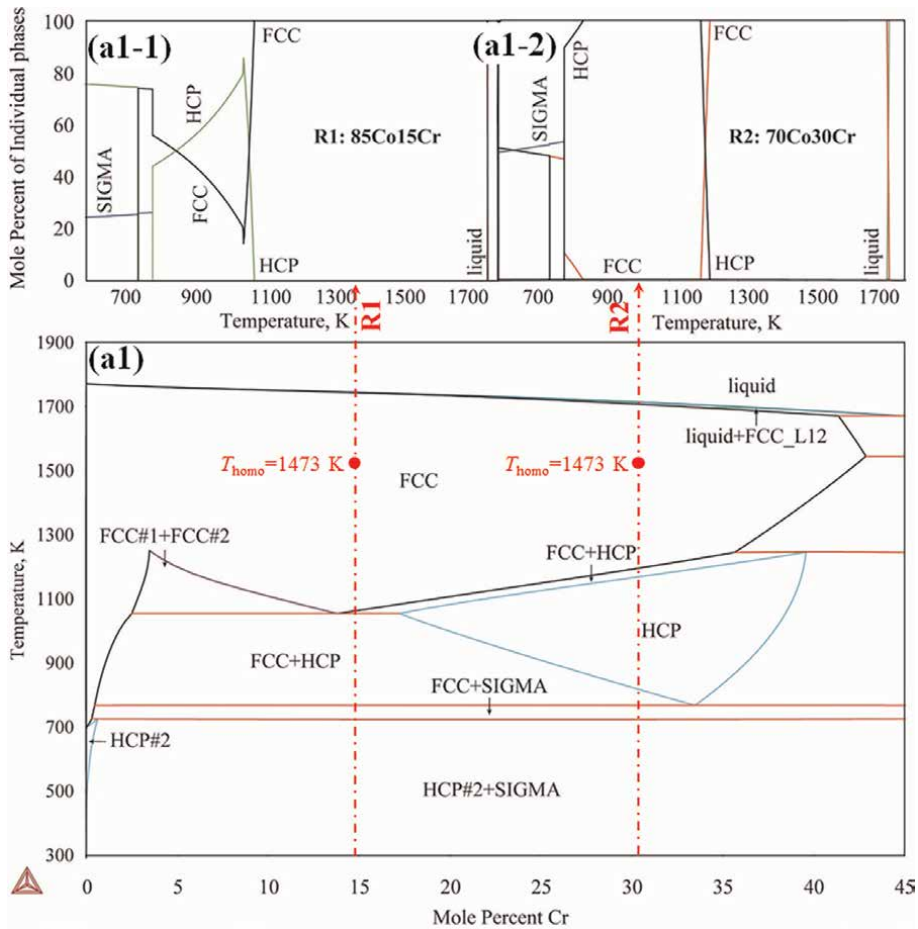


Figure 10. The calculated Co-Cr phase diagram (a1) and the phase fractions at various temperatures for Co-15Cr (a1-1) and Co-30Cr (a1-2) [40].

CALPHAD-based thermodynamic calculations, which are very important for facilitating various heat treatment processing optimization.

3.1.2 Kinetic analysis of heat treatment

The CALPHAD-based thermodynamic calculation is usually performed as a significant starting point for materials design, processing optimization, and so on. Sequentially, kinetic simulation tends to become an important link.

To perform kinetic simulation, it is necessary to combine a simulation module, which has been implanted in some specific kinetic models (e.g., 1D homogenization models [43–45]), and various thermodynamic and kinetic databases (Section 3.1). The simulation of diffusion is usually both time- and space-dependent and is particularly suitable for solving one-phase problems and moving boundary problems. Kinetic simulation for assisting to optimize processing parameters of homogenization heat treatment is an important application.

For homogenization heat treatment, the kinetic simulation is a valuable method to predict and optimize the specific processing parameter, especially for the relationship

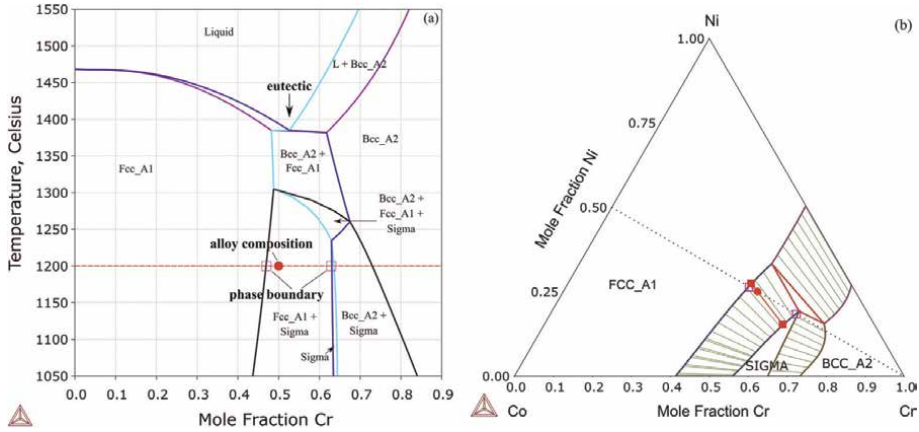


Figure 11. Calculated phase diagram of the Co-Cr-Ni system. The isoplethal section along with the Cr-Cr_{0.5}Ni_{0.5} pseudobinary section (a); and the isothermal section at 1200°C (b) [27].

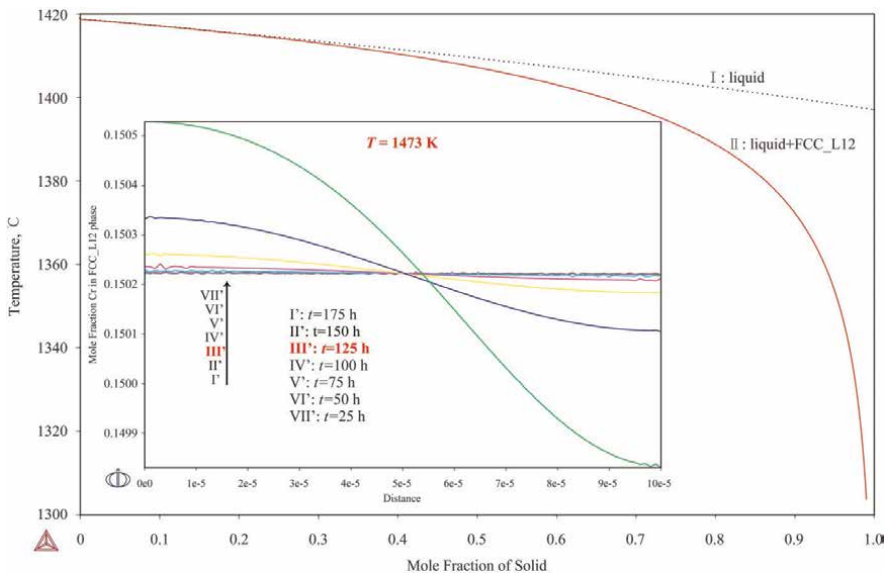


Figure 12. Solidification curves and homogenization heat treatment of M₅ alloy (thermodynamic and kinetic database: TCHEA2 and MOBNI2) [40] (This figure was not displayed in this reference).

between temperature, time, and distance in some given phases. Meanwhile, various heat treatments can be optimized by CALPHAD-based simulations, for instance, to facilitate appropriate heat treatment procedures for manipulating solid solution strengthening and precipitation hardening of HEAs [46], and so on.

3.2 Solidification and precipitation simulations

The Scheil-Gulliver solidification simulation [47, 48], also called Scheil solidification simulation, is usually performed on the basis of the CALPHAD method. For

analyzing solidification processes, some equations were used by assuming that the diffusivity in the solid phases is extremely slow to be treated as zero and the diffusion in the liquid phase is very fast. With the assumption, a type of nonequilibrium transformation can be treated as a local equilibrium state. An example of the Scheil solidification simulation can be found in [40] (**Figure 12**).

Various modules and packages mentioned in Section 3.1, such as TC-Prisma and Pandat, have been developed especially to predict the precipitation problems. Taking TC-Prisma as an example; for predicting the concurrent nucleation, growth, and coarsening of dispersed precipitate phases, the module built by the Langer-Schwartz theory [49] also adopted the Kampmann-Wagner numerical method [50] and many models [51]. To simulate multimodal particle size distribution of precipitate phase is a typical application.

As shown in **Figure 13**, to investigate the precipitation kinetics and to predict the temperature–time–transformation (TTT) diagram for high-entropy superalloys with a typical structure of γ matrix phase (i.e., disordered structure A1) and γ' coherent precipitate phase (i.e., ordered structure L1₂), various simulations can be performed by TC-Prisma with an available software development kits (SDKs) of TC-Python language combined with many thermodynamic and kinetic data-bases [52].

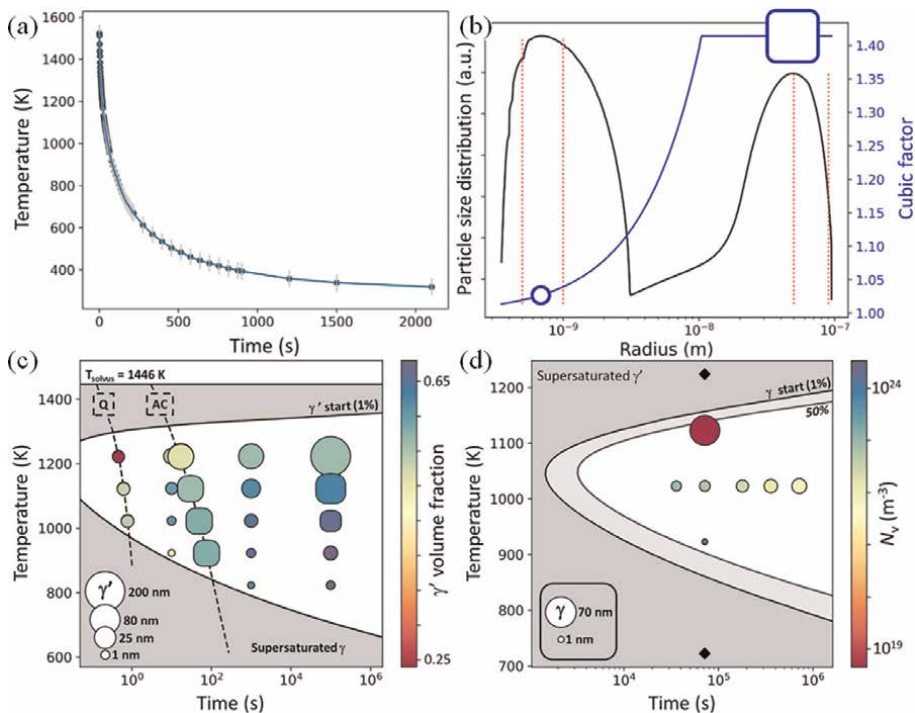


Figure 13. Experimental temperature profile for the alloys conducted by homogenization and solid solution heat treatment at 1500 K for 20 h and then air cooling to room temperature (a); based on the experimental temperature profile, simulated particle size distribution and cubic factor of the γ' precipitate phase for the alloys by continuous cooling from the solvus temperature (b); and the simulated TTT diagram for the γ' precipitate phase from the γ matrix phase (c and d) (The details can be found in [52]).

4. Theoretical understanding of materials properties and performances

4.1 Mechanical properties

Until now in this chapter, the application of the CALPHAD method in composition and structure design and the processing optimization has been briefly described in the previous sections. On the basis of the classical framework and the conventional research route in materials science, only left the last section here, i.e., the CALPHAD-based calculation and simulations for facilitating the theoretical understanding of materials properties and performances. The materials science computational modeling is a key crosslink point to connect the other three points, including composition and structure, processing, and properties and performances. In this section, the CALPHAD-based prediction in understanding mechanical properties, electrochemical corrosion, and high-temperature oxidation performances is described as follows.

As described previously, CALPHAD calculations and simulations are a coupling technique for experimental and theoretical phase diagrams, thermodynamic and kinetic information, and so on. Therefore, the thermodynamic and kinetic databases are compiled by a set of expressions of Gibbs energy and atomic mobility on the basis of a number of composition-/temperature- and time-/distance-dependent functions (also contain other influence factors, e.g., pressure, volume, magnetic, etc.). In this framework, predicting mechanical properties is probably not the main direction of the CALPHAD method. However, the characteristic of the thermodynamic and kinetic database also provides some fundamental data and information to establish various mechanical databases to predict the corresponding mechanical performances. Take CALPHAD-based prediction for the Young's moduli of the Ti-Nb-Zr-Ta/Mo system as an example [53–59]. Based on Young's moduli data through experimental investigation and/or theoretical calculations, the composition-dependent Young's moduli database can be built also from low-order systems to high-order systems like other thermodynamic and kinetic databases. In **Figure 14**, the predicted data are in good agreement with the experimental results for Young's moduli of the body-centered cubic (BCC) Ti-Nb-Zr-Mo system. It shows that the CALPHAD-based prediction for Young's moduli on the basis of the accurate database is a reliable method.

4.2 Electrochemical corrosion performance

From the corrosion mechanism perspective, electrochemical corrosion and high-temperature oxidation are the most important two types of corrosion. Therefore, both of the main kinds of corrosion predicted by the CALPHAD-based calculations and simulations will be introduced in the last two sections.

The electrochemical corrosion is usually treated as wet corrosion, i.e., the metal undergoes some reactions in various specific aqueous solutions. Therefore, understanding the electrochemical corrosion mechanism in thermodynamics and kinetics are two key points. The CALPHAD-based prediction is a powerful technique to study the thermodynamic theory of electrochemical corrosion; a typical representative application is the calculation of the Pourbaix diagram.

The Pourbaix diagram, i.e., potential-pH diagrams, derived by M. Pourbaix, collected thermodynamic information for the relevant electrochemical and chemical reactions. With the development of the experimental and theoretical thermodynamic data for the Pourbaix diagram, the calculation of the Pourbaix diagram can be applied

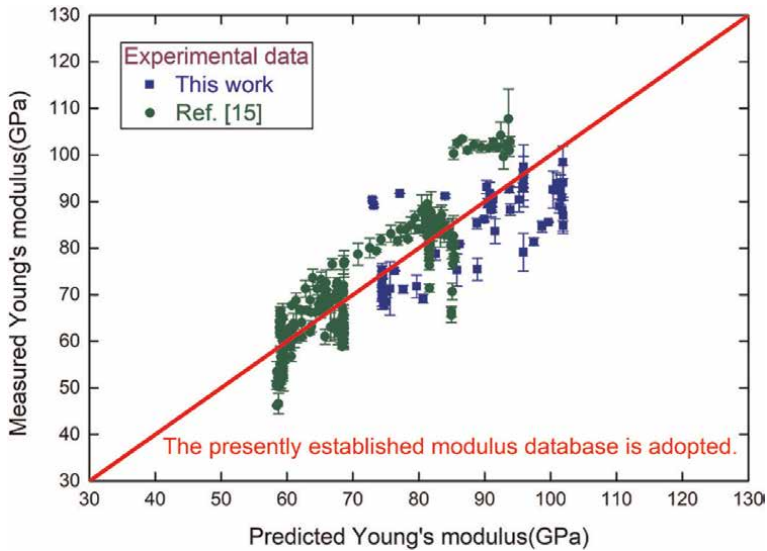


Figure 14. The diagram of Young's moduli of the BCC Ti-Nb-Zr-Mo system. The data (red line) [53] were predicted from Young's modulus database in comparison to the experimental results [53, 54] (blue and green points).

not only in corrosion science but also in hydrometallurgy and electrodeposition processing. In the field of corrosion science, the potential-pH domain represents two significant physical and chemical processes. That is, potential is an important characteristic parameter to reflect the metal either kept in an immunity state or reacted to various specific oxidation or ionic states; pH is a significant typical parameter to mirror the activities of H^+ or OH^- in corrosive media or environment. The two parameters usually represent the anodic and cathodic reactions, respectively. Therefore, the calculation of the Pourbaix diagram is a unique method to predict electrochemical corrosion behaviors.

Like other thermodynamic calculations, the calculation of the Pourbaix diagram also needs many thermodynamic databases especially to combine aqueous database (e.g., TCAQ3 database [60]). A calculated Pourbaix diagram and a diagram of the potential and the phase amount of compounds for CoCrFeNi alloy at pH = 7 are shown in **Figure 15** [20]. From the calculation results, some important information can be obtained, such as the main stable oxides and spinels in the passive layers, the specific potential and pH series for different oxidation and reduction reactions, and so on. It needs to notice that the potential in the Pourbaix diagram and in the real corrosion system represents equilibrium and nonequilibrium potential, respectively. Therefore, the equilibrium and non-equilibrium states should be distinguished when analyzing the corrosion behaviors.

4.3 High-temperature oxidation performance

Compared with the metallic materials suffering various types of destruction at room temperature, the high-temperature alloys (i.e., superalloys) undergo much more heavily deterioration at elevated temperatures. To take the turbine as an example, as the most important core component, like the skeleton for a human, in fossil-energy/nuclear power plants and vehicles, especially in aircraft, the

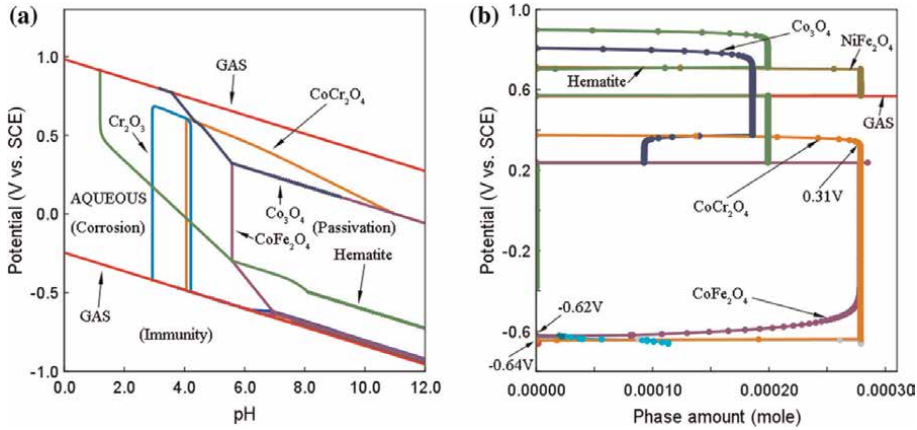


Figure 15. The calculated Pourbaix diagram (a) and the diagram of potential and the phase amount of oxides and spinels for CoCrFeNi alloy at pH = 7 (b) [20].

high-temperature metallic materials should conquer a series of complex chemical, physical, and metallurgical process, for instance, high corrosion, wear, fatigue, stress, and creep resistance performances, particularly for the interaction between these mechanics and corrosion factors. Therefore, the superalloys with high performances at elevated temperatures are the most significant materials in high-temperature components.

For the corrosion behaviors at room temperature and elevated temperature, the basic theories have some common points, such as thermodynamic and kinetic theories. However, the corrosion mechanisms of the high-temperature corrosion, usually called high-temperature oxidation, still have some specific theories including thermodynamics and kinetics in comparison with the theories for electrochemical corrosion at room temperature. To draw inferences from the above sections, perform the CALPHAD-based calculations, and simulations for high-temperature oxidation also focus on the thermodynamic and kinetic computation. That is, some predictions can be obtained from the above sections in this chapter, and some calculations and simulations can usually be performed especially to predict the behaviors of high-temperature oxidation. Some common examples are described in the following.

Some thermodynamic predictions for different usages based on the materials in specific environments or working conditions can be applied here. For instance, isothermal and isoplethal sections can be calculated for various HEA systems, not only for the alloying elements systems but also especially for the alloying element–oxygen systems. **Figure 16** shows the calculated stable phases of the Fe–Cr–O system at 650°C at various oxygen activities [61]. A spinel miscibility gap appears in the S1 + S2 region (S1: $\text{Fe}_{3-x}\text{Cr}_x\text{O}_4$, S2: $\text{FeCr}_{2-x}\text{Fe}_x\text{O}_4$), S1 and S2 represent the spinel phase between Fe_3O_4 and FeCr_2O_4 phase, and the miscibility gap will be disappeared above $\sim 665^\circ\text{C}$.

In the calculated phase diagram of the alloying element–oxygen systems, the oxygen can be exchanged for carbon, nitrogen, or sulfur, because the processes of oxidization, carbonization, nitridation, and vulcanization are treated as generalized oxidization.

In Sections 3.1.2 and 3.2, the application of the kinetic and precipitation simulations on heat treatment has been introduced. As described above, the thermodynamic calculations can be applied to study materials design, processing optimization, and

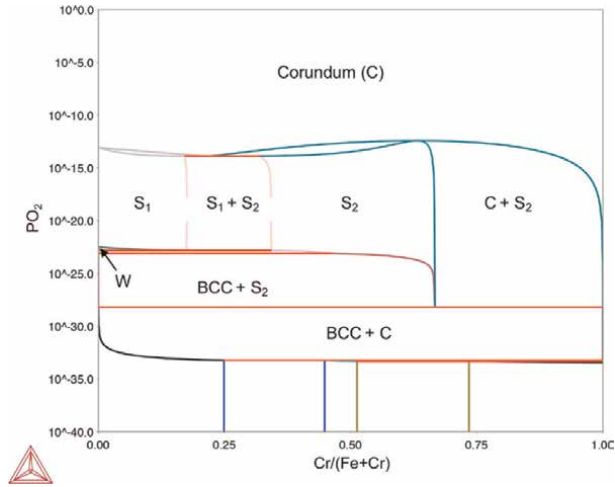


Figure 16. The calculated stable phases of the Fe-Cr-O system at 650°C at various oxygen activity. C: Corundum-type M_2O_3 , S1: $Fe_{3-x}Cr_xO_4$, S2: $FeCr_{2-x}Fe_xO_4$, W: $Fe_{1-x}O$, BCC: Ferrite structure [61].

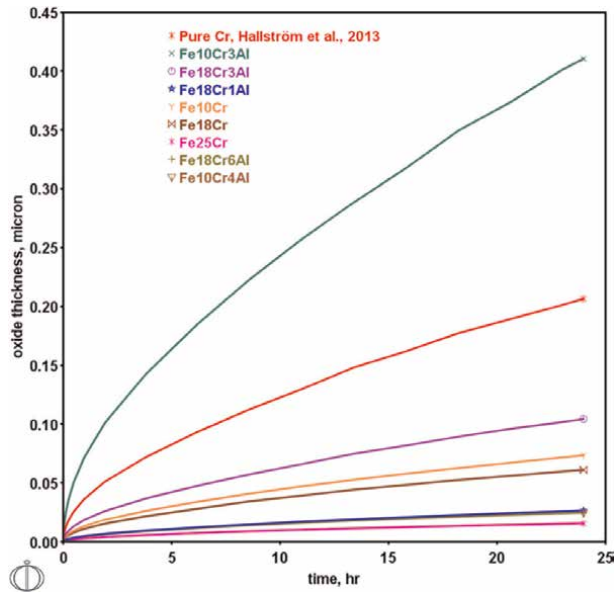


Figure 17. A Dictra simulation of high-temperature oxidation. The oxide thickness time was dependent on the Fe-Cr-Al system for 24 h at 600°C. the simulation sets an assumption that the bulk composition in alloys only is affected by the grain size and grain boundary diffusion in the oxide.

various properties and performance; however, each prediction has some different specific emphases for different studies. The kinetic and precipitation simulation is the same situation.

Kinetic simulation has the capability to predict the formation of oxide layers during the high-temperature oxidation. The thickness of the oxide layers formed with time for the Fe-Cr-Al system for 24 h at 600°C was simulated by Dictra, as shown in **Figure 17** [62].

The simulation sets an assumption that the bulk composition in alloys only is affected by the grain size and grain boundary diffusion in the oxide layers. Meanwhile, precipitation simulation is capable of predicting particle size distribution of precipitate phases. Until now, the studies of the precipitation simulation for the HEAs are not very common like steels. The reason probably is that the typical precipitation and inclusion in different HEA systems are not like M_7C_3 or $M_{23}C_6$ in steels. However, much stronger support for the precipitation simulation of the HEAs will be provided in the future resulting in more and more experimental investigation of HEAs [63–66].

5. Conclusions

In this chapter, the applications of the CALPHAD-based calculations and simulations in the recent advances and the new perspectives of HEAs were introduced briefly. The framework of the chapter is followed by the classical components, i.e., modeling, composition and structure, processing, and properties and performances. Here, the CALPHAD-based thermodynamic and kinetic modeling play the key role to connect the other three components. As can be seen, some examples were not only limited in the CALPHAD prediction in HEAs, but also contained some examples in different alloy systems, probably because not so much corresponding research was found. To draw inferences from the similar research, it is no problem to apply the similar thermodynamic and kinetic calculations and simulations in the specific HEAs systems if the specific alloy systems have the matched databases. Besides the content described in this chapter, there still exist a number of other research studies on the basis of the CALPHAD computations, and many techniques can also couple with the CALPHAD data or combined with CALPHAD software programs. These new trends extremely extend the boundaries of the CALPHAD method. For instance, the CALPHAD modeling can couple with first principle, phase field, machine learning, etc.; meanwhile, many conventional CALPHAD software can interact with Python or MATLAB through specific application programming interfaces (APIs).

HEA is a fast-growing field attractive to the scientists of different backgrounds. Many emerging applications of CALPHAD have not been included in this chapter, such as the refractory HEAs, high-entropy ceramics (HECs), additive manufacturing of HEAs, etc. These areas would offer new chances of exploring the unexpected and exciting features of HEAs. Hope CALPHAD could play a more important role in the new journey of discovering advanced HEAs.

Acknowledgements

W. Wang would like to acknowledge the funding from a Key R & D item in Science and Technology Development Project / International Collaborative in Science and Technology Development Project, Science and Technology Department of Jilin Province in China (Grant No. 20200401106GX and 20210402061GH). W. Wang would like to acknowledge the funding from the Opening Project of Shanxi Key Laboratory of Controlled Metal Solidification and Precision Manufacturing, North University of China (Grant No. MSPM202001). Z. Li would like to acknowledge the National Natural Science Foundation for Youth of China (Grant No. 52001098).

Conflict of interest

The authors declare that they have no known competing financial interests or personal relationships that could have appeared to influence the work reported in this chapter.

Author details


Wei Wang^{1*} and Zhou Li^{2*}

1 Northeast Electric Power University, Jilin, China

2 Shandong First Medical University, Jinan, China

*Address all correspondence to: wei6@kth.se and lizhou_alfred2011@hotmail.com

IntechOpen

© 2022 The Author(s). Licensee IntechOpen. This chapter is distributed under the terms of the Creative Commons Attribution License (<http://creativecommons.org/licenses/by/3.0>), which permits unrestricted use, distribution, and reproduction in any medium, provided the original work is properly cited. 

References

- [1] Gao MC, Yeh JW, Zhang Y. High-Entropy Alloys: Fundamentals and Applications. Switzerland: Springer International Publishing; 2016. p. 493
- [2] Spencer PJ. A brief history of CALPHAD. *Calphad*. 2008;**32**:1-8. DOI: 10.1016/j.calphad.2007.10.001
- [3] Andersson JO, Helander T, Hoglund LH, Shi PF, Sundman B. THERMO-CALC & DICTRA, computational tools for materials science. *Calphad*. 2002;**26**:273-312
- [4] Chen SL, Daniel S, Zhang F, Chang YA, Yan XY, Xie F, et al. The PANDAT software package and its applications. *Calphad*. 2002;**26**: 175-188
- [5] Bale CW, Chartrand P, Degterov SA, Eriksson G, Mahfoud RB, Melançon J, et al. FactSage thermochemical software and databases. *Calphad*. 2002; **26**:189-228
- [6] Lukas HL, Fries SG, Sundman B. *Computational Thermodynamics: The Calphad Method*. Cambridge: Cambridge University Press; 2007
- [7] Saunders N, Miodownik AP. CALPHAD (Calculation of Phase Diagrams): A Comprehensive Guide. Oxford: Pergamon; 1998
- [8] Hillert M. The compound energy formalism. *Journal of Alloys and Compounds*. 2001;**320**:161-176
- [9] Pelton AD, Blander M. Thermodynamic analysis of ordered liquid solutions by a modified quasichemical approach—Application to silicate slags. *Metallic and Materials*. 1986;**17**:805-815
- [10] Kikuchi R. A theory of cooperative phenomena. *Physics Review*. 1951;**81**(6): 988-1003
- [11] Liu ZK. Computational thermodynamics and its applications. *Acta Materialia*. 2020;**200**:745-792
- [12] Kaufman L, Ågren J. CALPHAD, first and second generation – Birth of the materials genome. *Scripta Materialia*. 2014;**70**:3-6
- [13] Ye YF, Wang Q, Lu J, Liu CT, Yang Y. High-entropy alloy: Challenges and prospects. *Materials Today*. 2016;**19**: 349-362
- [14] Miracle DB, Senkov O. A critical review of high entropy alloys and related concepts. *Acta Materialia*. 2017;**122**: 448-511
- [15] George EP, Raabe D, Ritchie RO. High-entropy alloys. *Nature Reviews in Materials*. 2019;**4**:515-534
- [16] Guruvidyathri K, Murty BS, Yeh JW, Hari Kumar K. Gibbs energy-composition plots as a tool for high-entropy alloy design. *Journal of Alloys and Compounds*. 2018;**768**:358-367
- [17] Wu M, Wang S, Huang H, Shu D. CALPHAD aided eutectic high-entropy alloy design. *Materials Letters*. 2020;**262**: 127175
- [18] Choi WM, Jung S, Jo YH, Lee S, Lee BJ. Design of new face-centered cubic high entropy alloys by thermodynamic calculation. *Metals and Materials International*. 2017;**23**:839-847
- [19] Thermo-Calc Software. CALPHAD Software and Database, T.-C.S.A., Stockholm, Sweden, <https://thermocalc.com>

- [20] Zhang B, Zhang Y, Guo SM. A thermodynamic study of corrosion behaviors for CoCrFeNi-based high-entropy alloys. *Journal of Materials Science*. 2018;**53**:14729-14738
- [21] Wu PH, Niu N, Zhou PJ, Peng Z, Du WD, Wang XJ, et al. Microstructures and liquid phase separation in multicomponent CoCrCuFeNi high entropy alloys. *Materials Science and Technology*. 2016;**32**:576-580
- [22] Butler TM, Weaver ML. Investigation of the phase stabilities in AlNiCoCrFe high entropy alloys. *Journal of Alloys and Compounds*. 2017;**691**: 119-129
- [23] Mao H, Chen HL, Chen Q. TCHEA1: A thermodynamic database not limited for “High Entropy” alloys. *Journal of Phase Equilibria and Diffusion*. 2017;**38**: 353-368
- [24] Pandat Thermodynamic Calculations and Kinetic Simulations. CompuTherm LLC, M., WI, USA – 53719
- [25] Feng R, Gao MC, Lee C, Mathes M, Zuo T, Chen S, et al. Design of light-weight high-entropy alloys. *Entropy*. 2016;**18**:333
- [26] MacDonald BE, Fu Z, Wang X, Li Z, Chen W, Zhou Y, et al. Influence of phase decomposition on mechanical behavior of an equiatomic CoCuFeMnNi high entropy alloy. *Acta Materialia*. 2019;**181**:25-35
- [27] Chen H, Mao H, Chen Q. Database development and Calphad calculations for high entropy alloys: Challenges, strategies, and tips. *Materials Chemistry and Physics*. 2018;**210**:279-290
- [28] Zhang C, Yang Y. The CALPHAD approach for HEAs: Challenges and opportunities. *MRS Bulletin*. 2022
- [29] Feng R, Zhang C, Gao MC, Pei Z, Zhang F, Chen Y, et al. High-throughput design of high-performance lightweight high-entropy alloys. *Nature Communications*. 2021;**12**:4329
- [30] Zeng Y, Man M, Bai K, Zhang YW. Revealing high-fidelity phase selection rules for high entropy alloys: A combined CALPHAD and machine learning study. *Materials and Design*. 2021;**202**:109532
- [31] Qiao L, Liu Y, Zhu J. A focused review on machine learning aided high-throughput methods in high entropy alloy. *Journal of Alloys and Compounds*. 2021;**877**:160295
- [32] Senkov ON, Miller JD, Miracle DB, Woodward C. Accelerated exploration of multi-principal element alloys with solid solution phases. *Nature Communications*. 2015;**6**:6529
- [33] Pandat Software. An Integrated Modeling Platform for Materials Design. Madison, USA: CompuTherm LLC
- [34] FactSage. The Integrated Thermodynamic Databank System. Montreal, Canada: FactSage Software
- [35] High Entropy Alloys Databases. Version TCHEA5 and MOBHEA2, released 2021, Thermo-Calc Software AB
- [36] Thermodynamic database (TH), Mobility database (MB), and Molar volume (MV) database for multi-component 3rd transition metal high entropy alloys (HEA), PanHEA database, released 2021, CompuTherm LLC
- [37] Cantor B, Chang ITH, Knight P, Vincent AJB. Microstructural development in equiatomic multi-component alloys. *Materials Science and Engineering A*. 2004;**375-377**:213-218

- [38] Huang PK, Yeh JW, Shun TT, Chen SK. Multi-principal-element alloys with improved oxidation and wear resistance for thermal spray coating. *Advanced Engineering Materials*. 2004; **6**:74-78
- [39] Gorsse S, Miracle DB, Senkov ON. Mapping the world of complex concentrated alloys. *Acta Materialia*. 2017; **135**:177-187
- [40] Wang W, Hou Z, Lizarraga R, Tian Y, Babu RP, Holmstrom E, et al. An experimental and theoretical study of duplex fcc+hcp cobalt based entropic alloys. *Acta Materialia*. 2019; **176**:11-18
- [41] Wang W, Chen HL, Larsson H, Mao H. Thermodynamic constitution of the Al–Cu–Ni system modeled by CALPHAD and ab initio methodology for designing high entropy alloys. *Calphad*. 2019; **65**:346-369
- [42] Pfizenmaier P, Ulrich AS, Galetz MC, Glatzel U. Determination of heat treatment parameters by experiments and CALPHAD for precipitate hardening of Cr-Alloys with Si, Ge and Mo. 2020; **116**:106636
- [43] Larsson H, Engström A. A homogenization approach to diffusion simulations applied to $\alpha + \gamma$ Fe–Cr–Ni diffusion couples. *Acta Materialia*. 2006; **54**:2431-2439
- [44] Larsson H, Höglund L. Multiphase diffusion simulations in 1D using the DICTRA homogenization model. *Calphad*. 2009; **33**:495-501
- [45] Larsson H. A model for 1D multiphase moving phase boundary simulations under local equilibrium conditions. *Calphad*. 2012; **47**:1-8
- [46] He F, Wang Z, Wu Q, Niu S, Li J, Wang J, et al. Solid solution island of the Co-Cr-Fe-Ni high entropy alloy system. *Scripta Materialia*. 2017; **131**:42-46
- [47] Gulliver GM. The quantitative effect of rapid cooling upon the constitution of binary alloys. *Journal of Instrumental Metals*. 1913; **9**:120-157
- [48] Scheil E. Comments on the formation of stratified crystals. *Zeitschrift fuer Metallkunde*. 1942; **34**:70-72
- [49] Langer JS, Schwartz AJ. Kinetics of nucleation in near-critical fluids. *Physics Review A*. 1980; **21**:948-958
- [50] Kampmann R, Wagner R. Kinetics of precipitation in metastable binary alloys—Theory and application to Cu-1.9 at% Ti and Ni-14 at% Al. In: Haasen P, Gerold V, Wagner R, Ashby MF, editors. *Decomposition of Alloys the Early Stages*. Oxford: Pergamon; 1984. pp. 91-103
- [51] Chen Q, Jou HJ, Sterner G. *TC-PRISMA User's Guide and Examples*. Stockholm, Sweden: Thermo-Calc Software AB; 2011
- [52] Gorsse S, Chen YT, Hsu WC, Murakami H, Yeh AC. Modeling the precipitation processes and the formation of hierarchical microstructures in a single crystal high entropy superalloy. *Scripta Materialia*. 2021; **193**:147-152
- [53] Ling J, Wen Z, Yang G, Wang Y, Chen W. A CALPHAD-type Young's modulus database of Ti-rich Ti–Nb–Zr–Mo system. *Calphad*. 2021; **73**:102255
- [54] Ling J, Huang D, Bai K, Li W, Yu Z, Chen W. High-throughput development and applications of the compositional mechanical property map of the β titanium alloys. *Journal of Materials*

Science and Technology. 2021;**71**:
201-210

[55] Ling J, Chen W, Sheng Y, Li W, Zhang L, Du Y. A MGI-oriented investigation of the Young's modulus and its application to the development of a novel Ti-Nb-Zr-Cr bio-alloy. *Materials Science and Engineering: C*. 2020;**106**: 110265

[56] Marker C, Shang SL, Zhao JC, Liu ZK. Effects of alloying elements on the elastic properties of bcc Ti-X alloys from first-principles calculations. *Computational Materials Science*. 2018; **142**:215-226

[57] Marker C, Shang SL, Zhao JC, Liu ZK. Elastic knowledge base of bcc Ti alloys from first-principles calculations and CALPHAD-based modeling. *Computational Materials Science*. 2017; **140**:121-139

[58] Wang X, Liu LB, Wang MF, Shi X, Huang GX, Zhang LG. Computational modeling of elastic constants as a function of temperature and composition in Zr-Nb alloys. *Calphad*. 2015;**48**:89-94

[59] Shang SL, Wang Y, Kim DE, Zacherl CL, Du Y, Liu ZK. Structural, vibrational, and thermodynamic properties of ordered and disordered Ni_{1-x}Ptx alloys from first-principles calculations. *Physical Review B*. 2011;**83**: 144204

[60] Aqueous Solutions Databases: TCAQ3 Database. Available from: <https://thermocalc.com/products/databases/aqueous-solutions>

[61] Jonsson T, Larsson H, Karlsson S, Hooshyar H, Sattari M, Liske J, et al. High-temperature oxidation of FeCr(Ni) alloys: The behaviour after breakaway. *Oxidation of Metals*. 2017;**87**:333-341

[62] Bigdeli S, Kjellqvist L, Naraghi R, Höglund L, Larsson H, Jonsson T. Strategies for high-temperature corrosion simulations of Fe-based alloys using the Calphad approach: Part I. *Journal of Phase Equilibria and Diffusion*. 2021;**42**:403-418

[63] Wang W, Wang Y, Mu W, Park JH, Kong H, Sukenaga S, et al. Inclusion engineering in Co-based duplex entropic alloys. *Materials and Design*. 2021;**210**: 110097

[64] Fan J, Fu L, Sun Y, Xu F, Ding Y, Wen M, et al. Unveiling the precipitation behavior and mechanical properties of Co-free Ni_{47-x}Fe₃₀Cr₁₂Mn₈Al_xTi₃ high-entropy alloys. *Journal of Materials Science and Technology*. 2022;**118**:25-34

[65] Wang W, Mu W, Hou Z, Sukenaga S, Shibata H, Larsson H, et al. In-situ real time observation of martensite transformation in duplex fcc +hcp cobalt based entropic alloys. *Materialia*. 2020;**14**:100928

[66] Daniel R, Zalesak J, Matko I, Baumegeger W, Hohenwarter A, George EP, et al. Microstructure-dependent phase stability and precipitation kinetics in equiatomic CrMnFeCoNi high-entropy alloy: Role of grain boundaries. *Acta Materialia*. 2022; **223**:117470

Section 4

Applications

Development of Orthopedic Implants with Highly Biocompatible Ti Alloys

Yoshimitsu Okazaki and Kiyoyuki Chinzei

Abstract

The material properties of metallic materials used for manufacturing of orthopedic implants are important for understanding the factors affecting the biological, biomechanical, and biochemical performances of orthopedic implants. This chapter will provide the test method for characterizing potential materials for metallic orthopedic device such as artificial joints and osteosynthesis. Particularly, the alloy design and low-cost manufacturing processes of titanium (Ti) metals, cytocompatibility of metals, biocompatibility and corrosion resistance of Ti alloys, and mechanical compatibility of orthopedic implants are summarized. Future trends on both materials and biological evaluation methods are also introduced here. Three-dimensional (3D) layer manufacturing technologies are expected as new technologies for manufacturing, artificial hip joint stems, acetabular cups, and femoral components and tibial trays of artificial knee joints among others. 3D layer manufacturing technologies are also expected for manufacturing porous materials such as acetabular components. It is possible to obtain marketing approval for highly biocompatible implants that are optimized for the skeletal structures and needs of patients by combining 3D layer manufacturing technologies with imaging technologies such as computed tomography (CT).

Keywords: orthopedic implant, Ti alloys, biological evaluation, mechanical compatibility, manufacturing process

1. Introduction

Orthopedics is a medical field that deals with the diagnosis and treatment of diseases of the musculoskeletal system including bones, joints, ligaments, and muscles. Patients range from children to the elderly. The organs treated in orthopedics include the spine, spinal cord, peripheral nerves, joints, arms, and legs. The clinical conditions treated by orthopedic specialists include congenital diseases, degenerative diseases, inflammatory diseases, bone and soft tissue tumors, age-related changes, and traumatic conditions such as fractures and dislocations. As we are entering into a super-aging society, the use of orthopedic implants is increasing yearly with the

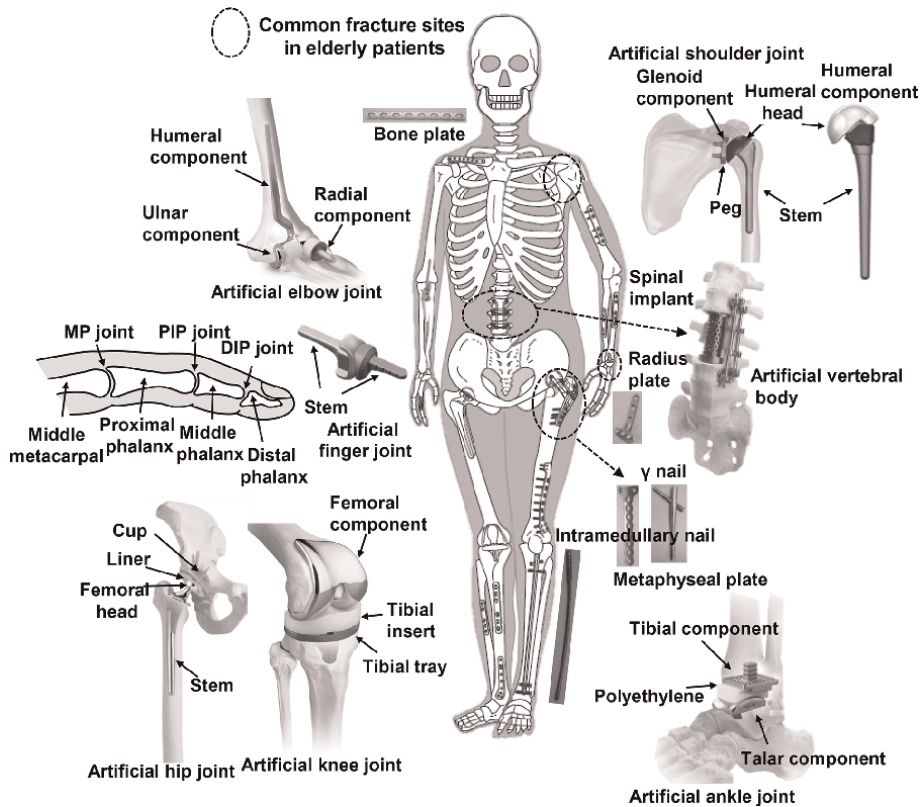


Figure 1.
Artificial bones and joints currently in use in aging society.

increasing number of patients with fractures caused by aging and osteoporosis, among others. **Figure 1** shows orthopedic implants currently in use. There are various implant products, such as bone plates, metaphyseal plates, bone screws, compression hip screws (CHSs), short femoral (γ) nails, intramedullary nails, artificial femoral heads, artificial hip joints, artificial knee joints, artificial shoulder joints, artificial elbow joints, artificial ankle joints, artificial finger joints, and spinal fixation devices. Biochemical and biomechanical compatibilities as well as biological safety are required for orthopedic implant devices. Therefore, metallic orthopedic devices, which are manufactured from various metals having excellent mechanical properties, are widely used in the orthopedic field. To determine biological safety, and biochemical and biomechanical properties, various chemical, biological, and mechanical evaluations are performed for device development and obtaining marketing approval of implant devices. This chapter will provide the evaluation methods for characterizing potential materials for metallic orthopedic devices such as artificial joints and osteosynthesis devices. Recent chemical, biological, and mechanical test results of new biocompatible materials are introduced here, as well as the development of new orthopedic devices. The compatibility of implants with bone geometry and size matching is especially important for elderly patients with fractures around the joints. The risk of damage to tendons and ligaments around joints after implant arthroplasty is likely to increase when there are discrepancies in size and bone geometry.

2. Implantable metals and cytocompatibility of metals

2.1 Main metals used in orthopedic implants

Stainless steel, cobalt (Co)-chromium (Cr)-molybdenum (Mo) alloys, commercially pure titanium (C.P. Ti), and Ti alloys are widely used in orthopedic implants. In particular, the use of Ti-6 mass% aluminum (Al)-4 mass% vanadium (V) (Ti-6Al-4V) alloys has been increasing in various orthopedic implant devices. The biological safety and corrosion resistance of stainless steel are improved by increasing the amount of Cr and Mo alloying elements added to the steel. Fatigue strengths are increased to a level equivalent to those of Ti alloys by adding nitrogen (N) and 20% cold working. The fatigue strengths of an industrial Ti material are improved by increasing the amount of trace elements such as oxygen (O) and iron (Fe), whereas the fatigue strength of C.P. Ti grade 4 can be close to those of Ti alloys by 20% cold working. Ti alloys have higher biocompatibility and corrosion resistance than C.P. Ti owing to zirconium (Zr), niobium (Nb), and tantalum (Ta) elements is added. Moreover, the fatigue strengths of materials are substantially improved by changing the conditions of hot forging and heat treatment.

Ti alloys, C.P. Ti, and stainless steel are globally used in various osteosynthesis devices, whereas Co-28Cr-6Mo alloy is widely used in bearing parts of various artificial joints. Artificial hip joint stems are classified into cement hip stems that are fixed to bone using polymethylmethacrylate (PMMA) bone cement and cementless stems that are fixed to bone by osseointegration without PMMA bone cement. Ti alloys with high biocompatibility are used for the cementless hip stem. Cementless stems are coated with bioactive ceramics such as hydroxyapatite (HA) to enhance new bone formation. Co-28Cr-6Mo alloy and high-N stainless steel with high stiffness and strength are popularly used for the cemented hip stem materials.

2.2 Mechanism of cytotoxicity of metal ions

In recent years, the toxicity of Co ions released from metal-on-metal artificial hip joints has attracted attention. Moreover, there have been reports on aseptic lymphocytic vasculitis-associated lesions (ALVALs) associated with Co ions [1]. There are also several clinical reports on the *in vivo* effect of metal ions released from orthopedic implants. Particularly, the clinical concern about the toxicity of V ions has been reported [1]. When the relative growth ratio is 1 or lower in the cytotoxicity tests, cytotoxicity increases. V and Al ions strongly inhibit the cell growth of both mouse fibroblast L929 and osteoblastic MC3T3-E1 cells compared with Co, Ni, and lead (Pb) ions, causing a marked decrease in relative growth ratio at a concentration of 0.1 ppm or above [1].

Figure 2 shows a schematic illustration of the incorporation of metal ions into cells. Metal ions are incorporated through various ion channels and bind to proteins and amino acids [1]. To clarify the mechanism of cytotoxicity expression, the quantities of V and other metal ions incorporated into mouse fibroblast L929 and osteoblastic MC3T3-E1 cells have been investigated using an inductively coupled plasma-mass spectrometry (ICP-MS) system [1]. **Figure 3** shows the relationship between the concentrations of various metals in the cell culture medium and the mean quantity [(femtogram (fg), 10^{-15} g)] of incorporated metal ions. The quantities per cell of metal ions incorporated into the L929 and MC3T3-E1 cells increase with increasing metal concentration in the culture medium, depending on the metal ion type. Lower quantities of gold (Au), Ti, Zr, Nb, Ta, and Cr ions are released into the medium and also

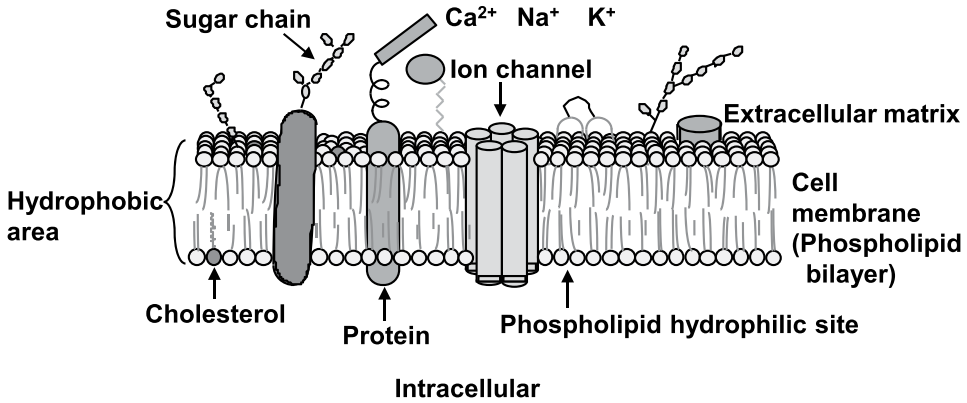


Figure 2. Schematic illustration of incorporation of metal ions into cells.

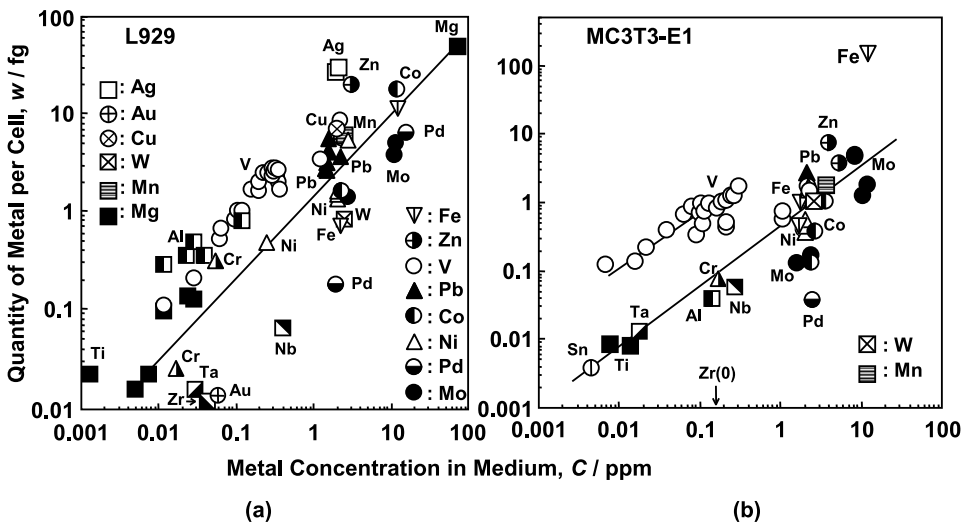


Figure 3. Relationship between metal concentration in medium and quantity of metal per cell. (a) L929 cells and (b) MC3T3-E1 cells.

incorporated into the cells. Higher quantities of magnesium (Mg), palladium (Pd), Mo, Fe, Ni, Co, Mn, and tungsten (W) ions are incorporated. Moreover, silver (Ag), Pb, V, Cu, and Zn are incorporated at the highest quantities. As shown in **Figure 3b**, higher quantities of Zn, Pb, Fe, and V ions are incorporated into the MC3T3-E1 cells. The quantity of V ions incorporated into the MC3T3-E1 cells is considerably higher than those of other metal ions. Thus, the cytotoxicity of a metal ion changes with the quantity of the metal ion incorporated into cells. Particularly, V ions are incorporated into cells through xanthine derived from fetal bovine serum. The strong interactions of Mo, Co, and Ni with amino acids have also been clarified by high-performance liquid chromatography (HPLC) [1].

The effects of lipopolysaccharide (LPS) (positive control), V, and Ni concentrations in a medium on the relative growth ratio of mouse-macrophage-like J774.1 cells have been investigated in Ref. [1]. The relative growth ratio at approximately 0.05 ppm V ion

concentration decreases from 1. For V ion concentration, its IC_{80} (20% inhibitory concentration) is 0.5 ppm and its IC_{50} is 0.8 ppm. On the other hand, for Ni ion concentration, its IC_{80} is 1.5 ppm and its IC_{50} is 3 ppm. The cytotoxicity of V ions for J774.1 cells is approximately 10-fold than that of Ni ions. The rate of increase in the concentration of nitric oxide (NO) released with the activation of J774.1 cells starts to increase at a concentration of V ions 10 times lower than that of Ni ions [1].

Also, an increase in the concentration of cytokines such as tumor necrosis factor- α (TNF- α) and interleukin-6 (IL-6) causes osteoclast differentiation and promotes bone resorption in the orthopedic implant field. Bone resorption is promoted by osteoclasts around artificial joints. Marked increases in TNF- α and IL-6 concentrations in patients with rheumatic disease accelerate bone resorption [1]. The release of TNF- α from J774.1 cells starts at approximately 0.5 ppm V concentration; the concentrations of IL-6 and transforming growth factor- β (TGF- β) markedly increase at a high rate above 1 ppm V concentration. The Ni concentration required to produce cytokines is higher than the V concentration [1].

2.3 Biocompatibility of various metals

The relationship between the cytocompatibility and polarization resistance of various pure metals is summarized in **Figure 4a** and **b** [2–5]. Cytotoxicity of various pure metals is shown in **Figure 4c**. V ion cytotoxicity is strongly concentration-dependent

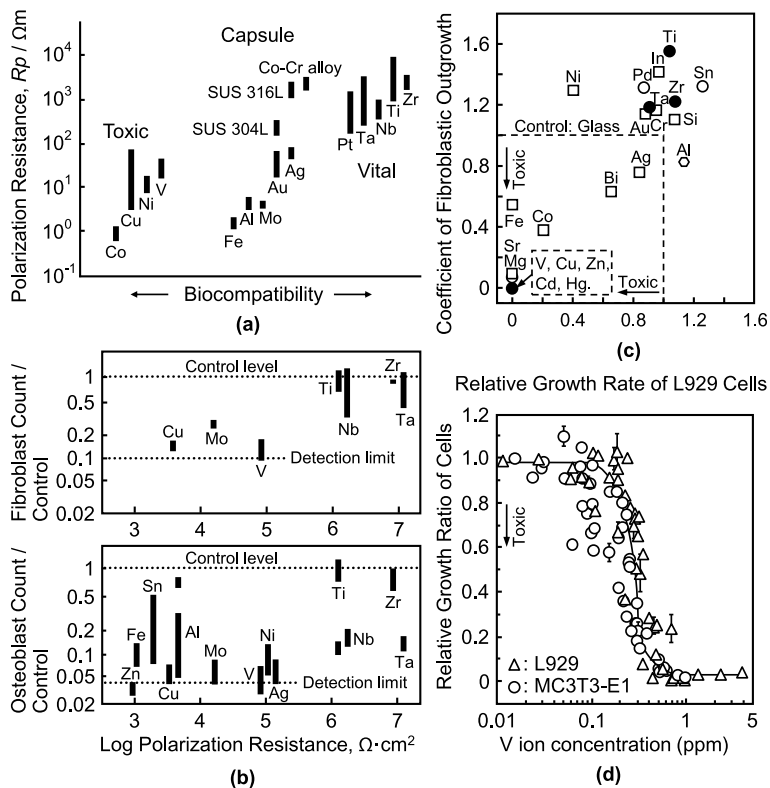


Figure 4. (a), (b) Relationship between the polarization resistance and biocompatibility of various pure metals and alloys. (c) Cytotoxicity of various pure metals and (d) that at different V ion concentrations.

as shown in **Figure 4d**. On the other hand, Zr, Nb, and Ta elements exhibit excellent biocompatibility and corrosion resistance, all of which belong to the vital (loose connective vascularized) group with regard to tissue reactions. In the 70 metals in the periodic table of elements, only Ti and Zr elements show excellent cytocompatibility with both bone-derived mouse osteoblast cells and soft-tissue-derived mouse fibroblast cells.

3. Low-cost manufacturing processes of biocompatible Ti alloys

3.1 Material design of highly biocompatible Ti alloys

The Ti alloys are classified into three types depending on their microstructure: alpha-type (α -) alloys having a hexagonal-close-packed (hcp) structure, beta-type (β -) alloys having a body-centered-cubic (bcc) structure, and alpha-beta-type (α - β -) alloys having a mixed structure comprising α - and β -phases. In the α - β -Ti alloys, Ti-6Al-4V alloy is widely used for various orthopedic implants. The α - β -Ti alloys have higher fatigue strength than that of the β -Ti alloys. Another α - β -Ti alloy, Ti-15mass% Zr-4mass% Nb-(0–4)mass% Ta [Ti-15Zr-4Nb-(0–4)Ta] alloys, is developed in Japan as an excellent biocompatible alloy for long-term orthopedic implant applications and is standardized in JIS T 7401-4 [6].

Zr, Nb, and Ta elements are effective alloying elements of Ti alloys for resulting excellent long-term biocompatibility and corrosion resistance. However, the excessive addition of Ta and Nb to Ti alloys brings a higher manufacturing cost. Therefore, to develop low-cost manufacturing processes, we have investigated the effects of hot-forging and continuous hot-rolling conditions on the hot forgeability, microstructure, biochemical, and biological properties, tensile properties, and fatigue properties of Ti-15Zr-4Nb-(0–4) Ta alloys [7, 8].

3.2 Low-cost manufacturing processes

To develop the biocompatible orthopedic implant devices, Ti-15Zr-4Nb-(0–4) Ta alloys are vacuum-arc melted. The Ti-15Zr-4Nb-(0–4) Ta alloy ingots are homogenized at approximately 1200–1250°C for more than 5 h and beta (β)-forged from the same temperature to forging ratios (cross section before forging/cross section after forging) of more than 3. Then, beta (β)-forgings are conducted to minimize the beta (β , bcc)-phase at 1000 to 1150°C relative to the forging ratio and the size of the billet. Afterward, α - β -forgings at starting temperature of $T_{\beta}-30^{\circ}\text{C}$ are conducted to obtain α (hcp)- and β (bcc)-phases by decoupling the fine β -phase. T_{β} indicates the β -transus temperature (100 vol% β -phase). Finally, 1-m-long \times 100-mm-square Ti alloy billets are hot-forged by α - β -forging, which are performed using a 1200-ton forging machine under atmospheric conditions. To prevent the edge of the billet from cracking caused by heat loss, the forging time is minimized by adjusting the forging reduction and forging width/speed. The reheating of the ingot and forging are repeated once or twice to optimize the ingot size and microstructure. Between β - and α - β -forgings, the billet surface is ground with a grinder to prevent cracking due to the oxide scale formed on the ingot surface.

A continuous hot-rolling process for Ti alloys is shown in **Figure 5**. A continuous hot rolling is conducted using 1-m-long \times 100-mm-square Ti alloy billets. After maintaining them at $T_{\beta}-60^{\circ}\text{C}$ for 2 h, the Ti alloy billets are hot-rolled continuously in the α - β -temperature region (below T_{β}) at a low rolling speed to prevent an increase in

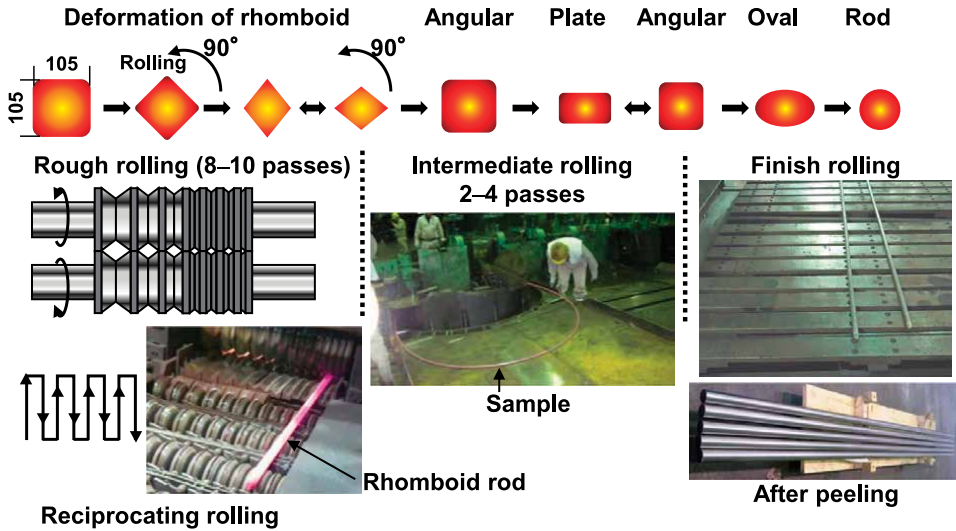


Figure 5. Schematic illustration of continuous hot rolling of Ti-Zr alloy to obtain rod specimens.

the internal temperature of the rolling rod. After α - β -rolling, the annealing of the Ti alloy is generally followed by the removal of internal stress, heat treatment at 700°C for 2 h to optimize the microstructure, and then cooling in air.

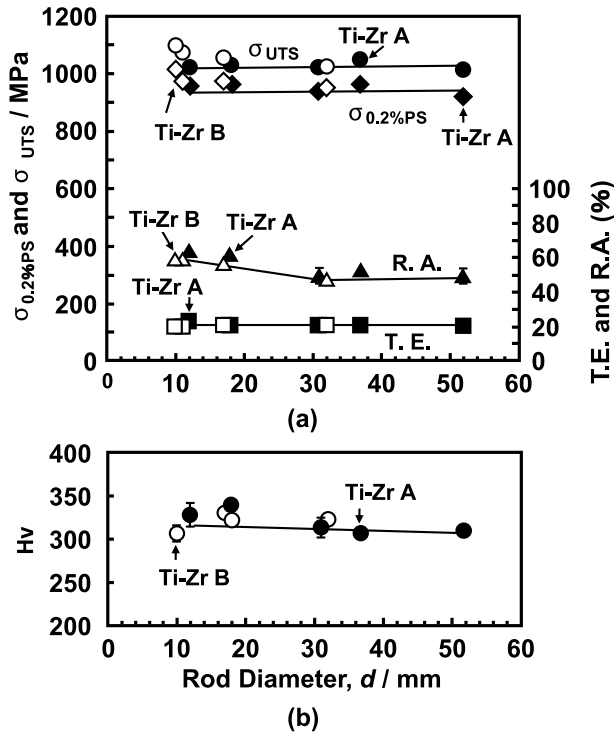


Figure 6. Effects of rod diameter on (a) room temperature mechanical properties ($\sigma_{0.2\%PS}$, σ_{UTS} , T.E., and R.A.) and (b) room temperature Vickers hardness (H_v) of hot-rolled Ti-1.5Zr-4Nb-4Ta (Ti-Zr A) and Ti-1.5Zr-4Nb-1Ta (Ti-Zr B) alloys.

Figure 6 shows the room temperature mechanical properties (0.2% proof strength, $\sigma_{0.2\%PS}$; ultimate tensile strength, σ_{UTS} ; total elongation, T.E.; and reduction in area, R.A.) of continuously hot-rolled Ti-15Zr-4Nb-4Ta (Ti-Zr A) and Ti-15Zr-4Nb-1Ta (Ti-Zr B) alloy rods. High strength, high hardness, and excellent ductility are obtained in this continuous hot-rolling process for each rod diameter (12 to 50 mm) [8].

4. TEM analysis of passive films formed on Ti alloys

Figure 7a–d shows field emission transmission electron microscopy (FE-TEM) images of the passive oxide films formed on the annealed Ti-6Al-4V alloy, Ti-15Zr-4Nb-1Ta alloy, solution-treated high-N stainless steel, and Co-28Cr-6Mo alloy surfaces by anodic polarization up to 0 V vs. SCE (saturated calomel electrode) in 0.9% NaCl at 37°C [9]. To compare the distribution of each metallic element in the passive oxide films formed on metal surfaces, 0 V vs. SCE is selected as the potential in the passive region. As can be seen from the FE-TEM images, the surface of each passive oxide film is protected by carbon, and a passive oxide film is observed on the metal surface. According to the electron diffraction patterns of the Ti-6Al-4V and Ti-15Zr-4Nb-1Ta alloys, the metals have a hexagonal-close-packed (hcp) structure, whereas the oxide films have an amorphous structure. Thin passive oxide films of 3.2 ± 0.2 nm, 4.2 ± 0.2 nm, 2.3 ± 0.1 nm, and 1.7 ± 0.2 nm thicknesses (mean \pm standard deviation) are observed on the Ti-6Al-4V alloy, Ti-15Zr-4Nb-1Ta alloy, high-N stainless steel, and Co-28Cr-6Mo alloy surfaces after anodic polarization up to 0 V vs. SCE, respectively [9]. Energy-dispersive X-ray spectrometry (EDX) analysis revealed that the passive oxide film that formed on Ti-15Zr-4Nb-1Ta alloy consists of TiO_2 containing Zr and small quantities of Nb and Ta. The oxide film on Ti-6Al-4V alloy consists of TiO_2 containing Al and a small quantity of V. The oxide film on high-N stainless steel consists of Cr_2O_3 containing Fe and a small quantity of Ni. The oxide

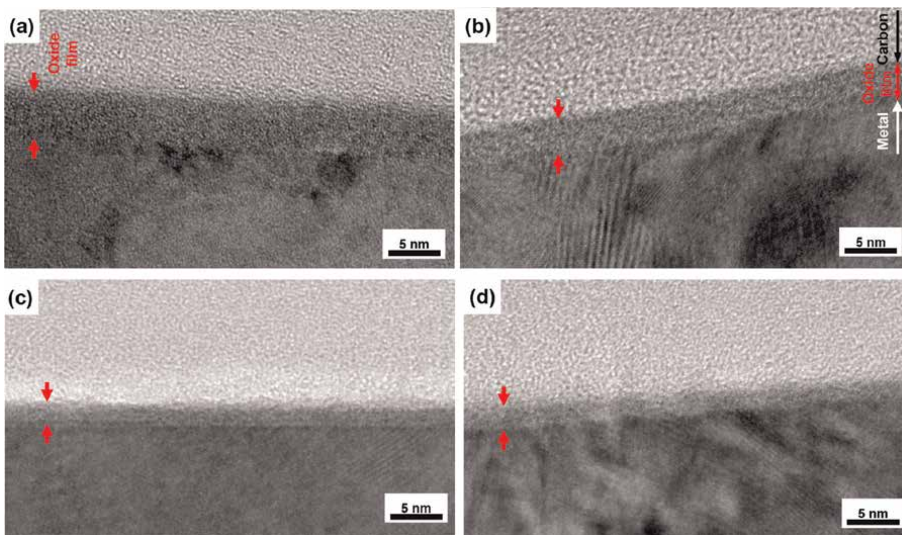


Figure 7. FE-TEM images of oxide films formed on (a) Ti-15Zr-4Nb-1Ta, (b) Ti-6Al-4V, (c) Co-28Cr-6Mo alloy, and (d) high-N stainless steel surfaces by anodic polarization up to 0 V vs. SCE in 0.9% NaCl at 37°C.

film on Co-28Cr-6Mo alloy consists of Cr_2O_3 containing Co and a small quantity of Mo. **Figure 8** shows the changes in the concentration (at%) of each element in the oxide films from the oxide/metal interface to the oxide film surface obtained by the EDX analysis of the oxide films. At the oxide/metal interface, the metal concentration is relatively high, and with increasing distance from the oxide/metal interface, the metal concentration decreases and the oxygen (O) concentration increases. The Ti-15Zr-4Nb-1Ta alloy has a higher oxygen concentration in the oxide film than the Ti-6Al-4V alloy. In the oxide films formed on the high-N stainless steel and Co-28Cr-6Mo alloy surfaces, the concentrations of Fe and Co at the oxide/metal interface are high and decrease as the distance from the oxide/metal interface increases. This high oxygen concentration in the oxide films is due to the formation of ZrO_2 , Nb_2O_5 , and Ta_2O_5 from Zr, Nb, and Ta, respectively.

The metal surface of an oxide film (electric double layer) is equivalent to a capacitor. The oxide film resistance (R_P) and capacitance (C_{CPE} , μF) diagrams of implantable metals have been investigated by electrochemical impedance spectroscopy (EIS) [9]. The oxide film resistance (R_P , $\text{M}\Omega$) is expressed by $R_P = \varepsilon_o \cdot \varepsilon_r \cdot k_{OX} / C_{CPE}$, where ε_o and ε_r are the vacuum permittivity ($8.854 \times 10^{-8} \mu\text{F}/\text{cm}$) and the relative dielectric constant of the oxide film, respectively, and k_{OX} is the resistivity ($\text{M}\Omega \cdot \text{cm}$) of the

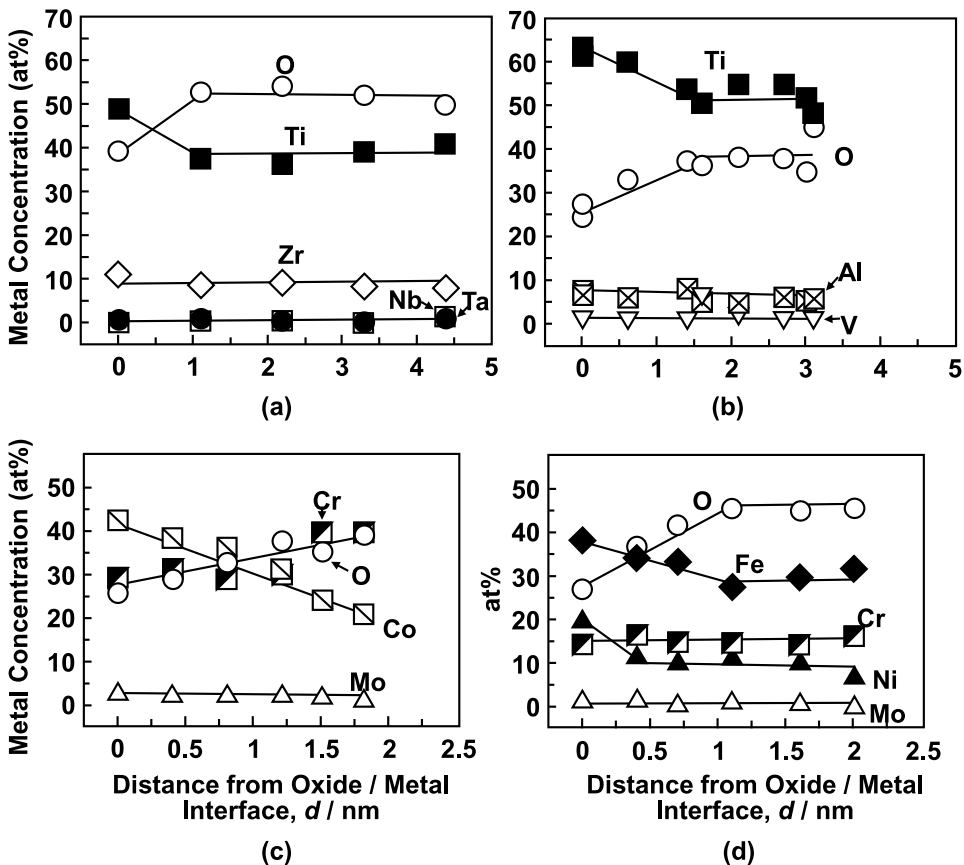


Figure 8. Changes in metal concentrations (at%) in oxide films formed on (a) Ti-15Zr-4Nb-1Ta, (b) Ti-6Al-4V, (c) Co-28Cr-6Mo, and (d) high-N stainless steel from oxide/metal interface to oxide film surface.

oxide film. R_P and C_{CPE} are inversely proportional. The Ti-15Zr-4Nb-(0 to 4) Ta alloys have large R_P (maximum: $13 \text{ M}\Omega \cdot \text{cm}^2$) and small C_{CPE} (minimum: $12 \mu\text{F} \cdot \text{cm}^{-2} \cdot \text{s}^{n-1}$, $n = 0.94$) values.

5. Metal ion release *in vitro* and *in vivo*

Concerns such as metal sensitivity remain with regard to the long-term exposure to metal ions released from metallic orthopedic implant devices into the body. Seven-day static immersion tests of alloys are conventionally performed to examine the quantities of metal ions released from an alloy in different solutions and their pH dependence [10]. The effects of pH on the quantities of metal ions released from Ti-6Al-4V and Ti-15Zr-4Nb-4Ta alloys, respectively, are reported in Ref. [10]. Bottles of each solution without a specimen are prepared as blanks. The weekly quantity of each metal ion released ($\mu\text{g}/\text{cm}^2$) is estimated as (amount of solution: 50 ml) \times [(metal concentration in each solution)–(mean metal concentration of three blank bottles)]/(surface area of specimen).

The quantities of metal ions released from Ti-6Al-4V alloy markedly increase with decreasing pH from 4 to 2, although the changes are relatively small above pH 4. In contrast, even a low pH has virtually no effect on the quantity of each metal ion released from Ti-15Zr-4Nb-4Ta alloy, with the exception of Ti; the quantity of released Ti ions starts to increase below pH 3.5, although more gradually than that of Ti-6Al-4V alloy. Thus, 0.9%NaCl containing HCl (0.9%NaCl+HCl) solution adjusted to pH 2 by adding HCl is suitable for accelerated immersion tests.

In metal ion release test *in vivo*, the metal quantity in a solution containing dissolved bone tissue is measured using ICP-MS (inductively coupled plasma mass spectrometry). The quantities ($\mu\text{g}/\text{g}$) of various metals released into the bone tissue are calculated by dividing the amount (μg) of each metal in the dissolved bone tissue solution by the weight (g) of lyophilized bone tissue [11]. The Ti quantity in the rat tibia tissue-implanted Ti-15Zr-4Nb-4Ta alloy is considerably lower than that in the tibia tissue-implanted Ti-6Al-4V alloy. The Zr, Ta, and Nb quantities are not significantly higher than those of the control sample (without an implant). The Ti quantity in the tibia tissue-implanted Ti-15Zr-4Nb-4Ta alloy is about 40% lower than that in the tibia tissue-implanted Ti-6Al-4V alloy. The total quantity (Zr + Nb + Ta) of Zr, Nb, and Ta is approximately 20% lower than the total quantity (Al + V) of Al and V.

6. Biological safety evaluation under the accelerated extraction condition

6.1 Accelerated extraction condition for biological safety evaluation

Biological safety evaluation tests of two Ti-Zr alloys are performed under the normal extraction condition in accordance with the ISO 10993 series and under the accelerated extraction condition [12]. Ta-free Ti-15Zr-4Nb (Ti-15-4) and Ti-15Zr-4Nb-1Ta (Ti-15-4-1) alloys are used for various biological safety evaluation tests. Plate specimens each with dimensions of 20 mm \times 20 mm \times 1 mm (thickness) are cut from these Ti-15-4 and Ti-15-4-1 alloys for extraction in the biological safety test. The surface of each plate specimen is polished with 1000-grit waterproof emery paper. Rod specimens with a diameter of 1.2 mm and a length of 2.5 mm are used for rat implantation. Each specimen is ultrasonically cleaned in ethanol.

Cell culture medium containing serum is used for extraction in cytotoxicity test, because it supports cellular growth as well as enables the extraction of both nonpolar and polar substances. For normal extraction in main biological safety tests except for cytotoxicity test, plate specimens are extracted in the 0.9%NaCl solution at 121°C for 1 h. On the other hand, the accelerated extraction (0.9%NaCl+HCl) solution adjusted to pH 2 can be prepared in accordance with ISO 16428 as follows [12]. 1 mol/L hydrochloric acid is added to 0.9%NaCl (physiological saline) solution, and the mixed (0.9%NaCl+HCl) solution is adjusted to pH 2. All test specimens are ultrasonically cleaned in ethanol and then sterilized in an autoclave at 121°C for 15 min. After drying, the test specimens are immersed for 7 d in the accelerated (0.9%NaCl+HCl, pH = 2) solution at 37°C. After sufficient stirring, the pH of the accelerated (0.9%NaCl+HCl) solution after extraction is neutralized to 6 ± 1 using 0.1 and 1 mol/L NaOH solutions to obtain various biological evaluation test extracts. Blank extracts (blank control) are similarly prepared without the Ti-15Zr-4Nb-(0 to 4) Ta alloy specimen. Positive control and negative (blank control) groups, and test specimen-treated group are established under different conditions necessary for each biological safety evaluation test to confirm the sensitivity of the test systems.

In implantation tests, new bone formation, bone contact, and osteoid formation rates are compared between test and control specimens. The behavior of newly formed bone tissue around implants can be calculated using the following three parameters. New bone formation rate (%) = (total length of new bone formed around implant)/(length of surrounding implant), bone contact rate (%) = (total length in direct contact with implant)/(length of surrounding implant) $\times 100$, and osteoid formation rate (%) obtained by Villanueva staining = [(total area of osteoid bone)/total area of new bone (osteoid plus calcified bone)].

6.2 Test results of biological safety evaluation

Biological safety evaluation test results obtained with Ti-15Zr-4Nb (Ti-15-4) and Ti-15Zr-4Nb-1Ta (Ti-15-4-1) alloys are reported in Ref. [12]. The effects of normal condition (in 0.9%NaCl and medium) and accelerated condition (in 0.9%NaCl+HCl, pH 2) extracts are compared using Ti-15Zr-4Nb alloys. All of the tests performed in accordance with the ISO 10993 series show no effect (negative) of either extract.

1. No decrease (93–101%) in the colony formation rate is obtained by the colony formation tests at six (3.13, 6.25, 12.5, 25, 50, and 100%) concentrations of the medium extracts for the Ti-15Zr-4Nb and Ti-15Zr-4Nb-1Ta alloys. These results indicate that the Ti-15Zr-4Nb and Ti-15Zr-4Nb-1Ta alloys are noncytotoxic.
2. For skin sensitization evaluation (in maximization tests), an average score of 1 or higher is considered positive for skin reactions in accordance with the ISO 10993-10 standard. The average scores for the accelerated condition (in 0.9% NaCl+HCl) extracts are 0 for the test specimens subjected to 24- and 48-h treatments, indicating that the Ti-15Zr-4Nb and Ti-15Zr-4Nb-1Ta alloys caused no sensitization (no erythema) response.
3. Normal condition and accelerated condition extracts of 0.2 mL each are intradermally injected in the irritation tests of rabbits. No edema and erythema are observed at any of the injection sites and the observation times in all groups, resulting in a score of 0 for intradermal reactions. No significant differences in

scores are observed among the blank extract-injected, normal condition extract-injected, and accelerated condition extract-injected groups, indicating that the Ti-15Zr-4Nb alloy causes no intradermal reactions.

4. For the acute systemic toxicity of normal condition and accelerated condition extracts, no effects of the extracts on the general conditions or the weight of any of the mice and no abnormalities are observed in either intrapleural or intraperitoneal organs. This result indicates that the normal condition and accelerated condition extracts from the test Ti-15Zr-4Nb alloy specimens have no acute systemic toxicity.

For normal condition (in 0.9%NaCl at 121°C for 1 h) extracts intravenously injected to rats for 21 days, there are no significant differences between the control and test Ti-15Zr-4Nb and Ti-15Zr-4Nb-1Ta alloy groups for both female and male rats in the weight, the quantity of food intake, and the results of the urine test. No toxicological significance is observed in the weights of organs and the results of the blood biochemical and hematologic tests. No abnormalities in the macroscopic examination of the systemic organs are also observed for both female and male rats. Moreover, no noteworthy abnormalities are observed in the histopathological examination for both female and male rats. These results show that no clear systemic toxicity is expressed when the normal condition extracts with the Ti-15Zr-4Nb and Ti-15Zr-4Nb-1Ta alloys are intravenously injected to female and male rats once a day for 21 days.

5. In the genotoxicity tests, (a) no increase in the number of revertant colonies is found for gene mutation inducibility. The Ti-15Zr-4Nb alloy immersed in the accelerated extraction 0.9%NaCl+HCl solution shows no gene mutation inducibility. (b) For chromosomal aberration inducibility, no increase in the frequency of appearance of cells with chromosomal aberrations is found. This indicates that the Ti-15Zr-4Nb and Ti-15Zr-4Nb-1Ta alloys do not induce chromosomal aberrations.
6. No cellular infiltration in the implantation tests is observed around the Ti-15Zr-4Nb and Ti-15Zr-4Nb-1Ta alloy specimens, and no degeneration, necrosis, bleeding, or other tissue reactions are found. The formation of new bone is observed around the test specimen in the histopathological examination: The new bone is in direct contact with the Ti-15Zr-4Nb and Ti-15Zr-4Nb-1Ta alloys and is calcified for all rats. Similar reactions are observed for the sites where the control Ti-6Al-4V alloy is implanted. These results indicate that the Ti-15Zr-4Nb and Ti-15Zr-4Nb-1Ta alloys are not inflammatory but osteoconductive, similar to the control Ti-6Al-4V alloy.

7. Fatigue property of Ti alloys

7.1 Fatigue test method

Fatigue resistance is one of the most important mechanical characteristics of structural biomaterials because biomaterials are generally used under cyclic loading conditions. Tension-tension fatigue tests are conducted in accordance with JIS T 0309 [13].

The fatigue tests are conducted in the tension-to-tension mode using sine wave. The testing conditions are a frequency of 10 or 15 Hz and a stress ratio ($R = \text{maximum stress} / \text{minimum stress}$) of 10. To obtain S-N curves (profiles of maximum stress vs. number of cycles to failure on logarithmic scale), the test specimens are cycled with a constant load amplitude for a maximum of 10^8 cycles or until they fail. Hourglass-shaped specimens are popularly used to fracture at the same position of minimum diameter. Rod-shaped specimens exhibit higher fatigue strength than plate-shaped specimens.

7.2 Fatigue strengths of Ti materials

Figure 9 shows the S-N curves obtained by tension-to-tension fatigue tests (10 Hz sine wave) using different types of annealed Ti-15Zr-4Nb-4Ta rod. The arrows on the symbols show the specimens in which fracture does not occur. Figure 9a shows the results obtained with hourglass-shaped and uniform rod specimens, which shows the same tendency. The number of cycles to failure increases with decreasing the maximum cyclic

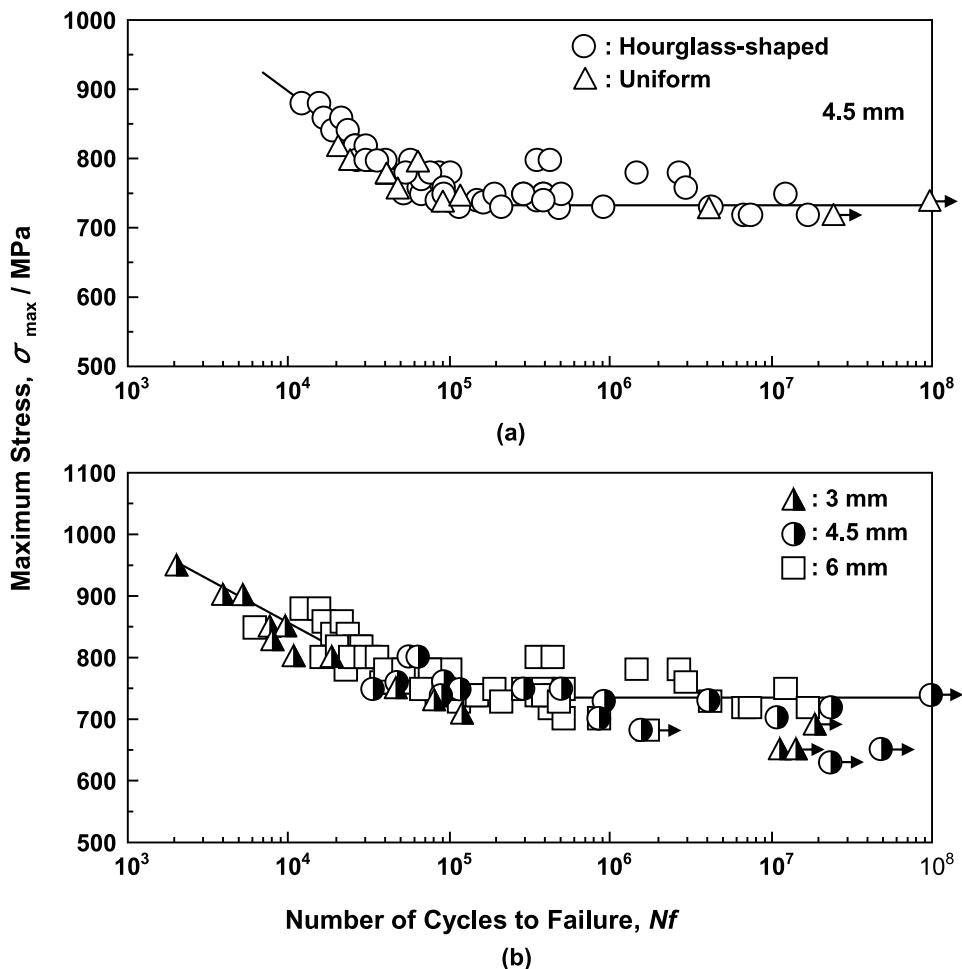


Figure 9. S-N curves obtained from tension-to-tension fatigue test with sine wave (10 Hz) in Ringer's solution at 37°C for annealed Ti-15Zr-4Nb-4Ta rods. (a) Effect of specimen shape (hourglass-shaped and uniform specimens); (b) effect of specimen diameter (3, 4.5, and 6 mm).

stress. The fatigue strength (maximum cyclic stress) at 1×10^8 cycles is approximately 730 MPa. The effect of specimen diameter on fatigue strength is weak as shown in **Figure 9b**. The curves of the hourglass-shaped and uniform plate specimens show similar patterns. The fatigue strength of the plate at 1×10^8 cycles is approximately 485 MPa [14]. Higher-grade C.P. Ti shows higher fatigue strength at 1×10^7 cycles: grade 2, 280 MPa; grade 3, 355 MPa; and grade 4, 485 MPa. The fatigue strengths of the annealed Ti-15Zr-4Nb-4Ta, Ti-6Al-4V, V-free Ti-6Al-7Nb, and Ti-6Al-2Nb-1Ta rods are approximately 730, 685, 600, and 700 MPa, respectively. The annealed Ti-6Al-4V alloy consists of an α -phase matrix with an approximately 20 vol% β -phase. The annealed Ti-15Zr-4Nb-4Ta mostly consists of an α -phase matrix with an approximately 25 vol% β -phase. **Table 1** shows the tensile properties of various implantable Ti metals. The means and standard deviations of 0.2% proof strength ($\sigma_{0.2\%PS}$), ultimate tensile strength (σ_{UTS}), total elongation (T.E.), and reduction in area (R.A.) are calculated with three test specimens. The fatigue ratios (fatigue strength at 1×10^7 cycles/ultimate tensile strength) are shown in **Table 1** and are above 65% for the α - β - and α -type Ti materials.

8. Hot die forging of artificial hip stems

8.1 Hot die forging method

The conditions for rolling Ti-15Zr-4Nb-(0-4) Ta alloy billets (100 mm square) into rods (e.g., 22 and 25 mm in diameter), which are optimal shapes for the high-temperature forging of artificial hip joint stems, are established as described in Section 3.2. With the β -transus temperature (T_β , 850°C) used as a reference, hot rolling is started at a temperature of $T_\beta - 50^\circ\text{C}$. Ti-15Zr-4Nb-(0-4)Ta alloy billets are

Alloy	$\sigma_{0.2\%PS}/\text{MPa}$	σ_{UTS}/MPa	T.E. (%)	R.A. (%)	E/GPa	σ_{FS}/σ_{UTS}
Ti-15Zr-4Nb-4Ta						
Annealed (Plate)	800±14	910±10	19±2			0.54
Annealed (Rod)	848±2	915±3	21±2	55±3	94±2	0.80
S.T. +Aged (Rod)	894±5	1020±8	15±2	48±3	98±2	0.89
C.P. Ti Grade 2	276±6	410±4	40±2	60±6	106±2	0.68
C.P. Ti Grade 3	380±2	540±2	32±2	54±2	108±3	0.66
C.P. Ti Grade 4	600±6	701±8	26±2	46±3	118±2	0.69
Ti-6Al-4V	849±1	934±1	16±1	42±3	102±4	0.73
Ti-6Al-7Nb	845±8	960±10	18±2	47±3	108±2	0.63
Ti-6Al-2Nb-1Ta	842±2	900±3	18±3	43±4	110±1	0.81
Ti-15Mo-5Zr-3Al						
Solution-annealed	910±10	930±8	19±2	50±2	92±2	0.38
Hot-forged	963±12	988±10	18±2	50±6	102±2	0.71

E: Young's modulus.

Table 1. Tensile properties of implantable metals and ratios of fatigue strength at 10^7 cycles (σ_{FS}) to ultimate tensile strength (σ_{UTS}) shown for comparison among the alloys tested.

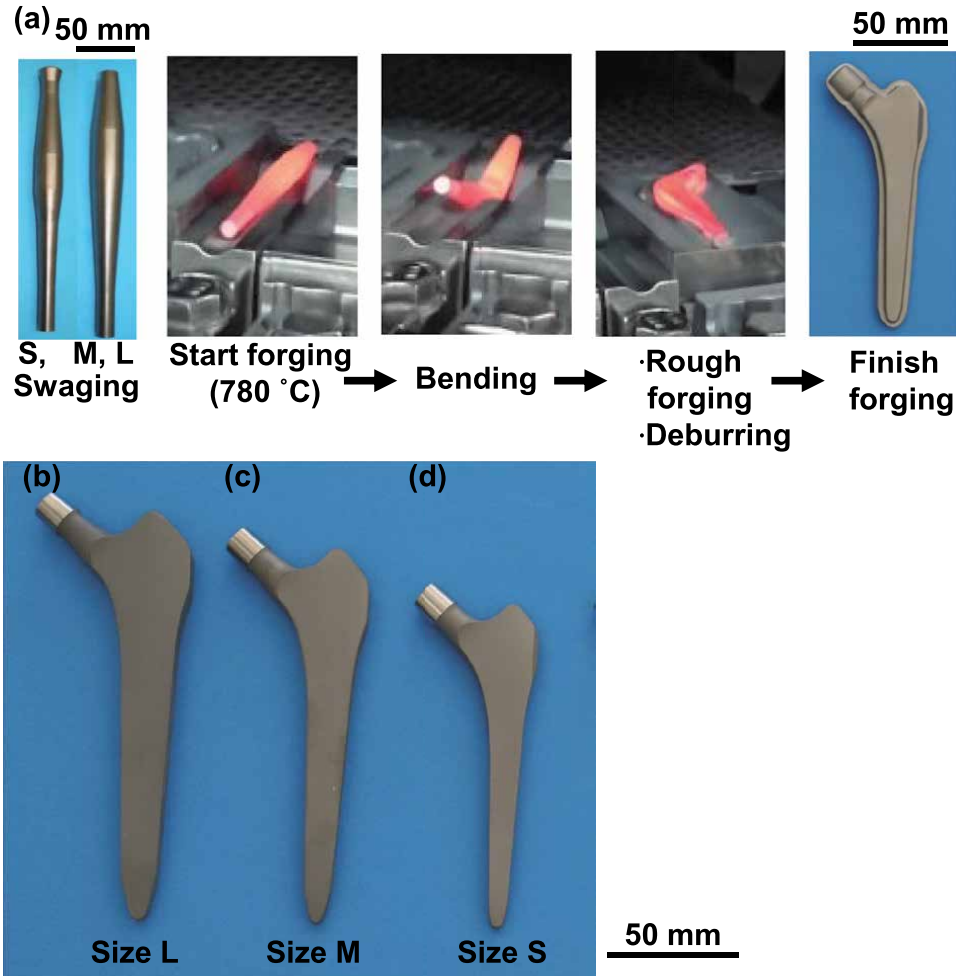


Figure 10.
(a) Mold forging of artificial hip stem at high temperature and (b), (c), (d) hot-forged hip stems of sizes L, M, and S, respectively.

continuously hot-rolled and shaped into rods with a diameter of 22 or 25 mm. The round bars [wrought Ti-15Zr-4Nb-(0–4) Ta alloy] are annealed at 700°C for 2 h [15].

Figure 10 shows the hot die forging for manufacturing cementless artificial hip stems. Ti-15Zr-4Nb alloy rods with a diameter of 22 or 25 mm are shaped into artificial hip stems by die forging at a high temperature [15]. Molds of three sizes, small size S, medium size M, and large size L are manufactured for forging artificial hip stems with the same shape as the approved product Alloclassic SL artificial hip stems. Two molds are set the upper and lower parts. Considering the forging ratio at positions where burrs are frequently generated, the swaging technique is used to shape a Ti-15Zr-4Nb alloy rod to be processed into a spindle to reduce the quantity of generated burrs. The Ti-15Zr-4Nb alloy rod is shaped into a spindle so that the forging ratio [(cross-sectional area after forging)/(cross-sectional area before forging)] is 1.5–2.0. The spindle-shaped Ti-15Zr-4Nb alloy specimens are continuously introduced into a high-frequency continuous heat treatment furnace, and die forging is started at a temperature of 740 or 780°C (mainly 780°C). The spindle-shaped Ti-15Zr-4Nb alloy

specimens are subjected to bending, rough forging, deburring, and finish forging to obtain three sizes (L, M, and S) of artificial hip stem. The oxidized layer formed on the artificial hip stem surface during hot forging is removed by blasting and pickling after annealing at 700°C for 2 h. Thereafter, the surface of artificial hip stems is grit-blasted to have surface roughness (Ra) of approximately 3 to 5 μm using 24-grit Fuji Random WA high-purity Al₂O₃ particles. This is similar to the Ra of the approved product Alloclassic SL artificial hip stems.

8.2 Microstructure of hot-forged artificial hip stems

Figure 11 shows an (a) optical micrograph and (b) SEM image of the transverse (T) section near the center at the 80-mm position from the head of the annealed Ti-

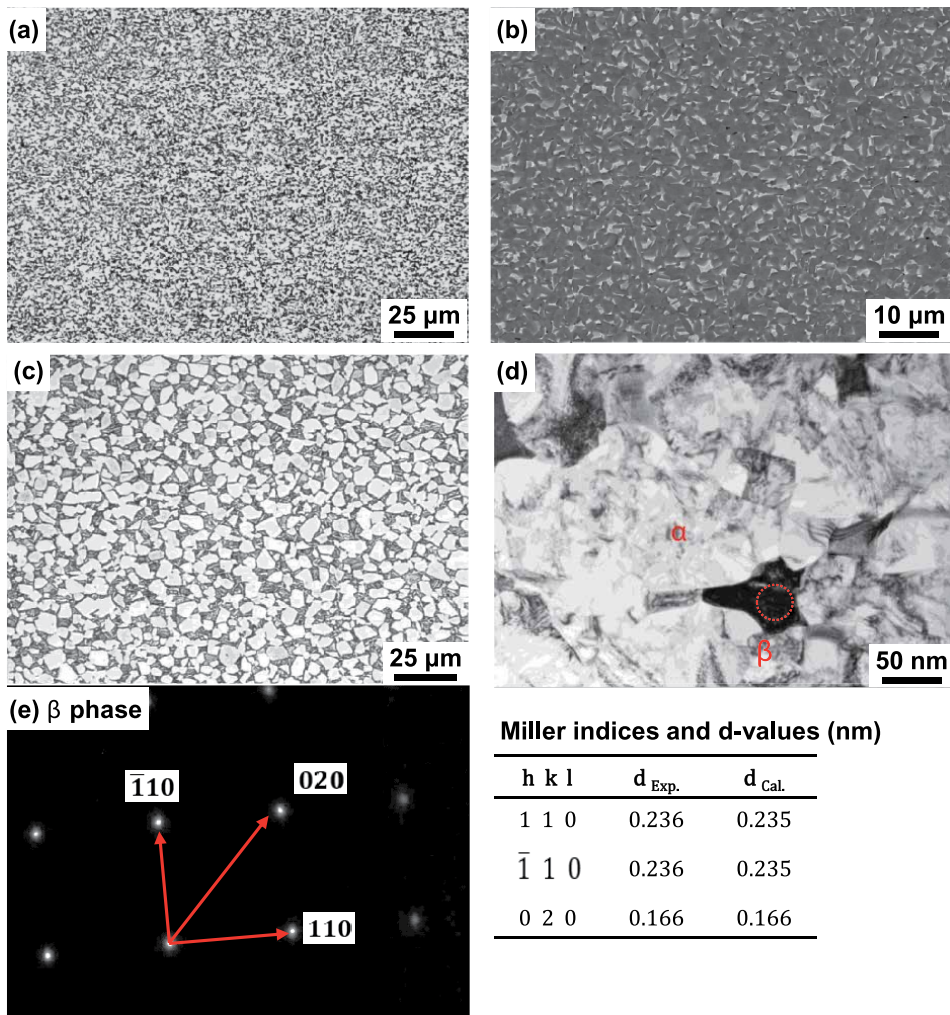


Figure 11. (a) Optical micrograph and (b) SEM and (d) TEM images of Ti-15Zr-4Nb stem hot-forged starting at 780 °C; (e) electron beam diffraction pattern of the encircled area in (d); (c) optical micrograph of Alloclassic SL stem.

15Zr-4Nb hip stem (size S) after hot forging [15]. As shown in **Figure 11b**, the β -phase (bcc) appears white in the SEM image. In the optical micrograph and SEM image of the annealed Ti-15Zr-4Nb hip stem, the β -phase that precipitated at the grain boundaries of the α -phase (hcp) matrix is found to be produced by hot forging. **Figure 11d** and **e** shows TEM images of the T sections of hot-forged artificial hip stem. **Figure 11e** shows Miller indices and the calculated and measured interplanar distances (d). There is good agreement between both interplanar distance (d) values. The lattice parameters $a = b = 0.295$ nm and $c = 0.468$ nm for α (hcp) Ti [ICDD (International Centre for Diffraction Data) No. 044-1294] and $a = b = c = 0.331$ nm for β (bcc) Ti (ICDD No. 044-1288) are used in the calculation of d values for the α (hcp)-phase and β (bcc)-phase. The β (bcc)-phase is found to precipitate at the grain boundaries of the α (hcp)-phase matrix from the results of electron beam diffraction analysis. The microstructure of the hot-forged Ti-15Zr-4Nb alloy artificial hip stem is finer than that of the Alloclassic Zweymüller SL artificial hip stem (Ti-6Al-7Nb alloy), as shown in **Figure 11c**. Similar microstructures are obtained for M and L stems.

8.3 Mechanical property of hot-forged artificial hip stems

Miniature mechanical specimens are cut from the hot-forged hip stems and subjected to tensile tests at room temperature and fatigue tests up to 10^7 cycles. Each of the five uniform rod specimens shown in **Figure 12b** [rod diameter, 3 mm; gauge length (GL), 15 mm] is cut from the hip stem at the position shown in **Figure 12a**. The tensile tests at room temperature are conducted at a crosshead speed of 0.5% of the GL/min until the proof stress reaches 0.2%. The test specimen is then pulled at a crosshead speed of 3 mm/min until the specimen fractures. The tensile properties ($\sigma_{0.2\%PS}$, σ_{UTS} , T.E., and R.A.) are measured with five specimens [15].

Tension-tension fatigue tests at room temperature under the air are carried out in accordance with JIS T 0309 [13]. Miniature hourglass-shaped rod specimens with 3 mm in minimum diameter and 50 mm in total length, as shown in **Figure 12c**, cut from hot-forged artificial hip stems at the position shown in **Figure 12a**. The tension-tension fatigue tests with cylindrical rods are conducted using a sine wave at a stress ratio R [(maximum cyclic stress (σ_{max}))/(minimum cyclic stress (σ_{min}))] of 10 and a frequency of 15 Hz in air. To obtain S-N curves [profiles of maximum stress (maximum applied load/area of cross section) vs. the number of cycles to failure on logarithmic scale], the rod specimens are cycled at various constant maximum cyclic loads until failure or maximum of 10^8 cycles. The fatigue strength (σ_{FS}) at 10^7 cycles is estimated from the S-N curves.

Table 2 shows the tensile properties ($n = 5$, mean \pm standard deviation) of miniature mechanical specimens cut from the Ti-15Zr-4Nb alloy artificial hip stems annealed at 700°C for 2 h after hot forging at 780 or 740°C. The tensile strength of the hot-forged artificial hip stem tends to be higher than that of the 22 or 25 mm (wrought) Ti-15Zr-4Nb alloy rod before hot forging. Also, the tensile strength of the hot-forged artificial hip stem at 780 or 740°C is close to that of the Alloclassic SL (Ti-6Al-7Nb alloy) artificial hip stem [15].

The fatigue strength of the Ti-15Zr-4Nb alloy hip stem hot-forged at 780°C is ~ 855 MPa and slightly higher than that of the artificial hip stem hot-forged at 740°C, which is higher than those of the Alloclassic SL artificial hip stem and wrought Ti-15Zr-4Nb alloy rod. The σ_{FS}/σ_{UTS} (0.85) of the hot-forged Ti-15Zr-4Nb alloy is slightly higher than that of the Alloclassic SL artificial hip stem (0.78). Thus, the fatigue strength of the hot-forged Ti-15Zr-4Nb alloy stem is higher than that of the

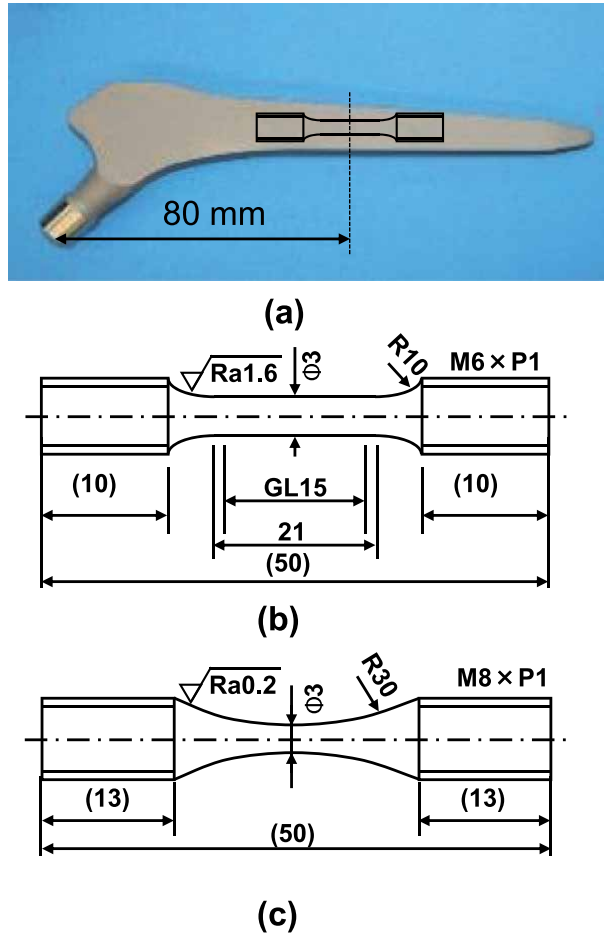


Figure 12. (a) Position of miniature specimens cut from hot-forged artificial hip stems; dimensions of specimens used for (b) room temperature tensile, and (c) fatigue tests.

Ti Alloy	$\sigma_{0.2\%PS}/\text{MPa}$	σ_{UTS}/MPa	T.E. (%)	R.A. (%)	σ_{FS}/MPa	σ_{FS}/σ_{UTS}
Hot-forged stems						
Ti-15Zr-4Nb rod (before forging)	887±5	942±2	20±1	60±1	785±17	0.83
780°C Forged Ti-15Zr-4Nb stem	919±10	983±9	21±1	58±2	855±14	0.86
740°C Forged Ti-15Zr-4Nb stem	912±6	979±7	19±2	55±5	840±5	0.85
SL stem (Ti-6-7)	949±23	1034±23	16±1	54±1	805±26	0.78

Table 2. Tensile properties ($\sigma_{0.2\%PS}$, σ_{UTS} , and T.E., R.A.), fatigue strength at 10^7 cycles (σ_{FS}), and fatigue ratio (σ_{FS}/σ_{UTS}) of hot-forged Ti-15Zr-4Nb stems.

Alloclassic SL artificial hip stem. It is considered that this improvement in the fatigue strength of the hot-forged Ti-15Zr-4Nb alloy hip stem is attributable to its fine microstructure, as shown in **Figure 11a**.

8.4 Durability of hot-forged artificial hip stems

Tension-tension durability tests of artificial hip stems are carried out in accordance with ISO 7206-4 standard (third edition) [16]. As shown in **Figure 13**, the artificial hip stem is fixed at angles of 10° (α) in adduction and β (9°) in flexion to stem axis, and at the vertical distance (D) from the head center of the artificial hip prosthesis to the upper level of the fixation. The D is set to 80 mm for the hot-forged Ti-15Zr-4Nb alloy artificial hip prosthesis. α (the angle between the load axis and the stem axis) is 10° (in abduction to stem axis), and β (the angle between the line from the center of the head to the tip of the artificial hip femoral stem and the longitudinal sectional stem axis when viewed from the back) is 9° (in flexion to stem axis). The durability tests are carried out under tension-tension loading with a sine wave at a

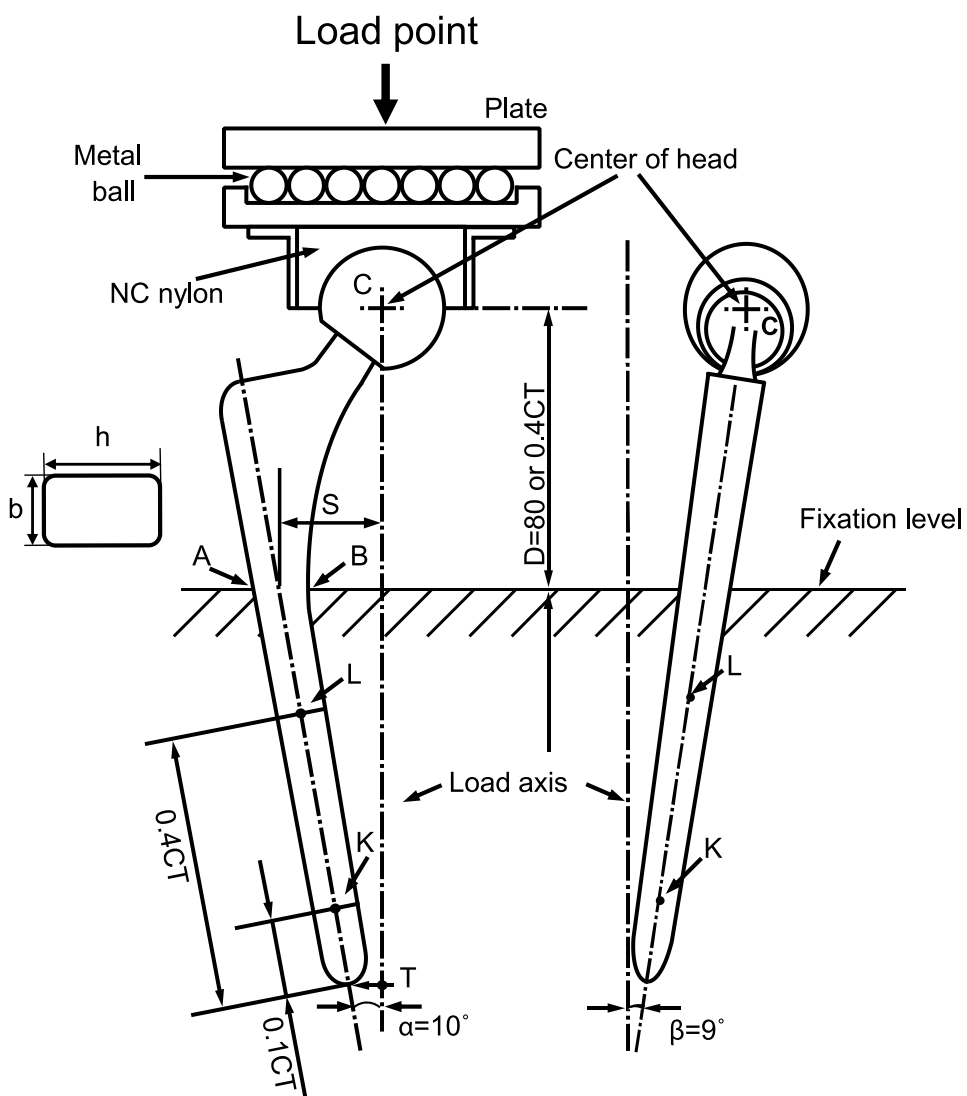


Figure 13.
Fixation method in durability test using artificial hip stem in accordance with ISO 7206-4.

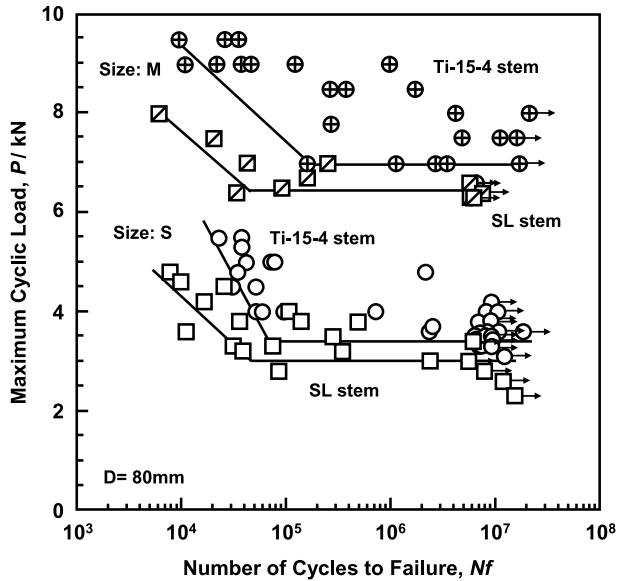


Figure 14. P-N curves of hot-forged Ti-15Zr-4Nb hip stems (sizes S and M) and Alloclassic SL stems (sizes S and M) obtained from the results of compression bending durability tests.

load ratio [(minimum cyclic load (P_{\min}))/(maximum cyclic load (P_{\max}))] of 0.1 and a frequency of 3 Hz in air. The durability limits (PD) at 5×10^6 cycles are determined from the P-N curves (profile of maximum load vs. number of cycles to failure on logarithmic scale). The durabilities of artificial hip femoral stems made of Ti-6Al-7Nb and Ti-6Al-4V alloys, which are globally used in clinical settings, are investigated for comparison with that of the Ti-15Zr-4Nb alloy. The cementless total hip femoral stems used are the Alloclassic Zweymüller SL artificial hip stems.

Figure 14 shows the P-N curves of Ti-15Zr-4Nb (Ti-15-4) alloy artificial hip stems (sizes M and S) and Ti-6Al-7Nb (Ti-6-7) alloy Alloclassic Zweymüller SL artificial hip stems. A durability test is conducted for more than 5 million cycles according to ISO 7206-4 standard [15]. The durability limits (PD) at 5 million cycles are 6800 ± 606 N for the size M stem and 3400 ± 495 N for the size S stem. The PDs of the Alloclassic Zweymüller SL artificial hip stem (Ti-6Al-7Nb alloy) are 6400 ± 463 N for the size M stem and 3000 ± 512 N for the size S stem. The Ti-15Zr-4Nb alloy artificial hip femoral stem hot-forged using the forging technology has a durability limit higher than that of the Ti-6Al-7Nb alloy Alloclassic Zweymüller SL artificial hip femoral stem. It fully satisfies the PD (durability limit) at 5 million cycles of 2300 N specified in ISO 7206-4 standard (third edition) [16]. Thus, the artificial hip stem manufactured by hot forging can be used clinically.

8.5 Stress analysis for durability of artificial hip stem

The stress analysis of the tension-tension durability test results of artificial hip stems is performed using the fatigue strengths shown in **Table 2** [15]. **Figure 15** shows the stress analysis for the durability test of artificial hip femoral stem according to ISO 7206-4

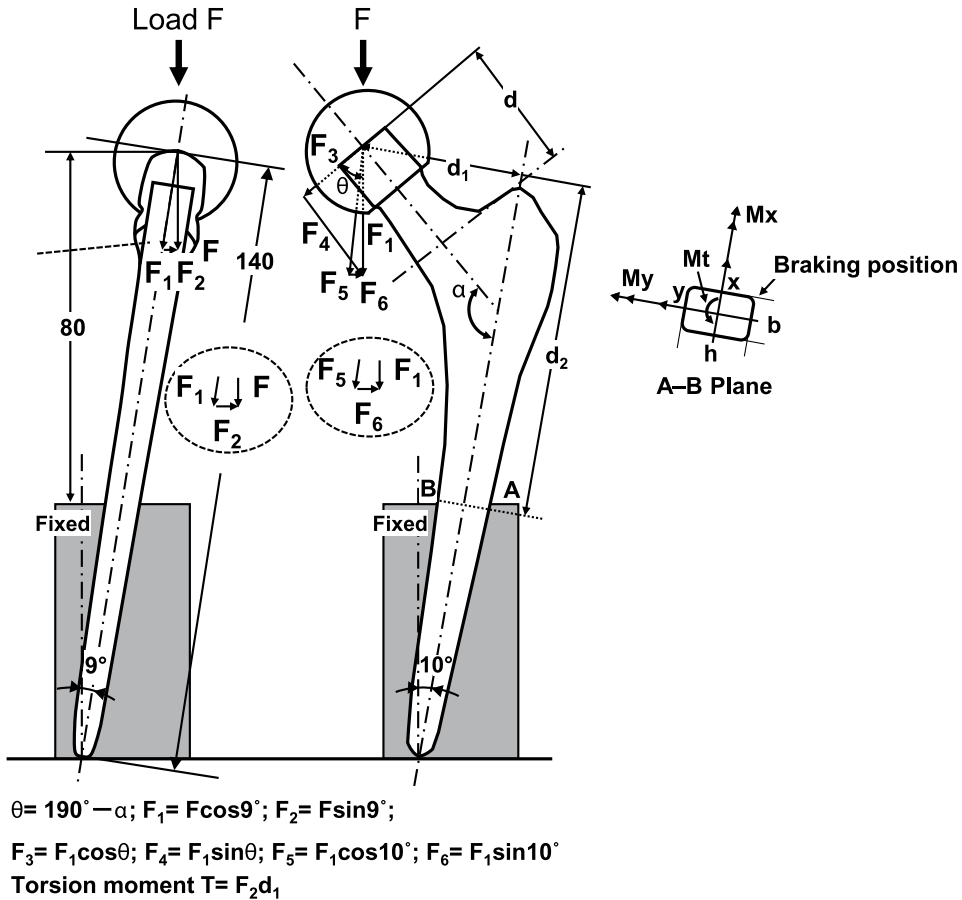


Figure 15.
 Stress analysis of results of durability tests in accordance with ISO 7206-4.

standard (third edition). Since the hip force F in A–B section is inclined by 9° from the vertical direction, it is resolved into two components, $F_1 = F \times \cos 9^\circ$ and $F_2 = F \times \sin 9^\circ$. As the neck angle (α) of the artificial hip femoral stem is 131° , the component force F_1 can be resolved into $F_3 = F_1 \times \cos (180^\circ - \alpha + 10^\circ) = F_1 \times \cos (190^\circ - \alpha)$ and $F_4 = F_1 \times \sin (190^\circ)$. Moreover, F_1 can be decomposed into two components ($F_5 = F_1 \times \cos 10^\circ$ and $F_6 = F_1 \times \sin 10^\circ$); $M_x = F_5 \times d_1$, $M_x = F_6 \times d_2$, and $M_y = F_2 \times d_2$ [15].

When the compressive stress is positive, the net axial stress of the cross section (σ_z) generated at position (x, y) on the A–B plane is given by the following:

$$\sigma_z = \frac{F_5}{\text{Cross-sectional area}} + \frac{M_x}{I_x} y - \frac{M_y}{I_y} x,$$

$$\sigma_z = \frac{F_5}{bh} + \frac{F_5 d_1 - F_6 d_2}{I_x} y - \frac{F_2 d_2}{I_y} x. \quad (1)$$

Here, the inertia moments are $I_x = b \times h^3/12$ and $I_y = h \times b^3/12$. The shear stresses τ_{ZX} and τ_{ZY} generated in the x and y directions, respectively, by the bending moment can be calculated as follows:

$$\tau_{zx} = -\frac{Q_y F_2}{b I_y}, \tau_{zy} = \frac{Q_x F_6}{h I_x},$$

$$Q_x = \frac{b}{2} \left(\frac{h^2}{4} - y^2 \right), Q_y = \frac{h}{2} \left(\frac{b^2}{4} - x^2 \right). \quad (2)$$

Here, fatigue crack is generated from the corners of the stem surface in this durability test of hip stem. Therefore, since Q_x and Q_y become zero at the material surface ($x = b/2, y = -h/2$ mm), the shear stresses (τ_{zx} and τ_{zy}) become zero.

In addition, torsion moment (T) is given by $T = F_2 \times d_1$. The shear force generated by the torsion moment is given by

$$\tau_{zx} = -\frac{T}{2 I_x} y, \tau_{zy} = \frac{T}{2 I_y} x. \quad (3)$$

The absolute values of the shear force generated by the bending moment and torque are used to calculate τ_{zx} and τ_{zy} , which are substituted into the following equation to determine the equivalent stress (σ_{eq}) using the Von Mises criterion:

$$\sigma_{eq} = [\sigma_z^2 + 3(\tau_{zx}^2 + \tau_{zy}^2)]^{\frac{1}{2}}. \quad (4)$$

The equivalent stress (σ_{eq}) can be used to directly compare the fatigue strengths as shown in **Table 3**. **Table 3** shows the maximum equivalent stress (σ_{eq}) calculated for the hot-forged Ti alloys with Eq. (4). σ_{eq} is calculated using the durability limits ($x = 3.6$ mm, $y = -5.5$ mm; 3400 N for Ti-15Zr-4Nb alloy and 3000 N for Alloclassic SL) of the S stems. The σ_{eq} values of the Ti-15Zr-4Nb and Alloclassic SL S stems are 871 and 791 MPa, which are close to those (855 and 805 MPa) shown in **Table 3**, respectively [15]. The σ_{eq}/σ_{FS} values of the Ti-15Zr-4Nb and Alloclassic SL S stems are 1.02 and 0.98, respectively, and a good match is obtained. The same can be calculated for a fracture at the neck. **Figure 16** shows the changes in σ_{eq} as a function of maximum cyclic load (N). This analysis is useful for developing artificial hip joints, identifying the worst specimens, and analyzing the durability test results of hip stems.

Figure 17 shows the calculation method of the first moment of area (Q_x and Q_y), second moment of area (I_x and I_y), and shear stress (τ_{zx} and τ_{zy}) required for the calculation when the cross-sectional shape of hip stem changes. The racetrack-shaped Q_x shown in **Figure 17** can be calculated by numerical integration from the y -coordinate of the breaking position to $(h + b)/2$ (e.g., numerical calculation in a trapezoidal shape) [15].

Specimen	σ_{eq} /MPa	x, y /mm	σ_{FS} /MPa	σ_{eq}/σ_{FS}
Hot-forged Ti-15Zr-4Nb	871	(3.6, -5.5)	855	1.02
Alloclassic SL	791	(3.6, -5.5)	805	0.98

Table 3. Maximum equivalent stress (σ_{eq}), coordinates (x, y) of the location of σ_{eq} , σ_{FS} , and the ratio of maximum equivalent stress to fatigue limit of A-B cross section.

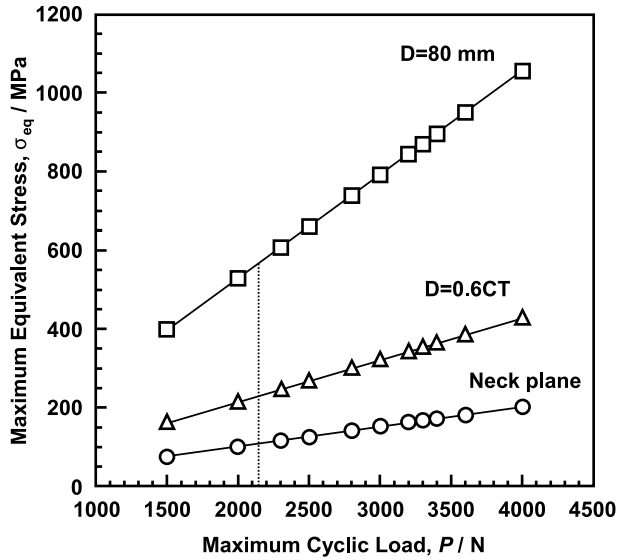


Figure 16. Changes in maximum equivalent (σ_{eq}) as a function of maximum cyclic load.

Cross-sectional shape	First moment of area (Q)	Second moment of area (I)
Circle 	$Qx = \frac{1}{12}(d^2 - 4y^2)^{\frac{3}{2}}$ $Qy = \frac{1}{12}(d^2 - 4x^2)^{\frac{3}{2}}$ $\tau_{zx} = -\frac{QyF_2}{Iyd} \quad \tau_{zy} = \frac{QxF_3}{Ixd}$	$I_x = \frac{\pi}{64}d^4$ $I_y = \frac{\pi}{64}d^4$
Racetrack shape 	$y > \frac{h}{2}$ $Qx = \int_y^{h+b} 2 \sqrt{\left(\frac{b}{2}\right)^2 - \left(y - \frac{h}{2}\right)^2} y dy$ <p>(Numerical integration)</p> $Qy = (b^2 - 4x^2) \left[\frac{h}{8} + \frac{1}{3}(b^2 - 4x^2)^{\frac{1}{2}} \right]$ $\tau_{zx} = -\frac{QyF_2}{bly} \quad \tau_{zy} = \frac{QxF_6}{(b+h)Ix}$	$I_x = \frac{b}{4} \left[0.055b^3 + 0.7854b(0.1801b^2 + 0.849bh + h^2) + \frac{h^3}{3} \right]$ $I_y = \frac{b^3(16h + 3\pi b)}{192}$
Ellipse 	$Qx = \frac{2b}{3a}(a^2 - y^2)^{\frac{3}{2}}$ $Qy = \frac{2a}{3b}(b^2 - x^2)^{\frac{3}{2}}$ $\tau_{zx} = -\frac{QyF_2}{2bly} \quad \tau_{zy} = \frac{QxF_6}{2alx}$	Cross-sectional area $A = \pi ab$ $I_x = \frac{\pi ba^3}{4}$ $I_y = \frac{\pi ab^3}{4}$

Figure 17. Calculation of first moment of area, second moment of area, and shear stress.

8.6 Implantation of grit-blasted Ti-15Zr-4Nb alloy rods in rabbits

The effects of the maximum pullout properties of grit-blasted Ti-15Zr-4Nb (Ti-15-4) and Ti-15Zr-4Nb-4Ta (Ti-15-4-4) alloys have been investigated by implantation in rabbits. **Figure 18** shows a schematic illustration of the method of implantation into the femur of

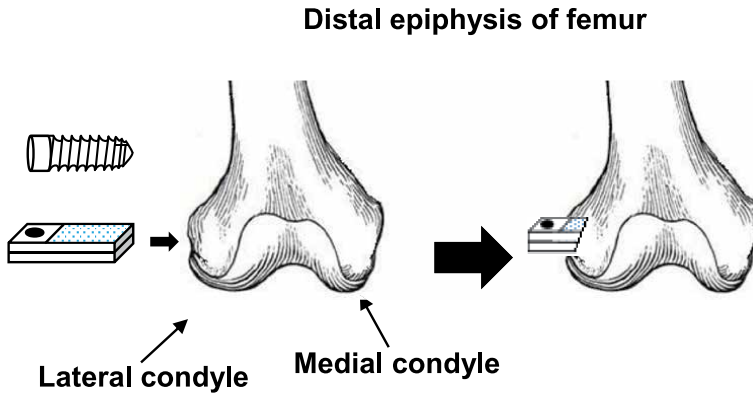


Figure 18.
Schematic illustration of method of implantation into femur of rabbit.

rabbits [12]. For comparison, rods made of grit-blasted Ti alloys (Ti-15Zr-4Nb and Ti-6Al-7Nb), shot-blasted Ti-15Zr-4Nb-4Ta alloy, and smooth-surface and machined Ti-15Zr-4Nb alloys are implanted into the distal epiphysis of the femur. After the grit-blasted, shot-blasted, and machined Ti-15Zr-4Nb rods are implanted for 4, 8, 12, 16, and 24 weeks, the pullout test is carried out at a cross-head speed of 0.5 mm/min. Maximum pullout loads are determined from load-displacement curves.

The effect of surface modification is commonly evaluated by a withdrawal test after the implantation test using rabbits. **Figure 19** shows the changes in maximum pullout load after implantation into rabbits as a function of implantation period. The maximum pullout loads of the grit-blasted, shot-blasted, and machined Ti-15Zr-4Nb, Ti-15Zr-4Nb-4Ta, Ti-6Al-7Nb (Ti-6-7), and Ti-6Al-4V (Ti-6-4) alloys increase linearly with

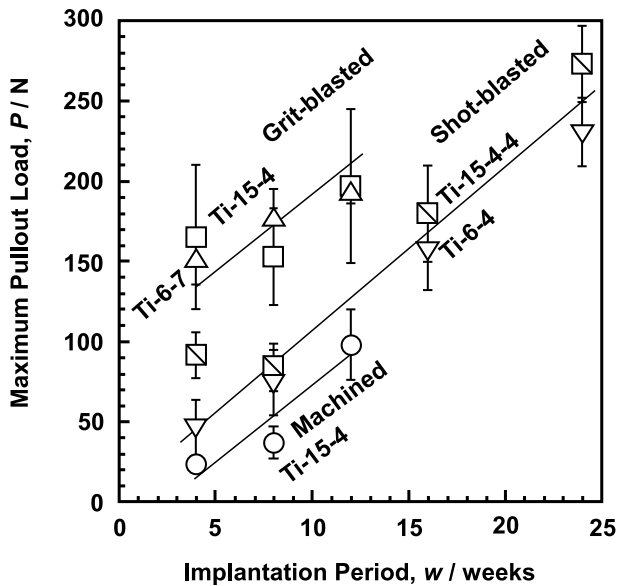


Figure 19.
Maximum pullout loads after implantation in rabbits.

implantation period. The pullout load of the grit-blasted Ti-15Zr-4Nb alloy rods is higher than that of the shot-blasted ones. The area ratios of residual Al_2O_3 particles of the grit-blasted Ti-15Zr-4Nb and Alloclassic stem surfaces are 9.1 ± 0.4 and $10.4 \pm 1.6\%$, respectively [12].

8.7 Relationship between durability limit and bending strength of osteosynthesis devices

M-N curves (maximum bending moment vs. number of cycles to failure on logarithmic scale) of osteosynthesis devices are measured for the compression bending and four-point bending durability tests [17]. The maximum bending moments (M) are calculated as $M = L \times P_m$ for the compression bending durability test and $M = h \times P_m/2$ for the four-point bending durability test, where P_m is the maximum cyclic load (N) in the compression bending durability or four-point bending test. L is lever arm in compression bending tests. h is the distance between the supporting and loading rollers in four-point bending test. The durability limit of various types of osteosynthesis devices linearly increases with increasing bending strength. **Figure 20** shows the relationship between the durability limit (at 10^6 cycles) and the bending strength plotted on a log-log graph. The relationship (durability limit at 10^6 cycles) = $0.67 \times$ (bending strength) (N·m) ($R^2 = 0.85$) is obtained for bone plates, spinal rods, intramedullary nail rods, CHSs, short femoral nails, and epiphyseal plates by regression. This slope of 0.67 is close to the ratio of the fatigue strength to the tensile strength of the raw metals. The relationship for the highly biocompatible Ti-15Zr-4Nb alloy is also linear [17].

Mechanical properties of metallic screws and bone models are used for mechanical testing have been investigated in Ref. [18].

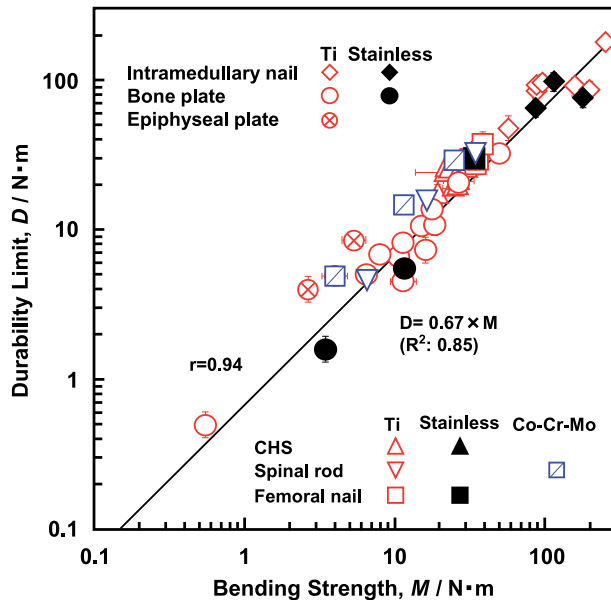


Figure 20. Relationship between durability limit and bending strength of osteosynthesis devices determined by four-point bending and compression bending tests.

9. Selective laser melting of Ti alloy artificial hip stems

9.1 Selective laser melting conditions

Ti-15Zr-4Nb-4Ta alloy powder is prepared by LPW Technology Ltd. (Cheshire, United Kingdom). Ti-15Zr-4Nb-4Ta and Ti-6Al-4V (EOS GmbH Electro Optical System, Krailling, Germany) powders are prepared by plasma atomization [15]. The Ti-15Zr-4Nb-4Ta and Ti-6Al-4V powders are selective laser-melted in Ar atmosphere using a system comprising an EOS M290 machine (EOS GmbH Electro Optical System, Krailling, Germany), EOSPRINT v. 1.5 and HCS v. 2.4.14 software, and the Ti64 Performance M291 1.10 parameter set. The laser beam power (P) is 280–300 W; the hatch spacing between scan passes (H) is 0.13–0.14 mm; the laser scan speed (V) is fixed from 1200 to 1300 mm/s; powder-deposited layer (stacking) thickness (T) is 0.03 mm; the laser spot focus diameter is 0.1 mm. The volumetric energy density (E) calculated as $E = P/(H \cdot T \cdot V)$ is about 60 J/mm³ [15].

Cylindrical rods with diameter of 9 mm and height of 50 mm built by selective laser melting are cut from the support materials. The building direction of the cylindrical specimens is set to 90° or 0° direction for the base plate using the Ti-15Zr-4Nb-4Ta powders. The Ti-15Zr-4Nb alloy cylindrical rods after selective laser melting are heat-treated at 760°C for 4 h followed by air cooling. For comparison, Ti-6Al-4V alloy stems and Ti-6Al-4V alloy rods are similarly selective laser-melted. The selective laser-melted Ti-6Al-4V alloy specimens are annealed at 840°C for 4 h followed by air cooling [15].

9.2 Microstructure and mechanical properties of selective laser-melted Ti alloys

Figure 21 shows optical micrographs and SEM and TEM images of the T section of annealed Ti-15Zr-4Nb-4Ta rods after selective laser melting (90° direction) [15]. The selective laser-melted Ti-15Zr-4Nb-4Ta rod has an acicular structure. TEM images of the selective laser-melted Ti-15Zr-4Nb-4Ta rod show that the rods consisted of fine α' (hcp) lath martensitic structure (lattice parameters $a = b = 0.295$, $c = 0.468$ nm) that precipitated with the fine β (bcc)-phase (lattice parameters $a = b = 0.331$ nm) at the grain boundary of the α' lath martensitic matrix caused by rapid solidification.

Tensile properties of the selective laser-melted Ti-15Zr-4Nb-4Ta and Ti-6Al-4V alloy rods are shown in **Table 4**. The tensile properties of the selective laser-melted Ti-15Zr-4Nb-4Ta and Ti-6Al-4V rods are similar to those of the hot-forged Ti-15Zr-4Nb rod shown in **Table 2**. The tensile strengths of the selective laser-melted Ti rods are close to that of the wrought Ti-15Zr-4Nb alloy rod. The tensile properties of the selective laser-melted Ti-15Zr-4Nb-4Ta and Ti-6Al-4V alloy rods fully satisfy those ($\sigma_{0.2\%PS} \geq 780$, $\sigma_{UTS} \geq 860$ MPa, and T.E. $\geq 10\%$) specified in JIS T 7401-4 and ISO 5832-3 [19]. The fatigue strengths (σ_{FS}) of the 90°-direction-built Ti-15Zr-4Nb-4Ta (once-melted) and Ti-6Al-4V (once- and 10-times-melted) alloy rods are ~ 640 , ~ 680 , and ~ 660 MPa, respectively. It is considered that to increase the fatigue strength of selective laser-melted Ti alloys, it is effective to improve the morphology of the α' lath martensitic structure and change the α' lath martensitic structure to α (hcp)- β (bcc)-two-phase structure by heat and hot isostatic press (HIP) treatments. Selective laser melting is a promising new manufacturing technology for artificial hip stems in the future.

Dimples are observed on the fracture surfaces after room temperature tensile test. A fatigue crack develops with a fatigue fracture from the internal parts of the specimen, and striations are observed.

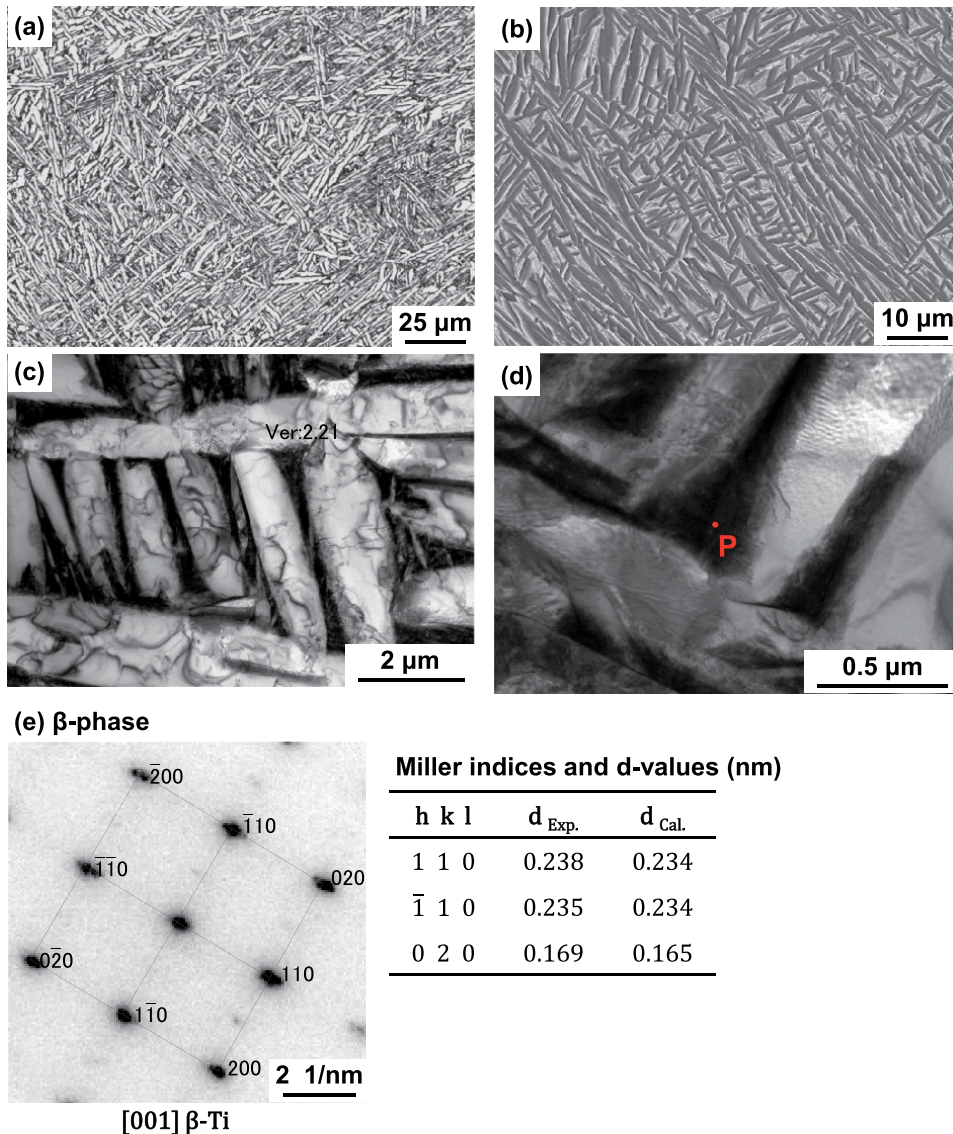


Figure 21. (a) Optical micrograph and (b) SEM and (c), (d) TEM images of selective laser-melted Ti-15Zr-4Nb-4Ta; (e) electron beam diffraction pattern obtained at the location indicated by P in (d) (precipitation).

9.3 Durability of selective laser-melted artificial hip stems

Tension-tension durability tests of selective laser-melted Ti-15Zr-4Nb-4Ta and Ti-6Al-4V alloy artificial hip stems are performed to obtain the P-N curves (maximum cyclic load vs. the number of cycles to failure on logarithmic scale) according to ISO 7206-4 standard (third edition) [16]. The artificial hip stem is fixed at D (vertical distance from head center of artificial hip prosthesis to upper level of the fixation) = 80 mm and at angles of α (in adduction) = 10° and β (in flexion) = 9°, as shown in **Figure 13**. On the other hand, D was $0.4 \times CT$ in ISO 7206-4 second edition. CT (stem length) is the distance between the head center of the artificial hip

Ti/Alloy	$\sigma_{0.2\%PS}/$ MPa	$\sigma_{UTS}/$ MPa	T.E. (%)	R.A. (%)	$\sigma_{FS}/$ MPa	$\sigma_{FS}/$ σ_{UTS}
Selective laser-melted rods						
Once-melted 0° Ti-15Zr-4Nb-4Ta	880±2	1032±1	14±1	31±2		
Once-melted 90° Ti-15Zr-4Nb-4Ta	860±3	1022±2	16±1	36±7	640±11	0.63
Once-melted 90° Ti-6Al-4V	949±3	1041±2	15±1	46±2	680±37	0.65
10-times-melted 90° Ti-6Al-4V	946±2	1036±2	15±1	47±1	660±14	0.64

Table 4. Tensile properties ($\sigma_{0.2\%PS}$, σ_{UTS} , T.E., and R.A.), fatigue strength at 10^7 cycles (σ_{FS}), and fatigue ratio (σ_{FS}/σ_{UTS}) of selective laser-melted Ti-15Zr-4Nb-4Ta and Ti-6Al-4V rods.

prosthesis (C) and the tip of the hip stem (T). At this $D = 80$ mm fixation, it is assumed that the cement is loose in a cement-type stem. The cementless-type stem, for example Alloclassic SL artificial hip femoral stem, is fixed by the fixing force of the autologous bone from the proximal portion to the distal portion. Therefore, for the selective laser-melted Ti-15Zr-4Nb-4Ta and Ti-6Al-4V alloy artificial stems, considering that the stem is the cementless type, $D = 0.4 \times CT$; α and β are 10° and 9° , respectively. The tension-tension durability tests are performed at room temperature in air with a sine wave at a minimum-to-maximum load ratio of 0.1. The frequency is 3 Hz. The durability limits (PD) at 5×10^6 cycles are estimated from the P-N curves.

Figure 22 shows the L-N curves of the selective laser-melted Ti-15Zr-4Nb-4Ta and Ti-6Al-4V stems and the approved product HA-TCP and S-ROM stems.

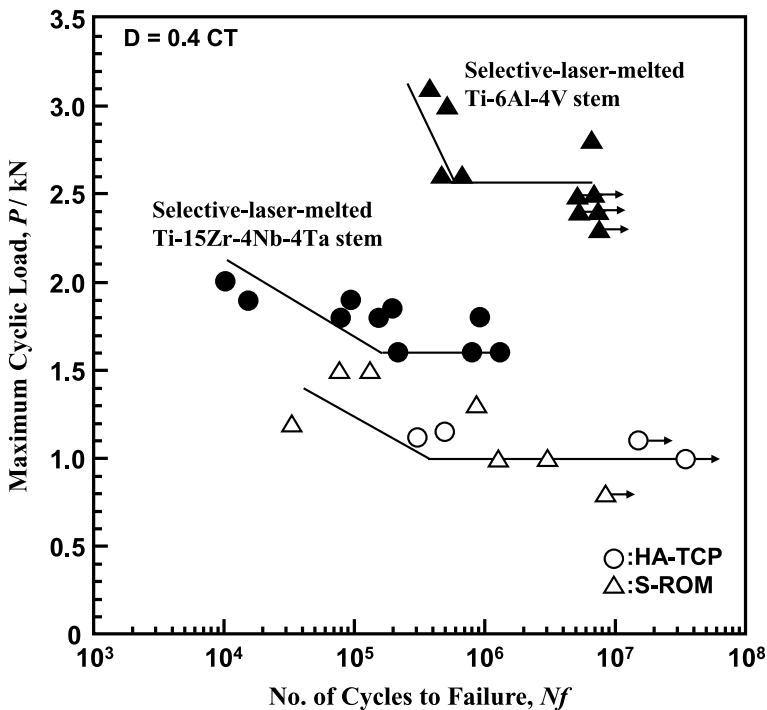


Figure 22. L-N curves of selective laser-melted Ti-15Zr-4Nb-4Ta and Ti-6Al-4V hip stems (size S), approved product HA-TCP fiber metal, and S-ROM hip stems obtained by compression bending durability tests.

The durability limit of the selective laser-melted Ti-15Zr-4Nb-4Ta stem is lower because the selective laser melting conditions developed for the Ti-6Al-4V alloy are used and the selective laser melting conditions for the Ti-15Zr-4Nb-4Ta alloy are as yet not developed. On the other hand, the durability limit of the selective laser-melted Ti-6Al-4V stem is ~2500, which is much higher than those of the approved product HA-TCP and S-ROM stems. With a load of 2300 N and the laser-melted Ti-6Al-4V artificial hip femoral stem fixed at $D = 80$ mm, the stems brake after around 100,000 cycles. To clarify the durability limit of 2300 N at fixation of 80 mm, it is necessary to consider the selective laser melting conditions of the Ti-6Al-4V hip stem. The durability of artificial hip femoral stem can be improved by examining the annealing conditions after the selective laser melting. On the other hand, in the cementless type, the stem is fixed by the fixing force of the autologous bone from the proximal part to the distal part. Even in the durability test with fixation $D = 0.4$ CT (52 mm), the fixation position is clinically lower. Therefore, selective laser melting (SLM) can be applied to manufacture of custom-made artificial hip stems [20]. SLM is also a new promising manufacturing technology for fabricating Co-Cr-Mo alloy TKA (Total Knee Arthroplasty) femoral component [21].

10. Evaluation of bearing parts of artificial prostheses

Artificial prostheses such as total hip arthroplasty (THA) and total knee replacement (TKR) are performed in increasing numbers of elderly patients. The differences between bipolar hip arthroplasty (BHA) and total hip arthroplasty (THA) are shown **Figure 23**. The human hip joint consists of the femur and pelvis. The femoral head fits into the concave part of the pelvis called the acetabulum and is moved by ligaments and muscles around it. The surfaces of the femoral head and acetabulum are covered by an elastic tissue called the cartilage, which absorbs shocks so that the joint moves smoothly and experiences less abrasion. In BHA, only the femoral head is removed and replaced with an artificial femoral head in cases of fractures caused by a fall, for which the preservation of the femoral head is difficult. The functions of the acetabulum,

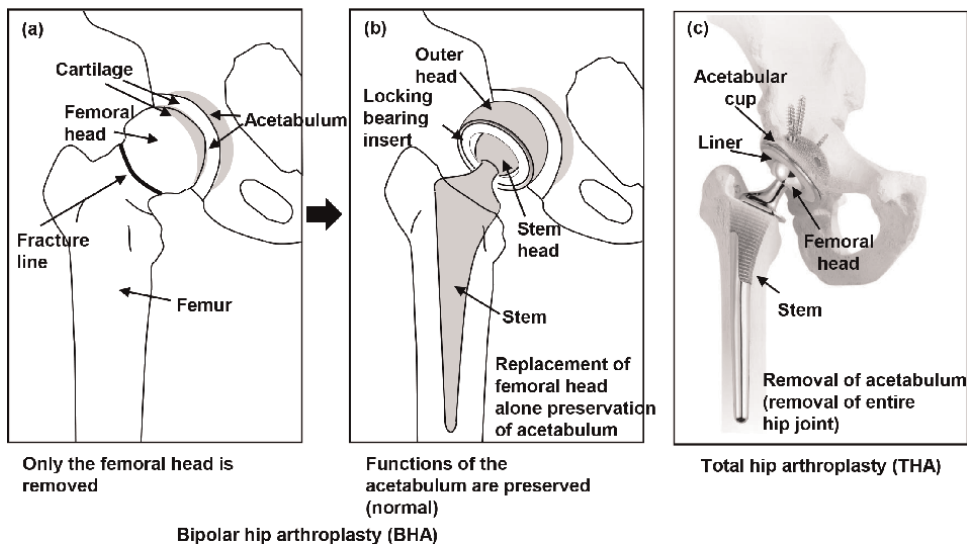


Figure 23.
Differences between bipolar hip and total hip arthroplasties.

namely, the sliding of the human hip joint, are maintained. On the other hand, in THA, the acetabulum of the pelvis is removed and the entire hip joint is replaced with an artificial hip joint. In contrast to BHA, the evaluation of wear characteristics of the sliding part of the hip joint is required in THA because the acetabular component is secured to the pelvis with bone screws. Most bearing part of the artificial hip joints consists of the acetabular and femoral components. The acetabular component consists of a liner made of ultrahigh-molecular-weight polyethylene (UHMWPE) with high density and average molecular weight and an acetabular cup. The femoral component consists of a stem and a stem femoral head. GUR1020, GUR1050, and GUR 4150 UHMWPE materials are popularly used for the bearing inserts of artificial hip joints.

Among the greatest advantages of implant arthroplasty are the recovery from the bedridden state and joint pain relief. The sliding part of an artificial hip joint is generally made of a combination of metal and UHMWPE (metal on polyethylene). As the hard-on-soft bearing of THA, metal-on-polyethylene and ceramic-on-polyethylene bearings are being used worldwide. There are currently three types of UHMWPE material: conventional UHMWPE (CPE), highly cross-linked UHMWPE (XLPE), and vitamin E-containing highly crosslinked UHMWPE (VEPE). Hip simulator wear tests are specified in ISO 14242-1 standard [22]. The volumetric wear rate per million cycles (mm^3/Mc) of artificial hip joints made of XLPE markedly decreases when the joints are subjected to a radiation dose of 40 kGy or higher [23]. As shown in **Figure 24**, the hip volumetric wear rates per million cycles (mm^3/Mc) of both CPE and XLPE slightly increase with increasing femoral head diameter [23].

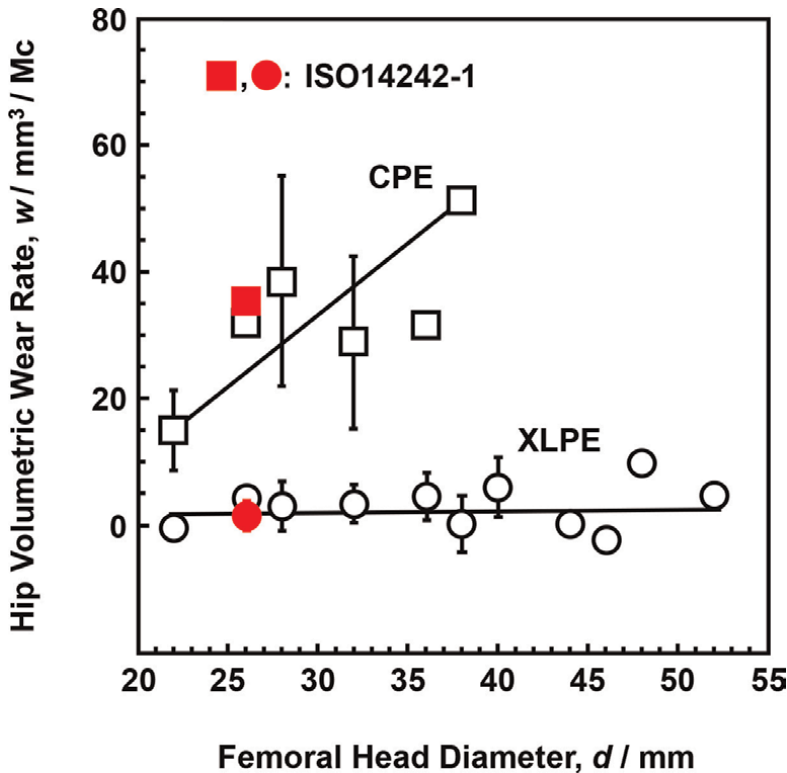


Figure 24. Effect of femoral head diameter on hip volumetric wear rates of conventional UHMWPE and highly cross-linked UHMWPE.

The penetration of the femoral head into a UHMWPE acetabular cup is evaluated using Eq. (5) [24, 25].

$$\delta_V = \pi R_1^2 \times p / [1 + (R_2 - R_1) / p] \quad (5)$$

Here, δ_V (volumetric wear) represents the volume of the UHMWPE removed by wear (mm^3), p is the penetration (linear wear) of the femoral head into the UHMWPE acetabular cup (mm/year), and R_1 and R_2 are the radii of the femoral head and acetabular cup (mm), respectively. A linear wear of $0.1 \text{ mm}/\text{year}$ or less is recommended so that osteolysis does not occur; this value is the osteolysis threshold. The UHMWPE wear rate in clinical use can be estimated using Eq. (5). A bearing with a highly cross-linked UHMWPE (XLPE) insert shows a low wear rate, ($5 \text{ mm}^3/\text{Mc}$) suggesting its excellent long-term clinical performance.

In artificial knee prostheses, there is a variation in the constraint of the tibial insert depending on whether the posterior cruciate ligament is preserved [cruciate retaining (CR)] or sacrificed [posterior stabilized (PS)] at the time of knee joint surgery. The wear rates of artificial knee joint UHMWPE inserts are examined using a knee joint simulator that satisfies ISO 14243-1 (load control) [26] or ISO 14243-3 (displacement control) [27] standard. The volumetric wear rate of XLPE knee joint markedly decreases when the joints are exposed to a radiation dose of 40 kGy or higher [21]. Volumetric wear rates of $3 \text{ mm}^3/\text{Mc}$ for XLPE knee joint inserts and $15 \text{ mm}^3/\text{Mc}$ for CPE knee joint inserts are recommended as goals for the development of new knee joints. The volumetric wear rate ($7.2 \pm 2 \text{ mm}^3/\text{Mc}$) of the CPE insert against the selective laser-melted (SLM) Co-28Cr-6Mo femoral component is lower than that ($15.1 \pm 1.2 \text{ mm}^3/\text{Mc}$) of CPE insert against cast Co-28Cr-6Mo femoral component (**Figure 25**) [21]. Since the effect of precipitates of the π (π)-phase [$(\text{Cr}, \text{Mo}, \text{W})_{12}\text{Co}_8(\text{C}, \text{N})_4$] on the increase in the wear rate is negligible, SLM is a promising new manufacturing technology for knee femoral components.

In bipolar hip arthroplasty (BHA), clinically, the bearing part is not excised and the bearing part of the femur is preserved, so it is not necessary to evaluate their wear property using a simulator. In particular, the pullout properties of a bipolar cup are important [28], particularly, the negative correlation between the maximum pullout load and oscillation angle (OA) in the bipolar cup.

11. Future trends

11.1 Orthopedic implant application of highly biocompatible Ti-Zr-Nb alloys

Ti-15Zr-4Nb alloy has excellent room temperature strength and fatigue properties with high biocompatibility. Moreover, for Ti-Zr-Nb alloy, a body-centered cubic $\text{Zr}_{50}\text{Ti}_{35}\text{Nb}_{15}$ medium-entropy alloy with unique properties has been developed in Ref. [29]. This $\text{Zr}_{50}\text{Ti}_{35}\text{Nb}_{15}$ shows a unique combination of Young's modulus (62 GPa), yield strength (657 MPa), tensile ductility (22%), and excellent corrosion resistance.

11.2 Applications of additive manufacturing (AM) technologies

3D layer manufacturing technologies are expected as new technologies for manufacturing acetabular cups, artificial hip joint stems, and femoral components and tibial trays of artificial knee joints among others. 3D layer manufacturing technologies are also expected for manufacturing porous materials such as acetabular components. It is possible to obtain marketing approval for highly biocompatible implants that are

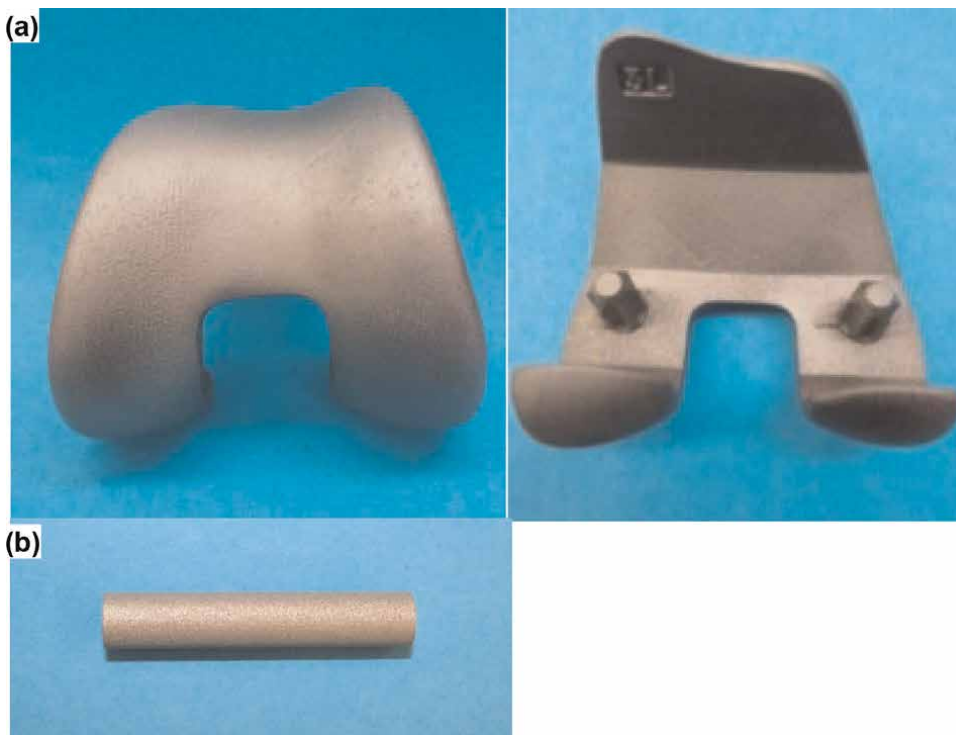


Figure 25.
(a) Selective-laser-melted (as-built) Co-28Cr-6Mo femoral component and (b) cylindrical specimen.

optimized for the skeletal structures and needs of patients by combining 3D layer manufacturing technologies with imaging technologies such as CT. 3D layer manufacturing technologies using Co-28Cr-6Mo alloy powder can be also applied to the manufacture of humeral components of artificial shoulder joints, metacarpal and proximal phalanx components of artificial finger joints, tibial and talar components of artificial ankle joints, and femoral components of artificial knee joints.

Additive manufacturing (AM) by selective laser melting is used to fabricate 3D objects in a single stage directly from their computer-aided design (CAD). In a conventional casting process, materials constantly expand and contract during the formation of wax patterns, investment, and casting. Relatively dense femoral components free of blow holes are formed with AM technology, reducing the occurrence of problems such as the breakage of femoral components caused by casting defects. In selective laser melting, a laser is scanned along metal powders on the basis of slice data to obtain a layer of a product. The powder for the next layer is placed on the melted layer, and the laser is again scanned on the basis of the data for the next slice [15]. The development of orthopedic implants customized to the skeletal structure and symptoms of each patient is now possible.

12. Conclusion

Zirconium (Zr), niobium (Nb), and tantalum (Ta) are effective alloying elements for Ti alloys to achieve long-term superior biological, biochemical, and

biomechanical compatibilities. The oxides ZrO_2 , Nb_2O_5 , and Ta_2O_5 strengthen the passive (oxide) films and prevent metal ion release in long-term clinical use. Ti-15Zr-4Nb alloy has excellent mechanical compatibility (room temperature strength and fatigue properties). Indeed, the biological compatibility of this alloy has been proven in cytotoxicity, sensitization, irritation, systemic toxicity, genotoxicity, and rat and rabbit implantation tests. This has led to high expectations for the long-term future use of this alloy as a viable implant material. The durability limit of various types of osteosynthesis devices linearly increases with increasing bending strength. The relationship (durability limit at 10^6 cycles) $= 0.67 \times$ (bending strength) (N·m) ($R^2 = 0.85$) is obtained for bone plates, spinal rods, intramedullary nail rods, CHSs, short femoral nails, and epiphyseal plates by regression. This slope of 0.67 is close to the ratio of the fatigue strength to the tensile strength of the raw metals. The relationship for the highly biocompatible Ti-15Zr-4Nb alloy is also linear. The fatigue strength of the Ti-15Zr-4Nb alloy stem hot-forged at $780^\circ C$ is 850 MPa, which is higher than that of the Alloclassic SL Stem. Selective laser melting is a promising new manufacturing technology for artificial hip stems and artificial knee femoral components, and artificial joints. A bearing with a cross-linked UHMWPE (XLPE) insert shows a low wear rate ($5 \text{ mm}^3/\text{Mc}$), suggesting its excellent long-term clinical performance.

The oxide coloring of a Ti materials surface is globally used in osteosynthesis devices. As shown in **Figure 26**, the correlation of color tone and oxide film thickness (Y, nm) can be determined with respect to anodic oxidation potential (X, V), yielding a linear correlation given by $Y = 0.286 + 1.521 [X]$, $R^2 = 1.0$ [30].

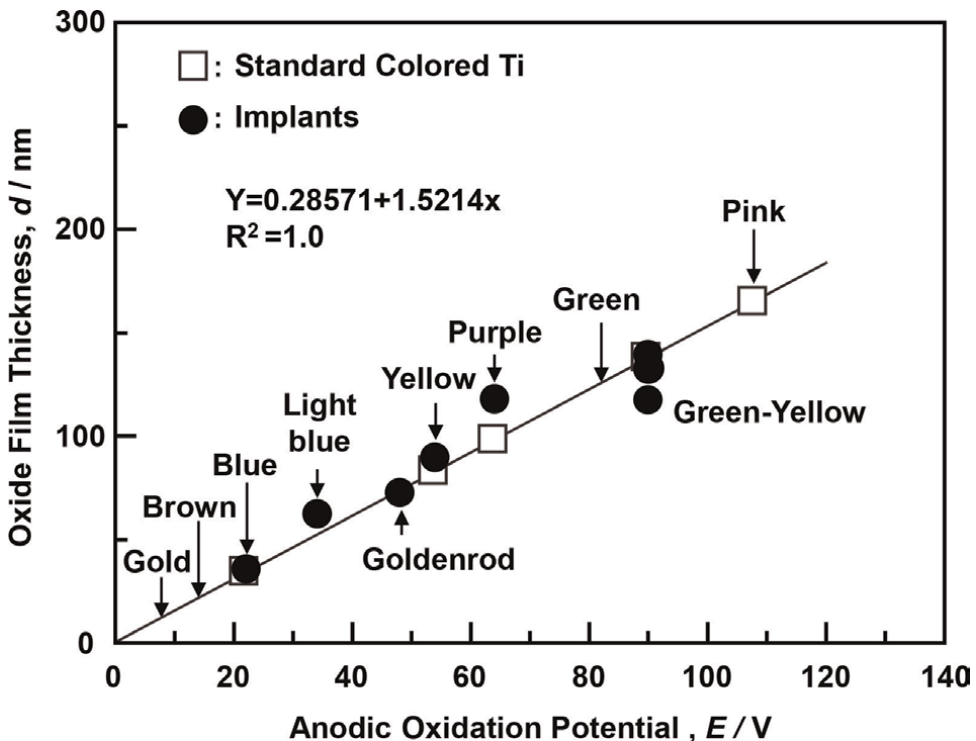


Figure 26.
Correlation between oxide film thickness and anodic oxidation potential.

Owing to the rapid progress of 3D layer manufacturing technologies, the development of orthopedic implants customized to the skeletal structure and symptoms of each patient is now possible.

Conflict of interest


The authors declare no conflict of interest.

Author details

Yoshimitsu Okazaki* and Kiyoyuki Chinzei
National Institute of Advanced Industrial Science and Technology, Tsukuba, Japan

*Address all correspondence to: y-okazaki@aist.go.jp

IntechOpen

© 2022 The Author(s). Licensee IntechOpen. This chapter is distributed under the terms of the Creative Commons Attribution License (<http://creativecommons.org/licenses/by/3.0>), which permits unrestricted use, distribution, and reproduction in any medium, provided the original work is properly cited. 

References

- [1] Okazaki Y, Gotoh E. Metal ion effects on different types of cell line, metal ion incorporation into L929 and MC3T3-E1 cells, and activation of macrophage-like J774.1 cells. *Materials Science and Engineering: C*. 2013;**33**: 1993-2001. DOI: 10.1016/j.msec.2013.01.015
- [2] Steinemann SG. Corrosion of surgical implants-*in vivo* and *in vitro* tests. In: Winter GD, Leray JL, de Groot K, editors. *Evaluation of Biomaterials*. Chichester, UK: Wiley; 1980. pp. 1-34
- [3] Steinemann SG. Compatibility of titanium in soft and hard tissue-the ultimate is osseointegration. In: Stallforth H, Revell P, editors. *Materials for Medical Engineering*. Weinheim, Germany: Wiley-VCH; 1999. pp. 199-203
- [4] Okazaki Y, Ito Y, Ito A, Tateishi T. Effect of alloying elements on mechanical properties of titanium alloys for medical implants. *Materials Transactions, JIM*. 1993;**34**:1217-1222
- [5] Okazaki Y, Rao S, Asao S, Tateishi T, Katsuda S, Furuki Y. Effects of Ti, Al and V concentrations on cell viability. *Materials Transactions, JIM*. 1998;**39**: 1053-1062
- [6] JIS. T 7401-4, Titanium Materials for Surgical Implant Applications Part 4: Wrought Titanium 15-Zirconium 4-Niobium Alloy. Tokyo, Japan: Japanese Standards Association; 2022
- [7] Okazaki Y. On the effects of hot forging and hot rolling on the microstructural development and mechanical response of a biocompatible Ti alloy. *Materials*. 2012;**5**:1439-1461. DOI: 10.3390/ma5081439
- [8] Okazaki Y. Development of low-cost manufacturing process and effects of adding small amounts of Ta, O, and N on the physical and mechanical properties of highly biocompatible Ti alloys. *Materials Transactions*. 2019;**60**:1769-1778. DOI: 10.2320/matertrans.ME201917
- [9] Okazaki Y. Characterization of oxide films of implantable metals by electrochemical impedance spectroscopy. *Materials*. 2019;**12**:3466. DOI: 10.3390/ma12213466
- [10] Okazaki Y, Nagata H. Comparisons of immersion and electrochemical properties of highly biocompatible Ti-15Zr-4Nb-4Ta alloy and other implantable metals for orthopedic implants. *Science and Technology of Advanced Materials*. 2012;**13**:064216. DOI: 10.1088/1468-6996/13/6/064216
- [11] Okazaki Y, Gotoh E, Manabe T, Kobayashi K. Comparison of metal concentrations in rat tibia tissues with various metallic implants. *Biomaterials*. 2004;**25**:5913-5920. DOI: 10.1016/j.biomaterials.2004.01.064
- [12] Okazaki Y, Katsuda S. Biological safety evaluation and surface modification of biocompatible Ti-15Zr-4Nb alloy. *Materials*. 2021;**14**:732. DOI: 10.3390/ma14040731
- [13] JIS. T 0309, Testing Method for Fatigue Properties of Metallic Biomaterials. Tokyo, Japan: Japanese Standards Association; 2009
- [14] Okazaki Y, Gotoh E. Comparison of fatigue strengths of biocompatible Ti-15Zr-4Nb-4Ta alloy and other titanium materials. *Materials Science and Engineering: C*. 2011;**31**:325-333. DOI: 10.1016/j.msec.2010.09.015

- [15] Okazaki Y, Mori J. Mechanical performance of artificial hip stems manufactured by hot forging and selective laser melting using biocompatible Ti-15Zr-4Nb alloy. *Materials*. 2021;**14**:732. DOI: 10.3390/ma14040732
- [16] ISO. 7206–4, Implants for Surgery - Partial and Total Hip Joint Prostheses - Part 4: Determination of Endurance Properties of Stemmed Femoral Components. Geneva, Switzerland: International Organization for Standardization; 2010
- [17] Okazaki Y, Gotoh E, Mori J. Strength–durability correlation of osteosynthesis devices made by 3D layer manufacturing. *Materials*. 2019;**12**:436. DOI: 10.3390/ma12030436
- [18] Okazaki Y, Hayakawa E, Tanahashi K, Mori J. Mechanical performance of metallic bone screws evaluated using bone model. *Materials*. 2020;**13**:4836. DOI: 10.3390/ma13214836
- [19] ISO. 5832–3, Implants for Surgery–Metallic Materials–Part 3: Wrought Titanium 6-Aluminium 4-Vanadium Alloy. Geneva, Switzerland: International Organization for Standardization; 2016
- [20] Okazaki Y. Development trends of custom-made orthopedic implants. *Journal of Artificial Organs*. 2012;**15**: 20-25. DOI: 10.1007/s10047-011-0584-6
- [21] Okazaki Y. Effects of fine microstructures and precipitates of laser-sintered Co–28Cr–6Mo alloy femoral components on wear rate of UHMWPE inserts in a knee joint simulator. *Journal of the Mechanical Behavior of Biomedical Materials*. 2020;**112**:103998. DOI: 10.1016/j.jmbbm.2020.103998
- [22] ISO. 14242–1, Implants for Surgery - Wear of Total Hip-Joint Prostheses - Part 1: Loading and Displacement Parameters for Wear-Testing Machines and Corresponding Environmental Conditions for Test. Geneva, Switzerland: International Organization for Standardization; 2012
- [23] Okazaki Y. Effect of head size on wear properties of metal-on-metal bearings of hip prostheses, and comparison with wear properties of metal-on-polyethylene bearings using hip simulator. *Journal of the Mechanical Behavior of Biomedical Materials*. 2014; **31**:152-163. DOI: 10.1016/j.jmbbm.2013.10.021
- [24] Dowson D, Jobbins B, Seyed-Harraf A. An evaluation of the penetration of ceramic femoral heads into polyethylene acetabular cups. *Wear*. 1993;**162–164**: 880-889. DOI: 10.1016/0043-1648(93)90090-9
- [25] Dowson D. A comparative study of the performance of metallic and ceramic femoral head components in total replacement hip joint. *Wear*. 1995;**190**: 171-183. DOI: 10.1016/0043-1648(96)80015-9
- [26] ISO. 14243–1, Implants for Surgery–Wear of Total Knee-Joint Prostheses–Part 1: Loading and Displacement Parameters for Wear-Testing Machines with Load Control and Corresponding Environmental Conditions for Test. 2nd ed. Geneva, Switzerland: International Organization for Standardization; 2009
- [27] ISO. 14243–2, Implants for Surgery–Wear of Total Knee-Joint Prostheses–Part 2: Methods of Measurement. Geneva, Switzerland: International Organization for Standardization; 2016

[28] Kaku N, Tabata T, Tsumura H. Relationship between pull-out strength and oscillation angle in bipolar cups: an in vitro study. *Journal of Orthopaedic Surgery*. 2016;**24**:209-215

[29] Yan X, Zhang Y. A body-centered cubic $Zr_{50}Ti_{35}Nb_{15}$ medium-entropy alloy with unique properties. *Scripta Materialia*. 2020;**178**:329-333.
DOI: 10.1016/j.scriptamat.2019.11.059

[30] Okazaki Y. Interference colors and thickness of oxide film on colored titanium implants. *Japanese Journal of Clinical Biomechanics*. 2010;**31**:227-230

High-Entropy Alloys for Bone Tissue Engineering: Recent Developments in New Methods of Manufacture

Agripa Hamweendo, Chiluba I. Nsofu and Terence Malama

Abstract

The demand for bone implants with superior biocompatibility and mechanical properties in bone tissue engineering is increasing due to rising demand for artificial bones and bone implant to replace degraded bones in human bodies. The causes of bone degradation in human bodies are not just due to rising number of road traffic accidents but are also due to disease burdens and injuries due to war and game activities. As a result, there is an urgent need to develop modern methods of manufacturing materials for implantable bone substitutes required in defective skeletal structures that cannot grow or heal on their own. It is believed that high-entropy alloys (HEAs) are best alternative materials for bone implants and development of modern methods for processing such materials could lead to manufacturing bone implants with the superior biocompatibility and mechanical properties. Therefore, this chapter examines the recent advances made in developing new methods for manufacturing bone implants using HEAs as raw materials. The chapter finally recommends the most appropriate methods for this purpose.

Keywords: high-entropy alloys, biomaterials, bone tissue engineering, recent development, manufacturing methods

1. Introduction

The demand for bone implants with superior biomechanical properties is increasing due to rising number of causes for degraded bones in human bodies. These may include road traffic accidents, disease burdens, and injuries arising from wars and game activities [1]. As a result, there is an urgent need to develop modern materials for implantable bone substitutes required in defective skeletal structures that cannot grow or heal on their own. Generally, these biomaterials need to be biocompatible; that is, they must be bio-inert, with tensile strength of 3.7–140 MPa, Young's modulus of 0.16–18.1 GPa, high corrosion resistance, and porosity of 30–60% for easy osseointegration [2–5]. These properties have contradicting existence and therefore require careful preparation methods.

In the recent past, several research activities have been carried out to develop biomaterials with most favorable properties such as good biocompatibility, appropriate corrosion resistance, low elastic modulus, and comparable scratch hardness [6–13]. According to literature, titanium (Ti) alloys, especially with nickel (Ni) as an alloying element, emerged to be the most suitable biomaterials and these have been extensively investigated for possible application in biomedical implants. In addition, TiNi alloys are preferred due to their super elastic ability and shape memory properties [14]. Further, TiNi displays excellent biocompatibility due to the formation of a thin titanium oxide surface [15]. Moreover, the addition of extra elements to Ti such as copper resulted in an alloy with the improved properties. Therefore, TiNiCu alloy has attracted interest for biomedical and other applications due to superelastic behavior, better fatigue, and improved shape memory properties [16, 17]. From the aforementioned, it can be seen that alloying is among the most appropriate methods for improving properties of metal materials. Moreover, studies have shown that when there is an increase in the number of alloying materials, a significant improvement in the properties of the alloy occurs. Consequently, high alloy materials also called high-entropy alloys (HEAs) are emerging to be among the best alternative materials with the favorable properties for newer applications [18, 19]. However, further research suggests that the medical application of HEAs especially those that are Ti-based is limited as these materials are still being developed. This implies that there is not yet any comprehensive *in vivo* evaluation of the Ti-based HEAs as implants to assess aspects such as biomechanics, biocompatibility, histology, and osseointegration [13, 20].

On the whole, studies have proved that during examining the traditional alloys, it was established that there was one principal metallic element that was seldom mixed with more than three principal metallic elements. Such a practice was common in alloys such as steels that are usually based on iron, and are sometimes made as super alloys that include nickel and cobalt as alloying elements, and intermetallics that had two metallic elements such as nickel-aluminum as compounds and metal-matrix composites that were based on three elements such as nickel, titanium, and aluminum. As such, under these traditional arrangements, metallurgists could make and process the alloys, and study their microstructure and properties for targeted applications. Obviously, the degrees of freedom in the alloy development are confined by the alloying concept. However, the development of new metal alloys took center stage in the recent past in order to improve the properties of the materials to meet the modern demands. As a consequence, alloys composed of multiple elements having higher mixing entropy than conventional alloys are being proposed with a view to improve their properties mostly due to mixing enthalpy that allows the addition of suitable alloying elements to improve their properties [20].

As such, several research works have been carried out to develop metallic biomaterials with the highest biocompatibility and least toxicity properties. As a result, more complex compositions with higher mixing entropies have been introduced. However, such complex compositions do not necessarily guarantee a complex structure and microstructure due to accompanied brittleness. Conversely, significantly higher mixing entropy from complex compositions could simplify the structure and microstructure and impart attractive properties to the alloys [20]. Accordingly, high-entropy alloys (HEAs) are emerging to be among the best alternative materials with favorable biocompatibility properties. In this respect, this chapter examines the HEAs and, based on their structure and properties, suggests them as alternative materials for biomedical implants. The chapter also examines the traditional and concurrent methods of manufacturing to guide processing engineers during selection of the most suitable method.

2. High-entropy alloy (HEA)

2.1 Definition of HEAs

High-entropy alloys (HEAs) are defined as those alloys with at least five alloying elements, each of which has an atomic concentration between 5 and 35% and are mixed in equal or relatively large proportions. Prior to the synthesis of these alloys, typical base metal alloys comprise one or two major components with smaller amounts of other elements. The alloying elements can be added to base alloys to improve their properties, thereby creating a complex alloy, but typically in fairly small proportions. The alloys are created by a typical solid solution process. This makes the high-entropy alloys to be among the most novel class of materials. The term “high-entropy alloys” was coined because the large number of alloying elements increases the mixing proportions that are also more nearly equal. This mixing strategy significantly distorts the crystallographic structure of the HEAs with a high tendency to improve their properties thereby making these materials to be currently the focus of significant attention in materials science and engineering because they can be made with potentially desirable properties. Furthermore, literature indicates that some HEAs have considerably better strength-to-weight ratios, with a higher degree of fracture resistance, tensile strength, and corrosion and oxidation resistance than conventional alloys [20–22].

2.2 Lattice structures of HEAs

It is well known that the introduction of several alloying elements through substitution solute atoms into a solvent parent matrix causes the displacement of neighboring atoms from their ideal lattice positions. These displacements do not only generate significant lattice distortions but also generate a strain energy field that also induces changes in bulk lattice parameter, as illustrated in **Figure 1**. The introduction of strain energies induces new properties to the metal crystals. Also, these localized distortions around the solute atom will interact elastically with dislocations moving through the material, resulting in solid solution with enhanced altered properties [23]. A schematic representation of localized lattice distortion effect in HEAs is illustrated in **Figure 1**. As shown in this **Figure 1**, the four colors (green, orange, red, and blue) represent the four elements in the HEA alloyed by substitution to create the distinctive distortion in the lattice structures. These distortions induce distinctive properties to the alloy. What is also vivid from this structure is that the geometric orientation, and the extension and location of the lattice distortions are influenced by the type, size, and location of the alloying element. This effect is very vital in choosing the type of alloying elements, sequencing of atoms, and method(s) of alloying.

Well-established models for solution strengthening have been produced for both dilute and concentrated alloys, and their modification for HEAs is discussed in the literature [14]. A number of studies have suggested that severe lattice distortion contributes significantly to new HEA properties, most notably with respect to increasing alloy strength. Importantly, however, it is apparent that the strengthening effect of precipitates may have been overlooked in some cases. It has been suggested that these distortions arise not only from atomic size misfit, but also differences in the crystal structure and bonding preferences of alloying elements before [14].

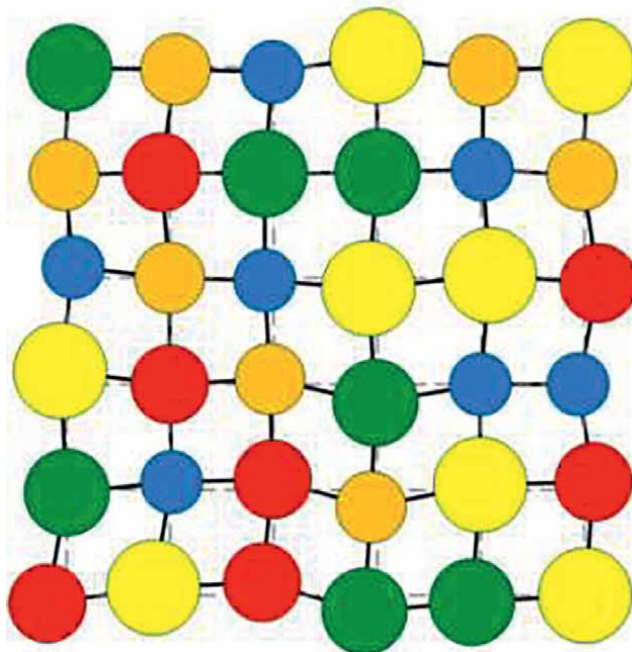


Figure 1.
Schematic representation of strained lattices in HEA [14].

2.3 Properties of HEAs

Several studies that have been carried out and are reported in the literature demonstrate that the HEAs could be made, processed, and analyzed just like conventional alloys. Moreover, these alloys exhibit several interesting features that are also reported in the literature. These alloys can be formed by simple solid solution phases such as FCC and BCC with nanostructures or even amorphous structures. The following are selected properties possible in HEAs materials:

- Elevated temperature strength and oxidation resistance.
- Improved resistance to (stress) corrosion.
- Low density.
- Super plasticity and high-strain-rate.
- Surface hardness with Hv100 to Hv 1100.
- Good thermal stability in microstructure [20, 24]

2.4 Applications of HEAs

Due to the above special properties, HEAs have many potential traditional and nontraditional engineering applications: firstly, traditional applications such as

aerospace, marine, furnaces, and several other parts requiring the properties of high strength, thermal stability, and wear and oxidation resistances, anticorrosive high-strength materials in chemical plants, and foundries. Secondly, nontraditional applications such as biomedical implants, special game tools, super elastic alloys, ultra-large-scale integrated circuits, and soft magnetic films for ultra-high-frequency communication [13, 24].

3. Methods for manufacturing HEAs

The methods for manufacturing HEA can generally be classified as traditional bulk material consolidation methods and nontraditional additive manufacturing. Bulk consolidation methods include casting and sintering or powder metallurgy, while additive manufacturing methods include surface coating technologies such as thermal spraying, laser cladding, magnetron sputtering, selective laser melting. Among these methods, powder metallurgy and selective laser melting are the most used techniques to prepare the HEAs, while laser cladding and magnetron sputtering methods are commonly used in order to prepare HEA thin films or coatings. The advantages and limitations of selected methods of preparation for HEAs are listed in **Table 1**.

These methods are viable and advanced means of production and also the use of technological method to improve the quality of the products such as metal alloys and/or high-entropy-alloying processes, with the relevant technology being described as “advanced,” “innovative,” or “cutting edge.” These technologies evolved from conventional processes some of which have been developed to achieve various components of alloys [15]. The following are the selected methods used to produce HEAs.

Preparation methods	Advantages	Limitations
Powder metallurgy	<ul style="list-style-type: none"> • Near-net shape forming • Higher utilization of material • Uniform composition • Save metals and reduce costs 	<ul style="list-style-type: none"> • Poor toughness • Higher die cost
Magnetron sputtering	<ul style="list-style-type: none"> • Film thickness can be controlled by adjusting sputtering parameters. • Low requirements on target composition • High sputtering rate, and low base temperature can obtain a dense film surface 	<ul style="list-style-type: none"> • Higher preparation cost. • Complex equipment • Lower target utilization
Laser cladding	<ul style="list-style-type: none"> • High melting and cooling rate • Small heat-affected zone • Metallurgical combination of coating and substrate 	<ul style="list-style-type: none"> • The cladding layer is easy to crack • Uneven distribution of composition

Table 1. *Advantages and limitations of methods for preparations of HEAs [25].*

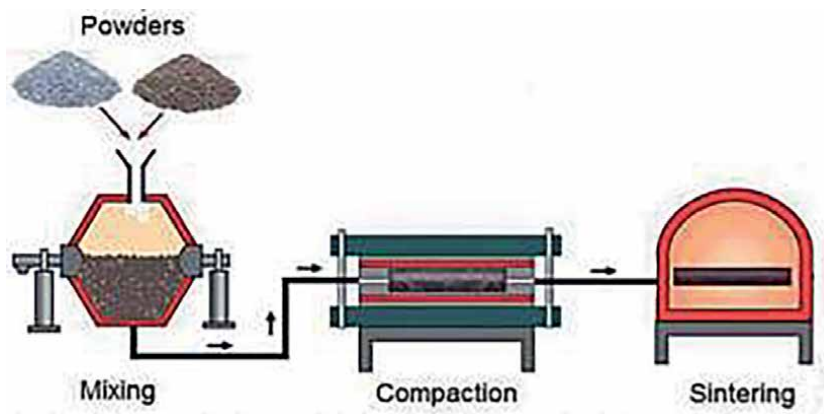


Figure 2.
Powder metallurgy process [26].

3.1 Powder metallurgy

Powder metallurgy (PM) also called bulk sintering, illustrated in **Figure 2**, is one of the widely applied methods for manufacturing titanium alloys. This method can also be applied to make HEAs. In this method, the feedstock powder elements are mixed thoroughly using a suitable powder blender, followed by compaction of the mixture under high pressure and by sintering at appropriate temperature for suitable duration. In this manner, the powder particles bond to each other with minor change in their shapes. The porosity of the alloy can be regulated by controlling the sintering temperature and time. When properly implemented, this method can produce accurate parts with near-net shapes. The major advantages derived from this methods include good mechanical properties of the products, near-net shape, lower cost, full dense materials, minimal inner defect, nearly homogenous microstructure, good particle-to-particle bonding, and low internal stress [26].

3.2 Magnetron sputtering

Magnetron sputtering is one of the additive manufacturers, which uses certain high-energy particles to bombard the surface of a specific material. This process is shown in **Figure 3**, in which argon gas is placed in a magnetron sputtering drum, in which due to the action of strong electric field, argon particles are initially ionized into argon ion and electrons. Then, these ions are accelerated toward the cathode in the electric field to bombard target surface with high energy. Thus, the impact of the ions causes the sputtering of the target. As a result, the target material will emit secondary electrons and ionizes due to continued bombard of the target causing the target to sputter deposition on the substrate surface to form a thin film [27].

3.3 Laser cladding

Laser cladding, illustrated in **Figure 4**, is one of the additive methods applicable in manufacturing of HEAs. This method is sometimes called surface modification process because it is predominantly a surface technology. As such, this process can improve the surface hardness, wear resistance, and corrosion resistance of the surface

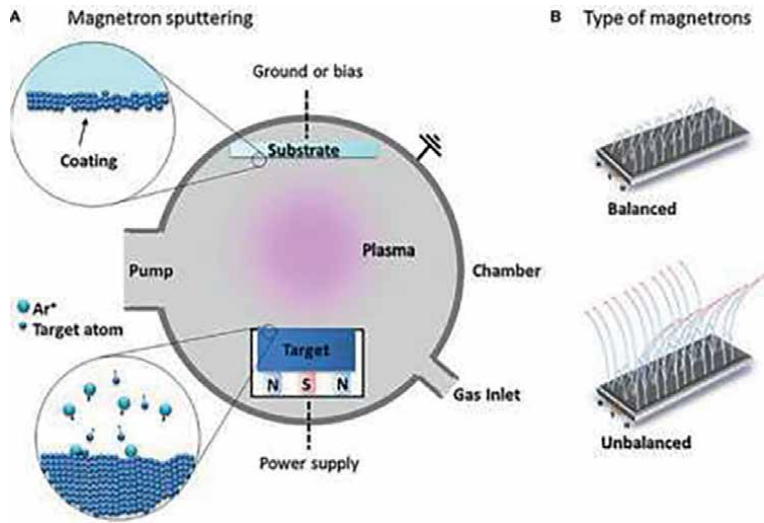


Figure 3. (A) The schematic of magnetron sputtering and (B) balanced and unbalanced types of magnetron configurations [27].

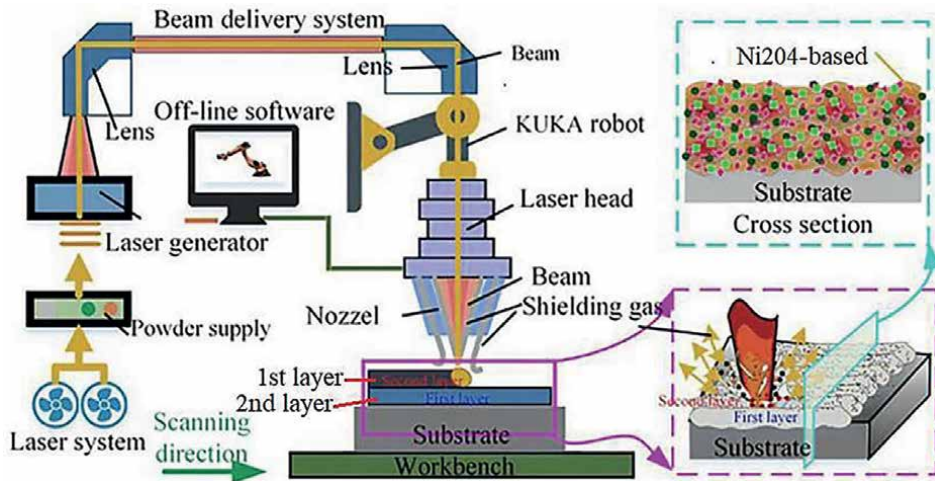


Figure 4. Schematic diagram of the laser cladding [18].

by cladding the alloy powder on the substrate. Laser cladding can also be carried out using either a wire (including hot or cold wire) or powder feedstock. The laser developed provides the energy to melt the pool on the surface of the work piece into which the wire or powder is simultaneously added. The result of the melt is that a metallogically bonded layer is created and usually, this is tougher than the layer that can be achieved with thermal spray and less dangerous to health than the process of hard chromium plating. This process is flexible because the operator can easily mix many powders and he can control the feed rate for both separately and independently thus making this process suitable for fabricating heterogeneous components on functionally graded materials. In addition, this technology allows the material gradient to be altered at the microstructural level due to the localized fusion and mixing in the melt

pool. This means that the clad materials can be designed to meet the performance requirement of the added layer [18].

4. Conclusion

In conclusion, the properties and the need for HEAs have been reviewed, in which it was established that HEAs are materials of the choice for future generation alloys. Selected methods of manufacture for HEAs were briefly discussed, from which it was evident that these methods range from traditional bulk forming to newer additive manufacturing technologies. With the advances in technologies, this trend in manufacturing technologies for HEAs offer a new and exciting approach for alloy design and manufacturing to meet the complex demand in bone tissue engineering. In this respect, it is recommended that the research activities should move away from trying to obtain single-phase HEAs, but instead develop alloys that possess the correct balance of desired properties for biomedical implants.

Conflict of interest


The author declares no conflict of interest.

Author details

Agripa Hamweendo*, Chiluba I. Nsofu and Terence Malama
School of Engineering and Technology, Department of Engineering (Mechanical),
Mulungushi University, Kabwe, Zambia

*Address all correspondence to: ahamweendo@mu.ac.zm

IntechOpen

© 2022 The Author(s). Licensee IntechOpen. This chapter is distributed under the terms of the Creative Commons Attribution License (<http://creativecommons.org/licenses/by/3.0>), which permits unrestricted use, distribution, and reproduction in any medium, provided the original work is properly cited. 

References

- [1] Maji PK, Banerjee PS, Sinha A. Application of rapid prototyping and rapid tooling for development of patient-specific craniofacial implant: An investigative study. *The International Journal of Advanced Manufacturing Technology*. 2008;**36**:510-515
- [2] Yang R, Hao Y, Li S. Development and application of low-modulus biomedical titanium alloy Ti2448. *Biomedical Engineering Trends*. 2011;**10**:225-247
- [3] Biswas A. Porous NiTi by thermal explosion mode of SHS: Processing, mechanism and generation of single phase microstructure. *Acta Materialia*. 2005;**53**:1415-1425
- [4] Keaveny TM, Morgan EF, Niebur GL, Yeh OC. Biomechanics of the trabecular bone. *Annual Review of Biomedical Engineering (California, USA)*. 2001;**3**:307-333
- [5] Li Y-h, Rong L-j, Li Y-y. Pore characteristics of porous NiTi alloy fabricated by combustion synthesis. *Journal of Alloys and Compounds*. 2001;**325**:259-262
- [6] Zhu SL, Yang XJ, Fu DH, Zhang LY, Li CY, Cui ZD. Stress-strain behaviour of porous NiTi alloys prepared by powders sintering. *Materials Science and Engineering A*. 2005;**408**:264-226
- [7] Yang F, Gabbitas B, Mukhtar A, Downing W. Preparation of titanium alloy rods by powder compact extrusion. *Advanced Materials Research*. 2014;**1019**:241-247
- [8] Tarik A, Sakir B. Enhanced sintering of TiNi shape memory foams under Mg vapor atmosphere. *The Minerals, Metallurgical and Materials Transactions*. 2012;**43A**:5173-5181
- [9] Sun J, Han Y, Cui K. Innovative fabrication of porous titanium coating on titanium by cold spraying and vacuum sintering. *Materials Letters*. 2008;**62**:3623-3625
- [10] Chu CL, Lin PH, Chung CY. Characterization of transformation behaviour in porous Ni-rich NiTi shape memory alloy fabricated by combustion synthesis. *Journal of Materials Science*. 2005;**40**:773-776
- [11] Minnath MA. Metals and alloys for biomedical applications. In: *Fundamental Biomaterials: Metals*. Woodhead Publishing; 2018. pp. 167-174. DOI: 10.1016/B978-0-08-102205-4.00007-6. ISBN: 9780081022054
- [12] Hamweendo A, Malama T, Botef I. Titanium-nickel alloys for bone tissue engineering application via cold spray. *International Conference on Competitive Manufacturing 2016 (COMA'16)*. 2016;**6**:273-279. DOI: 10.13140/RG.2.1.4046.9527
- [13] Sidambe AT. Biocompatibility of advanced manufactured titanium implants—A review. *Materials*. 2014;**7**:8168-8188. DOI: 10.3390/ma7128168, ISSN 1996-1944
- [14] Yuan B, Chung CY, Zhang XP, Zeng MQ, Zhu M. Control of porosity and superelasticity of porous NiTi shape memory alloys prepared by hot isostatic pressing. *Smart Materials and Structures*. 2005;**14**:S201-S206. DOI: 10.1088/0964-1726/14/5/005
- [15] Ismail MH, Goodall R, Davies HA, Todd I. Formation of microporous NiTi by transient liquid phase sintering of elemental powders. *Materials*

Science and Engineering C. 2012;**32**:
1480-1485

[16] Brantley WA, Guo W, Clark WA, Iijima M. Microstructural studies of 35 o C copper NiTi orthodontic wire and TeM confirmation of low temperature martensite transformation. Dental Materials. 2008;**24**(2):204-210

[17] Iijima M, Brantley WA, Guo WH, Clark WA, Yuasa T, Mizoguchi I. X-ray diffraction study of low-temperature phase transformations in nickel-titanium orthodontic wires. Dental Materials 2008;**24**(11):1454-1460. DOI: 10.1016/j.dental.2008.03.005

[18] Ma N, Liu S, Liu W, Xie L, Wei D, Wang L, et al. Research Progress of titanium-based high entropy alloy: Methods, properties, and applications. Review, Frontiers in BioEngineering and BioTechnology. 2020;**8**:603522. DOI: 10.3389/fbioe.2020.60352

[19] Liu F, Liaw PK, Zhang Y. Recent progress with BCC-structured high-entropy alloys. Metals. 2022;**12**:501. DOI: 10.3390/met12030501

[20] Yeh J-W, Chen Y-L, Lin S-J, Chen S-K. HIGH-ENTROPY ALLOYS – A New Era of Exploitation. Hsinchu, Taiwan: Department of Materials science and Engineering, National Tsing Hua University; 2007

[21] Wu Y, Liaw PK, Zhang Y. Preparation of bulk TiZrNbMoV and NbTiAlTaV high-entropy alloys by powder sintering. Metals. 2021;**11**:1748. DOI: 10.3390/met11111748

[22] Yin X, Shuqiong X. Properties and preparation of high entropy alloys. MATEC Web of Conferences. 2018;**142**:03003. DOI: 10.1051/mateconf/201814203003, ICMAE2017

[23] Pickering EJ, Jones NG. High-entropy alloys: A critical assessment of their founding principles and future prospects. Full Critical Review. 2016. DOI: 10.1080/09506608.2016.1180020

[24] Yeh J-W. Recent Progress in high-entropy alloys. Annales de Chimie Science des Matériaux. 2006;**31**:633-648

[25] Ma N, Liu S, Liu W, Xie L, Wei D, Wang L, et al. Research Progress of titanium-based high entropy alloy: Methods, properties, and applications. Review, Frontiers in BioEngineering and BioTechnology. 2020;**8**:1-18. DOI: 10.3389/fbioe.2020.60352

[26] Agripa H, Botef I. Modern production methods for titanium alloys: A review. In: Titanium Alloys. Novel Aspects of their Manufacturing and Processing. London: IntechOpen; 2019. DOI: 10.5772/intechopen.81712

[27] Yin X, Xu S. Properties and preparation of high entropy alloys. MATEC Web of Conferences. 2018;**142**:03003. DOI: 10.1051/mateconf/201814203003

Iron-Based Superconductors

Gedefaw Mebratie Bogale and Dagne Atnafu Shiferaw

Abstract

Superconductivity is the phenomenon of vanishing an electrical resistivity of materials below a certain low temperature and superconductors are the materials that show this property. Critical temperature is the temperature below which superconducting state occurs. Based on temperature superconductors can be grouped into high-temperature superconductors and low-temperature superconductors. Based on the mechanism, they can be grouped into conventional and unconventional superconductors. Based on magnetism superconducting materials can also be separated into two groups: type-I and type-II superconductors. In this chapter, we will discuss superconductivity, the Meissner effect, type-I and type-II superconductors, convectional and unconvictional superconductors, heavy fermions, cuprates, iron-based superconductors, and high entropy alloy superconductors. High-entropy alloys (heas) are defined as alloys containing at least five elements with concentrations between 5 and 35 atom%. The atoms randomly distribute on simple crystallographic lattices, where the high entropy of mixing can stabilize disordered solid-solution phases with simple structures. The superconducting behavior of heas is distinct from copper oxide superconductors, iron-based superconductors, conventional alloy superconductors, and amorphous superconductors, suggesting that they can be considered as a new class of superconducting materials.

Keywords: superconductivity, resistivity, temperature, magnetism, BCS theory, heavy fermions, cuprates, iron-based superconductors, high entropy superconductors

1. Introduction

Superconductivity is the set of physical properties observed in certain materials at low temperatures, characterized by the complete absence of electrical resistance or the resistance of the material to the electric current flow is zero [1]. It is a phenomenon in which the resistance of a material to electric current flow is zero. Any material exhibiting these properties or which have no resistance to the flow of electricity is known as a superconductor [2]. It was discovered by Dutch physicist Heike Kamerlingh onnes of Leiden University in 1911, who was studying the resistance of solid mercury at extremely low temperature using the recently discovered liquid helium as a refrigerant. At the temperature of about 42K (−452°F, −252°F), when he cooled to the temperature of liquid helium, He observed that the resistance abruptly or suddenly disappeared. The current was flowing through the mercury wire and nothing was stopping it, the resistance was zero (see **Figure 1** which shows a graph of resistance versus temperature of mercury wire which Onnes produced) [3].

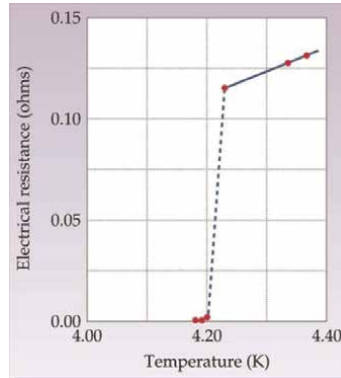


Figure 1. Resistance in ohms of a specimen of mercury versus absolute temperature. This plot by Kamerlingh Onnes marked the discovery of superconductivity [1].

2. Characteristics of superconductivity

2.1 Temperature effect

According to Onnes, “Mercury has passed into a new state; he named this new state, called superconductivity” [4]. The temperature at which superconducting state starts is called the critical temperature (T_c). In one of Onnes experiments, he started a current flowing through a loop of lead wire cooled at a liquid helium range, a year later the current was still flowing without significant current loss. He found that the new material exhibited what he called persistent currents. He discovered superconductivity and was awarded the Nobel Prize in 1913. Based on the temperature effect the superconductivity grouped under low-temperature superconductor with the temperature below 30K such as He, Al, Cd, Sn, Hg, U, Nb, Nb₃Ge, etc. and high-temperature superconductors with transition temperature above 30K such as Cuprates and Iron base superconductors [5].

2.2 Meissner effect

In addition to zero resistance, a new scientific discovery is made in 1933 by W. Meissner and R. Ochsenfeld that superconductors, which have an interesting magnetic property of excluding a magnetic field, are more than a perfect conductor of electricity. Because of Faraday’s law, the magnetic field inside a superconductor cannot change; there is no electromotive force due to the lack of electric resistance [6]. The flow of current-induced magnetic field on the Fermi-surface of superconductor cancels out the external field. A superconductor, when it is cooled below the critical temperature T_c , expels the magnetic field and does not allow the magnetic field to penetrate inside it (see **Figure 2(a)**). This phenomenon in superconductors is called the Meissner effect [3]. The most spectacular demonstration of the Meissner effect is the levitation effect [7]. That is if a small bar magnet rests on a superconducting dish; the magnet will levitate above the superconducting dish when the temperature is lowered below T_c .

The Meissner effect will occur only if the magnetic field is relatively small. If the magnetic field becomes too great, it penetrates the interior of the metal and the metal

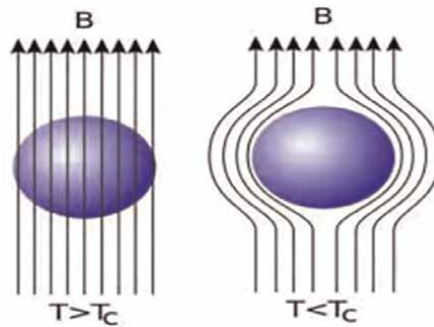


Figure 2.
Expulsion of applied magnetic flux field [7].

loses its superconductivity [8]. The certain value of magnetic field beyond which superconductor returns back to its ordinary state is called critical magnetic field. The Meissner effect is so strong that a magnet can actually be levitated over a superconductive material. Following the discovery of the Meissner effect, in 1935 two London brothers Fritz and Heinz proposed the first phenomenological theory known as the London equation which explains the Meissner effect, where in a material exponentially expels all internal magnetic fields as it crosses the superconducting threshold [9]. By using the London equation, one can obtain the dependence of the magnetic field inside the superconductor on the distance to the surface.

The London equations explained not only the Meissner effect, but also provided an expression for the first characteristic length of superconductivity known as the London penetration length (λ_L). The next theoretical advance came in 1950 with the theory of Ginsburg and Landau, which described superconductivity in terms of an order parameter and provided a derivation for the London equations [10]. This theory provides an expression for the penetration length similar to the London equations and also the expression for the second characteristic length known as the Ginsburg-Landau coherence length (ξ) which is a measure of the distance within which the superconducting electron concentration cannot change drastically in a spatially varying magnetic field [11]. A. A. Abrikosov used these concepts to roll up alloy for superconductors. He observed that if the electronic structure of the superconductor were such that the coherence length becomes less than the penetration depth, one would get magnetic behavior similar to type II superconductors, with two critical fields B_{c1} and B_{c2} . In the same year, the quantum theory of superconductivity was predicted theoretically by H. Frohlich that the T_c would decrease as the average isotopic mass increased. This effect is called the isotope effect which is observed in experimentally the same year by Maxwell [12]. The isotope effect provided support for the electron-phonon interaction mechanism of superconductivity.

3. Type I and Type II superconductors

Based on the applied magnetic field superconductors are grouped under Type I and Type II. Superconductors those converts into a normal state abruptly at the critical field below critical temperature are known as Type I super conductors as

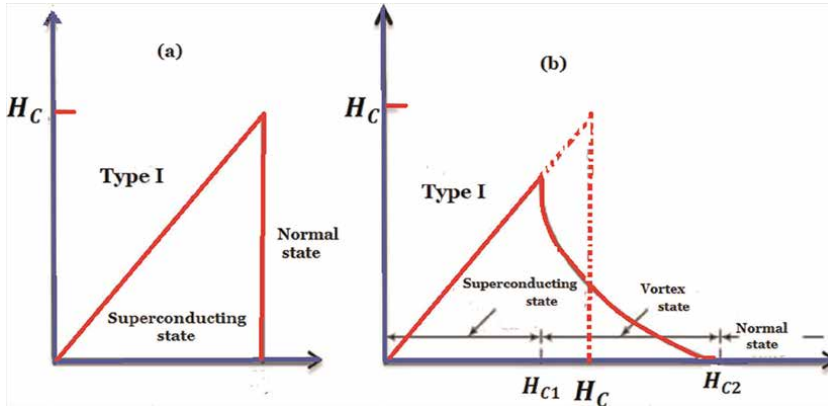


Figure 3.
Type of superconductors based on applied magnetics [1].

shown in **Figure 3(a)** [13]. These types of superconductors are usually of low-critical temperature materials, such as metals and metal alloys (such as aluminum, lead, indium, Nb_3Ge , etc.). These superconductors have only one critical field (H_C) at which it converts into normal state. And the critical magnetic field for such superconductor is very low; it is of the order of $0.01\text{--}0.2 \text{ Wb/m}^2$. Type II superconductors are depicted in **Figure 3(b)** as superconductors whose diamagnetic property increases with applied magnetic field up to a certain value (H_{C1}), after that, decreases gradually and drops to zero at the magnetic field H_{C2} and converts completely into the normal state [14].

4. Conventional superconductors

The first widely accepted and detailed microscopic theory was developed in 1957 by American physicists John Bardeen, Leon Cooper, and John Schrieffer. This theory is called BCS theory. According to BCS theory, superconductivity is quantum effect which result from the cloud of electron pair, which is called the Cooper pair and was first discovered by L. Cooper [15]. A Cooper pair is the electrons that are bound together. The BCS theory assumes that superconductivity arises due to Cooper pair, a state in which the attractive interaction dominates the repulsive Coulomb force [16]. A Cooper pair is an electron–electron pair mediated by electron–phonon interaction.

This attractive interaction is due to the attraction of negative charge ion by the core ion known as positive charged ion results distort of its lattice in such a way as to attract other electrons (the electron–phonon interaction) [17]. **Figure 4** shows that a Cooper pair is a bound state of two electrons with opposite spin and momentum which is one in the state ($k \uparrow$) and the other in the state ($k \downarrow$) [18].

The Cooper pair of the bound state becomes boson in an ordered manner therefore, the flow of electric current is able to move easily through the lattice without any electrical resistance. The BCS theory explored superconductivity at a temperature close to zero for elements and simple alloys (conventional) superconductors. However, at high temperature and with different superconductor system, the BCS theory has subsequently become inadequate to fully explain how superconductivity occurs [19].

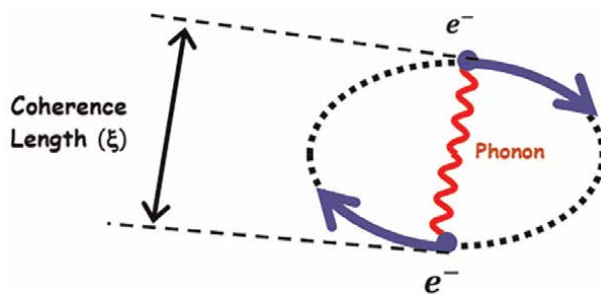


Figure 4.
The bound state of Cooper pair.

5. Unconventional superconductor

Unconventional superconductors are materials that display superconductivity which does not conform to either the conventional BCS theory or Nikolay Bogolyubov's theory. The first unconventional triplet superconductor, organic material $(\text{TMTSF})_2\text{PF}_6$, was discovered by Denis Jerome and Klaus Bechgaard in 1979. The superconducting properties of CeCu_2Si_2 , a type of heavy fermion material, were reported in 1979 by Frank Steglich [9, 20].

5.1 Heavy fermions

In the late 1970s and early 1980s, superconductivity was discovered in heavy fermions systems and in nearly magnetic systems [10]. These heavy fermions are metallic materials that hold rare earth elements, such as Yb or Ce, or actinide elements such as U with partially filled 5f shells. The name heavy fermion is given because the effective mass of electrons in these superconductors is in the order of a hundred times larger than the mass of usual electrons at low temperatures [21]. In heavy fermion compounds, the superconducting charge carriers are bound together in pairs by magnetic spin–spin interactions [22], showing that spin fluctuations (electron–electron interaction) mediate the electron pairing that leads to superconductivity in heavy fermion compounds, such as URu_2Si_2 , UPd_2Al_3 , and UNi_2Al_3 .

5.2 Cuprates

Until 1986, physicists had believed that BCS theory forbade superconductivity at temperatures above about 30K. Then, in 1986, a truly breakthrough discovery was made in the field of superconductivity. Georg Bednorz and Alex Muller, working at IBM in Zurich Switzerland, were experimenting with a particular class of metal oxide ceramics of lanthanum-based LaBaCuO called cuprate perovskites material which had a transition temperature of 35K (Nobel Prize in Physics, (1987)). Bednorz and Muller surveyed hundreds of different oxide compounds [23]. What made this discovery so remarkable was that ceramics are normally insulators. They do not conduct electricity well at all. Similar to the heavy fermion compounds, high-temperature cuprate compounds also show a delicate balance between superconductivity and magnetism. In order to understand the coexistence of superconductivity and magnetism in cuprate, it is important to know the layered perovskite-like crystal structure of these superconductors [24]. Cuprates are the second class of unconventional superconductors.

The layered structure includes CuO_2 planes. The CuO_2 plane acts as a charge reservoir and is responsible for doping (electrons or holes) into the CuO_2 planes. The movements of holes or electrons in the CuO_2 planes cause to result in superconductivity [25]. The parent compound of cuprate compound is a Mott insulator, which ought to be metal according to the band theory of electrons, but it is insulating, due to electron–electron interactions. From a common temperature versus dopant concentration, phase diagram for cuprate at very low doping concentration, antiferromagnetic (AFM) order exists in the cuprate system, and the temperature dependence of the resistivity shows an insulating behavior [26].

Increasing the doping concentration, AFM order is felled rapidly and vanishes at a certain doping level, and the superconducting order rises. As the doping level increases, T_c increases. At an optimum value of doping level, T_c reaches a maximum and the system behaves as a non-Fermi liquid. On further increasing the doping concentration, T_c decreases and finally vanishes [15]. The phase diagram suggests that AFM order does not play a conclusive role in the suppression of superconductivity, because superconductivity does not appear immediately as AFM order vanished, rather, it rises gradually with increasing doping level. Many other cuprate superconductors have since been discovered, and the theory of superconductivity in these materials is one of the major outstanding challenges of theoretical condensed matter physics [9]. Since about 1993, the highest-temperature superconductor has been a ceramic material consisting of mercury, barium, calcium, copper, and oxygen ($\text{HgBa}_2\text{Ca}_2\text{Cu}_3\text{O}_{8+\delta}$) with $T_c = 133\text{--}138\text{K}$ [20, 21]. The latter experiment (138K) still awaits experimental confirmation [27].

6. Iron-based superconductors

The third class of unconventional superconductors is iron-based superconductors. The first report of superconductivity in an iron superconductor was F-doped LaOFeP below 5K in 2006 [22]. On February 23, 2008, a group from Tokyo Institute of technology published paper in (*JACS*) *Journal of the American Society*, in which they reported that the fluorine-doped lanthanum Oxide Fe-As superconductors at 26K [28]. Similar to cuprates and several heavy fermion superconductors, superconductivity emerges here in close proximity to AFM state and like to cuprate superconductors, high-temperature superconductivity in the iron-based superconductors (FebSC) systems is also induced from electron or hole doping of their parent compounds. Parent compounds show long-range AFM static order. AFM order is suppressed on electron/hole doping to induce superconductivity. In FebSCs magnetism arising from nesting which induced spin density wave, unlike cuprates where the parent compounds are Mott insulators, strongly repulsive electronic correlations yield an insulating and ground state despite a half-filled conduction band [8].

There are several good reasons why FebSC is so interesting. First, they show the coexistence of superconductivity and magnetism. Second, they have too much variety of compounds for research and, their multi-band electronic structure offer the hope of finally discovering the mechanism of high-temperature superconductivity and finding a way to increase T_c . Lastly, they are quite encouraging for a wide scope of applications. Having a much higher critical field (H_c) than cuprates and high isotropic critical currents, they are attractive for electrical power and magnetic applications.

Compared to Cuprates, iron-based superconductors (FebSc) have some similarities. Firstly, both of their parent compounds are antiferromagnets. Increased doping

can destroy antiferromagnetism and lead to superconductivity. Secondly, superconductivity occurs in specific planes. In cuprates, it is Cu-O plane. While in FebSc, it is Fe-As plane [29]. They also have significant differences. For Cuprates, its parent compound is a special type of antiferromagnet—Mott insulator, which are a result of strong local interaction; While in FebSc, it is an antiferromagnetic—“spin-density-wave” metal. They are magnetic bad metals, originating from long-range (non-local) magnetic correlations. Moreover, the $\text{Cu}3d_{x^2-y^2}$ (a single electron) contributes to superconductivity; while in iron-based superconductors, all five Fe 3d orbitals contribute to superconductivity. Superconductivity can be achieved in both cases by doping, but doping directly to the superconducting layers is allowed only in FebSc, likely because they are more itinerant than cuprates. In superconducting samples, cuprates have Sc order parameter with a sign-changing d-wave symmetry, while the symmetry of the FebSc has a sign-changing s-wave symmetry. These differences make this new type of high-temperature superconductors very interesting.

One of the most prominent issues in the physics of Fe-based superconductors is the interplay between the magnetic and superconducting order parameters when charge doping, pressure, or other parameters are modified. In this chapter, we describe literature about iron-based superconductors. Electronic and crystal structures of iron-based superconductors, magnetic ordering and spin density wave, electron, and crystal structure of SrFe_2As_2 , the effect of nickel substitution on SrFe_2As_2 , superconductivity in $\text{SrFe}_{2-x}\text{Ni}_x\text{As}_2$, superconductivity, and magnetism [30].

According to a general phase diagram of temperature vs. dopant concentration for cuprate, at very low doping concentrations, the cuprate system has an antiferromagnetic order and the resistivity's temperature dependency behaves as an insulator. As the doping is increased, the antiferromagnetic order quickly dissipates and disappears, while the superconducting order emerges. T_c increases as doping levels rise. T_c reaches its maximum and the system behaves as a non-Fermi liquid when doping is at its optimal level. T_c decreases with increasing doping until it reaches zero. Like cuprate superconductors, FebSc systems derive their high temperature superconductivity from electron or hole doping of their parent compounds. These parent compounds exhibit long-range AFM static order, which is suppressed by electron or hole doping to induce superconductivity. In contrast to cuprates, magnetism in FebSCs results from a nesting-induced spin density wave [31].

The iron-based superconductors (FebSc) have many different systems that greatly enlarge the family of unconventional superconductors [32]. The first FebSc system $\text{LaFePO}_{1-x}\text{F}_x$ was discovered by H. Hosono et al. in 2006 with $T_c \sim 4\text{K}$, but it did not draw much attention until the same group substituted P by As and discovered a T_c of 26K in $\text{LaFeAsO}_{1-x}\text{F}_x$ in 2008. Before 2013, many FebSc compounds were discovered with different crystal structure classes and compositions. Different systems are denoted by the stoichiometric ratios of the chemical elements in their parent compounds of FebSc. Therefore, the major FebSc systems are 1111, 122, 111, 11, and 245 (e.g., LaFeAsO , SrFe_2As_2 , NaFeAs , FeTe , and $\text{Rb}_2\text{Fe}_4\text{Se}_5$). Even though they have different structures, all the FebSc systems share a building block: iron-based square-planar sheets. Like to cuprates, in which copper and oxygen form the superconducting layer, FebSc systems have iron-based layers which are crucial to their unconventional superconductivity [18].

The FebSc classes listed above can be grouped into two groups according to the elemental group of the atom that forms the superconducting layer with iron. The first group is the iron-pnictides (nitrogen family from the periodic table), that iron makes a zigzag layer with arsenic or phosphorous (Fe-As or Fe-P). The 1111, 111, and 122

classes grouped to iron pnictides [33]. Pnictides have similar magnetic structures but they have different crystal structures and symmetry groups. The second group is iron-chalcogenides (oxygen family from the periodic table), that is the iron-selenium (Fe-Se) or iron-tellurium (Fe-Te) makes the superconducting layer; this family includes the 11 and 245 classes. Both the 11 and 245 classes have special properties. The 11 class has only one system: $\text{Fe}_{1+y}\text{Te}_{1-x}\text{Se}_x$. It does not have any buffer layers between the Fe-(Te,Se) layers, and the T_c is determined by Se doping level and related to the amount of extra iron in the compound. The 245 class is a relatively new discovered of iron-based superconductors [34].

Iron pnictides and iron chalcogenides share many intriguing common properties. They both have the highest T_c s. The superconducting gaps are close to being isotropic (not varying in magnitude) around Fermi surfaces, and the ratio between the gap and T_c , $2\Delta/T_c$, is much larger than the BCS ratio, 3.52, in both families. However, the electronic structures in the two families, and the Fermi surface topologies (geometrical properties), are quite different in the materials that reach high T_c [35].

6.1 Crystal structure of iron-based superconductors

Figure 5 illustrates that the structural unit common to Fe-based materials is the square net of Fe^{2+} (formal charge) coordinated tetrahedrally by four pnictogen or chalcogen atoms. The iron containing plane is not flat; pnictogen or chalcogen atoms extend above and below the iron plane because the pnictogen and chalcogen atoms are much larger than iron atoms. They pack themselves in edge-sharing tetrahedral [13]. By contrast, the similar size difference between the copper and oxygen atoms in cuprate superconductor leads to corner-sharing octahedral packing. This structural difference is crucial. Due to their tetrahedral configuration of iron-based superconductors, the Fe atoms are close to each other than the Cu atoms in cuprate superconductors. Both Fe and Cu occupy the same row of the periodic table. Their valance electrons occupy 3d orbitals. But because of the Fe atoms' close packing, all five Fe 3d orbitals contribute charge carriers. In the cuprate, only one Cu 3d orbital contributes. The chalcogen and pnictogen also play an important role. Their p orbitals also

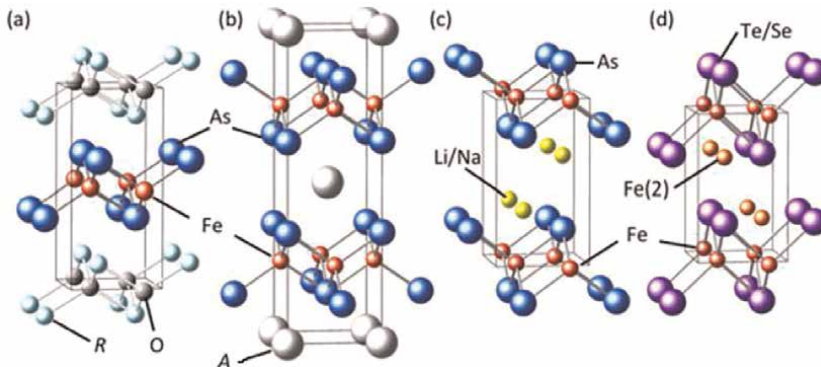


Figure 5. Four families of iron-based superconductors, (a) the 1111 family compounds ($P4/nmm$), (b) the 122 family compounds ($I4/mmm$), (c) the 111 family compounds ($P4/nmm$), and (d) the 11 family compounds ($P4/nmm$) [24].

hybridize with the five 3d orbitals leading to a complicated electron band structure and a characteristic multicomponent Fermi surface. The local structure of the Fe-pnictide layer is affected directly by the atomic (or ionic) size of M (where M indicates a metallic element such as an alkali metal, alkaline earth, or rare earth element that lies between Fe-pnictide layers) because M elements in the blocking layer bond to Pn elements [23]. Most of the iron-pnictides become superconductors only when doped (adding an impurity) with holes or electrons. T_c depends on doping concentration.

6.1.1 The 1111 iron-based superconductor family

Soon after the discovery of LaFePO in 2006, several others with similar crystal structure, were discovered. La can be substituted for almost any other rare-earth element and the superconductivity will still exist. That is because of the alternating layered structure of FeAs and RO sheets (R as rare-earth element). From theoretical studies, we can predict, that superconductivity mainly occurs in FeAs layer, while RO layer provides a charge reservoir. These materials go through structural phase transition around 160K—from tetragonal to orthorhombic lattice structure. If we drop temperature even lower, materials become antiferromagnetic [36].

LaOFeAs and other rare earth substituted compounds have a layered crystal structure and they crystallize with ZrCuSiAs type structure belonging to the tetragonal $P4/nmm$ space group [21], and the unit cell contains La_2O_2 and Fe_2As_2 molecules, and the chemical formula is represented by $(\text{La}_2\text{O}_2)(\text{Fe}_2\text{As}_2)$. The Fe_2As_2 layer is sandwiched between the La_2O_2 layers and it serves as a carrier conduction path. Conduction carriers are two-dimensionally confined in the Fe_2As_2 layer, that causing strong interactions among the electrons [37].

6.1.2 The 122 iron-based superconductor family

Next type is AFe_2An_2 , where (A stands for Alkaline earth metals like Ba, Sr, or Ca and Eu) and An is pnictide (As, P). Superconductivity can be achieved by introducing dopants. There are several ways to introduce dopants. These are (1) hole doping is achieved by substituting A for monovalent B^+ ($\text{B} = \text{Cs}, \text{K}, \text{Na}$) atoms partially in the blocking layer and this substitution should add an extra hole into the system, for example, $\text{Ba}_{1-x}\text{K}_x\text{Fe}_2\text{As}_2$; (2) partially substitute Fe for transition metals (Co, Ni, Pd, Rh) into FeAs layers and yields electrons into the system. In this way, dopants are directly substituted into the Fe layer, which can additionally stabilize the system, for example, $\text{Co}(\text{A}(\text{Fe}_{1-x}\text{Co}_x)_2\text{As}_2)$, $\text{Rh}(\text{A}(\text{Fe}_{2-x}\text{Rh}_x)\text{As}_2)$, $\text{Ni}(\text{A}(\text{Fe}_{1-x}\text{Ni}_x)_2\text{As}_2)$ and we get electron-doped pnictide that forms a rich phase diagram where the superconductivity and magnetism compete or coexist; and (3) replacing arsenic partially with phosphorus, and Phosphorus generates a chemical pressure effect that suppress SDW and emerges superconductivity at the corresponding unit-cell volume [38].

The 122 Fe-based superconductors crystallize with tetragonal ThCr_2Si_2 -type crystal structure with space group $I4/mmm$. 122 systems, for example, SrFe_2As_2 system contain practically identical layers of edge-sharing FeAs_{4/4} tetrahedra, similar to LaOFeAs but they are separated by Sr. atoms instead of LaO sheets and Sr. layer act as a charge reservoir and FeAs as superconducting layer. The compound undergoes a structural phase transition around 205K from tetragonal ($I4/mmm$) to orthorhombic ($Fmmm$) [39].

6.1.3 The 111 iron-based superconductor family

This type is AFeAs type and A stands for alkali elements (Li or Na). Crystal structure of this type is known as the CeFeSi type, with a tetrahedral P4/nmm space group-FeAs 4 layers, separated with double layer of A ions. Distance between Fe-Fe atoms in different layers is significantly shorter than in 1111 or 122 structure [36]. The crystal structures of 111 type is similar to those of 1111 type superconductors with [LaO] layers substituted by Li layers. LiFeAs has $T_c = 18\text{K}$ without extra doping. Wang *et al.* ($T_c = 18\text{K}$: LiFeAs) and Tapp *et al.* ($T_c = 18\text{K}$: NaFeAs) first reported superconductivity without doping for 111-type materials [33].

6.1.4 The 11 iron-based superconductor family

The simplest form of Fe-based superconductors are ferrochalcogenides FeSe and FeTe and their ternary combination $\text{FeSe}_x\text{Te}_{1-x}$ and $\text{Fe}_{1+y}\text{Se}_x\text{Te}_{1-x}$. Crystal structure is similar to those FeAs layers mentioned above, only that this chalcogen does not have a separating layer. T_C for FeSe is around 8K. The FeSe is much easier to synthesize, since it does not include toxic arsenic [21].

6.1.5 The 245 iron-based superconductors family

The attempts to intercalate the 11 family FeSe, the simplest FeSc, resulted in discovery of a new family $\text{A}_x\text{Fe}_{2-y}\text{Se}_2$ (A stands for alkali metal like K, Rb, Cs, and Tl). The first alkali iron selenide (245) system $\text{K}_y\text{Fe}_{1.6+x}\text{Se}_2$ was discovered in late 2010 with $T_c = 33\text{K}$. More superconductors were discovered with almost the same T_c when K was replaced with other alkali metals (Rb, Cs) or alkali metals were partially substituted with Tl. This family is most often called 245 because of its parent compound $\text{A}_{0.8}\text{Fe}_{1.6}\text{Se}_2 = \text{A}_2\text{Fe}_4\text{Se}_5$ [16]. This type of material has a unique crystal structure, and a unique magnetic structure with an unusually high structural/magnetic transition temperature; their phase diagrams and spin dynamics are also very different from those of other FeSc systems. Despite the strange crystal and magnetic structure, the 245 systems (1) have a huge moment of $\sim 30 - 34\mu_B$, which is the highest moment among all FeSc systems; (2) have a Neel temperature of more than 550K, much higher than typical FeSc Neel temperatures ($< 200\text{K}$), and similar to those in cuprates; and (3) in the small samples, are insulators [18].

6.2 Electronic structure of electron-doped iron-based superconductors

According to theories the parent compounds of iron-based superconductors are semi-metallic and the density of state near Fermi surface is mainly contributed by the iron 3d electrons and all five of the 3d electrons cross Fermi surface. The shape of the electronic band structure depends on the doping level. In electron-doped materials, such as 122 Fe-based superconductor compounds, the Fermi surface contains several quasi-2D warped cylinders centered at Γ point ($k = 0, 0$) and M point ($k = \pi, \pi$) in a 2D cross-section, and may also contain a quasi 3D pocket near $k_z = \pi$ as shown in the **Figure 6** [15, 17, 31].

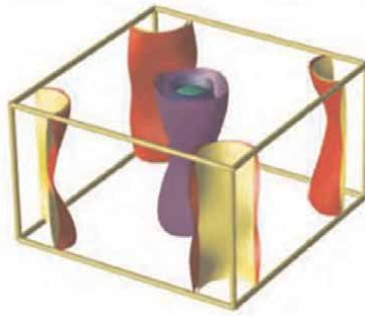


Figure 6.

The schematic electronic structure of electron-doped iron-based superconductors. In weakly and moderately electron-doped materials, the Fermi surface consists of quasi-2D warped cylinders centered at $(0, 0)$ and (π, π) in a 2D cross-section. The ones near $(0, 0)$ are hole pockets (filled states are outside cylinders), and the ones near (π, π) are electron pockets (filled states are inside cylinders) [17, 31].

6.3 The phase transitions iron-based Superconductors

The phase transitions of most FeAs-based superconductors undergo structural and/or magnetic phase transitions as presented in **Figure 7**. These superconductors show different ground states (structural, magnetic, and superconducting) which are close to each other and sometimes compete with each other. It can be detected by using X-ray and neutron scattering techniques [13]. The FeAs-based compound exhibits a tetragonal-to-orthorhombic structural phase transition at low temperatures. A tetragonal structure has the same length of the lattice parameters “ a and b ” ($a = b$)

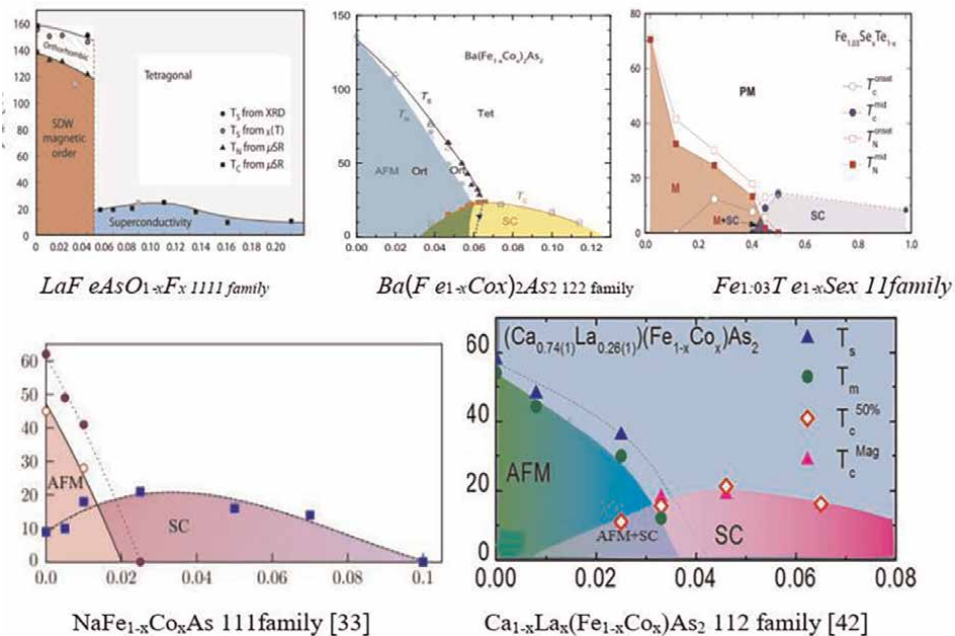


Figure 7.

Phase transition of some Iron base superconductors [31, 40–42].

whereas the lattice parameters a and b ($\neq a$) are different in an orthorhombic structure. By measuring the difference in the peak positions, we can find the respective lattice parameters and see a tetragonal-to-orthorhombic structural phase transition. A typical measure of the tetragonal-to-orthorhombic phase transition is the distortion ($\delta = \frac{a-b}{a+b}$). The structural transition was first noticed in macroscopic measurements. Magnetic order is found in many systems below some transition temperature [18].

Magnetic phase transition of the Bragg peaks depends on the periodicity of the crystal structure. The AFM ordering gives rise to a magnetic structure that has different symmetry elements (usually a subgroup of the crystallographic space group) from the crystal structure which is in the vicinity of an antiferromagnetic (AFM) phase transition [37]. Antiferromagnetism in the iron-based superconductors originates from conduction electrons that also form the Cooper pairs below T_c and the antiferromagnetic is believed to arise from the Fermi surface nesting driven spin-density-wave order (when parallel sheets of the Fermi surface can be translated by a nesting vector and superposed). Magnetism in iron-based superconductors may have both itinerant-electron and local-moment characters. In this point of view, many theories and models have been proposed in which itinerant electrons and localized moments coexist in iron-based superconductors and they play some roles in magnetism. A measure of intensities of AFM Bragg peaks as a function of a control parameter, such as temperature, is termed the AFM order parameter [38].

The phase transition of some Fe base compounds are: (1) the 1111 family compounds undergo a structural phase transition from a high temperature tetragonal ($P4/nmm$) to an orthorhombic ($Cmma$) at low temperature. (2) The undoped state, the 122 family compound exhibits simultaneous structural and magnetic phase transitions below 140K, changing from the high-temperature paramagnetic tetragonal phase to the low-temperature orthorhombic phase with the collinear AFM structure. (3) The NaFeAs 111 family compounds undergo a structural phase transition from a high temperature tetragonal ($P4/nmm$) at temperature $T_s \sim 55K$ to an orthorhombic ($Cmma$) at low temperature AFM emerges at $\sim 37K$, but not in LiFeAs. (4) The 11 family compounds undergo a structural phase transition from a high-temperature tetragonal $P4/nmm$ to an orthorhombic $Cmmm$ at low temperature. But the structural transitions are affected by subtle differences in the stoichiometry [39].

7. High entropy superconductors

As we have discussed above, cuprates are high-temperature superconductors, which are discovered by Bednorz and Mueller in 1986 and superconductivity occurs predominantly in the CuO_2 planes. Interlayer and intra-layer interactions in layered Cuprates play an important role in the enhancement of T_c , whereas T_c has been found to be proportional to the number of $Cu-O$ layer in cuprate compounds. Examples include Y-Ba-Cu-O, Bi-Sr-Ca-Cu-O, Tl-Ba-Ca-Cu-O, Hg-Ba-Ca-Cu-O, bismuth-based superconductors, etc.

Entropy is the disorder experienced in material media. For one mole of Bismuth-based cuprates, the entropy is found to be $5.603 \times 10^{-24} JK^{-1}$ at the T_c of $Bi_2Sr_2CuO_6$ (20K), $Bi_2Sr_2CaCu_2O_8$ (95K), and $Bi_2Sr_2Ca_2Cu_3O_{10}$ (110 K). When the temperature is lowered from a higher value (T_c) to a lower value, the entropy also decreases and the Cuprate materials become more ordered and entropy decreases with

an increasing number of CuO_2 planes. Entropy per mole is constant not depending on CuO_2 planes. When considered per unit mass entropy decreases with an increase in the number of CuO_2 planes [43].

Layered superconductors often exhibit high superconducting transition temperatures, such as cuprate superconductors, iron-based superconductors, and nitride-based layered superconductors. High-entropy alloys (HEAs) are defined as alloys containing at least five elements with concentrations between 5 and 35 atom%. The atoms randomly distribute on simple crystallographic lattices, where the high entropy of mixing can stabilize disordered solid-solution phases with simple structures. The HEA concept can be useful to develop new superconducting materials containing an HEA site and/or HEA-type layers. ROBiS_2 ($R = \text{La} + \text{Ce} + \text{Pr} + \text{Nd} + \text{Sm}$) is a BiS_2 -based layered superconductor that is composed of alternating stacking sequences of BiS_2 and RO layers. Superconductivity of BiS_2 -based compounds can be induced by carrier doping and/or in-plane chemical pressure. The critical temperatures of ROBiS_2 single crystals were nearly 2–4K. The superconducting critical temperature and superconducting anisotropies of R-site mixed high-entropy samples increased with a decrease in the average ionic radius of the R-site. Moreover, a deviation in the tendency to exhibit superconducting properties was observed based on the difference in the R-site mixed entropy. R-site mixed entropy in ROBiS_2 superconductors may affect their superconducting properties.

Experimentally, ROBiS_2 ($R = \text{La} + \text{Ce} + \text{Pr} + \text{Nd} + \text{Sm}$) single crystals were grown using CsCl flux. The starting materials for the growth of ROBiS_2 single crystals were La_2S_3 , Ce_2S_3 , Pr_2S_3 , Nd_2S_3 , Sm_2S_3 , Bi_2S_3 , Bi_2O_3 , and CsCl flux. Scanning electron microscopy (SEM) was conducted using a TM3030 system from Hitachi High-Technologies. The compositional ratio of the grown ROBiS_2 single crystals was evaluated using energy-dispersive X-ray spectrometry. The valence states of the La, Ce, Pr, Nd, and Sm components in the obtained single crystals were estimated by X-ray absorption spectroscopy [40].

HEA superconductor displays an excellent mechanical properties and it robust superconductivity and quiet high upper critical field that occur to be favorable for potential practical applications. The flux-pinning mechanism that control the field and temperature dependence of critical current density is very important to the practical application [41].

The superconducting behavior of HEAs is distinct from copper oxide superconductors, Fe-based superconductors, conventional alloy superconductors, and amorphous superconductors, suggesting that they can be considered as a new class of superconducting material. Until now, four types of HEA superconductors have been discovered. These are: (1) type-A HEA superconductors (e.g., the Ta-Nb-Hf-Zr-Ti superconductors) crystallize on a small unit cell BCC lattice, (2) type-B HEA superconductors (e.g., the $(\text{HfTaWIr})_{1-x}\text{Re}_x$ superconductors, $x < 0.6$) crystallize on a larger-unit-cell cluster-based BCC lattice, (3) type-C HEA superconductors (e.g., the Sc – Zr – Nb – Ta – Rh – Pd superconductors) crystallize on small cell CsCl-type lattice, and (4) type-D HEA superconductors (e.g., the $\text{Re}_{0.56}\text{Nb}_{0.11}\text{Ti}_{0.11}\text{Zr}_{0.11}\text{Hf}_{0.11}$ superconductor) crystallize on an HCP lattice. The HEA superconductors that crystallize on the small cell BCC or CsCl-type lattices have the highest transition temperatures.

Even if the type-A and type-B HEA superconductors have highly disordered atoms on simple lattices, the effects of elemental makeup and valence electron count on their physical properties are important. For this property, the T_c values mimic the classic Mathias behavior observed for binary alloys, although not in detail, and are limited by the chemical stability. Increasing the configurational entropy by adding elements has

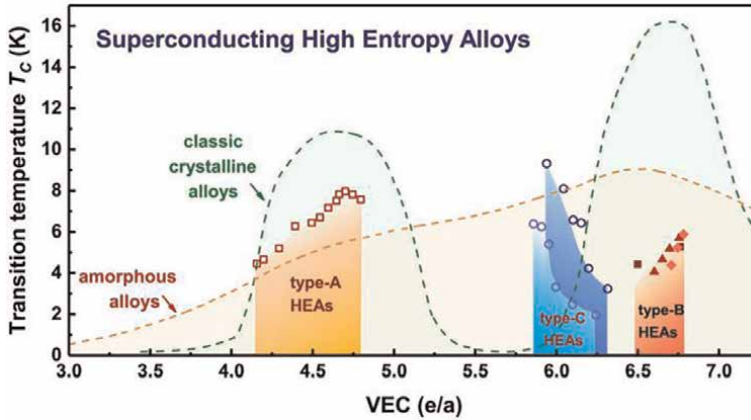


Figure 8. Valence electron count (VEC) dependence of the superconducting transition temperatures for type-A, type-B and type-C HEA superconductors compared to amorphous alloys and classic crystalline alloys [42].

no conclusive effect on the T_c of the HEA superconductors, but can stabilize their cocktail-like crystal structures. Applying pressure, the HEA superconductors exhibit vigorous superconductivity against volume shrinkage without structural phase transitions, with the common feature that T_c saturates at a constant optimal value at a critical pressure that changes from system to system.

At the present time, the HEA superconductors display type-II superconducting behavior. Therefore, the upper critical magnetic fields of the current HEA superconductors are not as high as those of NbTi or Nb₃Sn. They are employed in fabrication of the majority of commercial superconducting magnets at this time, researches expect that future superconducting HEAs may be good candidate materials for the fabrication of the superconducting magnets. The superconducting T_c s of the HEAs so far found are intermediate between those of amorphous alloys and simple binary alloys, at a fixed VEC following a trend of increasing T_c with decreasing disorder [42] as shown in **Figure 8**.

8. Conclusion

The phenomenon of vanishing of electrical resistivity of materials below a particular low temperature is called superconductivity and the materials which exhibit this property are called superconductors. The superconducting state of a material is decided by three parameters such as temperature, external magnetic field, and the current density flowing through the material. These three parameters are coupled together to define the superconducting limits of a material. For the occurrence of superconductivity in a material, the temperature must be below T_c , the external magnetic field must be below H_c and the current density flowing through the material must be below J_c [20].

After 20 years of the discovery of Onnes, a major breakthrough came in 1933 when Walther Meissner and his student Robert Ochsenfeld discovered an important magnetic property of superconductors. They observed that [12] when a specimen (sample) is placed in a magnetic field and is then cooled through the transition temperature for superconductivity, the magnetic flux originally present is ejected from the specimen [35] and exhibits diamagnetic behavior [8]. The Meissner effect suggests that perfect diamagnetism is an essential property of the superconducting state [35].

BCS theory is a comprehensive theory developed in 1957 by the American physicists John Bardeen, Leon N. Cooper, and John R. Schrieffer to explain the microscopic behavior of superconducting materials [30]. The principal insight of the theory is that superconductivity results when electrons in a material form microscopic particles known as Cooper pairs. Electrons are fermions, which are subject to the Pauli Exclusion Principle; Cooper pairs are bosons, meaning they can collect in the same low energy ground state that is the superconducting state [39]. It makes a crucial assumption that is an attractive force exists between electrons. This force is due to the Coulomb attraction between the electron and the crystal lattice. An electron passes through the lattice and the positive ions are attracted to it, causing a distortion in their nominal positions and a slight increase in positive charges around it. This increase in positive charge will, in turn, attract another electron. These two electrons are Cooper pairs [31] which are discovered by Cooper [30]. These are also referred to as superelectrons [8]. Superconductivity requires a low temperature that means the thermal vibration of the lattice must be small enough to allow the forming of Cooper pairs. In a superconductor, the current is made up of these Cooper pairs, rather than individual electrons [2].

Based on temperature superconductors can be grouped into high-temperature superconductors and low-temperature superconductors, and based on the mechanism they can be grouped into conventional and unconventional superconductors [7]. Based on magnetism superconducting materials can also be separated into two groups: type-I and type-II superconductors [9, 20]. Type-I materials, while in the superconducting state, are completely diamagnetic which is characterized by the Meissner effect [8]. They have sharp critical magnetic field, which is usually very low. There are two critical fields for type-II superconductors, the lower critical field and the upper critical field. If the external magnetic field is less than the lower field, the field is completely ejected and the material act the same as a type-I superconductor [8, 35].

The discovery of high transition temperature (T_c) superconductor is a landmark in the history of condensed matter physics. In 1979, the discovery of superconductivity in the heavy fermion compound, CeCu_2Si_2 [22] came as a surprise, because the pairing of heavy fermions through electron-phonon interaction, as postulated by BCS theory [7], is highly unlikely. After this discovery, other heavy fermions were discovered. It has been suggested that in these compounds, the superconducting charge carriers are bound together in pairs by magnetic spin-spin interactions. Cuprates are the second class of high T_c superconductors and was discovered in 1986 by J. G. Bednorz and K. A. Müller with $T_c = 35\text{ K}$ in $\text{La}_{2-x}\text{Ba}_x\text{CuO}_4$. The other class of high T_c materials are iron-based superconductors (FeSc) which were discovered in 2008 by Hosono and co-workers with $T_c = 26\text{ K}$ in LaOFeAs [7].

The first group is the iron-pnictides (nitrogen family from the periodic table [8]), in which iron forms a zigzag layer with arsenic or phosphorous (Fe-As or Fe-P). The 1111, 111, and 122 classes group to iron pnictides. Despite their different crystal structures and symmetry groups, they have similar magnetic structures. The second group is iron-chalcogenides (oxygen family from the periodic table [8]), in which iron-selenium (Fe-Se) or iron-tellurium (Fe-Te) forms the superconducting layer; this group includes the 11 and 245 classes.

The superconducting dome is asymmetric, with rather sharp onset and more gradual offset of superconductivity as a function of concentration. At the edge of the dome, the width in temperature of the superconducting transitions increases, and the diamagnetic screening fraction is substantially decreased. These characteristics may be taken as signatures of inhomogeneous superconductivity appearing at the edges of

the superconducting phase region, even though the chemical doping distribution appears chemically homogeneous throughout the entire substitutional range [37].

High-entropy alloys (HEAs), newly discovered materials that were proposed in 2004, are typically composed of five or more major elements in similar concentrations, ranging from 5 to 35 atom% for each element. Until now, four types of HEA superconductors have been discovered. The type-A HEA superconductors (e.g., the Ta-Nb-Hf-Zr-Ti superconductors) consist of the early transition metals and crystallize on a small unit cell BCC lattice. Type-B HEA-superconductors (e.g., the $(\text{HfTaWIr})_{1-x}\text{Re}_x$ superconductors, $x < 0.6$) mainly consist of the 5d transition metals, and crystallize on a larger-unit-cell cluster-based BCC lattice. Type-C HEA superconductors (e.g., the Sc – Zr – Nb – Ta – Rh – Pd superconductors) are composed of the early transition metals and the late transition metals and crystallize on a small cell CsCl-type lattice. Type-D HEA superconductors (e.g., the $\text{Re}_{0.56}\text{Nb}_{0.11}\text{Ti}_{0.11}\text{Zr}_{0.11}\text{Hf}_{0.11}$ superconductor) crystallize on a HCP lattice [42].

Acknowledgements

We acknowledge Mrs. Mintamr Lewoyehu for typing the first draft of the chapter.

Funding

Not applicable.

Conflict of interest

We confirm there are no conflicts of interest.

Author details


Gedefaw Mebratie Bogale^{1*} and Dagne Atnafu Shiferaw²

1 Department of Physics, Natural and Computational Science, Mekdela Amba University, Tulu Awuliya, Ethiopia

2 Department of Physics, Natural and Computational Science, Dilla University, Dilla, Ethiopia

*Address all correspondence to: gedefawmebratie22@gmail.com

IntechOpen

© 2022 The Author(s). Licensee IntechOpen. This chapter is distributed under the terms of the Creative Commons Attribution License (<http://creativecommons.org/licenses/by/3.0>), which permits unrestricted use, distribution, and reproduction in any medium, provided the original work is properly cited. 

References

- [1] Beiser A. Concepts of modern physics. 6th ed. New York: Tata McGraw-Hill Education; 2003
- [2] Marder MP. Condensed Matter Physics. Hoboken, New Jersey: John Wiley & Sons; 2010
- [3] Shekhter RI, Galperin Y, Gorelik LY, Isacsson A, Jonson M. Shuttling of electrons and Cooper pairs. *Journal of Physics: Condensed Matter*. 2003;**15**(12):R441
- [4] Scalapino DJ. A common thread: The pairing interaction for unconventional superconductors. *Reviews of Modern Physics*. 2012;**84**(4):1383
- [5] Aswathy PM, Anooja JB, Sarun PM, Syamaprasad U. An overview on iron based superconductors. *Superconductor Science and Technology*. 2010;**23**(7):073001
- [6] Hosono H, Kuroki K. Iron-based superconductors: Current status of materials and pairing mechanism. *Physica C: Superconductivity and Its Applications*. 2015;**514**:399-422
- [7] Chubukov AV, Efremov DV, Eremin I. Magnetism, superconductivity, and pairing symmetry in iron-based superconductors. *Physical Review B*. 2008;**78**(13):134512
- [8] Ishida S, Nakajima M, Liang T, Kihou K, Lee C-H, Iyo A, et al. Effect of doping on the magnetostructural ordered phase of iron arsenides: A comparative study of the resistivity anisotropy in doped BaFe₂As₂ with doping into three different sites. *Journal of the American Chemical Society*. 2013;**135**(8):3158-3163
- [9] Canfield PC, Bud'Ko SL. FeAs-based superconductivity: A case study of the effects of transition metal doping on BaFe₂As₂. arXiv preprint arXiv:1002.0858. 2010
- [10] Werner P, Casula M, Miyake T, Aryasetiawan F, Millis AJ, Biermann S. Satellites and large doping and temperature dependence of electronic properties in hole-doped BaFe₂As₂. *Nature Physics*. 2012;**8**(4):331-337
- [11] Hu J, Hao N. S₄ symmetric microscopic model for iron-based superconductors. *Physical Review X*. 2012;**2**(2):021009
- [12] Wang F, Lee D-H. The electron-pairing mechanism of iron-based superconductors. *Science*. 2011;**332**(6026):200-204
- [13] Yin ZP, Haule K, Kotliar G. Spin dynamics and orbital-antiphase pairing symmetry in iron-based superconductors. *Nature Physics*. 2014;**10**(11):845-850
- [14] Gurevich A. Iron-based superconductors at high magnetic fields. *Reports on Progress in Physics*. 2011;**74**(12):124501
- [15] Tarantini C, Gurevich A, Jaroszynski J, Balakirev F, Bellingeri E, Pallecchi I, et al. Significant enhancement of upper critical fields by doping and strain in iron-based superconductors. *Physical Review B*. 2011;**84**(18):184522
- [16] Johannes MD, Mazin II, Parker DS. Effect of doping and pressure on magnetism and lattice structure of iron-based superconductors. *Physical Review B*. 2010;**82**(2):024527
- [17] Xu G, Zhang H, Dai X, Fang Z. Electron-hole asymmetry and quantum

- critical point in hole-doped BaFe_2As_2 . EPL (Europhysics Letters). 2009;**84**(6): 67015
- [18] Han Q, Chen Y, Wang ZD. A generic two-band model for unconventional superconductivity and spin-density-wave order in electron-and hole-doped iron-based superconductors. EPL (Europhysics Letters). 2008;**82**(3): 37007
- [19] Li LJ, Luo YK, Wang QB, Chen H, Ren Z, Tao Q, et al. Superconductivity induced by Ni doping in BaFe_2As_2 single crystals. New Journal of Physics. 2009;**11**(2):025008
- [20] Chu J-H, Analytis JG, Kucharczyk C, Fisher IR. Determination of the phase diagram of the electron-doped superconductor $\text{Ba}(\text{Fe}_{1-x}\text{Co}_x)_2\text{As}_2$. Physical Review B. 2009;**79**(1): 014506
- [21] Duncan WJ, Welzel OP, Harrison C, Wang XF, Chen XH, Grosche FM, et al. High pressure study of BaFe_2As_2 the role of hydrostaticity and uniaxial stress. Journal of Physics: Condensed Matter. 2010;**22**(5):052201
- [22] Ren Z, Tao Q, Jiang S, Feng C, Wang C, Dai J, et al. Superconductivity induced by phosphorus doping and its coexistence with ferromagnetism in $\text{EuFe}_2(\text{As}_{0.7}\text{P}_{0.3})_2$. Physical Review Letters. 2009;**102**(13):137002
- [23] Johrendt D, Pöttgen R. Superconductivity, magnetism and crystal chemistry of $\text{Ba}_{1-x}\text{K}_x\text{Fe}_2\text{As}_2$. Physica C: Superconductivity. 2009;**469**(9-12):332-339
- [24] Chen H, Ren Y, Qiu Y, Wei Bao RH, Liu G, Wu T, et al. Coexistence of the spin-density wave and superconductivity in $\text{Ba}_{1-x}\text{K}_x\text{Fe}_2\text{As}_2$. EPL (Europhysics Letters). 2009;**85**(1):17006
- [25] Böhmer AE, Hardy F, Wang L, Wolf T, Schweiss P, Meingast C. Superconductivity-induced re-entrance of the orthorhombic distortion in $\text{Ba}_{1-x}\text{K}_x\text{Fe}_2\text{As}_2$. Nature Communications. 2015;**6**(1):1-7
- [26] Evtushinsky DV, Inosov DS, Zabolotnyy VB, Viazovska MS, Khasanov R, Amato A, et al. Momentum-resolved superconducting gap in the bulk of $\text{Ba}_{1-x}\text{K}_x\text{Fe}_2\text{As}_2$ from combined ARPES and μSR measurements. New Journal of Physics. 2009;**11**(5):055069
- [27] Sbeia IR, Ivanovskil AL. Electronic structure of new oxygen-free 38 K superconductor $\text{Ba}_{1-x}\text{K}_x\text{Fe}_2\text{As}_2$ in comparison with BaFe_2As_2 from first principles. Письма в Журнал экспериментальной и теоретической физики. 2008;**88**(1-2):115-118
- [28] McLeod JA, Buling A, Green RJ, Boyko TD, Skorikov NA, Kurmaev EZ, et al. Effect of 3d doping on the electronic structure of BaFe_2As_2 . Journal of Physics: Condensed Matter. 2012;**24**(21):215501
- [29] Hosono H, Yamamoto A, Hiramatsu H, Ma Y. Recent advances in iron-based superconductors toward applications. Materials Today. 2018;**21**(3):278-302
- [30] Fukazawa H, Yamazaki T, Kondo K, Kohori Y, Takeshita N, Shirage PM, et al. ^{75}As NMR study of hole-doped superconductor $\text{Ba}_{1-x}\text{K}_x\text{Fe}_2\text{As}_2$ ($T_c \approx 38$ K). Journal of the Physical Society of Japan. 2009;**78**(3):033704
- [31] Nuwal, Anuj, and Shyam Lal Kakani. Theoretical study of specific heat and density of states of MgB_2 superconductor in two band model. World Journal of Condensed Matter Physics. 2013;**3**:1-10. DOI:10.4236/wjcmp.2013.31006

- [32] Plakida NM. Thermodynamic green functions in theory of superconductivity. *Condensed Matter Physics*. 2006; **77**(10): 105004
- [33] Chanpoom T, Seechumsang J, Chantrapakajee S, Udomsamuthirun P. The study on hybridized two-band superconductor. *Advances in Condensed Matter Physics*. 2013;**2013**:1-7. DOI: 10.1155/2013/528960
- [34] Mohapatra R, Rout GC. Spin density wave interaction in two band model for the iron-based superconductors. *International Journal of Scientific and Engineering Research*. 2014;**5**(3):2229-5518
- [35] Kidanemariam T, Kahsay G, Mebrahtu A. Theoretical investigation of the coexistence of superconductivity and spin density wave (SDW) in two-band model for the iron-based superconductor $\text{BaFe}_2(\text{As}_{1-x}\text{P}_x)_2$. *The European Physical Journal B*. 2019;**92**(2):1-12
- [36] Rotter M, Pangerl M, Tegel M, Johrendt D. Superconductivity and crystal structures of $(\text{Ba}_{1-x}\text{K}_x)\text{Fe}_2\text{As}_2$ ($x=0-1$). *Angewandte Chemie International Edition*. 2008;**47**(41):7949-7952
- [37] Jiang S, Xing H, Xuan G, Wang C, Ren Z, Feng C, et al. Superconductivity up to 30 K in the vicinity of the quantum critical point in $\text{BaFe}_2(\text{As}_{1-x}\text{P}_x)_2$. *Journal of Physics: Condensed Matter*. 2009;**21**(38):382203
- [38] Alireza PL, Chris Ko YT, Gillett J, Petrone CM, Cole JM, Lonzarich GG, et al. Superconductivity up to 29 K in SrFe_2As_2 and BaFe_2As_2 at high pressures. *Journal of Physics: Condensed Matter*. 2008;**21**(1):012208
- [39] Fukazawa H, Takeshita N, Yamazaki T, Kondo K, Hirayama K, Kohori Y, et al. Suppression of magnetic order by pressure in BaFe_2As_2 . *Journal of the Physical Society of Japan*. 2008;**77**(10): 105004
- [40] Fujita Y, Kinami K, Hanada Y, Nagao M, Miura A, Hirai S, et al. Growth and characterization of ROBiS_2 high-entropy superconducting single crystals. *ACS Omega*. 2020;**5**(27):16819-16825
- [41] Gao L, Ying T, Zha Y, Cao W, Li C, Xiong L, et al. Fishtail effect and the vortex phase diagram of high-entropy alloy superconductor. *Applied Physics Letters*. 2022;**120**(9):092602
- [42] Sun L, Cava RJ. High entropy alloy superconductors: Status, opportunities and challenges. *Physical Review Materials*. 2019;**3**(9):090301
- [43] Jared OO, Wanjala MJ. Specific heat and entropy of a three electron model in bismuth based cuprate superconductor. *World Journal of Applied Physics*. 2018;**3**(2):19-24



Edited by Yong Zhang

High Entropy Materials - Microstructures and Properties summarizes recent developments in multicomponent materials. It discusses properties, processing, modeling, and applications of high-entropy materials, including metallic alloys and oxides. It also discusses solidification, sputtering, cryogenic treatments, CALPHAD methodology, biomedical implants, Fe-based superconductors, Fe-rich high-entropy alloys, and more.

Published in London, UK

© 2023 IntechOpen
© Philipp Tur / iStock

IntechOpen

